Imperial College London

Gravure Printed and Solution-Processed Polymer Semiconductor Devices

Dae-Young Chung

Experimental Solid State Group, Department of Physics

Imperial College London

– 2011 –

A thesis submitted in fulfilment of the requirements for the degree of Doctor of Philosophy of Imperial College London

Declaration of Originality

"Except where specific is made to the work of others, this work is original and has not been already submitted either wholly or in part to satisfy degree requirements at this or any other university."

Dae-Young Chung

Acknowledgement

Doing a Ph.D degree delivered me a fulfillment of joyfulness regarding research and investigation of new phenomenon. Although a 4-years research in organic electronic fields made me to concentrate fully on the laboratory, a completion of Ph.D could be never succeeded without enormous assists from many people. I would like to thank all of people for delivering me this joyfulness. First of all, I would like to thank God for guiding me in his way and letting me learn not only knowledge throughout the research but wisdom about how to deal with difficulties. I would like to very specially thank to Dr Alasdair Campbell for his every supervision during the study and he always gave me useful suggestions and provided me all the equipment required for the research. He also allowed me to spend six months for doing a couple of internships in Samsung Advanced Institute of Technology (SAIT) and LG Electronics, which brought me a great experience by broadening my view on the Ph.D research. Professor Donal Bradley also supported me by offering his knowledge from a broad experience and suggestions with scarce insights. Developing high efficient bilayer PLEDs was built based on his suggestion. Dr Ji-Seon Kim also suggested me with useful ideas for the phase separation of F8BT:TFB blend even though the work is still ongoing. Also, Professor Jenny Nelson offered me her generosity on experimental supports and advice. I had a great experience from two internships and would like to thank Dr Jong-Min Kim, Dr Byoung-Lyong Choi, Dr Eun-Kyung Lee, Dr Tae-Ho Kim, Dr Kyung-Sang Cho, Mr Sang-Jin Lee, Dr Jong-Jin Park for their helps in SAIT and Dr Young-Hwan Choi, Mr Jae-Won Chang, Dr Sung-Eun Lee, Dr Jung-Hoon Son for their helps in LG Electronics laboratory.

A lot of people in EXSS group contributed to my research and I would like to specially thank Mrs Carolyn Dale, Mrs Patel Bhavna, Mrs Loli Sanchez Rey and Mrs Claudia Harriott for

their administrative supports. Professor Lesley Cohen for her sincere cares, Dr Dong-Seok Leem for his significant supports on using of Cs_2CO_3 and inverted PLEDs, Dr Jingsong Huang for his helpful discussions on printing and PLEDs, Dr Monika Voigt for training me on using of gravure printer and guidance at the beginning of the Ph.D, Dr Xuhua Wang for her careful supports on the experiments and discussions based on her previous experiments, Dr Xiangjun Wang for her contribution on discussing about inverted PLEDs, Dr Alex Guite, who started Ph.D together on the Contact Project, for his useful discussion, helps and time spent on drinking after long day experiments, Mr Yoon Hong for his every supports as a best flat mate and a photographer and discussion on the optical laser, Mr Justin Dane for his supports on contact angle measurements, Dr Jongin Hong for offering me his excellent advises based on his experience, Dr Peter Levermore for his previous research on PLEDs, Mr Sung-Soo Kim and Dr Gihan Ryu for being an excellent adviser.

Also I would like to thank other EXSS group people who have kindly supported me with their time and assistance. I would like to thank Dr Thomas Anthopoulos, Dr Paul Savrinou, Dr Colin Belton, Dr Paul Woebkenberg, Dr Ruidong Xia, Dr Pedro Atienzar, Dr Sachetan Tuladhar, Dr Thilini Ishwara and Dr Thomas Wellinger for their useful suggestions and discussions. I also thank lovely people in Huxley H722, who have shared a nice office, Dr Johannes Gambari, Dr Peter Seem, Dr. Hemmel Amrania, Ms Emma Lewis, Ms Martina Mohr, Mr Liam O'Brien, Mr Huang Zeng, Mr Florian Colleaux, Mr Robert Ward, Mr João Sampaio, Mr Stuart Thomas and Mr John McGurk.

I also would like to thank Dr Fanshun Meng, Dr Joachim Steinke and Dr Alan Mosley for their helps on the Contact Project.

I sincerely thank Dr Eun-Hyuk Kim and Mrs Hyun-Ok Kim for enormous cares for settling in U.K. Finally, I would like to thank my mom and dad who have supported me both financially and emotionally during the study. I also never forget enormous supports from my sister Jina and Min.

Abstract

The idea of printing optoelectronic devices has been developed over the last decade by various printing techniques such as screen printing, transfer printing, and inkjet printing, attributed to the advent of soluble organic semiconducting (OSC) materials. Printing of optoelectronic devices provides economical advantages for its fast and simple processing stages which is conceptually similar to the graphical printing. The advantage is expected to overcome the relatively low performance of organic materials where its charge transport is occurred by hopping process which is limited by its hopping distance and conformation of molecular chains. Printing techniques currently available should be optimized further to attract a huge impact. For example, the inkjet printing has a drawback of its low printing speed although it offers the printing of high definition pixels with its width around 60 μm.

In this Thesis, gravure printing, a high throughput printing technique, is discussed to experimentally demonstrate its feasibility as a production method of optoelectronic devices. The targeted device structures are organic light-emitting diodes (OLEDs) and field-effect transistors (OFETs). Both printed OFETs and OLEDs have reached device performance similar to reference devices with the same materials and structures fabricated by spin-coating. Unlike the graphic art printing, such as is used to fabricate newspapers, magazines and posters, the printing of OSC optoelectronic devices is very sensitive to processing conditions attributed to a thickness of very thin layers, usually less than 100 nm. Therefore, the surface uniformity of the printed layers must be very planar, with a surface roughness root mean square (RMS) value typically less than 3 nm. It is found that controlling hydrodynamic forces during the thin film formation, such as the coffee stain convection flow and the surface tension driven Marangoni flow, offer a clear opportunity for achieving devices with high performance in gravure contact printed thin films.

Chapter 2 and 3 discuss background theory related to experiments in this thesis. Chapter 4 is an experimental chapter explaining materials used and experimental techniques. In Chapter 5, gravure printing of OLEDs with printed poly(3,4-ethylenedioxythiophene): poly(styrenesulfonate) (PEDOT: PSS) hole injection and LUMATION Green 1300 (LG1300) light emissive layers is developed with discussions of wetting of printing formulations and fluidic movements observed during film formation. A mixture of solvent method provides the circulation of hydrodynamic flows inside the printed formulation providing a deposition of highly uniform thin film after solvent evaporation. As a result, high performance of OLEDs with its performance of 8.8 cd/A and 5.4 lm/W with a maximum brightness of 66,000 cd/m^2 is reported in OLEDs where both PEDOT: PSS and LG1300 are gravure printed. The performance is the highest up to date among the OLEDs printed by the same printing method.

Chapter 6 introduces an inverted structure type OLED where its high work function anode is placed on the top of the device so that it consequently improves device stability as high work function metals such as Au or Ag are less sensitive to ambient dopants. The use of carbonate or oxide layers on the top of a high workfunction metal at the bottom of the device induced efficient injection of electrons to the device. A very thin layer of caesium carbonate (Cs_2CO_3) around 5-10 nm was gravure printed onto the ITO electrode. The printed Cs_2CO_3 layer showed that the surface roughness is highly improved owing to molecular ordering is affected and improved by the mechanical forces such as pressure and thermal energy engaged during the printing. The inverted OLEDs with the printed Cs_2CO_3 layer recorded the device performance of 10 cd/A and 3 lm/W with a maximum brightness of around 7,500 cd/m^2. This is a first report showing that a very thin and inorganic layer can also be gravure printed.

Chapter 7 describes charge balancing and position of recombination zone in inverted OLEDs using poly (9,9-dioctylfluorene-*co*-benzothiadiazole) (F8BT) and poly (9,9-dioctylfluorene-*co*-N-(4-butylphenyl)-diphenylamine) (TFB) bilayer structure. The two layers are either hole or electron transporting materials and can form a large energy offsets between the HOMO levels and the LUMO levels of the two materials at the interface which confines a large number of injected charge carriers there. It is shown that a position of recombination zone and the charge carrier confinement effect are dependent with the thicknesses of the two polymer layers. The confined charged carriers induce the recombination zone to be

positioned close to the interface where charge carrier tunnelling and Föster energy transfer occur more frequently than the bulk. The experimentally optimized thicknesses of the two layers record the highest efficiency of 36 cd/A and 23 lm/W with a bright emission of 51,200 cd/m^2 at a low voltage around 4 V. The efficiency is the highest efficiency reported so far to the best of our knowledge using fluorescence materials.

Chapter 8 explains gravure printing of OFETs using a thiophene polymer. Poly(3-hexylthiophene)-2,5-diyl (P3HT) OSC, two dielectric layers, and top Ag gate electrode are sequentially gravure printed. The annealing condition of P3HT, choice of dielectric layer and issues related to printing P3HT are discussed. Fully gravure printed OFETs on the pre-patterend ITO source and drain pattern report a high mobility of 3×10^{-2} cm^2/Vs and an on/off current ratio of $10^{4.62}$. The performance is the highest among the printed OFETs using P3HT.

Table of Contents

I. Introduction 1

II. Organic Semiconductor Optoelectronic Devices 6

2.1 Introduction 6
2.2 Organic Optoelectronic Materials 7
2.2.1 Carbon chemistry 8
2.2.2 Organic materials 10
2.2.3 Conjugated polymers 11
2.2.4 Electronic molecular states 12
2.3 Organic Field-Effect Transistors (OFETs) 15
2.3.1 Device structure 16
2.3.2 Device operation 18
2.3.3 Charge carrier transport 20
2.3.4 Charge injection 24
2.3.5 Device geometry 25
2.3.6 Dielectric layer and self-assembled monolayer (SAM) 27
2.3.7 Device characteristics 32
2.4 Organic Light-Emitting Diodes (OLEDs) 36
2.4.1 Device structure 37
2.4.2 Device operation 40
2.4.3 Charge injection and transport 43
2.4.4 Charge carrier recombination 46
2.5 Reference 48

III. Printing Techniques for Organic Semiconductor Optoelectronic Devices 53

3.1 Introduction 53
3.2 Printing Techniques 54
3.3 Physical Parameters in Printing 66
3.3.1 Surface tension 66
3.3.2 Shear force, Viscosity – Newtonian fluid 67
3.3.3 Capillary force 68
3.3.4 Solubility 68
3.4 Fluidic Movements inside Ink Formulation 70
3.4.1 Coffee stain effect 70
3.4.2 Surface tension driven Marangoni flow 74
3.5 Hydrodynamics in Printing Process 77
3.5.1 Application in ink-jet printing 77
3.5.2 Application in other printing 81
3.5.3 Research work in this Thesis 83
3.6 Conclusion 85
3.7 Reference 86

IV. Experimental Techniques and Materials 89

4.1 Organic Materials used in the Thesis 89
4.1.1 Poly(3,4-ethylenedioxythiophene): poly(styrenesulfonate) (PEDOT: PSS) 89
4.1.2 Poly (9,9-dioctylfluorene-*co*-benzothiadiazole) (F8BT) 90
4.1.3 Poly (9,9-dioctylfluorene-*co*-N-(4-butylphenyl)-diphenylamine) (TFB) 91
4.1.4 Poly(9,9-dioctylfluorene-*co*-bithiophene) (F8T2) 91
4.1.5 Lumation Green (LG)1300 92
4.1.6 Poly(3-hexylthiophene)-2,5-diyl (P3HT) 93
4.2 Gravure Contact Printing 93
4.2.1 Printing procedure 94

4.2.2 Engaged force 95
4.2.3 Engraved cliché pattern 96
4.2.4 Control printing parameters 97
4.3 Device Characterization 98
4.3.1 Field-effect transistor (FET) measurement 98
4.3.2 Current density-voltage-luminescence (*J-V-L*) characteristic 99
4.4 Spectroscopy and Electroluminescence 99
4.4.1 Absorption 99
4.4.2 Photoluminescence (PL) 100
4.4.3 Electroluminescence (EL) 101
4.5 Contact Angle Measurement 102
4.6 Atomic Force Microscopy (AFM) 106
4.7 Reference 108

V. High Performance, Flexible Polymer Light-Emitting Diodes (PLEDs) with Gravure Printed Organic Layers 110

5.1 Introduction 110
5.2 Experimental 111
5.3 Printing of PEDOT:PSS Formulation (high surface tension and polar) 113
5.4 Printing of LG1300 Formulation (low surface tension and dispersive) 121
5.5 Morphology in Nanoscale of Printed Layers 127
5.6 Device Performance Compared to Spin-coated Films 128
5.7 Conclusion and Future Work 131
5.8 Reference 132

VI. Flexible Multilayer Hybrid Polymer Light-Emitting Diodes (PLEDs) with a Gravure Printed Cs_2CO_3 Layer 135

6.1 Introduction 135
6.2 Experimental 137
6.3 Structural Design of F8BT/TFB Bilayer 139
6.4 Gravure Printing of Cs_2CO_3 Layer 143

6.5 Device Characteristics of Inverted PLEDs 146
6.6 Conclusion and Future Work 151
6.7 Reference 152

VII. Air-Stable, Flexible F8BT/TFB PLEDs having High Efficiency 154

7.1 Introduction 154
7.2 Experimental 157
7.3 Comparison of Structural and Material Type 158
7.4 Thickness Variation of F8BT and TFB Layers 166
7.5 Exciton Formation and Decay 173
7.6 Device Characterization of F8BT/TFB Multilayer 175
7.7 Conclusion and Future Work 179
7.8 Reference 180

VIII. Developing Gravure Contact Printed Flexible Polythiophene Thin-Film Transistors (TFTs) 183

8.1 Introduction 183
8.2 Experimental 185
8.3 Annealing Effects on P3HT OFETs 187
8.4 Gate Insulators with Different Dielectric Constant κ 190
8.5 Dedoping Treatment 194
8.6 Printed P3HT and Related Issues in OFETs 196
8.7 Fully Gravure Printed P3HT OFETs 203
8.8 Printed Ag Metal Inks 206
8.9 Conclusion and Future Work 209
8.10 Reference 211

IX. Conclusion and Future Work 215

Chapter I
Introduction

Organic materials are intriguing subjects of scientific research which are different from conventional inorganic materials. They have unique electrical and chemical properties. Organic compounds are comprised of organic molecules mainly of carbon and hydrogen atoms which are bonded by weak intermolecular forces (van der Waals forces), while inorganic materials are constituted by other elements which are covalently bonded. The weakness of bonding in organic materials provides soft and malleable material properties and can be dissolved in common organic solvents. Also, electrical property of organic materials is an interesting point. Their electric charge carrier mobility is quite low having usually less than 10^{-2}-10^{-3} cm^2/Vs for amorphous polymers which is far lower than inorganic crystalline materials, which is more than 1,000 cm^2/Vs. Transportation of quasi-particle charge carriers occurs by the hopping process between localized states in organic materials where the mean free path of carriers is lower than the mean atomic distance, while in inorganic semiconductors charge transport occurs in delocalized states and is limited by phonon scattering.

Even though electrical properties of organic materials are inferior to inorganic materials, they provide a lot of advantages in terms of reduced costs and fabrication processing. They are much cheaper than inorganic materials and can be easily produced and modified by chemical synthesis. Solution processability of organic materials pioneered a novel way toward mass production of large area optoelectronic devices using printing techniques[1, 2]. Conjugated polymers are representative organic materials with long chain molecules first synthesized by Alan J. Heeger, Alan MacDiarmid, and Hideki

Shirakawa, for which they were awarded the Nobel prize in Chemistry in 2000. Also, some of small molecules can be dissolved in organic solvents. Conventional printing techniques such as ink-jet printing,[3, 4] contact stamping[5] and roll-to-roll gravure printing,[6-8] which have been mainly used for production of newspapers and magazines, can be implemented using organic semiconducting inks instead of writing inks. Unlike printed graphic arts, the printing of an optoelectronic device, which is comprised of a stack of tens of nanometer thickness layers, is strongly dependent on the surface homogeneity of printed thin films. Their surface variation should be spatially uniform with an RMS less than 3 nm for efficient charge injection and transport.

Understanding of hydrodynamics of semiconducting printing inks during the drying process is highly important. A coffee stain phenomena, which occurs by fast evaporation of a low boiling point solvent as a large portion of solute is transported to a pinned line at the edge of the droplet to compromise the losses from fast evaporation of solvent, is a main problem in printed optoelectronics.[9, 10] The Marangoni flow induced by the surface tension difference inside a drying droplet can generate an inward convection flow which balances evaporation rates of the droplet at all surfaces. Balancing of the fluidic movements inside the droplet improves surface homogeneity of the printed thin films. In addition, self-assembly of solutes can be induced by altering hydrodynamics of solvents.[10, 11] Self-assembly of nanoparticles have been reported by various methods[12-16]. Preferentially oriented polymer chains by solution processing method are expected to enhance electrical conductivity of organic materials.

Recently, solution processable small molecules such as TIPS-pentacene have been proposed. It achieved OTFTs with more than 1 cm^2/Vs field-effect mobility in 2007[17]. Inorganic materials can also be solution processed by a form of colloidal nanomaterials[18] or sol-gel process[19]. Trends on increasing solubility of small molecules and solution processing of inorganic materials are expected to compromise a low stability of solution processable polymers in future but it is still important to further investigate various phenomena in terms of hydrodynamics using solution processing.

Innovative applications have already been introduced attributed to the solution processability of semiconducting materials. Ink-jet printed colour filter in LCD-TFT display was first manufactured at industrial level by Seiko Epson in 2006. Optoelectronic devices such as OLEDs, OTFTs and OPVs, manufactured by printing techniques, have been developed in depth. Printed devices are usually processed at low temperature on flexible substrates and the flexibility of devices is suitable for unique applications such as rollable display, foldable mobile phones and stretchable displays.[20-22] Attributed to the various advantages, I strongly believe that the future of solution processing of optoelectronic devices is bright.

In this Thesis, an overview of main research topics is briefly presented in Chapter 1 as an introductory chapter. Chapter 2 and 3 are theoretical background chapters which include important research subjects to help with effective understanding of the thesis. A concept of organic materials and device physics of two optoelectronic devices, OLEDs and OFETs, are discussed in Chapter 2. Related topics on printing of optoelectronic devices are explained in Chapter 3. Experimental techniques and materials used in this thesis are described in Chapter 4. In Chapter 5, OLEDs with gravure contact printed organic layers are demonstrated. A comparative study of printed OLEDs with conventionally spin-coated device using same materials shows identical device performance. The device performance of printed OLEDs records the highest efficiency and luminance among the printed OLEDs reported so far. In Chapter 6, OLEDs using sequentially solution processed multilayer of F8BT/TFB in an inverted structure is demonstrated. Ink modification techniques related to build the structure are discussed. Also, an ultra thin Cs_2CO_3 layer is gravure contact printed and the device with the gravure printed Cs_2CO_3 layer is compared to the device with spin-coated Cs_2CO_3 layer. Chapter 6 first confirms that an ultra thin layer (~5-10 nm) of inorganic materials is roll-to-roll printable. In Chapter 7, device efficiencies of 35 cd/A and 23 lm/W are reported using F8BT/TFB multilayer inverted PLEDs, which are the highest efficiencies reported so far using fluorescent polymers. The position of the recombination zone and charge confinement effects at different thicknesses of both F8BT and TFB emissive layers are discussed. Also, various types of emissive materials and device structures are compared in an application of inverted PLEDs. Issues related to gravure contact printed OTFTs

using a polycrystalline p-type polymer are studied and state-of-the-art device characteristics of fully printed OTFTs are demonstrated in Chapter 8. All layers except the pre-patterned ITO source and drain electrodes are sequentially printed. Finally, a list of summaries and future plans of the experimental chapters are presented in Chapter 9 as a conclusion chapter.

[1] H. Sirringhaus, *Nature* **2009**, *457*, 667.

[2] M. Berggren, D. Nilsson, N. D. Robinson, *Nature Materials* **2007**, *6*, 3.

[3] H. Sirringhaus, T. Kawase, R. H. Friend, T. Shimoda, M. Inbasekaran, W. Wu, E. P. Woo, *Science* **2000**, *290*, 2123.

[4] B. J. de Gans, P. C. Duineveld, U. S. Schubert, *Advanced Materials* **2004**, *16*, 203.

[5] J. A. Rogers, Z. Bao, K. Balwin, A. Dodabalapur, B. Crone, V. R. Raju, V. Kuck, H. Katz, K. Amundson, P. Drzaic, *Proc. Natl. Acad. Sci. U.S.A.* **2001**, *98*, 4835.

[6] F. C. Krebs, S. A. Gevorgyan, J. Alstrup, *Journal of Materials Chemistry* **2009**, *19*, 5442.

[7] M. Tuomikoski, R. Suhonen, M. Valimakia, T. Maaninen, A. Maaninen, M. Sauer, P. Rogin, M. Mennig, S. Heusing, J. Puetz, M. A. Aegerter, *Manufacturing of polymer light-emitting device structures - art. no. 619204*, SPIE-INT SOC OPTICAL ENGINEERING, BELLINGHAM **2006**.

[8] P. Kopola, M. Tuomikoski, R. Suhonen, A. Maaninen, *Thin Solid Films* **2009**, *517*, 5757.

[9] T. Kajiya, E. Nishitani, T. Yamaue, M. Doi, *Physical Review e* **2006**, *73*.

[10] J. Park, J. Moon, *Langmuir* **2006**, *22*, 3506.

[11] J. A. Lim, W. H. Lee, H. S. Lee, J. H. Lee, Y. D. Park, K. Cho, *Advanced Functional Materials* **2008**, *18*, 229.

[12] Y. Lalatonne, J. Richardi, M. P. Pileni, *Nature Materials* **2004**, *3*, 121.

[13] P. A. Smith, C. D. Nordquist, T. N. Jackson, T. S. Mayer, B. R. Martin, J. Mbindyo, T. E. Mallouk, *Applied Physics Letters* **2000**, *77*, 1399.

[14] F. Dumestre, B. Chaudret, C. Amiens, M. Respaud, P. Fejes, P. Renaud, P. Zurcher, *Angewandte Chemie-International Edition* **2003**, *42*, 5213.

[15] F. Kim, S. Kwan, J. Akana, P. D. Yang, *Journal of the American Chemical Society* **2001**, *123*, 4360.

[16] L. S. Li, J. Walda, L. Manna, A. P. Alivisatos, *Nano Letters* **2002**, *2*, 557.

[17] S. K. Park, T. N. Jackson, J. E. Anthony, D. A. Mourey, *Applied Physics Letters* **2007**, *91*.

[18] S. Coe, W. K. Woo, M. Bawendi, V. Bulovic, *Nature* **2002**, *420*, 800.

[19] J. Y. Kim, S. H. Kim, H. H. Lee, K. Lee, W. L. Ma, X. Gong, A. J. Heeger, *Advanced Materials* **2006**, *18*, 572.

[20] D. H. Kim, J. H. Ahn, W. M. Choi, H. S. Kim, T. H. Kim, J. Z. Song, Y. G. Y. Huang, Z. J. Liu, C. Lu, J. A. Rogers, *Science* **2008**, *320*, 507.

[21] T. Sekitani, H. Nakajima, H. Maeda, T. Fukushima, T. Aida, K. Hata, T. Someya, *Nature Materials* **2009**, *8*, 494.
[22] S. I. Park, A. P. Le, Y. Huang, X. Li, J. A. Rogers, *Adv. Mater*. **2010**, *22*, 3062.

Chapter II

Organic Semiconductor Optoelectronic Devices

2.1 Introduction

Electronic devices covering a wide range of applications are currently typically manufactured from inorganic semiconducting materials such as Si and GaAs. Since the discovery of organic semiconductors, in which the constituent semiconducting molecules are bonded together by relatively weak van der Waals forces into the solid-state, a broad area of research has opened up targeted at realizing functional electronic devices using these materials.

There are advantages of using organic materials over inorganic materials for optoelectronic devices. Organic materials are relatively cheap and offer simple fabrication methods. The rise in the demand for materials such as indium and lithium has caused the price of inorganic semiconductors to increase enormously. However, organic materials are less affected by this as their precursors are virtually unlimited in supply. Deposition of inorganic materials usually requires a high thermal energy and a high vacuum for zone refining, crystal growth and molecular beam epitaxy. Because of chemical similarities between organic semiconducting materials and organic solvents, organic materials can be dissolved in organic solvents and can be solution processed even at room temperature. This versatility of solution processing opens up the

possibility of optoelectronic devices being printed using common techniques such as ink-jet printing and roll-to-roll printing, conventionally used for the production of newspapers and magazines. Roll-to-roll printing can pattern substrates at speeds of up to ~60 m^2/s in the case of gravure printing. This is ideal for large area displays, where size ultimately depends on the width of the printing roll. This processing advantages of organic materials has attracted a considerable amount of interest in the optoelectronics industry.

In this Chapter, the device physics and operation of organic field-effect transistors (OFETs) and organic light-emitting diodes (OLEDs) are explained. Also, a brief introduction of organic materials is presented. OFETs are alternatively called thin-film transistors (TFTs) as they involve a stack of thin layers. They can be used in many applications as current amplifiers, switches or in complementary logic circuits, the latter involving both n- and p-type transistors. Organic TFTs can also be used in liquid crystal displays (LCDs) to control the voltage supplied to each back-lit liquid crystal pixel. Unlike these light-shutter type LCD pixels, the OLED is an electroluminescent device that directly emits light of a wavelength dependent on the energy-gap of the semiconductor. The combination of both types of device can also form the pixel arrays of an active-matrix OLED (AMOLED) display, where each pixel comprises two switching TFTs and one drive TFT which are coupled to one OLED.

2.2 Organic Optoelectronic Materials

The chemical structure of organic semiconducting materials determines the different energy levels in both single molecules and polymer chains. Unlike inorganic materials, where excited states are delocalized throughout the bulk solid, excited states in organic materials are highly localized on individual molecules and chain segments. Therefore, the wavevector **k** is not appropriate to describe the states in organic electronic materials.

2.2.1 Carbon chemistry

A single carbon atom have 6 electrons in its orbital with a $1s^2 2s^2 2p_x 2p_y$ ($1s^2 2s^2 2p^2$) configuration. As two $1s^2$ electrons are bonded tightly to the carbon nucleus, they are less effective in carbon bonding. Similar to other chemical elements, carbon forms covalent bonds which fills electronic shells and achieves energetic stability by sharing electrons with neighbouring atoms. It may be possible to derive that two outermost atoms ($2p^2$) are solely engaged in carbon bonding by forming two single bonds. However, it is not the case and carbon forms four bonds via intermediate steps known as "promotion" and "hybridization". At the beginning of the process, one of the 2s electrons is promoted into the empty p_z orbital, changing its configuration into $1s^2 2s^1 2p^3$. The remaining 2s electron can be hybridized with either all three 2p orbitals (sp^3 hybrids), two 2p orbitals (sp^2 hybrids) or just one 2p orbital (sp hybrids). A hybridization process of sp^2 orbitals in carbon atoms is represented in Figure 2.1.

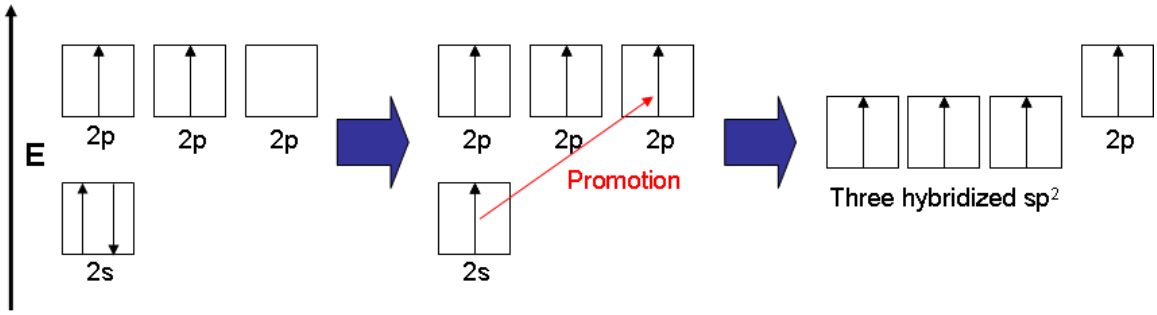


Figure 2.1 The formation of sp^2 hybridized orbitals in a carbon atom.

sp^3 hybridization

This is a case for if all three 2p orbitals are involved in the hybridization with the remained one 2s orbital. The four orbitals are energetically stabilized consisting of 4 lobe points in the direction of one corner of a regular tetrahedron. The angle between the lobes is 109.5°. Four orbitals are overlapped and configured in a form of either four single bonds with four hydrogen atoms (methane) or three hydrogen atoms and one carbon atom (ethane). The overlap of orbitals generate either σ (bonding) or σ* (anti-bonding) orbitals, where the σ-orbitals are fully occupied by sp electrons and the σ*-

orbitals are empty. The energy difference between σ and σ* generally exceeds the ionization potential, hence polymers with this configuration (sp^3) have more like insulating property.

sp^2 hybridization

In this configuration, two 2p orbitals are involved in the hybridization. The electron wavefunctions of the three hybridized sp^2 orbitals locate in a plane separated by 120°. The remaining unhybridized p_z orbital is positioned orthogonal to the plane. Ethene (C_2H_4) is one of examples. A carbon atom consists of three hybridized sp^2 orbitals containing two of them bonded with two hydrogen atoms and the third overlaps with the sp^2 orbital of the adjacent carbon atom to form a σ-bond. The remaining p_z orbitals of the neighbouring carbon atoms also overlap to form another carbon-carbon bond and it is π-bond. The combination of one σ-bond and one π-bond is known as a carbon-carbon double bond (C=C).

sp^1 hybridization

Only one 2p orbital is engaged in the hybridization. The two hybridized sp^1 orbitals have two lobes located along the same axis at 180° to each other, and two remaining unhybridized 2p orbitals are orientated orthogonal to the hybridized orbitals. Ethyne (C_2H_2) is an example molecule in this configuration. In ethyne, one of the two hybridized sp^1 orbitals of each of the two carbon atoms bonds with a hydrogen atom, while the other orbital overlaps with the sp^1 orbital of the adjacent carbon to form a σ-bond. The two remaining 2p orbitals of each carbon atoms then overlap with the other neighbouring carbon atom to form two π-bonds. The combination of one σ-bond and two π-bonds corresponds to a carbon-carbon triple bond (C≡C). Examples of hybridizations are shown in Figure 2.2.

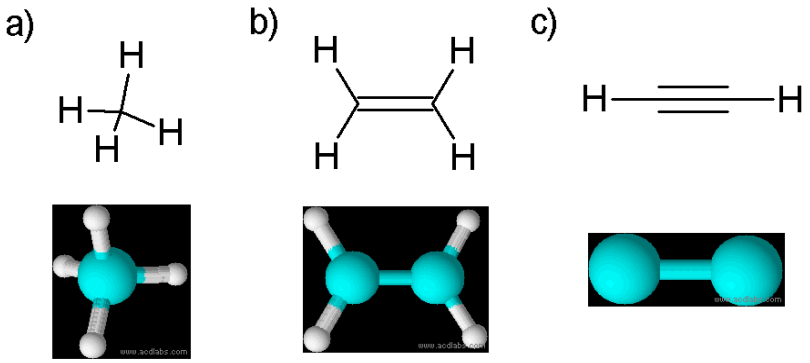


Figure 2.2 Schematics of hybridization: a) sp^3 (CH_4), b) sp^2 (C_2H_4), and c) sp^1 (C_2H_2) hybridization.

2.2.2 Organic materials

Organic materials can be divided by three popular types of materials depending on molecular chain length and weight: small molecules, polymers and dendrimers. Small molecules are known as compounds with clearly defined molecular structure with relatively low molecular weight. They are typically processed via sublimed vacuum evaporation because they likely lose its electrical conductivity when it is solution processed. Crystallinity of the material is highly important compared to polymers where its charge carrier transport in solution processed films is available owing to conjugated system of comprised molecules. On the other hand, polymers comprise of long constituent repeated units (CRUs) called monomers. Polymers with a single type of monomers are called homopolymers while polymers with more than two monomers are called copolymers. Copolymers can be categorized by three groups as alternating copolymers, block copolymers and statistical copolymers. The iteration of different monomers of alternating sequence of monomer units and repeating sequence groups of monomers are called alternating copolymers and block copolymers respectively. If the arrangement of monomers is randomly positioned, it is called statistical copolymer. Figure 2.3 describes different structural types of polymer molecules.

Dendrimers are relatively new materials. It contains characteristics of both small molecules and polymers depending on the number of generations which is the number of repeated branching side-chains called dendrons. Therefore, they can theoretically

possess both superior performance of small molecules and the high solution processability of polymers.

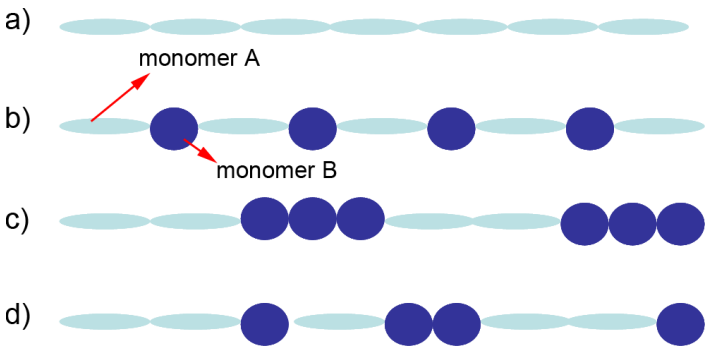


Figure 2.3 Molecular structures of various polymers. a) Homopolymer, b) Copolymer, c) block copolymer, and d) Statistical copolymer.

2.2.3 Conjugated polymers

Organic materials can have a semiconducting property owing to an alternating arrangement of single and double (triple) bonds with the sp^2 (or sp^3) hybridization of carbon, which is called a conjugated system. The delocalization of electrons in a π-bond occurs because they are not specifically confined to the region between the nuclei and they exist as a cloud of electron density above and below the plane of the σ-bond. These π-electron clouds can spread out adjacent to single bonds which creates a delocalised system over the entire molecule.

Conjugated polymers can be regarded as quasi-one dimensional systems owing to their strong intramolecular electronic interactions and relatively weak intermolecular electronic interactions. This quasi-one dimensional localization also means that electron-electron interactions are weakly screened. Strong electronic correlations, therefore, plays an important role in determining the character of the electronic states. As well as electron-electron correlations, the electrons and the lattice are strongly coupled in such a low dimensional system, which also affects the character of the electronic states. The conjugation length, the delocalization length of the charged and neutral electronic states, of conjugated polymers is typically around 5 nm (typically 10-20 repeat units).

2.2.4 Electronic molecular states

Solitons

It is possible for conjugated polymers, for example trans-polyacetylene, to have the same electronic structure if the order of the single and double bonds are switched. This type of degeneracy results in the possibility of a special kind of defect or excitation, the soliton and the antisoliton, being created between regions where the bond sequence switches. Such defects can move along a polymer chain without dissipating energy. The energy level of the soliton lies inside the energy gap. Adding (or removing) an electron from the LUMO (or HOMO) of such a degenerate polymer results in the creation of a negative or positive soliton.

Polarons

When there is an isolated electron or hole on a chain, the chain proceeds to relax or deform within ~100 femtoseconds (fs) so as to lower the energy of the carrier. The charge and the resulting deformation constitute a polaron, denoted as P^+ or P^- for positively or negatively charged polaron.

Polarons provide two energy levels located symmetrically about the centre of the gap. The locations of the polaron levels are located just below and above the LUMO or the HOMO edge respectively. The LUMO and the HOMO are analogous to the conduction band edge and valence band edge in inorganic materials, and they stand for the lowest unoccupied molecular orbital and the highest occupied molecular orbital respectively. The size of the gap also depends on the conjugation length of polymer and it becomes smaller for longer chain lengths. Polarons can be generated by either electrical excitation or chemical doping.

In the case of light-emitting diode, for example, electrons injected at the cathode flow into P^- states, holes injected at the anode into P^+ states. An electric field sweeps them toward each other. When a P^+ and a P^- meet, they are likely to form an exciton. This

electrically formed exciton has the same properties as a photogenerated exciton. Correspondingly, when an exciton in a conducting polymer is dissociated, a pair of polarons is formed, a property which is exploited in photovoltaic (PV) cells.

Excitons

When a P^+ and a P^- recombine under an applied electric field, or an electron in the ground state is optically excited by a photon of light, an exciton is generated. They are quasi-particles which form the neutral excited state. In three-dimensional inorganic semiconductors the excitons are usually weakly bound (~10 meV), with large particle-hole separations (4-10 nm), and are well described by a hydrogenic model. Excitons with these properties are known as Mott-Wannier excitons. In the case of conjugated polymers, this model does not apply, the exciton forming a strongly bonded excited state with a small particle-hole separation (< 0.5 nm). These strongly bound excitons are referred as Frenkel excitons in molecular crystals. The binding energy of this type of exciton is around 0.1 ~ 1 eV. Molecular crystals also experience charge-transfer excitons, which are like Frenkel excitons but with larger electron-hole separations, so that the exciton wavefunction is spread over nearest-neighbour molecules. The description of excitons is shown in Figure 2.4.

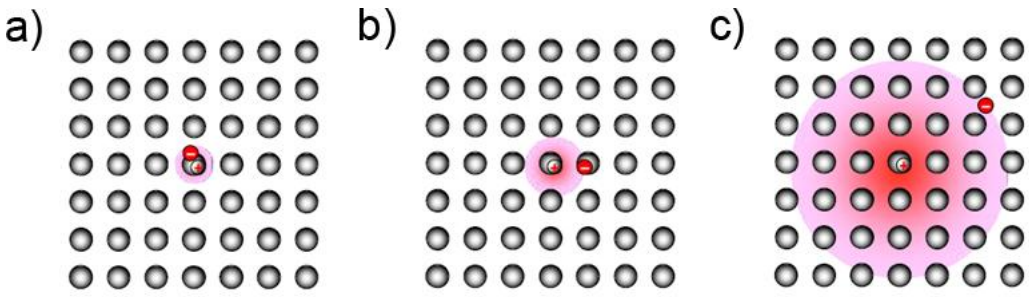


Figure 2.4 Various excitons: a) Frenkel exciton, b) Charge transfer exciton, and c) Mott-Wannier exciton.

Excimers

Excimers are due to an exciton on one molecule achieving a lower energy by forming a single excited state with one of its nearest-neighbours in the ground state. This couples

the two molecules together to effectively form the excited state of the equivalent molecular dimer. Excimers have a charge-transfer component, corresponding to an electron on one of the molecules and a hole on the other. This charge transfer component further stabilizes the excimer in a couple of ways. Firstly, the intermolecular Coulomb attraction induces an attraction between the electron-hole pair, which results in a weakly bound charge-transfer exciton. Secondly, the inter-chain one-electron Hamiltonian couples the charge-transfer component with the exciton component. The excimer emission is broad, featureless and red-shifted in comparison to the molecular emission. Since the pair of molecules in the excited state experience an attraction that does not exist in the ground state, the equilibrium geometry of the excimer corresponds to a repulsive ground state potential. Hence, upon the emission of a photon or phonons, the excimer decays to two separate molecular monomers in the ground state.

Exciplexes

An exciplex is an excited complex of two different molecules. They are similar in their properties and emission features to excimers. The main difference is that exciplexes are formed by the interaction of an excited molecular entity with a ground state counterpart of a different chemical structure. The transition dipole moment of excimers and exciplexes with the ground state, which directly relates to its lifetime, is a function of the relative orientation of the two molecules. Parallel molecules in an excimer have a zero transition dipole moment, whereas collinear molecules have an enhanced dipole moment.

Excimers and exciplexes can be observed in both small molecules, polymers and their blends.

2.3 Organic Field-Effect Transistors (OFETs)

Since organic FETs were first reported by Koezuka *et al*. in 1987[1, 2], various studies have been reported which demonstrate the versatility of OFETs as electronic components. The performance of OFETs using small molecules can achieve a mobility of 5 cm^2/Vs for vacuum deposited [3] and it is comparable to its targeted inorganic TFT using amorphous silicon (a-Si), which is typically in the range 0.5-1 cm^2/Vs mobility and an on/off current ratio of 10^6-10^8. Recently, high mobility of 1.5 cm^2/Vs Pentacene OFET has been published with an on/off current ratio of ~10^8 at room temperature.[4] For a case of a long chain polymer, state-of-the-art characteristics have been reported with a mobility of 0.6 cm^2/Vs.[5] Even though the device performance of OFETs is much lower than inorganic FETs, its research potential has been focussed on the ease of processing in large-area electronic device applications and it is expected to eventually replace conventional inorganic TFTs. Soluble small molecules[6, 7] and inorganic materials using cadmium selenide (CdSe) or cadmium sulphide (CdS)[8-10] are alternative routes where solution processing technology can be applied, hence they offer both high performance and material stability via solution processing.

In this Section, a case of polymer FETs (PFETs) having polycrystalline structure is discussed. Polymer FETs can be categorized using two approaches: (1) achieving high charge-carrier mobility by implying polycrystalline[10] or liquid-crystalline[11, 12] order through self-organization. Poly (3-hexylthiophene) (P3HT) is one of standard polycrystalline materials for p-type semiconductor and its performance has been reported with mobilities up to 0.1-0.3 cm^2/Vs.[13, 14] (2) providing a uniform path for charge transport at the interface with a dielectric by using amorphous materials. Its stability has been found to be more enhanced in amorphous OFETs, while mobility is much higher in polycrystalline OFETs.

Amorphous OFETs typically implement materials such as regioirregular polythiophene or polyacetylene, which are known to have mobility limited to less than 10^{-3}-10^{-4} cm^2/Vs. It can also be further improved in materials based on triarylamine, its examples

are poly(triarylamine) (PTAA) derivatives or poly(9,9-dialkylfluorene-*alt*-triarylamine) (TFB), up to 10^{-3}-10^{-2} cm^2/Vs.

Microcrystalline or polycrystalline polymers provide enhanced mobility owing to strong π-π interchain interactions separated by layers of solubilising and insulating side chains, so that offer a fast in-plane charge transport. Also, its mobility can be altered by head-to-tail regioregularity and deposition conditions. Kim *et al*. reported enhanced energy harvesting property of P3HT:PCBM photovoltaic (PV) cell by improving regioregularity of P3HT.[15] Boiling point of solvents can affect degree of crystallinity.[16] Larger grain boundary was observed from cases using high boiling point solvents, hence achieved higher mobility.[17, 18] In addition, increased molecular weight show increased mobility. Zen *et al*. have explained molecular weight related mobility by introducing a concept that a less planar polymer backbone was observed in the case of low-molecular-weight fractions.[18]

2.3.1 Device structure

A field-effect transistor, as shown in Figure 2.5, consists of three terminals (electrodes), so called source, drain and gate contacts. Currents flow from the drain to the source through the conducting channel and no currents flow between the channel and the gate in theory as a dielectric is located. Hence, a FET can be thought as a capacitor where one plate is the conducting channel between the source and the drain forming either ohmic or Schottky contacts and the other plate is the gate electrode. The density of charge carriers in the channel is multiplied by the voltage applied to the second plate of the capacitor, the gate electrode. A small amount of applied gate voltage can cause a large variation in the current flow in the channel, which explains how a transistor amplifies signals.

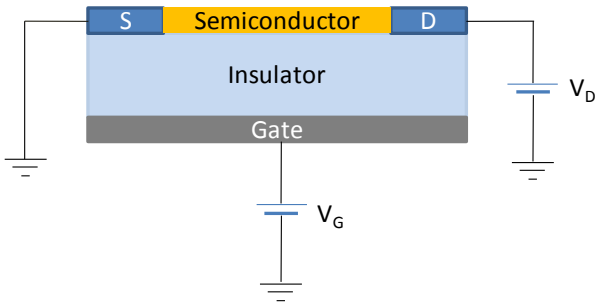


Figure 2.5 Schematic view of an organic field-effect transistor.

There are different types of either inorganic or organic FETs depending on their structure and functionality as illustrated in Figure 2.6. The first form of FET is MISFET (metal-insulator-semiconductor) where an insulating layer exists between metal and semiconductor interface. Another popular FET is MESFET (metal-semiconductor) where a Schottky barrier is used between metal and semiconductor interface as a rectifying contact. A type of FET, called a thin-film transistor (TFT), was introduced by Weimer in 1962 in the case of polycrystalline cadmium sulphide (CdS).[8] It contains a thin semiconducting layer, typically of 100 nm, which is even thinner than dielectric layer, with two ohmic barriers at the source and the drain contacts and a gate insulator between an active channel and the gate electrode. Due to ohmic contacts for charge carrier injection in OTFTs from the contacts, an active channel is formed in the accumulation regime with a very low V_G at the interface between insulator and organic semiconductor (OSC).

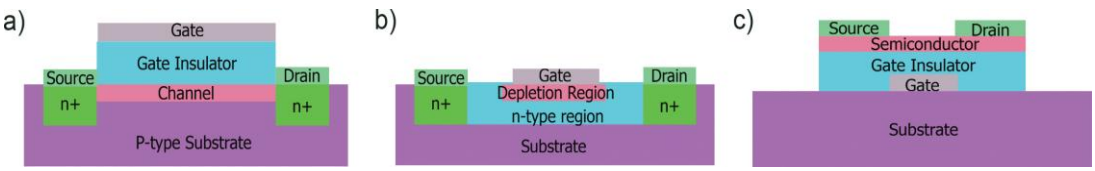


Figure 2.6 Schematic views of field-effect transistors (FETs). a) Metal-Insulator-Semiconductor FET (MISFET), b) Metal-Semiconductor FET (MESFET), and c) Thin-Film Transistor (TFT).

2.3.2 Device operation

As briefly mentioned in Section 2.3.1, OTFTs normally operate in the accumulation regime for ohmic contacts formed at the source and drain contacts, where the increase in magnitude of V_{GS} enhances channel conductivity, unlike conventional inorganic crystalline Si transistors operating in the inversion regime. The operation of OTFTs can be better understood by comparing two similar device structures such as MISFET and TFT where the latter does not have a depletion region and its operation regime is different.

First of all, if we consider the case of a n-channel MISFET device formed on a p-type substrate, the n^+ source and drain regions are diffused or implanted on a relatively lightly doped p-type substrate. When a positive V_G is applied to the gate electrode, an inversion layer is grown at the interface between insulator and semiconductor forming an active channel between the source and the drain electrodes, where a negative charge is induced. With an applied voltage to V_D, I_D currents start to flow through the channel. The amount of I_D increases proportionally to V_D. Hence, it is called the linear regime. Once V_D approaches and equal to V_G, the channel depth at the drain becomes zero. This refers to pinch-off (or saturation) voltage, $V_{D,sat}$. As V_D is further increased, the pinch-off point moves toward the source electrode. The amount of carriers arriving at the pinch-off point remains same at voltages over $V_{D,sat}$, the drain current saturates to a constant value, $I_{D,sat}$. The transistor is now in the saturation regime. The overall process of MISFET is described in Figure 2.7.

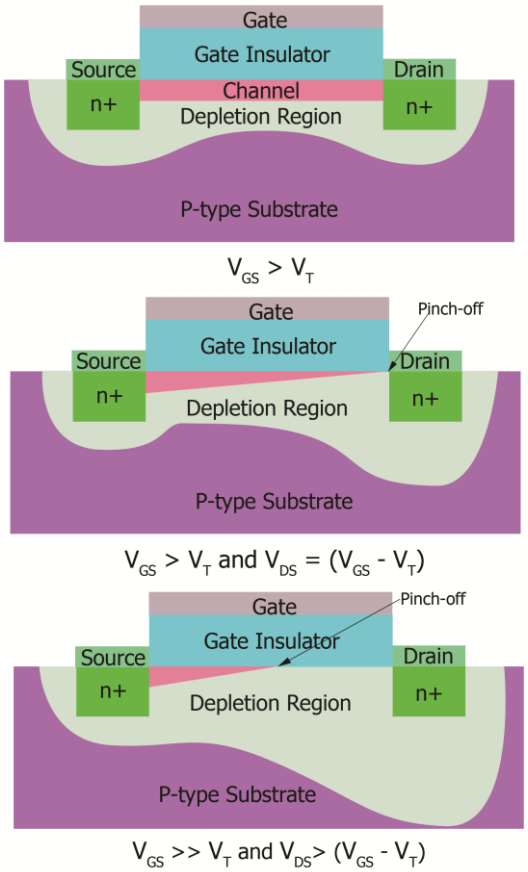


Figure 2.7 n-channel MISFET cross-sections under different operating conditions (V_T is referred as threshold voltage)

Alternatively, the concept of the TFT was first proposed by Weimer in 1962[8]. This configuration is particularly suitable for materials with low conductivity such as amorphous silicon transistors. There is no depletion region in this structure (Figure 2.6c) to isolate the conducting channel from the substrate. Low off-current is guaranteed in this structure for low conductivity in semiconducting materials. In TFT structure where an active channel is formed between two ohmic contacts at metal/OSC of the source and drain contacts, an active channel is very thin around 100 nm and it is located at the interface between insulator and OSC. For ohmic contacts, I_D currents can flow in the accumulation regime when V_G is applied. Majority carriers can flow at positive V_G for n- type OSC and vice versa. The amount of I_D current increases proportionally to V_D until it exceeds V_G in the linear regime similar to the operation of MISFET. However, when V_D, equal to V_G, is applied the conducting channel starts to deplete

from the drain side of the channel and its depletion point (pinch-off point) moves toward the source contact with larger V_D. The I_D starts to saturate in the depletion mode. The schematic operation of TFT is shown in Figure 2.8.

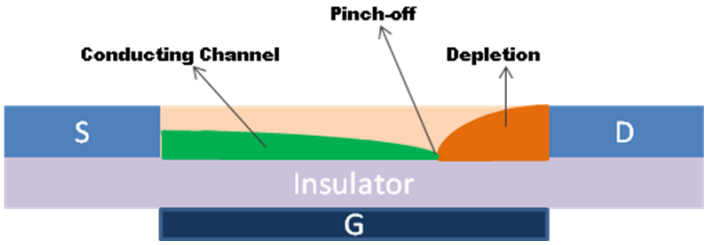


Figure 2.8 Schematic view of TFT operation

2.3.3 Charge carrier transport

Hopping

In OFETs, charge carriers travel across the active channel between the drain and source electrodes. In n-type organic semiconductor, electron mobility is much higher than hole mobility and vice versa in p-type organic semiconductor. In disordered materials such as organic semiconductors or amorphous silicon, charge transport occurs by hopping of charges via tunnelling between localized states. Hence, the charge transport is limited by hopping distance and conformation of the polymer backbone. Transport mainly occurs via delocalized states in inorganic semiconductors, which is limited by the scattering of the carriers, mainly by phonons. Phonons refer to lattice vibrations by scattering of the carriers. The main difference between the two transports is that the transport is phonon assisted in organic semiconductors whereas the transport is limited in inorganic semiconductors. Therefore, charge mobility is decreased for conventional semiconductors whereas it is increased in the most organic materials in relation to increasing density of phonons. Similarly, the charge mobility decreases with temperature in inorganic semiconductors while the increased mobility is obtained in high temperature in most of organic semiconductors.[19]

Localization in the conjugated organic materials happens due to the formation of polarons. The creation of a polaron originates from the deformation of the conjugated chain under injection of charge carriers. In a conjugated molecule, a charge is self-trapped by the deformation in the chain. The mechanism of self-trapping can be described by considering the creation of localized states in the gap between the valence band and the conduction bands. The localized states are referred to polaronic levels. Observation of such levels in doped conjugated polymers and oligomers can be identified by UV-visible spectroscopy.

The properties of small molecules and polymers are quite similar and excitonic states dominate their optical properties. An exciton, which is a molecular excited state and mobile within solid, hops between molecule to molecule in small molecules and in the case of polymers it travels between chains as well as along the polymer backbone until it recombines to generate either light in a radiative process or heat in a non-radiative process.[20] An exciton in polymer is often called a polaron-exciton. The main form in organic materials is the Frenkel exciton, which is a tightly bound as approximately 1 eV, hence an electron-hole pair is normally localized on a single molecule at a time.

Unlikely in inorganic semiconductors where charge carrier mobilities of around 10^2 to 10^4 cm^2/Vs at room temperature, organic semiconductors can only achieve mobilities of 1 cm^2/Vs for highly ordered molecular crystals and 10^{-3} to 10^{-5} cm^2/Vs for more disordered form and polymers at room temperature.

Multiple Trapping and Release

Multiple trapping and release (MTR) model[21] is the most widely used to account for charge transport in amorphous silicon. In the model, a narrow delocalized band is described with a high concentration of localized levels which traps charge carriers. Charge carriers interact with the localized levels through trapping and thermal release while they transit through the delocalized levels. In order to explain qualitatively this movement of charge carriers, a couple of assumptions have to be understood.[19] Firstly, the carriers arriving at a trap are instantaneously trapped with a probability close

to one. Secondly, the release of trapped carriers is controlled by a thermally activated process. The drift mobility of charge carriers for a single trap, $\mu_{D,}$ can be related to the mobility μ_0 in the delocalized band by an expression in Equation 2.1.

$$\mu_D = \mu_0 \alpha \exp\left(-\frac{E_t}{kT}\right) \qquad (2.1)$$

For a single trapping level, E_t corresponds to the energy difference between the trap level and the delocalized band edge, and α is the ratio of the effective density of states at the delocalized band edge to the concentration of traps. If a charge carrier experiences energy-distributed traps, effective values of E_t and α have to be calculated.

The density of localized states as a function of energy, the so-called density of states (DOS), can be related to MTR model. Even though a direct relation of two concepts is difficult to explain, Spear and Le comber developed a method based on simplified description of the accumulation layer with a constant density of carriers up to a given thickness λ[22, 23]. The accumulation layer is assumed to function similar to a depletion (Schottky) layer. This method has been recently further developed by Powell who provides a rough estimate of the trap distribution using Equation 2.2[24].

$$N_t(E) = \frac{N_{t0}}{kT_0} \exp\left(-\frac{E_c - E}{kT_0}\right) \qquad (2.2)$$

where N_{t0} is the total density of traps and T_C is a characteristic temperature that accounts for the slope of the distribution.

Field-Dependent Mobility

As hopping; the main charge transport mechanism in organic materials, is temperature dependent, it can also be dependent on the applied electric field. Field-dependent mobility in an organic material can be measurable at high electric fields of more than ~10^5 V/cm.[25] A first explanation of this phenomenon was made by the Poole-Frenkel

mechanism, in which the coulombic potential near the localized levels is modified by the applied field in such a way as to increase the tunnel transfer rates between sites. Equation 2.3 describes the dependence of the mobility.

$$\mu(\mathrm{F}) = \mu(0)\exp\left(\frac{\mathrm{q}}{\mathrm{kT}}\beta\sqrt{\mathrm{F}}\right) \qquad (2.3)$$

where $\mu(0)$ is the mobility at zero field, $\beta = (q/\pi\varepsilon)^{0.5}$ is the Frenkel factor, and F the magnitude of the electric field.

Also, Bässler presented a study about a statistical Monte-Carlo computation which is based on a hopping model with a Gaussian distribution of localized levels.[26, 27] According to the model, Bässler distinguished between diagonal (energetic) and off-diagonal disorder. The energetic disorder is depicted by a Gaussian distribution with a standard deviation σ and the off-diagonal disorder by a standard deviation Σ. In this model, the jump rate along localized states was assumed to be of the Millers-Abrahams type. Finally, Bässler arrives at a universal law relating the mobility to the degree of both diagonal (energetic) and off-diagonal disorder as in Equation 2.4.

$$\mu = \mu_0 \exp\left[-\left(\frac{2}{3}\frac{\sigma}{\mathrm{kT}}\right)^2\right]\exp\left\{\mathrm{CF}^{1/2}\left(\left(\frac{\sigma}{\mathrm{kT}}\right)^2 - \Sigma^2\right)\right\} \qquad (2.4)$$

where μ_0 is the mobility in the absence of energetic disorder, σ the variance of the Gaussian DOS, Σ describes spatial disorder, and F is the applied field.

In addition, a study of Bürgi *et al.*[28] suggested that during the transport of charge carriers, most of the charges are transferred to or from source/drain electrodes through the accumulation layer at the interface between organic semiconductor and insulator. The charge transport in the bulk is negligible. Charge transport occurs in the first few polymer chains adjacent to the interface between dielectric and semiconducting layers, making it more sensitive to energetic disorder and interfacial traps. Charge carrier mobility is hence closely related to energetic disorder and an interchain hopping distance at the interface.

Trap-Limited Transport

Since Thiais group announced a charge transport model in OFETs based on the multiple trapping and release (MTR) model in 1991[29,30], various studies have been performed to investigate the underlying physics in charge transport related to field-effect mobility in OFETs. Interestingly, in the case of TFTs, which operate in the accumulation regime, the Fermi level approaches the nearest delocalized band edge as the gate bias is increased, hence its field-effect mobility is found to be gate bias-dependent.[31] In amorphous silicon or organic materials, a substantial density of localized levels, which function as traps for charge carriers, exist near to the delocalized bands. Therefore, in low gate bias voltage mobility is low and it reaches to the maximum level once the traps in the channel are fully filled by injected charge carriers. As the gate voltage increases, the Fermi level approaches the delocalized band and more and more traps are filled, which eventually leads to direct injection of mobile carriers into the delocalized levels. Trap-free mobility is obtained in high gate bias voltage. In some materials, mobility does not saturate even at high gate bias voltage, which indicates that the density of traps is huge and it would be saturated beyond the gate bias voltage applied.

2.3.4 Charge injection

The contact resistance between an organic semiconductor and source/drain contacts significantly affects organic transistor performance and operation in terms of charge carrier mobility and turn-on voltage (V_T).[32, 33] A charge carrier is injected at the source electrode and extracted from the drain electrode. Charge carriers can experience a Schottky barrier between work function of the electrode and ionization potential of the polymer. According to Bürge *et al*.,[34] good contacts with typically less than 0.3 eV of the barrier in P3HT with Au electrodes, for example, show a low contact resistance of less than 50 kΩ and the device performance becomes more dependent on bulk properties of the organic semiconductor. In contrast, for a relatively large Schottky barrier with values greater than 0.3 eV for the case of F8T2 with Au electrodes, the asymmetry between the source and the drain occurs and a considerably larger voltage is needed to inject holes at the source than to extract at the drain. It can be said that the

OFET is contact (injection) limited and the source electrode influences more on device performance than the drain electrode. The choice of electrode needs to be matched with the ionization potential of the polymer in order to improve OTFT performance. Also, the channel length of OTFTs can affect the contact resistance. The device performance is contact limited for L < 10 μm in the top contact OTFTs and for even greater than 30 μm in the bottom contact OTFTs.[32]

However, Gundlach *et al*.[32] reported that the matching of metal electrodes is not the only factor concerned with contact effects but also for investigation of the charge injection process in case of the asymmetry source and drain contact metals. In the study, OTFT performance was varied with the choice of the contact metal and the biasing configuration. Au – Pd (source – drain) contacts showed better performance than Ni – Pd contacts although the work function of Au and Ni is similar. This suggests that an organic semiconductor can be formed with different crystallinity structures which may be dependent on the surface energy of the metal electrodes.

Contact effects are known to be a critical factor influencing device performance of OTFTs. However, it is a complicated issue and still needs to be investigated further by considering various aspects.

2.3.5 Device geometry

In OFETs, four different configurations are available depending on the position of the gate electrode and the active semiconducting material. If a gate electrode is deposited at last on the top of a device, the device is called top gate OTFT whereas gate electrode is deposited prior to source and drain contacts in bottom gate OTFT. The geometry can be further segmented by the position of the active material. A device with an active layer deposited on the top of the source and drain contact is called bottom contact structure. For a device with source and drain contacts are positioned on the top of the active layer, the device is called top contact OTFT. The schematic views of four geometries are shown in Figure 2.9.

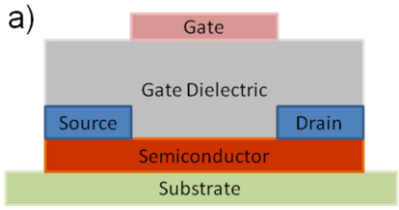
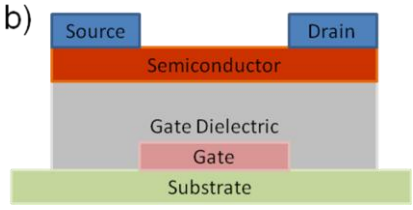
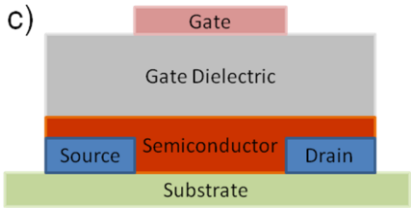
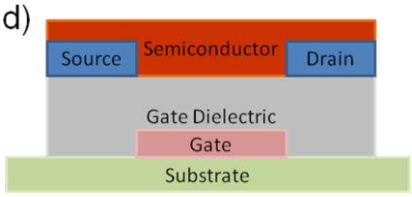
	Top Gate	Bottom Gate
Top Contact		
Bottom Contact		

Figure 2.9 Geometry of OTFTs. a) Coplanar structure, b) Inverted Staggered structure, c) Staggered structure, and d) Inverted Coplanar structure.

Polymer based transistors are normally in the top gate configuration because of solvent compatibility reasons between the organic layers. This limitation of the polymer FETs can be relieved by investigation of gate insulators which can be thermally crosslinked, for example, so that the constraint of choosing materials can be reduced.[35, 36] The bottom gate configuration generally achieves transistor characteristics easier than the top gate structure because a high off-current is typically observed in the top gate configuration by the addition of gate insulator layer or the introduction of impurities at the interface during sample preparation.[35] The difference between the top gate and the bottom gate structures using identical materials can be minimized by using a gate insulator which induces a low off-current of OFETs.

However, the top gate configuration provides the enhanced charge carrier transport due to higher mobility and change of density of states which is obtained from the improved film morphology or local polarization effects.[37] Typically, a roughness of organic semiconductor is smoother than most gate dielectric layers. Therefore, the roughness of the interface between active layer and gate insulator is improved in the top gate structure.[38] Also, the top gate structure is suitable with organic materials because the insulator which is deposited on the top of active layer relieves any damages onto the organic semiconductor, and consequently helps to protect from air-ambient impurities

doping into the active layer. The subjects related to the position of gate dielectric layer will be discussed in the Section 2.3.6 with a detailed explanation on dielectric layer in OFETs.

Also, the position of the source and the drain contact in OFETs can affect device performance according to Necliudov *et al*.[39] It has been suggested that non-linearity observed in the bottom contact configuration unlike in the top contact configuration due to the effect of nonlinear series resistances. Bottom contact OTFTs with a gate insulator with a low dielectric constant provides advantages from both easy integration of the bottom contact device and the high performance of the top contact device.[40]

2.3.6 Dielectric layer and Self-Assembled Monolayer (SAM)

Dielectric layer

The role of the dielectric layer positioned between a gate electrode and an organic semiconductor (OSC) layer is to 'switch' the channel between the source and the drain contacts where current flows throughout the channel. The capacitance of the dielectric layer is strongly dependent on the dielectric permittivity of the material, thickness of the dielectric layer, and the interface states between the dielectric layer and the OSC. OFETs with a high capacitance have high breakdown voltages which refer to the applied voltages at which the insulating layer start to lose its insulating properties. In other words, an insulating layer with a high capacitance can achieve sufficient capacitance even when made very thin. The thickness of the dielectric layer and its permittivity are important as they can determine the voltage required to turn on the OFETs. Equation 2.5 and 2.6 represent important parameters for gate insulator where D_{max} is the maximum electric displacement at which dielectric can sustain and C_i is the capacitance per unit area.

$$D_{max} = \varepsilon_0 k E_B \qquad (2.5)$$

where k is the dielectric constant and E_B is the dielectric breakdown field.

$$C_i = \varepsilon_0 (k/d) \qquad (2.6)$$

where d is the thickness of the dielectric layer.

Normally, the driving voltage increases with increasing thickness of a dielectric layer depending on its electric permittivity, so that it is important to keep the thickness of an insulating layer sufficiently thin to obtain low operating voltage. However, leakage current, which a current flowing from the active channel to the gate electrode, should be minimized for efficient device operation. However, it can be generally increased using thinner dielectric layers at the same dielectric constant. A compromise of these two parameters is made based on the device design criteria; alternatively it can be compensated by employing the following approaches.

One of the approaches is to use a high-k (permittivity) dielectric layer for high capacity of the dielectric layer. High-k dielectric materials provide both a relatively high breakdown voltage and a low operating voltage compared to low-k dielectric materials, which are typically defined as materials with less than 2.2 of dielectric constants. A critical disadvantage of using high-k dielectric materials is that it can cause serious unreliability in device operation attributed to defects, water and oxygen doping into the chains as high-k is more polar attracting oxygen and moisture more than low-k (non-polar) materials. Alternatively, using a low-k dielectric material has been emerged in recent development of OFETs. They offer improved stability in device operation and can be defect and pin-hole free film due to the low-polar property of the materials, while its capacitance is lower than high-k materials. In addition, the field-effect mobility can be enhanced by using low-k materials owing to reduced dipolar (energetic) disorder at the interface.[41] The low polar property of low-k dielectric materials minimizes interfacial stress at the interface with OSC, which is normally non-polar. Veres *et al*. reported that the highest mobility was found in OFETs with dielectric constant less than 2.2.[42] Cytop (ε = 2.1) is a prototype dielectric material in that range.[38] Achieving both high capacitance and mobility is important in OFETs for optimum performance, however, it is also necessary to sacrifice one of the two parameters for a certain application.

In addition, the position of a gate dielectric layer adjacent to the OSC can influence device performance. In the bottom gate structure, the homogeneity of the bottom dielectric layer is important for uniform charge path at the semiconductor-dielectric interface. A choice of solvent for the dielectric layer is directly related to the homogeneity of the layer. Also, the surface energy of the dielectric layer highly affects the mobility of the OSC.[43] Interestingly, enhanced mobility was observed in dielectrics with a low surface energy, in other words, a hydrophobic surface (showing a large contact angle with a water droplet). Oriented molecular structure with its main backbone perpendicular to the substrate is ideal for efficient charge transport and this structure is more likely to be obtained in OSC deposited on hydrophobic dielectric surface.[11] Controlling field-effect mobility by surface energy of dielectric surface is interesting and has given a large impacts in organic electronic fields. The low polar dielectric materials usually have a hydrophobic surface, so it again strengthens the versatility of low-k materials. Larger grain size of OSC was observed on the surface of low-k materials. It is more significant in cases where small molecules or polycrystalline materials are used, but amorphous materials are almost independent of the surface energy of the substrate and therefore mobility variation is much smaller.

For the top gate structure, however, it is less dependent on the surface energy of the dielectric layer. It has not been benefited from enhanced mobility due to increased degree of crystallinity, but it offers enhanced device stability compared to the bottom gate structure where the dielectric acts as a passivation layer for OSC against oxygen and moisture dopants. For fabrication in ambient condition, the top gate structure seems to be more appropriate. Veres *et al*. suggested that disadvantage of low-k insulator can be compensated by introducing a multi-insulating layer structure, where consisting of a high-k insulator for high capacitance and a low-k insulating layer above for encapsulation. They are located for minimizing the energetic disorder at the surface of the dielectric layer and the trapping from ambient dopants at the interface.[44] Interestingly, an OSC in the top gate structure can benefit from larger grain sizes by surface treatment of source and drain electrodes using a self-assembled monolayer (SAM).[4, 45] Therefore, it can be said that it is possible to obtain simultaneously both

high stability and enhanced mobility of OSC deposited on hydrophobic surface of the SAM treated source and drain electrodes having a top gate structure.

Self-Assembled Monolayer (SAM)

The SAMs comprise of a few of very thin monolayers normally less than 10 nm in thickness, which are deposited by a number of methods such as solution process or vapour deposition. Molecular compositions of SAMs are different for its purposes and the chemical property of the bottom surface. As it was previously mentioned, the grain size of active materials can be varied by surface properties of the bottom surface and SAMs are often used as materials for the treatment of the surface favourable to the active materials. Most active materials are non-polar therefore, it is important to treat a surface to be hydrophobic for larger grain size of the active material. Also, SAMs affect molecular orientation of the active materials and achieve high mobilities with more oriented polymer backbone.

To utilize advantages of SAMs effectively, the bottom gate structure is the best choice for crystallization of the OSC. The SAMs usually consist of alkanethiols such as thiol (R-SH) and dithiol (HS-R-SH) as molecular structures on Au surface, simple alkane chains of octyltrichlorosila-ne (OTS) and octadecyltrichlorosilane (ODTS), 3-mercaptopropyltrimethoxysilane (MPTMS), hexamethyldisilizane (HMDS) and various types of functionalized σ-π molecules on oxides forming a strong Si-O-Si bond for SiO_2. The electrical properties of SAMs composed of Cd^{2+} salts of fatty acids having different chain lengths were first characterized by Mann and Kuhn in 1971.[46] To date, it was believed that conducting mechanism throughout SAMs are either via tunnelling or hopping.[47] Choi *et al*. investigated experimentally that tunnelling is a dominant process for molecular lengths less than 4 nm and vice versa as depicted in Figure 2.10.

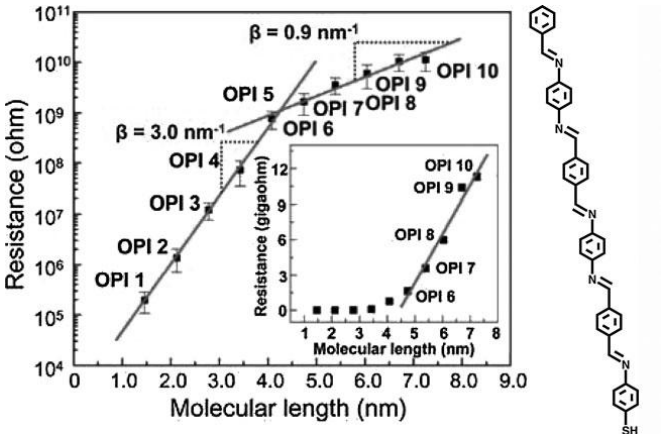


Figure 2.10 Change in resistance of OPI molecules based on molecular length, and OPI molecular structure. Adopted from Ref.[48].

Apart from the function as surface treatment, SAMs have been regarded as alternative materials acting as a gate insulator and an active material in ultra-thin TFTs. SAMs with high capacitance for use as a gate dielectric layer in OTFTs was first suggested by Vuillaume *et al*. in 1996.[49] In his paper, he used n-ODTS SAMs on Si native oxide showing a good insulating property with conducting current of ~10^{-8} A/cm^2 at 5.8 MV/cm and breakdown at 9-12 MV/cm even though the thickness of the SAMs was only 2.8 nm. Dramatically improved insulating property of SAMs was reported in OTFTs using pentacene as an active layer, a common small molecule semiconducting material.[50] The device operated at 2 V with μ = 1 cm^2/Vs and an on/off current ratio of ~10^6. The OTS-OPh SAM is tightly-packed owing to intra-SAM π-π interactions and had very low leakage currents of ~8 × 10^{-7} A/cm^2 at 2.5 V of V_G, large breakdown fields of 14 MV/cm and capacitance of 900 nF/cm^2.

Since it was found that pentacene and CuPc semiconductors showed a saturated mobility when just 6 monolayers were linked,[51] a notion of SAMs functionality as an active channel in TFTs has been studied by various research groups. Reduction of number of monolayers to 1~2 layers seems to be possible from a report by Dinelli *et al*. presenting a saturation of mobility with 2 monolayers of sexithiophene in 2005.[52] Also, Katz *et al*. reported a TFT with only 1.4 layers of 5,5′-bis(4-hexylphenyl)-2,2′-bithiophene (6PTTP6) monolayers, which exhibited a saturated mobility of 0.024 cm^2/Vs.[53] The mobility is still far beyond for high mobility TFTs using a group of

monolayers, even though it is an interesting research area. If one succeeds, an ultra-thin OTFT can be realized.

2.3.7 Device characteristics

In OFETs, typically two parameters are important to consider for high performance device: field-effect mobility and on/off current ratio. Field-effect mobility and on/off current ratio describes charge carrier mobility at the interface of OSC/dielectric layer and a current ratio between V_{SG} is applied above turn on voltage (I_{on}) and V_{SG} is zero (I_{off}), respectively. Field-effect mobility of an OSC is usually lower than mobility in the bulk due to carrier concentration at the surface being much larger as it is influenced by accumulated charges in the channel region. Also, undesired defects and traps exist at the interface of OSC/dielectric, which hinder charge transport in that region.

Output Characteristics

The drain current flowing into the channel can be derived as:

$$I_D = \frac{\overline{\mu_n} W C_i}{L}\left[(V_G - V_T)V_D - \frac{1}{2}V_D^2\right] \qquad (2.7)$$

where μ_n is a surface electron mobility, C_i is insulator capacity per unit area, W is the width of the channel, L is the length of the channel, and V_T is a threshold voltage. From the equation with $V_D << V_G - V_T$, the conductance of the channel in the linear regime can be obtained as:

$$g_m = \frac{\partial I_D}{\partial V_D} \cong \frac{W}{L}\overline{\mu_n} C_i (V_G - V_T) \qquad (2.8)$$

where $V_G > V_T$. As the drain voltage is increased, the voltage across the oxide decreases near the drain and the channel becomes pinched off at the drain end. Finally the current saturates. The saturation condition is approximately given by:

$$V_D(\text{sat.}) \cong V_G - V_T \qquad (2.9)$$

From the equation, the drain current in the saturation region can be obtained using Equation 2.7.

$$I_D(\text{sat.}) \cong \frac{1}{2}\overline{\mu_n} C_i \frac{W}{L}(V_G - V_T)^2 = \frac{W}{2L}\overline{\mu_n} C_i V_D^2(\text{sat.}) \qquad (2.10)$$

The transconductance in the saturation region can be obtained approximately by differentiating Equation 2.10 with respect to the gate voltage:

$$g_m(\text{sat.}) = \frac{\partial I_D(\text{sat.})}{\partial V_D} \cong \frac{W}{L}\overline{\mu_n} C_i (V_G - V_T) \qquad (2.11)$$

All the equations and explanations mentioned in the section are for n-channel device. For p-channel transistor, the drain, the gate and the threshold voltages are negative and the charge carriers flow from the source to the drain.

Bolognesi *et al*. reported that the non-linearity of output characteristic in low V_D is accounted by the field-effect dependence of the carrier mobility and the barrier height of the contacts.[54] An example of output characteristic of p-type TFT is shown in Figure 2.11. In the output characteristic, the drain current varies as a function of the drain bias.

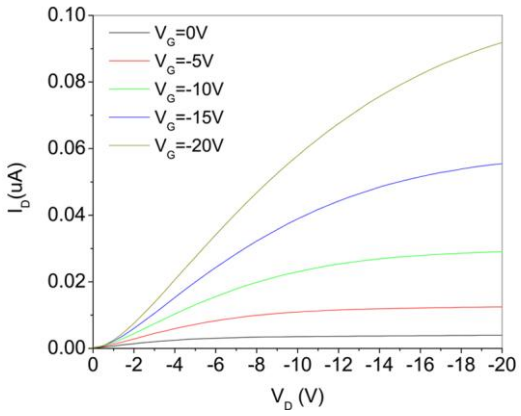


Figure 2.11 Output characteristic of a p-type OFET

Transfer Characteristic

The transfer characteristic plots the drain current as a function of the input gate bias with a fixed drain bias. In the linear region, the drain current should be a straight line versus the gate bias. The intercept of this line on the V_G axis is the linear region threshold voltage. An example of transfer characteristic curve is shown in Figure 2.12. The transconductance in the linear region can be obtained by differentiating Equation 2.8 with respect to gate bias. The transconductance is almost zero below the threshold voltage due to little amount of drain current. It goes at maximum at the point of inflection of the *J-V* curve, and then decreases. The decrease originates from two factors: a degradation of the effective channel mobility as a function of increasing transverse electric field across the dielectric layer and series resistance between the source and the drain contacts.

The transconductance in the saturation region can be obtained taking the square root of Equation 2.10 and it has a linear property as a function of V_G. In this case, the intercept on gate bias corresponds to the threshold voltage in the saturation region.

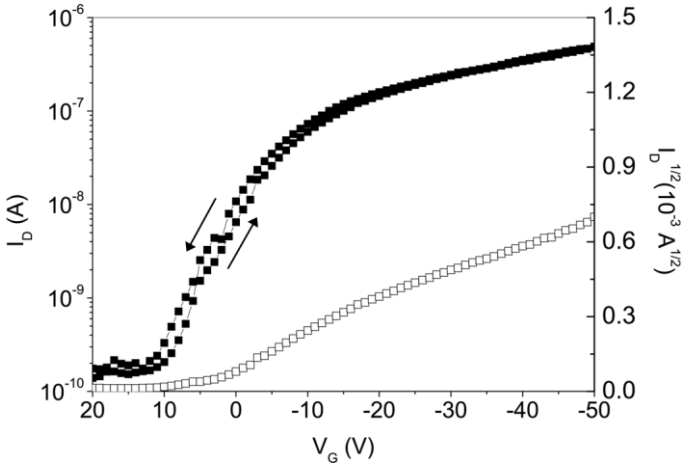


Figure 2.12 Transfer characteristic of a p-type OFET in saturation regime

On/off current ratio indicates the ratio of drain current between when it is maximum and minimum in transfer characteristic. A typical Si based TFT achieves an on-off current ratio around ~10^9 and a high performance organic TFT has a ratio around 10^6. The on/off current ratio represents the ability of a device to shut down and is particularly

relevant in applications such as active matrix displays and logic circuits where switching of TFTs is critically important.

On/off current ratio can be represented by Equation 2.12 and it needs to be maximized for a high contrast ratio of display. [55]

$$I_{on}/I_{off} = \mu C_i V_{SG}/2\mu_r q N_A t \qquad (2.12)$$

where μ and μ_r are field-effect and bulk mobility of an OSC respectively. C_i the capacitance per unit area of the insulator layer, q the electron charge, N_A the impurity concentration, and t is the thickness of OSC. There are ways of improving this parameter. The ratio can be increased by using annealing processes or by choosing an OSC having either/both a large mobility or/and a low off-conductivity value.

High mobility ensures a high on-current so normally as a large on-off current ratio. The on-off current ratio is not only dependent on the ratio of mobility to conductivity but also other parameters including insulator capacitance per unit area, thickness of the layer, and thr doping level of semiconductor.[19] Equation 2.13 and 2.14 explains the relationships between these parameters with the on-off current ratio for high and low doping level of semiconductor, respectively.[19]

$$\frac{I_{on}}{I_{off}} = 1 + \frac{\mu}{\sigma}\frac{C_i V_d}{2d} \qquad \text{(High doping level)} \qquad (2.13)$$

$$\frac{I_{on}}{I_{off}} = \frac{\mu}{\sigma}\frac{C_i^2 V_d^2}{qN_a d^2} \qquad \text{(Low doping level)} \qquad (2.14)$$

Here, μ represents mobility of the device, σ is the conductivity, C_i is the insulator capacitance per unit area, N_α is impurity doping level of semiconductor, and d is the thickness of the layer.

Extracting Field-effect mobility

Field-effect mobility represents how readily a charge carrier travels throughout the channel between source and drain electrodes. The mobility, therefore, is an important parameter and high value of mobility is required for applications where a fast switching is important. The mobility of OFETs can be measured by using an extrapolating method. By plotting I_D against V_G, a curve is obtained which has a linear region. The value of V_G, where the slope of I_D curve at the linear region reaches to, is called the threshold voltage, V_T. An ideal device has a threshold voltage of 0 V. The transconductance, g_m can be extrapolated by measuring a slope of the I_D curve.

Using obtained values of V_T and g_m, the mobility of linear and saturation regimes can be calculated using Equation 2.15 and 2.16 respectively.

When $-V_D << -(V_G-V_T)$,

$$g_m = \left.\frac{\partial I_D}{\partial V_G}\right|_{Vd=const.} = \frac{WC_i}{L}\mu_L V_D \qquad \text{(Linear mobility)} \qquad (2.15)$$

When $-V_D > -(V_G-V_T)$,

$$g_m = \left.\frac{\partial \sqrt{I_D}}{\partial V_G}\right|_{Vd=const.} = \sqrt{\frac{WC_i\mu_S}{2L}} \qquad \text{(Saturation mobility)} \quad (2.16)$$

W and L correspond to width and length of the channel. From the extraction of mobility, it was found experimentally that the amount of on-current is the strongest factor determining the mobility with an assumption that the channel dimension and insulator capacitance per unit area is equal.

2.4 Organic Light-Emitting Diodes (OLEDs)

Electroluminescence (EL) materials have been widely researched for display applications. There have been already large quantities of research published on

inorganic based LEDs using various inorganic semiconductors. Since the first report of light emission using organic small molecules of 8-hydroxyquinoline aluminium (Alq_3) and aromatic diamine as emissive layers in 1987,[56] light emitting diodes using organic materials have been investigated with a hope that can replace conventional inorganic LEDs where relatively limited rare metal resources such as indium or lithium are mainly used. Polymers, which are long chain molecules with improved solubility but inherent lower mobility than small molecules has also been adopted for EL material and its first EL device was demonstrated by Burroughes and Bradley *et al*. in 1990.[57]

Polymers can be dissolved in organic solvents and therefore exist as in liquid phase, which makes these materials able to be solution processed. Spin-coating is a popular and traditional method for deposition of the materials. Alternatively, printing deposition methods such as high resolution ink-jet printing[58] and roll-to-roll (R2R) printing are expected to enhance the feasibility of the materials for the next generation display in such areas of rollable and portable display applications on large area flexible substrates.[20, 59]

Also, advantages such as simple device structures, typically comprised of two electrodes (anode and cathode) and one or a few emissive layers, full viewing angle and video rate response times of OLEDs will compete with a display market highly dominated by liquid crystal displays (LCDs).

In this Section, polymer LED (PLED) is discussed. Its device physics related to operating principle and figure of merits are discussed here. The overall review papers about materials, device physics and operations of PLEDs can be found in Ref. [60, 61].

2.4.1 Device structure

Fluorescence materials have an energy gap between the delocalized π-electron bonding of antibonding (π*) and bonding (π) orbitals, which form LUMO and HOMO levels respectively. Normally the gap of an active polymer is around 2-3 eV corresponding to the wavelength of visible light.

The emissive materials can be divided into two groups; fluorescence and phosphorescence. Fluorescence emission is a faster process with a short lifetime of exciton before radiation in localized energy level states than phosphorescence with low quantum efficiency due to losses of a large number of excitons transferring to triplet states. In devices the proportion of triplet excitons formed is three times higher than singlet excitons. For phosphorescence, it is an inter-crossing multi-process of energy transferring of an exciton before losing its energy with higher quantum efficiency. However, it needs doping of suitable phosphorescence materials to allow a triplet exciton to transfer to a singlet state.[62] The concept of the two distinctive emission processes is explained in Section 2.4.2.

A simple organic light-emitting diode (OLED) is comprised of two electrodes for hole and electron injection and a light emissive material between the two electrodes. Electrons and holes are injected into low work-function metal (cathode) and high work-function metal (anode) respectively. Injected charge carriers are then transported to the emissive layer where a hole and an electron can be recombined as an electron-hole-pair (EHP). An EHP in the emissive layer is decayed into the ground states and relieves energy in a form of either light or heat. Crucial factors for OLEDs to achieve are high efficiency and long life time.[63] For high efficient OLEDs, hole and electron recombination should be made at the centre of the light emitting polymer (LEP) layer in the case of single emissive layer devices to avoid the electrode quenching effects and to maximize the optical outcoupling. The optimum thickness of the LEP layer for a single layer OLEDs is experimentally obtained as 70-80 nm.[64] A combination of two materials with a high mobility of either hole or electron can balance mobility of both types of charge carriers. Charge injection can be enhanced by inserting an injection layer which reduces energy level difference between metals and adjacent HOMO or LUMO levels of organic materials. Poly (styrenesulfonate) (PSS) doped poly (3,4-ethylenedioxy-thiophene) (PEDOT) is a well known hole injection material. Using a copolymer, which contains a combination of different arylene units with both hole and electron transporting properties, mobilities are reasonably high and more balanced than homopolymer, therefore increasing device EL efficiency further.[65, 66]

A bilayer with either two LEP layers[67, 68] or heterojunction[69] PLEDs is another efficient way to increase device efficiency by charge carrier blocking due to energy level difference at the interface between two layers or confinement of charge carriers in three layer structures. Charge carriers accumulate at an interface until a charge carrier of opposite sign passes across the interface to form an exciton. This also prevents leakage of currents through the device and exciton quenching at the other electrode. However, it can be slow with increasing number of excitons generated due to its recombination zone is limited to the interface only while in single layer structure recombination can occur all regions of the active layer.[70] Heterojunction PLEDs are known as the most efficient device structure as they provide charge blocking functionality as well as confinement of charge carriers within one LEP layer so that the recombination zone width is dependent with the width of the layer. However, adjacent layers should have a orthogonal polarity each other so that a solvent for an upper layer does not dissolve an underlying layer during its deposition via solution processing.[71] A choice of solvents for LEP materials is limited and most organic LEP materials are dissolved in dispersive solvent such as xylene and toluene. Recently, various ways have been developed to tackle this problem. The concepts including the crosslinking process, enhancing bonding between atoms by chemical treatment, of an underlying layer[72, 73] and synthesis of water soluble (polar liquid – orthogonal to dispersive organic solvents) materials[74-77] have been recently introduced. The schematic diagram of representing device structures of PLEDs are described in Figure 2.13.

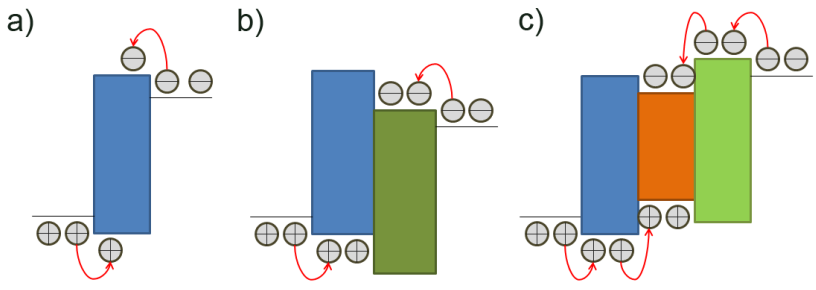


Figure 2.13 PLEDs structure. a) single layer PLEDs, b) bilayer PLEDs, and c) heterojunction PLEDs.

It is known that capping of organic device by passivation can improve the device lifetime and help to protect against oxygen and moisture dopants. Inherent weaknesses

of organic materials owing to photoxidation can also be significantly improved by using a hybrid structure, a combination of both inorganic and organic materials. Inorganic materials such as zinc oxide (ZnO),[68,78] titanium dioxide (TiO_2),[79-82] or zirconium dioxide (ZrO_2)[83] as a hole blocking material and molybdenum trioxide (MoO_3)[84, 85] or nickel oxide (NiO)[86] as an electron blocking material can be used as a capping layer on the top of the emissive layer or as a charge carrier blocking layer. They can also operate as an optical spacer positioned between an electrode and an emissive layer to prevent quenching of charge carriers and excitons.[80, 87]

Inorganic emissive materials can also be solution processed to form hybrid LEDs. Colvin *et al*. pioneered colloidal quantum-dot (QD) LED using cadmium selenide (CdSe) in 1994.[88] Various studies have exploited QD LED[89-91] and very recently Cho *et al*. presented a high luminance red emitting device (12,380 cd/m^2) with a low operating voltage (1.9 V) for display brightness as well as high power efficiency (2.41 lm/W).[81] Full colour display (RGB) using QDs has not yet been realized but development of soluble inorganic materials will enhance the stability of device operation and device life time.

2.4.2 Device operation

A simple representation of device operation of PLEDs is shown in Figure 2.14. Holes and electrons are injected at the anode and cathode respectively. These injected charge carriers undergo lattice relaxation to form polarons, which are charged states lying within the energy gap above or below the HOMO or LUMO levels, respectively. These positively (P^+) or negatively charged (P^-) polarons move through the material via charge carrier hopping, before meeting and undergoing recombination to form neutral excitons (Figure 2.14). The binding energy of the Frenkel excitons within organic materials with low dielectric constants is in the range 0.3 to 0.5 eV. Pairs of positively and negatively charged polarons can form either singlet (spin = 0) or triplet excitons (spin = ±1). For singlet excitons can decay into the ground state by either dipole allowed radiative decay or non-radiative decay. The radiative and non-radiative decay generate light and heat respectively. The mechanism of exciton formation is not yet completely clarified, but

according to simple spin statistics three triplet excitons are formed for every one single exciton. The existence of triplet excitons reduces the fluorescent-emitting organic LED efficiency by a factor of four. The lifetime of an exciton in the triplet excited state is around 10-50 μs before it decays to the ground state (in non-phosphorescent materials by non-radiative emission), as opposed to the singlet excited state lifetime of about 1 ns.

The possible decay processes for an exciton are described in Figure 2.15. When a singlet exciton is formed either optically (100% of all excitons will be singlets) or electrically (about 25% will be singlets), the electron will be positioned in the lowest singlet excited state S_1 energy level above the ground state S_0 energy level. Electrons in the S_1 state decay into the ground state radiatively (fluorescence) or non-radiatively, a high probability of photon emission requiring a strong coupling between S_1 and S_0 states. However, singlet excitons can also transfer to triplet excited states via inter-system crossing, the electron moving from S_1 to triplet T_1 energy levels. Triplet exciton T_1 states can also be excited optically into higher triplet excited states T_n. As decay from T_1 to S_0 states involves a change in spin, it is radiatively forbidden (photons carry no spin). Triplet excitons therefore normally decay non-radiatively. However, if high atomic number elements are included in the molecular structure (eg. Pt, Ir metal complexes), strong spin-orbit coupling can occur, mixing the states and breaking these selection rules. The lowest triplet excited states T_1 can then decay via photon emission. This is called phosphorescence.[92-95]

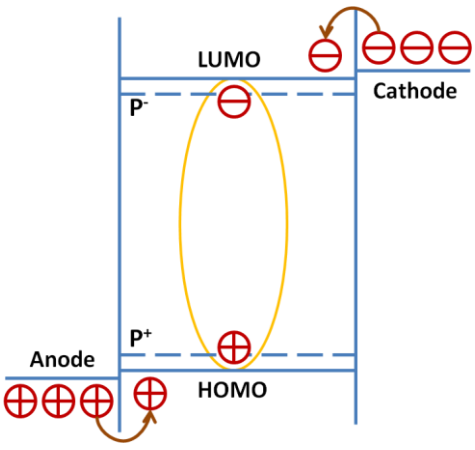


Figure 2.14 Device operation of simple PLEDs. P^- and P^+ denote negatively charged and positively charged polarons respectively.

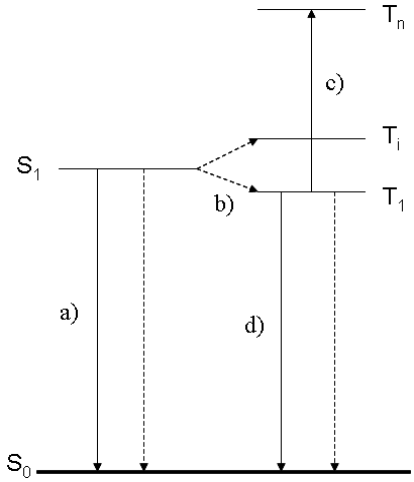


Figure 2.15 Schematic illustration for singlet decay as well as triplet exciton and decay. Solid arrows represent radiative processes corresponding to absorption or emission of light; dashed lines denote non-radiative processes. a) fluorescence, b) intersystem crossing, c) photo-induced triplet-triplet absorption, and d) phosphorescence.

A Jablonski diagram, which is illustrated in Figure 2.16, systematically represents energy level transitions including absorption and emission of light. The diagram also dictates how electrons in common fluorophores are excited from the ground state into higher electronic energy states (S_1 and S_2), and the events that occur as these excited molecules relax by photon emission and other mechanisms to fall back into the initial ground-level energy state (S_0). Each energy state contains a stack of horizontal lines. A thick energy level lines at bottom of each energy state corresponds to the electronic energy states while the thinner lines denote the various vibrational energy levels. Transitions between the states are illustrated as straight or wavy arrows which depend on whether the transition is associated with absorption or emission of a photon (straight arrow) or results from a molecular internal conversion or non-radiative relaxation process (wavy arrows). Fluorescence occurs by two main steps: i) Absorption of a photon relating transition into higher energy level states. ii) Decay of excited states into lower energy levels, either radiatively or non-radiatively. Radiative decay generates light with a wavelength corresponding to the energy gap (HOMO and LUMO difference) of the material. If the absorbed photon contains more energy than is necessary for crossing the energy gap, the excess energy is usually converted into heat

by phonon emission. The internal conversion process is a transition involving a change in spin between singlet and triplet states. Optically excited phosphorescence must include the intersystem crossing which changes the exciton from the lowest singlet state (S_1) to the lowest triplet state (T_1). The presence of heavy atoms such as iridium (Ir) or platinum (Pt) allows radiative transitions between the triplet and ground state. Excitons in triplet states (T_1) can also make a transition back to the excited singlet state, resulting in delayed fluorescence.

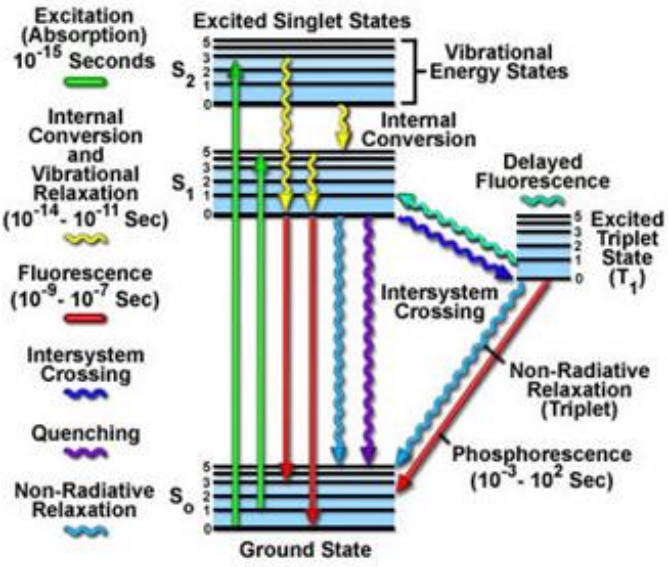


Figure 2.16 Jablonski diagram. [96]

2.4.3 Charge injection and transport

With an applied bias voltage, charge carriers (holes and electrons) are injected from electrodes into the emissive layers. Charged carriers are swept through the device by high electric fields typically more than 10^5 V/cm. Efficient injection can occur at the interface of metal/OSC less than 0.3 eV with ohmic contact characteristic. An interface with an energy gap of greater than 0.3 eV will be contact limited and rectifying current (Schottky contact) will be dominated until a sufficient electric field is applied for confined charged carriers to surmount the energy barrier at the interface.

The injected current comprises of both thermionic emission and tunnelling. Both components are field dependent and the proportion of tunnelling in a total injected current density increases more rapidly than thermionic emission with increased applied bias. For contacts with an energy barrier less than 0.3-0.4 eV, it can be said that it is space charge limited while it is contact limited with a higher barrier height. In theory, current density should increase linearly with applied voltage for an ohmic contact followed by space charge limited current. Additionally, there can be a jump in the current density level by trap limited current, which is then followed by a characteristic of space charge limited current. In this case, it means that there are a number of defect (trap) states exist at the interface of metal and conjugated polymer (CP), which are normally generated owing to deposition condition, impurities, ambient dopants such as oxygen and moisture, and the chemical structure of the material. Once the defect states are filled, then current can be said it is now trap-free space charge limited. The current in the space charge limited regime can be represented as follows:

$$j_{SCLC} = \frac{9}{8}\varepsilon_0\varepsilon_r\mu_m\frac{V^2}{d^3} \qquad (2.17)$$

where ε_r is the dielectric permittivity of the material, μ_m is the mobility of major carrier, V is the applied bias, and d is the layer thickness.

Thermionic emission is dominant in net drive current with a low energetic barrier. The amount of injected current due to tunnelling mechanism increases as the barrier height at the interface between an electrode and a semiconductor becomes higher and more injection limited, and it was reported that tunnelling becomes a main injection route when the barrier height is more than ~1.1 eV.[97] However, net drive current is much lower in a device where tunnelling is dominant than in the devices with low energetic barriers at high applied electric fields.

Thermionic emission is represented in Equation 2.18. [97]

$$j_{th} = A^{*}T^{2}e^{-\frac{q\Phi}{kT}} \qquad (2.18)$$

where A^* is material-dependent effective Richardson constant, e is the magnitude of the electron charge, q is the charge of the carrier, Φ is the potential barrier, k is Boltzmann's constant, and T is the absolute temperature.

Alternatively, for a barrier with a thickness usually less than ~3 nm, the tunnelling mechanism is dominant and the amount of field-induced tunnelling across a potential barrier can be calculated using the Fowler-Nordheim (FN) tunnelling equation (Equation 2.19) [97]:

$$j_{FN} = \frac{A^* T^2}{\Phi_B}\left(\frac{qE}{\alpha kT}\right)^2 e^{\frac{-2\kappa\Phi_B^{2/3}}{3qE}} \qquad (2.19)$$

where Φ_B is the potential barrier, E is the electric field, and κ is a parameter dependent on a barrier shape. The probability for the tunnelling depends strongly on the height and the width of the potential barrier.

Total net drive current is, therefore, a sum of currents from two different injection mechanisms. In 1996, Davids *et al*.[97] presented a relation about current injection in a hole only device structure as follows:

$$j_p(0) = j_{th} - j_{ir} + j_{FN} \qquad (2.20)$$

where $j_p(0)$ is the injected hole current at the contact (x=0) and j_{ir} is called the interface recombination due to current which falls back into the metal after being injected.[98, 99] Therefore, it is necessary to reduce the unnecessary current owing to interface recombination current (j_{ir}) to increase total current density and the overall efficiency of the device. For conjugated polymers with low mobility, amount of j_{ir} is much higher. Deposition of an oxide layer between OSC and a metal can significantly reduce j_{ir} as it functions as a spacer. Additionally, SAMs or LiF can function as a dipole layer which lowers an energy barrier although charge carriers need to tunnel through the layer. Figure 2.17 describes different charge injection mechanisms.

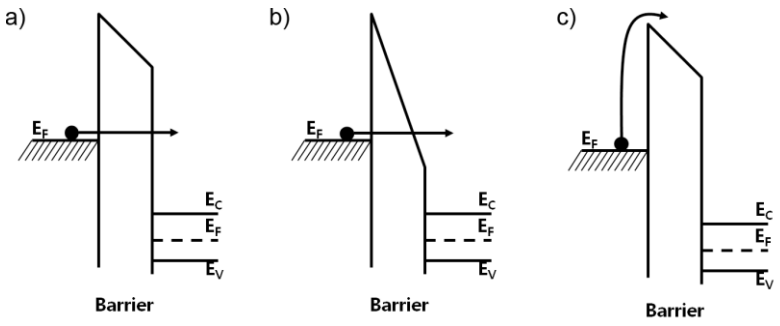


Figure 2.17 Charge injection mechanism: a) Normal tunnelling, b) Fowler-Nordheim tunnelling, and c) Thermionic emission.

Charge transport in OLEDs depends mainly on the bulk property of materials while charge transport in OFETs is induced by an electric field formed at the interface between the semiconductor and the insulating layer. Hence, it can be said that charge transport in OFETs is strongly influenced by the interface property of the device. For high efficient OLEDs, the density of holes and electrons should be similar in the light-emissive layer where the two oppositely charged carriers recombine. It is, therefore, important to balance mobility of holes and electrons in OLEDs.

2.4.4 Charge carrier recombination

With an applied bias, P^+ and P^- are injected from electrodes and attract each other. They meet in a semiconducting layer and form neutral states which are either singlet or triplet excitons. In both cases, the charge forming the exciton is bound to their oppositely charged carrier by a binding energy, which is believed to be a few tenths of an electron volt for conjugated polymers.[100]

Efficiency of electroluminescent devices can be measured by the number of photons generated per electron injected. This is internal quantum efficiency with an assumption that all the generated light is received by the detector. In real device, however, efficiency is dependent with refractive index of the polymer and external quantum efficiency is reduced by a factor of $2n^2$ from the internal efficiency, where n is refractive index of the polymer.[101] Hence, the efficiency of most polymer LED is around 0.1-5%.

External quantum efficiency (Φ_{EQE}) presents a figure of merit of devices including LEDs or PVs. It can be defined as:

$$\Phi_{EQE} = \gamma \Phi_{PL} \chi \sigma_{out} \qquad (2.21)$$

where γ is the recombination efficiency (≈ 1 for ideal case when two types of charge carriers are injected equally), χ is the fraction of singlet excitons formed ,and σ_{out} is the light outcoupling efficiency. Φ_{PL} corresponds photoluminescence quantum yield. It is possible to increase Φ_{EQE} by either/both using high quantum yield luminescence materials (Φ_{PL}) or/and modifying structural design of PLEDs so that the recombination zone is formed far away from the metal electrodes to reduce exciton and charge carrier quenching effect (γ and σ_{out}). The most important non-radiative decay channels which reduce Φ_{PL} are the presence of impurities or end-groups, related to morphological effects at the interface between layers.

The recombination rate, P_{rec}, which is defined as the number of generated excitons in time Δt divided by the number of minority carriers passing through the device in Δt, increases with decreasing transition time. The efficiency of an LED can be improved if the transition time and the mobility of the charge carriers are decreased, because then the steady state carrier concentration of both type of charges within the device is increased. This can be achieved by blending the active layer with an insulator[102] or with a polymer with opposite-charge so that higher mobility charge carriers can be trapped with counter type carriers and increase local charge density enhancing injection of opposite charge carriers[103, 104]. However, it should be reminded that the overall current flow through the device is decreased by decreasing the mobility of the carriers, so that higher bias voltages are required to obtain same luminescence as for the undiluted PLEDs.

In short, prerequisite characteristics for an efficient LED are: (1) all of the injected carrier should recombine in the active layer (2) the operating voltage should be the minimum value. In a single-layer LED, many numbers of either carriers are traverse to the counter contact without recombination if the other carrier type is in low concentrated respectively and has a low mobility. It is important to make sure that both

carrier types are injected equally and efficiently with balanced mobility. A multi-layer or a bilayer structure LED, which are compromised of more than one emissive or transporting layer for enhancing or blocking charge carriers injection and transport, can reduce the transverse of charge carriers effectively. The relative energy levels and the mobilities of the holes and electrons travelling in the device are important design parameters. The barrier heights for carrier injection at both contacts should also be minimized to reduce the operating voltage.

2.5 Reference

[1] H. Koezuka, A. Tsumura, T. Ando, *Synthetic Metals* **1987**, *18*, 699.

[2] H. Koezuka, A. Tsumura, *Synthetic Metals* **1989**, *28*, C753-C760.

[3] P. F. Baude, D. A. Ender, M. A. Haase, T. W. Kelley, D. V. Muyres, S. D. Theiss, *Applied Physics Letters* **2003**, *82*, 3964.

[4] Y. Y. Lin, D. J. Gundlach, S. F. Nelson, T. N. Jackson, *Ieee Electron Device Letters* **1997**, *18*, 606.

[5] I. McCulloch, C. Bailey, M. Giles, K. Genevicius, M. Heeney, M. Shkunov, D. Sparrowe, S. Tierney, M. Suzuki, *Abstracts of Papers of the American Chemical Society* **2005**, *229*, 288-PMSE.

[6] S. K. Park, T. N. Jackson, J. E. Anthony, D. A. Mourey, *Applied Physics Letters* **2007**, *91*.

[7] Y. N. Li, Y. L. Wu, P. Liu, Z. Prostran, S. Gardner, B. S. Ong, *Chemistry of Materials* **2007**, *19*, 418.

[8] P. K. Weimer, *Proc. IRE* **1962**, *50*, 1462.

[9] F. Y. Gan, I. Shih, *Ieee Transactions on Electron Devices* **2002**, *49*, 15.

[10] J. Debaets, J. Vanfleteren, I. Derycke, J. Doutreloigne, A. Vancalster, P. Devisschere, *Ieee Transactions on Electron Devices* **1990**, *37*, 636.

[11] H. Sirringhaus, P. J. Brown, R. H. Friend, M. M. Nielsen, K. Bechgaard, B. M. W. Langeveld-Voss, A. J. H. Spiering, R. A. J. Janssen, E. W. Meijer, P. Herwig, D. M. de Leeuw, *Nature* **1999**, *401*, 685.

[12] H. Sirringhaus, R. J. Wilson, R. H. Friend, M. Inbasekaran, W. Wu, E. P. Woo, M. Grell, D. D. C. Bradley, *Applied Physics Letters* **2000**, *77*, 406.

[13] Z. Bao, A. J. Lovinger, A. Dodabalapur, *Applied Physics Letters* **1996**, *69*, 3066.

[14] H. Sirringhaus, N. Tessler, R. H. Friend, *Science* **1998**, *280*, 1741.

[15] Y. Kim, S. Cook, S. M. Tuladhar, S. A. Choulis, J. Nelson, J. R. Durrant, D. D. C. Bradley, M. Giles, I. Mcculloch, C. S. Ha, M. Ree, *Nature Materials* **2006**, *5*, 197.

[16] J. F. Chang, B. Q. Sun, D. W. Breiby, M. M. Nielsen, T. I. Solling, M. Giles, I. McCulloch, H. Sirringhaus, *Chemistry of Materials* **2004**, *16*, 4772.

[17] R. J. Kline, M. D. McGehee, E. N. Kadnikova, J. S. Liu, J. M. J. Frechet, *Advanced Materials* **2003**, *15*, 1519.

[18] A. Zen, J. Pflaum, S. Hirschmann, W. Zhuang, F. Jaiser, U. Asawapirom, J. P. Rabe, U. Scherf, D. Neher, *Advanced Functional Materials* **2004**, *14*, 757.

[19] G. Horowitz, *Advanced Materials* **1998**, *10*, 365.

[20] S. R. Forrest, *Nature* **2004**, *428*, 911.

[21] P. G. Lecomber, W. E. Spear, *Physical Review Letters* **1970**, *25*, 509.

[22] W. E. Spear, P. G. LeComber, *J. Non-Cryst. Solids* **1972**, *8*, 727.

[23] A. Madan, P. G. Lecomber, W. E. Spear, *Journal of Non-Crystalline Solids* **1976**, *20*, 239.

[24] M. J. Powell, *Philosophical Magazine B-Physics of Condensed Matter Statistical Mechanics Electronic Optical and Magnetic Properties* **1981**, *43*, 93.

[25] D. M. Pai, *Journal of Chemical Physics* **1970**, *52*, 2285.

[26] L. Pautmeier, R. Richert, H. Bassler, *Synthetic Metals* **1990**, *37*, 271.

[27] H. Bassler, *Philosophical Magazine B-Physics of Condensed Matter Statistical Mechanics Electronic Optical and Magnetic Properties* **1984**, *50*, 347.

[28] L. Burgi, R. H. Friend, H. Sirringhaus, *Applied Physics Letters* **2003**, *82*, 1482.

[29] G. Horowitz, P. Delannoy, *J. Appl. Phys*. **1991**, *70*, 469.

[30] G. Horowitz, R. Hajilaoui, P. Delannoy, *J. Phys. III (Paris)* **1995**, *5*, 355.

[31] C. D. Dimitrakopoulos, I. Kymissis, S. Purushothaman, D. A. Neumayer, P. R. Duncombe, R. B. Laibowitz, *Advanced Materials* **1999**, *11*, 1372.

[32] D. J. Gundlach, L. Zhou, J. A. Nichols, T. N. Jackson, P. V. Necliudov, M. S. Shur, *Journal of Applied Physics* **2006**, *100*.

[33] B. H. Hamadani, D. Natelson, *Journal of Applied Physics* **2005**, *97*.

[34] L. Burgi, T. J. Richards, R. H. Friend, H. Sirringhaus, *Journal of Applied Physics* **2003**, *94*, 6129.

[35] H. G. O. Sandberg, T. G. Backlund, R. Osterbacka, M. Shkunov, D. Sparrowe, I. McCulloch, H. Stubb, *Organic Electronics* **2005**, *6*, 142.

[36] J. Zaumseil, C. L. Donley, J. S. Kim, R. H. Friend, H. Sirringhaus, *Advanced Materials* **2006**, *18*, 2708.

[37] R. C. G. Naber, M. Mulder, B. de Boer, P. W. M. Blom, D. M. de Leeuw, *Organic Electronics* **2006**, *7*, 132.

[38] J. Veres, S. D. Ogier, S. W. Leeming, D. C. Cupertino, S. M. Khaffaf, *Advanced Functional Materials* **2003**, *13*, 199.

[39] P. V. Necliudov, M. S. Shur, D. J. Gundlach, T. N. Jackson, *Journal of Applied Physics* **2000**, *88*, 6594.

[40] J. F. Yuan, J. Zhang, J. Wang, X. J. Yan, D. H. Yan, W. Xu, *Applied Physics Letters* **2003**, *82*, 3967.

[41] J. Veres, S. D. Ogier, S. W. Leeming, D. C. Cupertino, S. M. Khaffaf, *Advanced Functional Materials* **2003**, *13*, 199.

[42] J. Veres, S. Ogier, G. Lloyd, D. de Leeuw, *Chemistry of Materials* **2004**, *16*, 4543.

[43] D. J. Gundlach, C. C. S. Kuo, C. D. Sheraw, J. A. Nichols, T. N. Jackson, *Organic Field Effect Transistors* **2001**, *4466*, 54.

[44] J. Veres, S. D. Ogier, S. W. Leeming, D. Cupertino, S. M. Khaffaf, G. Lloyd, unpublished.

[45] S. F. Nelson, Y. Y. Lin, D. J. Gundlach, T. N. Jackson, *Applied Physics Letters* **1998**, *72*, 1854.

[46] B. Mann, H. Kuhn, *Journal of Applied Physics* **1971**, *42*, 4398.

[47] E. A. Weiss, M. J. Tauber, R. F. Kelley, M. J. Ahrens, M. A. Ratner, M. R. Wasielewski, *Journal of the American Chemical Society* **2005**, *127*, 11842.

[48] S. H. Choi, B. Kim, C. D. Frisbie, *Science* **2008**, *320*, 1482.

[49] D. Vuillaume, C. Boulas, J. Collet, J. V. Davidovits, F. Rondelez, *Applied Physics Letters* **1996**, *69*, 1646.

[50] M. Halik, H. Klauk, U. Zschieschang, G. Schmid, C. Dehm, M. Schutz, S. Maisch, F. Effenberger, M. Brunnbauer, F. Stellacci, *Nature* **2004**, *431*, 963.

[51] B. N. Park, S. Seo, P. G. Evans, *Journal of Physics D-Applied Physics* **2007**, *40*, 3506.

[52] A. R. Brown, C. P. Jarrett, D. M. de Leeuw, M. Matters, *Synth. Met*. **1997**, *88*, 37

[53] F. Dinelli, M. Murgia, P. Levy, M. Cavallini, F. Biscarini, D. M. de Leeuw, *Physical Review Letters* **2004**, *92*.

[54] A. Bolognesi, A. Di Carlo, P. Lugli, *Applied Physics Letters* **2002**, *81*, 4646.

[55] J. Huang, J. Sun, H. E. Katz, *Advanced Materials* **2008**, *20*, 2567.

[56] C. W. Tang, S. A. Vanslyke, *Applied Physics Letters* **1987**, *51*, 913.

[57] J. H. Burroughes, D. D. C. Bradley, A. R. Brown, R. N. Marks, K. Mackay, R. H. Friend, P. L. Burns, A. B. Holmes, *Nature* **1990**, *347*, 539.

[58] H. Sirringhaus, T. Kawase, R. H. Friend, T. Shimoda, M. Inbasekaran, W. Wu, E. P. Woo, *Science* **2000**, *290*, 2123.

[59] G. P. Collins, *Scientific American* **2004**, *291*, 74.

[60] R. H. Friend, R. W. Gymer, A. B. Holmes, J. H. Burroughes, R. N. Marks, C. Taliani, D. D. C. Bradley, D. A. Dos Santos, J. L. Bredas, M. Logdlund, W. R. Salaneck, *Nature* **1999**, *397*, 121.

[61] A. Kraft, A. C. Grimsdale, A. B. Holmes, *Angewandte Chemie-International Edition* **1998**, *37*, 402.

[62] M. A. Baldo, D. F. O'Brien, Y. You, A. Shoustikov, S. Sibley, M. E. Thompson, S. R. Forrest, *Nature* **1998**, *395*, 151.

[63] J. R. Sheats, H. Antoniadis, M. Hueschen, W. Leonard, J. Miller, R. Moon, D. Roitman, A. Stocking, *Science* **1996**, *273*, 884.

[64] R. H. Friend, R. W. Gymer, A. B. Holmes, J. H. Burroughes, R. N. Marks, C. Taliani, D. D. C. Bradley, D. A. Dos Santos, J. L. Bredas, M. Logdlund, W. R. Salaneck, *Nature* **1999**, *397*, 121.

[65] P. L. Burn, A. B. Holmes, A. Kraft, D. D. C. Bradley, A. R. Brown, R. H. Friend, R. W. Gymer, *Nature* **1992**, *356*, 47.

[66] P. L. Burn, A. Kraft, D. R. Baigent, D. D. C. Bradley, A. R. Brown, R. H. Friend, R. W. Gymer, A. B. Holmes, R. W. Jackson, *Journal of the American Chemical Society* **1993**, *115*, 10117.

[67] R. Jin, P. A. Levermore, J. S. Huang, X. H. Wang, D. D. C. Bradley, J. C. Demello, *Physical Chemistry Chemical Physics* **2009**, *11*, 3455.

[68] D. Kabra, M. H. Song, B. Wenger, R. H. Friend, H. J. Snaith, *Advanced Materials* **2008**, *20*, 3447.

[69] N. C. Greenham, S. C. Moratti, D. D. C. Bradley, R. H. Friend, A. B. Holmes, *Nature* **1993**, *365*, 628.
[70] A. R. Brown, N. C. Greenham, J. H. Burroughes, D. D. C. Bradley, R. H. Friend, P. L. Burn, A. Kraft, A. B. Holmes, *Chemical Physics Letters* **1992**, *200*, 46.
[71] H. Sirringhaus, *Advanced Materials* **2005**, *17*, 2411.
[72] L. D. Bozano, K. R. Carter, V. Y. Lee, R. D. Miller, R. DiPietro, J. C. Scott, *Journal of Applied Physics* **2003**, *94*, 3061.
[73] S. H. Khong, S. Sivaramakrishnan, R. Q. Png, L. Y. Wong, P. J. Chia, L. L. Chua, P. K. H. Ho, *Advanced Functional Materials* **2007**, *17*, 2490.
[74] F. Huang, Y. Zhang, M. S. Liu, A. K. Y. Jen, *Advanced Functional Materials* **2009**, *19*, 2457.
[75] S. Sax, N. Rugen-Penkalla, A. Neuhold, S. Schuh, E. Zojer, E. J. W. List, K. Mullen, *Advanced Materials* **2010**, *22*, 2087.
[76] W. L. Ma, P. K. Iyer, X. Gong, B. Liu, D. Moses, G. C. Bazan, A. J. Heeger, *Advanced Materials* **2005**, *17*, 274.
[77] G. Gustafsson, Y. Cao, G. M. Treacy, F. Klavetter, N. Colaneri, A. J. Heeger, *Nature* **1992**, *357*, 477.
[78] J. Smith, A. Bashir, G. Adamopoulos, J. E. Anthony, D. D. C. Bradley, R. Hamilton, M. Heeney, I. McCulloch, and T. D. Anthopoulos, *Adv. Mater*. **2010**, *22*, 3598.
[79] S. H. Park, A. Roy, S. Beaupre, S. Cho, N. Coates, J. S. Moon, D. Moses, M. Leclerc, K. Lee, A. J. Heeger, *Nature Photonics* **2009**, *3*, 297.
[80] J. Y. Kim, S. H. Kim, H. H. Lee, K. Lee, W. L. Ma, X. Gong, A. J. Heeger, *Advanced Materials* **2006**, *18*, 572.
[81] K. S. Cho, E. K. Lee, W. J. Joo, E. Jang, T. H. Kim, S. J. Lee, S. J. Kwon, J. Y. Han, B. K. Kim, B. L. Choi, J. M. Kim, *Nature Photonics* **2009**, *3*, 341.
[82] S. A. Haque, S. Koops, N. Tokmoldin, J. R. Durrant, J. S. Huang, D. D. C. Bradley, E. Palomares, *Advanced Materials* **2007**, *19*, 683.
[83] N. Tokmoldin, N. Griffiths, D. D. C. Bradley, S. A. Haque, *Advanced Materials* **2009**, *21*, 3475.
[84] D. Kabra, M. H. Song, B. Wenger, R. H. Friend, H. J. Snaith, *Advanced Materials* **2008**, *20*, 3447.
[85] Y. Nakayama, K. Morii, Y. Suzuki, H. Machida, S. Kera, N. Ueno, H. Kitagawa, Y. Noguchi, H. Ishii, *Advanced Functional Materials* **2009**, *19*, 3746.
[86] J. M. Caruge, J. E. Halpert, V. Bulovic, M. G. Bawendi, *Nano Letters* **2006**, *6*, 2991.
[87] G. Vaubel, H. Baessler, D. Mobius, *Chemical Physics Letters* **1971**, *10*, 334.
[88] V. L. Colvin, M. C. Schlamp, A. P. Alivisatos, *Nature* **1994**, *370*, 354.
[89] S. Coe-Sullivan, W. K. Woo, J. S. Steckel, M. Bawendi, V. Bulovic, *Organic Electronics* **2003**, *4*, 123.
[90] M. A. Reed, *Scientific American* **1993**, *268*, 118.
[91] S. Coe, W. K. Woo, M. Bawendi, V. Bulovic, *Nature* **2002**, *420*, 800.
[92] G. Schwartz, K. Fehse, M. Pfeiffer, K. Walzer, K. Leo, *Applied Physics Letters* **2006**, *89*.
[93] R. Meerheim, K. Walzer, M. Pfeiffer, K. Leo, *Applied Physics Letters* **2006**, *89*.

[94] G. F. He, M. Pfeiffer, K. Leo, M. Hofmann, J. Birnstock, R. Pudzich, J. Salbeck, *Applied Physics Letters* **2004**, *85*, 3911.

[95] Y. C. Chiu, J. Y. Hung, Y. Chi, C. C. Chen, C. H. Chang, C. C. Wu, Y. M. Cheng, Y. C. Yu, G. H. Lee, P. T. Chou, *Advanced Materials* **2009**, *21*, 2221.

[96] http://micro.magnet.fsu.edu/optics/timeline/people/jablonski.html

[97] P. S. Davids, S. M. Kogan, I. D. Parker, D. L. Smith, *Applied Physics Letters* **1996**, *69*, 2270.

[98] M. A. Abkowitz, H. A. Mizes, *Applied Physics Letters* **1995**, *66*, 1288.

[99] Y. N. Gartstein, E. M. Conwell, *Chemical Physics Letters* **1996**, *255*, 93.

[100] J. L. Bredas, J. Cornil, A. J. Heeger, *Advanced Materials* **1996**, *8*, 447.

[101] N. C. Greenham, R. H. Friend, D. D. C. Bradley, *Advanced Materials* **1994**, *6*, 491.

[102] A. R. Brown, D. D. C. Bradley, J. H. Burroughes, R. H. Friend, N. C. Greenham, P. L. Burn, A. B. Holmes, A. Kraft, *Applied Physics Letters* **1992**, *61*, 2793.

[103] P. K. H. Ho, J. S. Kim, J. H. Burroughes, H. Becker, S. F. Y. Li, T. M. Brown, F. Cacialli, R. H. Friend, *Nature* **2000**, *404*, 481.

[104] P. A. Levermore, R. Jin, X. H. Wang, J. C. de Mello, D. D. C. Bradley, *Advanced Functional Materials* **2009**, *19*, 950.

Chapter III

Printing Techniques for Organic Semiconductor Optoelectronic Devices

3.1 Introduction

The origin of the term ‘printing’ is referred to *1. the production of books, newspapers, etc. 2. a single impression of a book. 3. handwriting in which the letters are written separately* according to the Oxford English Dictionary. This is conventionally accurate as printing has been mainly implemented for graphical purposes in the past. Johannes Gutenberg invented wooden printing-press, a first form of mass printing, in late 14th century. He used wine as an ink and individual letters to build meaningful words at any time so that he did not need to manufacture printing plates for every page.

In the late 20th century or the early 21th century, the idea of mass production in printing technology was transformed by means of production tools for optoelectronic devices such as TVs, monitors or photovoltaics (PVs). Introduction of printing in optoelectronics has attracted industrial firms to reduce fabrication costs so that they can offer reduced price to customers with similar quality. The trend in the optoelectronics market is rapidly changing and production at low costs has become one of the most important factors for survival in the market.

In 2003, Wilson and Boland at Clemson University proposed that it is also possible to use printing technology for biological purposes.[1, 2] They designed a cell printer that places cells in positions that mimic their positions in an organ.[3] The complex human 3D organs would be printable prior to exact placing of different cell types in 3D engineered organs. Printing would use different kinds of ink for its purposes, but understanding of its fluidic movements, self-assembly properties, and physical properties will enhance development of a broad area of science as well as of graphic arts industry.

In this Chapter, printing for optoelectronics using inks with semiconducting properties is discussed. Various printing techniques are introduced in Section 3.2 with its distinguishable characteristics. The physical parameters which need to be considered for homogeneous printing of thin semiconducting layers are explained in Section 3.3. Fluidic movements inside ink formulations in drying process are analysed in Section 3.4. Practical applications of the fluidic movements in ink-jet printing and gravure printing are described in Section 3.5.

3.2 Printing Techniques

There have been a number of printing techniques introduced and explored as the next generation processing method for optoelectronic devices.[4, 5] The expensive and time consuming sublimed thermal evaporation process offers high yield rate attributed to high vacuum and purified condition during material deposition, but it is not suitable for large area displays as fabrication of large area displays will significantly increase the manufacturing costs. For example, 41 inch OLED TV demonstrated by Samsung and high definition (HD) 21 inch OLED TV already commercialized by Sony have both shown to have high retail prices at the time of the research. A novel approach to printing optoelectronic devices using solution processable materials such as long chain polymer molecules or few types of small molecule semiconductors has attracted great interest from the display industry although its current research level is rather far from being commercialized.

Potential printing techniques are known as screen printing, transfer printing (stamping), ink-jet printing, gravure printing, offset printing, and spray printing. Important properties of each printing technique include how small pattern it can print (resolution), how fast it can print (throughput), how thick it can print (thickness), and what the restriction on materials is (viscosity). These are listed in Table 3.1. The most important features among them can be said to be high resolution and high throughput speed. Achieving both parameters at good levels is problematic as high throughput speed often results in poor resolution attributed to high kinetic energy, for example, in gravure printing, while the high resolution advantage of ink-jet printing suffers from very low processing speed. Alternatively, offset gravure printing offers reasonable resolution and throughput speed. Figure 3.1 indicates numerical values of resolution and throughput graphically.

	Layer thickness (μm)	Resolution (μm)	Viscosity (cP)	Throughput (m^2/s)
Screen Printing	30~100	20~100	500~50,000	2~3
Stamping	1~2	5	>50	0.1
Gravure Printing	0.05~8	75	50~200	60
Offset Printing	0.5~1.5	10~50	40,000~100,000	5~30
Flexography	0.8~2.5	80	50~500	10
Ink-jet Printing	<0.5	5	1~30	0.01~0.5

Table 3.1 Processing parameters of various printing techniques.[6]

The printing techniques can be divided by two large segments of contact and non-contact printing methods. Contact printing, as the term suggests, is a method that an ink formulation physically meets a substrate with a certain pressure. Roll-to-roll (R2R) printings are representative methods. On the other hand, if an ink formulation drops and is deposited onto a substrate, it is regarded as a non-contact method. Ink-jet printing is one such technique.

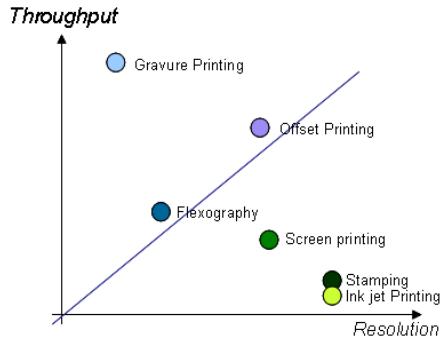


Figure 3.1 Graphical representation of a relation between throughput and resolution of printing techniques. (data from Ref. [6])

An early version of printing for optoelectronic device consisted of a metal frame with a patterned mesh. This method is called screen printing (SP) and its overall process is illustrated in Figure 3.2. An ink formulation is swept by a squeegee (or doctor blade) on the metal plate so that the ink formulation can penetrate through the mesh pattern on the plate. The penetrated ink formulation is finally then printed onto a substrate placed at the bottom of the plate. Normally, a high viscosity ink formulation is suitable with this printing technique as low viscosity inks can coalesce with inks penetrated from different mesh. Also, the resolution of this type of printing is relatively poor between 20~100 μm.[6] Dino *et al*. reported OLEDs with Alq_3 as an active layer with screen printed hole transporting layer (HTL) in 2000.[7] However, the device performance of the screen printed HTL showed that its driving voltage is higher and the total light output is less than spin-coated device with the same device structure. Figure 3.3 shows photoluminescence images of MEH-PPV polymer logos that were printed using the SP techniques.

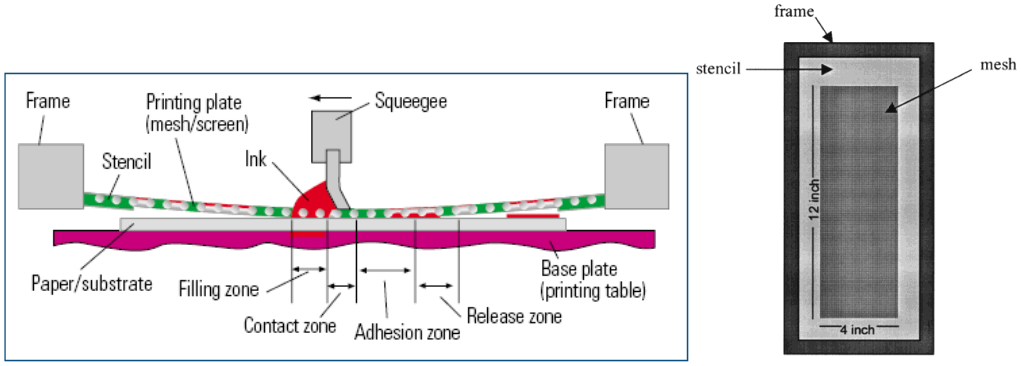


Figure 3.2 a) Schematic of overall process of screen printing. Adopted from Ref. [8] and b) top view of the mesh plate. A 120 mesh counts per inch. Adopted from Ref. [7].

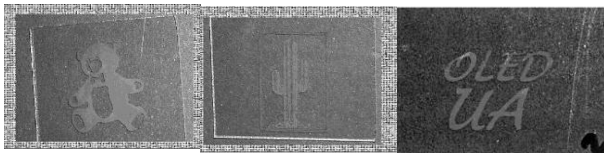


Figure 3.3 Photos of photoluminescence images of MEH-PPV polymer logos that were printed by screen printing technique. Adopted from Ref. [7].

Using an orthogonal solvent is critical in solution processed organic materials as an upper layer can dissolve the underlying layer upon its deposition if solvents used for both layers have similar solubility.[9] Sublimed small molecules can easily avoid this problem but deposition of materials which are solution processed sequentially is more difficult. Chemical modification of ink formulation for the upper layer or crosslinking of the already deposited bottom layer can resolve the problem but the former is limited only by cases in which there are many parameters to consider such as solubility, polarity, and boiling point of materials and the latter needs an extra crosslinking agent layer which may hamper efficient carrier transport at the interface.

Recently, stamping of a completely dried semiconducting layer has demonstrated an alternative method for successive deposition of multiple organic layers. The stamping process can be categorized by pad printing and stamping. As described in Figure 3.4, pad printing is a process of transferring an ink formulation from a patterned cliché while stamping is transferring an ink formulation using a patterned stamping medium. Polydimethylsiloxane (PDMS) is one of elastomers, which is a polymer with a viscoelastic property, and is a popular material as a transferring medium. However, PDMS is an organic material and incompatible with many organic solvents as they dissolve the elastomer. Kim *et al*. reported that they coated PDMS with Parylene-C polymer as a buffer layer prior to spin-coating of a quantum dot (QD) ink based in chloroform, which can dissolve PDMS.[10] The stamping process offers high resolution patterns around ~ few μms, which is ideal for source and drain electrodes in field-effect transistors.[11]

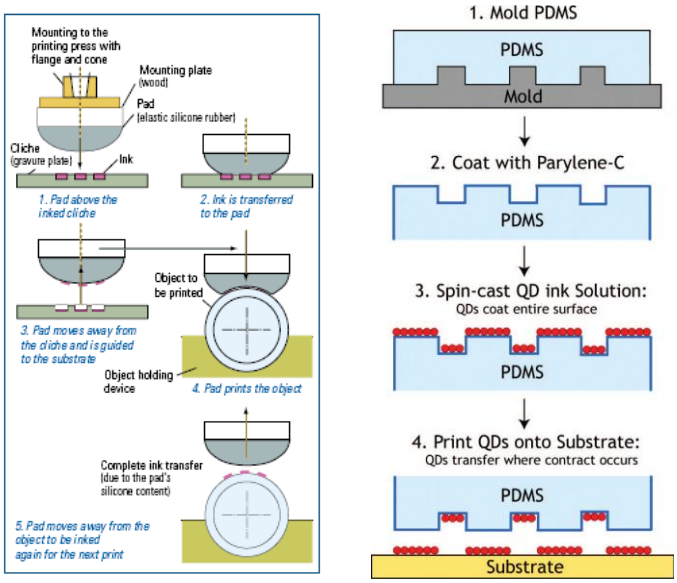


Figure 3.4 Schematics of transfer printing; a) pad printing and b) stamping. Adopted from Ref. [8,10].

Chen *et al*. demonstrated sequentially stamping-printed arrays of three different polymer layers having red, green, blue light-emitting properties. Each line has a width of 150 μm and photoluminescence (PL) of layers, which are excited by different wavelengths, are shown in Figure 3.5.[12] Also, Figure 3.6 illustrates QD-LEDs consisting of stamping printed QD arrays and its electroluminescence (EL).

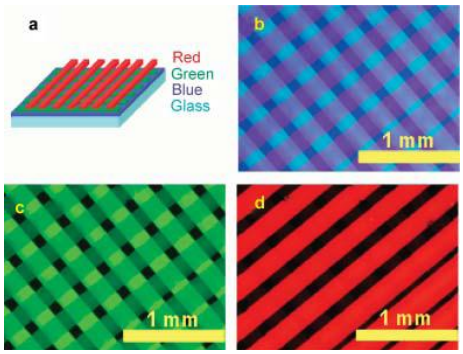


Figure 3.5 a) Schematic multilayer printed polymer structure comprising a uniform layer of blue emission polymer, and crossed stripes (~150 μm width) of green then red emission polymers deposited in sequence on a glass substrate. b) UV excitation (330-380 nm), c) blue excitation (465-495 nm), and d) green emission (510-560 nm). Adopted from Ref. [12].

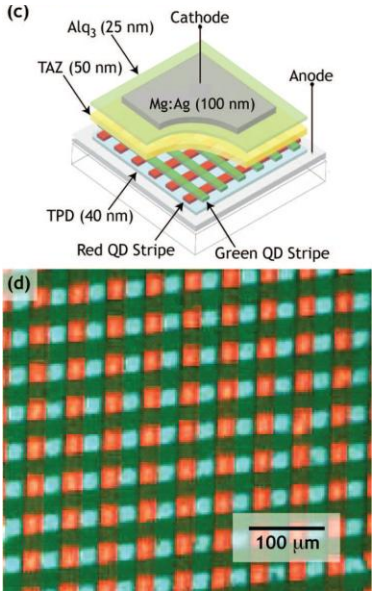


Figure 3.6 Schematic diagram of a structure of a QD-LED pixel patterned with 25 μm wide stamp features. Adopted from Ref. [10].

Roll-to-roll printing, which is originally invented for printing of newspapers, magazines and packages of PET bottles, can also be applied for fabrication of optoelectronic devices providing ultimate speeds up to 60 m^2/s. This is expected to reduce manufacturing costs significantly. Gravure printing and offset printing are representative types of R2R printing. Gravure printing offers the fastest manufacturing speed among other types of printing. However, its resolution is relatively poor around 75 μm.[6] An overview of the printing process is described in Figure 3.7. The printing procedure starts from dropping an ink formulation onto patterns which are engraved in a metal cliché. Then, a doctor blade squeezes the ink formulation as a cylinder pressing roll travels passing onto the cliché. The confined ink formulations in the patterns are then transferred onto a flexible substrate attached on the cylinder roll (Figure 3.7a). For successive transferring of ink formulation onto a substrate, the condition given in Equation 3.1 has to be made.

$$\sigma_{pattern} < \sigma_{Ink} < \sigma_{Substrate} \qquad (3.1)$$

where σ denotes surface energy of materials. Surface energy quantifies a disrupting energy of intermolecular bonding when a surface is created. Hence, if a surface is created with a complex structure at a molecular scale, it can be said that the surface

contains large energy. The surface energy has to be less than the energy of bulk otherwise the bulk will continuously change to a surface state as it can be defined as sublimation. Hence, it is often said that surface energy is an excess energy at the surface of a material compared to the bulk.

The transferred ink formulation on the substrate then starts to coalesce with adjacent inks to form a continuous thin layer of a few μms (Figure 3.7b). Organic solvents start to evaporate and its speed depends on the flash point of the solvent and environmental conditions such as temperature and humidity (Figure 3.7c). Finally, a thin layer film is formed (Figure 3.7d). The thickness of the thin film formed is dependent with the cell depth of cliché pattern, concentration of ink formulation, rolling pressure, and printing speed. Its thickness is normally within a range between 50 nm and 8 μm but recently it was proven experimentally that films as thin as 10 nm are also printable (later confirmed in Chapter 6).

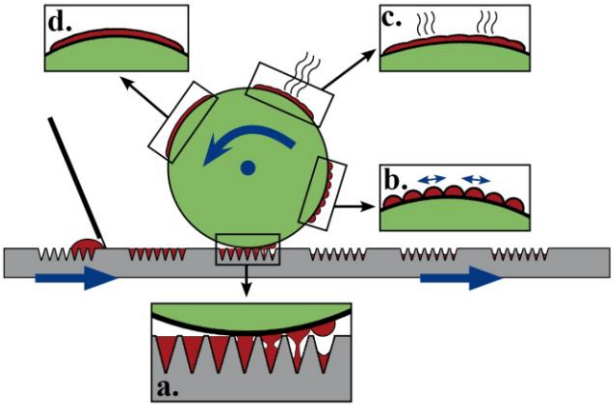


Figure 3.7 Schematic of overall process of gravure printing. Adopted from Ref. [13].

There have been reports on gravure printed optoelectronic devices such as OLEDs[14, 15], OFETs[16-18], and OPVs[19]. Similar to reports on other printing techniques, reports using gravure printing showed that its device performance is inferior to conventionally deposited by spin-coating procedure.[14,16,20] Non uniform surface profiles of gravure printed thin films are considered as primary factors for low performance and yield rate. Printing using a low viscosity ink is particularly important for highly uniform surface with its sufficient fluidic movements inside the printed

droplets, while high viscosity ink induces little hydrodynamic flows and can help to print relatively high resolution patterns but with poor homogeneity on the surface. It may be helpful to regard printing using high viscosity ink as the method similar to printing for graphical purposes such as newspapers and magazines. Printing of optoelectronic devices is completely different applications where the layer thickness is typically less than 100 nm and homogeneity is much more crucial than obtaining high resolution for functional devices. Printing of optoelectronic devices using low viscosity inks is demonstrated in Chapter 5 and 6. In Chapter 8, relatively high viscosity inks were implemented for developing functional OFETs whose device performance is less dependent on the surface homogeneity than for OLEDs where the uniformity of layers is closely related to the uniform emission of the light output.

Yan *et al*. demonstrated operational complementary metal oxide transistors (CMOS) which consists of gravure printed organic layers.[17] They compared surface homogeneity fabricated from various printing techniques. As it is shown in Figure 3.8, gravure printing technique delivered the most uniform thin film surface compared to other flexo and inkjet printings. As a result, only gravure printed OFETs showed performance comparable to the spin-coated control device.

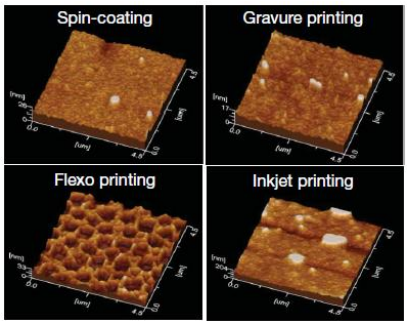


Figure 3.8 Atomic force microscopy (AFM) images of spin-coated and printed films. Adopted from Ref. [17].

Interestingly, Ali Javey at University of California at Berkeley proposed that preferentially aligned nanowires can be obtained using gravure printing.[21,22] As described in Figure 3.9, nanowires vertically grown on flexible donor substrates were transferred onto a receiver substrate and its aligned pattern parallel to the printing

direction was obtained. Although its homogeneity of aligned wires is not appropriate for functional devices yet, it opened up a new era of R2R printing. The results suggested that gravure printing is not only for fabrication of thin films but can be implemented with aligning of nanomaterials and molecular structures.

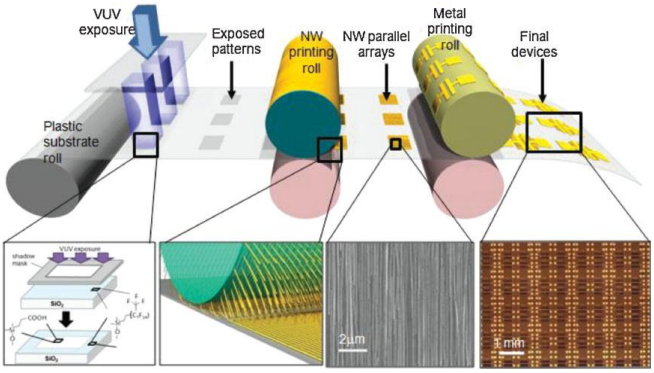


Figure 3.9 Schematic of an envisioned R2R printing set-up for nanowire electronics. Adopted from Ref. [23].

Another popular R2R printing is offset type printing.[24,25] This type can be distinguished from gravure printing as it has an additional roll or plate that transfers the ink formulation before it is actually printed onto the substrates while the ink formulation is directly printed as it is scraped by the doctor blade and confined into patterns on a cliché in gravure printing type. The technique offers improved resolution compared to gravure printing, which can usually obtain patterns with 10-50 μm resolution. The additional roll (plate), which is coated with a patterned soft plate, is the main reason for high resolution. Offset printing can be thought to be a combined method of gravure printing and stamping. An ink formulation uniformly scraped by a doctor blade (Gravure printing) is transferred onto a substrate by a patterned soft plate (Stamping). Ink viscosity needs to be relatively high for ink formulations to be maintained onto the rotational soft plate during the printing process. The overall process is described in Figure 3.10.

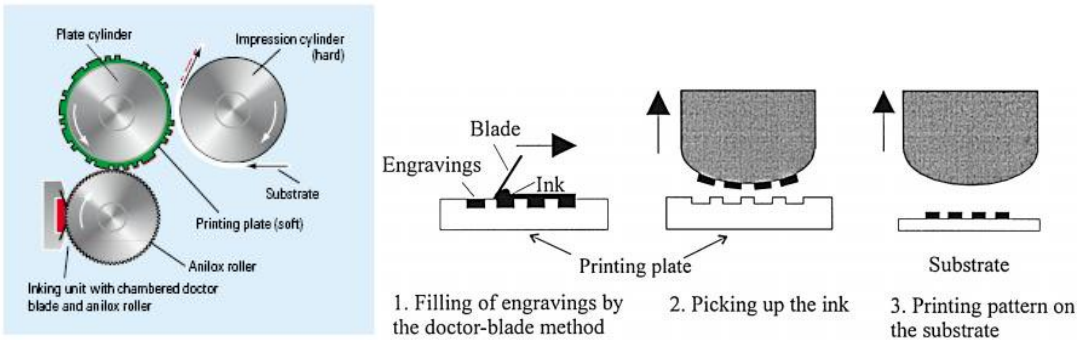


Figure 3.10 Overall thin film deposition process of offset printing. Adopted from Ref. [8, 24].

Ink-jet printing is a representative type of non-contact printing technique. It has a similar functional operation as ordinary document printing, but it uses semiconducting inks instead of writing inks. Optoelectronic devices also can be solution processed using this type of printing.[26-32] It is the most advanced type of printing reported so far and recently, a colour filter for LCD displays which is patterned by ink-jet printing technique was reported in 2006.[33,34] Ink-jet printing uses piezoelectric materials, which deforms when an electric field is applied to the material prior to its electrical polarization. If the electric field is applied parallel to the polarization direction, the material is extended along the field direction (bend mode) whereas if the electric field is orthogonally applied, the material becomes in shear mode. The ink droplet even less than 20 pl can be ejected from a nozzle by a repetition of applied electric fields along both parallel and orthogonal directions at each time deforming the piezoelectric material. A schematic of principal operation of ink-jet printing is illustrated in Figure 3.11.

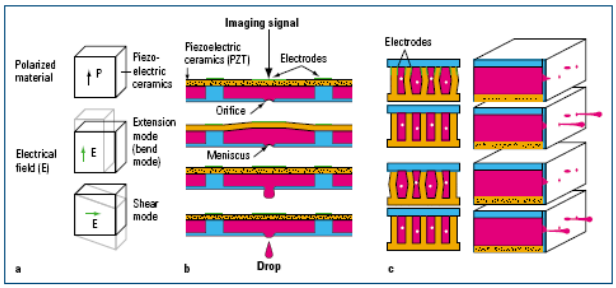


Figure 3.11 A schematic of ink-jet printing operation. Adopted from Ref. [8].

The resolution of ink-jet printed patterns can be achieved between 20 and 50 μm size in width. This range may be suitable with patterning of pixels for display, however, it is

not sufficient for defining source-drain electrodes of functional thin-film transistors (TFTs) which normally needs a channel length around 5-10 μm for efficient charge carrier transport between two electrodes achieving both high drive current and switching speed. Sirringhaus *et al*. reported ink-jet printed source and drain electrodes which have a channel length of about 5 μm as shown in Figure 3.12.[28] A substrate identified by two regions of different surface energies enabled high resolution. Aqueous PEDOT:PSS solution is hydrophilic and does not coat hydrophobic polyimide (PI). Similarly, ink-jet printed 66 μm pixel size pattern was demonstrated by using of a polymer barrier between pixels as shown in Figure 3.13.[35] Ink confinement by the polyimide polymer barriers offers significantly improved resolution.

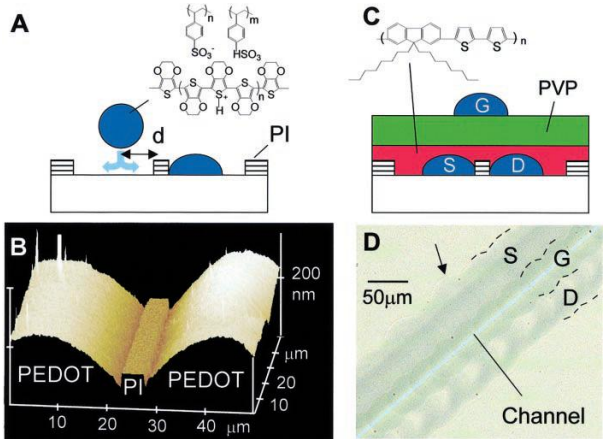


Figure 3.12 A) Schematic diagram of high-resolution ink-jet printing onto a pre-patterned substrate. B) AFM image showing source and drain PEDOT:PSS electrodes are separated by a repelling PI line with L = 5 μm. C) Schematic diagram of the top-gate TFT configuration with an F8T2 semiconducting layer. D) Optical micrograph of an ink-jet printed TFT (L = 5 μm). Adopted from Ref. [28].

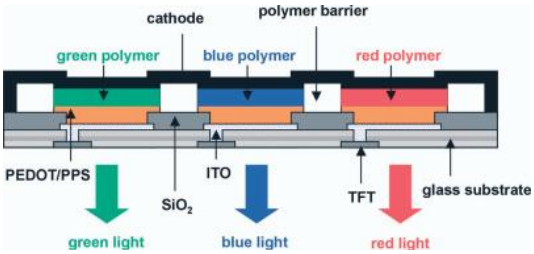


Figure 3.13 Schematic picture of a RGB multicolour PLED display. Adopted from Ref. [35].

Although ink-jet printing can pattern high resolution features, it has a couple of drawbacks that need to be improved for securing the leading position in printing

industry. Firstly, its printing speed is too slow. There are millions of pixels in a display depending on the size and ink-jet printing of all pixels using a single nozzle can take even several hours. Recently, an ink-jet head with multiple nozzles showed that its printing speed can be dramatically shortened. However, it is still too slow for fast production of optoelectronics compared to R2R type printing. A machinery innovation is required for further improvements. Secondly, it is more difficult to optimize ink formulations in ink-jet printing. Narrow nozzle size, gravitational effect while ink drops, and rheological sensitivity of ink formulations are main reasons. For example, a little variation of molecular weight may alter the filament length of the multiple droplets and no separate drops are formed.[35]

Another interesting printing technique has been recently introduced, which is called spray printing.[36-38] Low concentration polymer solutions can be ejected by inserting nitrogen gas throughout a syringe nozzle. Its overall operation scheme is described in Figure 3.14. If thermal treatment is applied onto a substrate while it is being printed, it is called spray pyrolysis printing. The term ‘pyrolysis’ corresponds to the chemical decomposition of condensed substances by heating. Ejected polymer solutions are deposited onto the substrate with patterns that are defined by a shadow mask.

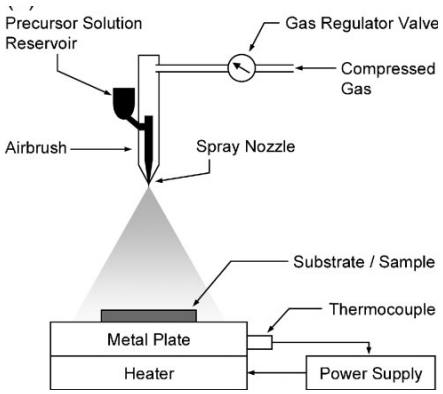


Figure 3.14 Schematic of overall operation of spray pyrolysis printing. Adopted from Ref. [37].

Spray printing provides easy and simple processing advantages but most of materials may be wasted due to spraying onto a whole area of the substrate. Also, the roughness of sprayed patterns can be non-uniform especially at the edge of patterns attributed to these areas are roughly covered by the shadow mask. As a result, undesirable areas can

be printed even though it is covered by the shadow mask. Tedde *et al*. demonstrated organic photovoltaics (OPVs) with spray printed organic layers. The device performance is comparable to the conventionally deposited device by spin-coating.[38] Figure 3.15 shows an example demonstration of the printing technique.

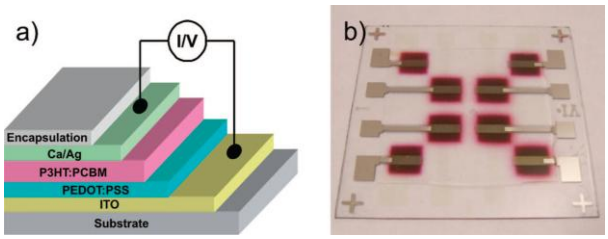


Figure 3.15 a) Layer stack of the organic photodiode. b) Images of spray coated organic photodiodes with active areas of 4 mm^2 each. Adopted from Ref. [38].

3.3 Physical Parameters in Printing

3.3.1 Surface tension

Surface tension describes a rheological property of a liquid surface. By considering the intensity of surface tension, attractive force between molecules of other solid or liquid surfaces can be estimated. Since the molecules on the surface interact with air (gas phase) unlike molecules in the bulk state which are surrounded by molecules at all sides, the intermolecular force between molecules in the surface is stronger than one in the bulk. Surface tension behaviour of a Newtonian fluid can be predicted. At the interface between two fluids, interfacial tension is created. The two fluids are attracted by intermolecular forces (van der Waals) at the interface. The attractive force between the two liquid phases creates an interfacial energy per area which acts to resist the formation of a new interface. Hence, the two liquids can exist without forming an interface if the two fluids are miscible, however if they are immiscible an interface is formed.

Another good example of surface tension related phenomenon is the pond-skater floating on a surface of pond. The pond-skater floats on the water due to its legs are

covered by hair rendering them hydrophobic. In addition, it is necessary to consider both curvature and buoyancy forces of floating objects. Figure 3.16 describes engaged forces on a floating object. Buoyancy and curvature forces are proportional to r and L_c. It is not obligatory to consider buoyancy forces in the case of the insect's legs as the floating objects are too small so that curvature forces are dominant.

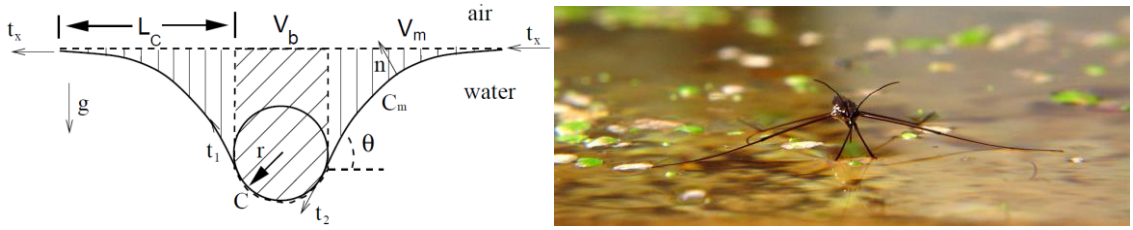


Figure 3.16 A non-wetting two-dimensional body of radius r and mass M floats on a free surface.

Hence, it can be said that curvature forces should be greater than the weight of the floating body. The following equation expresses a floating condition for small objects:

$$\frac{Mg}{2\sigma L_c \sin\theta} < 1 \qquad (3.2)$$

where g is the gravitational acceleration and σ is the surface tension of the liquid.

3.3.2 Shear force, Viscosity – Newtonian fluid

All fluids moving along a solid boundary are stressed by a shear force on that boundary. Under the no-slip condition, the speed of the fluid at the boundary becomes zero, but the flow speed increases and the speed becomes equal to the fluid speed as it is located at some distances from the boundary. The two-dimensional region along the points with identical speed is called boundary layer. The shear stress is proportional to the strain rate in the fluid where the viscosity is the constant value of proportionality for cases of Newtonian fluids. In non-Newtonian fluids, however, viscosity is dependent on the shear stress. The shear stress for a Newtonian fluid at a distance y from the boundary is given by:

$$\tau(y) = \mu \frac{\partial u}{\partial y} \qquad (3.3)$$

where μ is the dynamic viscosity of the fluid, u is the velocity of the fluid along the boundary, and y is the distance from the boundary. Liquids with low molecular weight such as water and alcohols are representative Newtonian fluid whereas liquids with high molecular weight such as molten polymers and colloids are non-Newtonian fluid.

3.3.3 Capillary force

The surface tension of water corresponds to tension inside water droplet which is equal to the intermolecular forces between water molecules. If some water is confined in a glass vial, water molecules will be attracted by an adhesion force from hydrogen bonds to the glass surface. Therefore, water adjacent to the vial surface can flow uphill along the glass surface. If the size of the vial is narrow, the adhesion force becomes relatively large compared to the intermolecular forces between water molecules. On the other hand, dispersive fluids such as alcohols experience the opposite case. A repellent force between the polar glass surface and the dispersive fluids can occur so that the height of dispersive fluids becomes lowered at the contact surface between the glass and the dispersive fluids.

3.3.4 Solubility

Solubility is particularly important in printing of organic semiconducting inks. Printing of a polymer dissolved in an organic solvent often induces swelling of an underlying polymer layer if the two materials have similar solubility. Using an orthogonal solvent for upper layer is a useful way to prevent this. However, most polymers have a similar solubility so that it is quite difficult to choose appropriate solvents for printing a multiple layer structure sequentially.

In organic compounds, molecules can have separated electric charge attributed to having an electric dipole. The molecules with dipoles are called polar molecules. Molecules with atoms such as fluorine, oxygen, and nitrogen tend to be polar due to its

high electronegativities, which exert a great pull on electrons and become negative ions. However, symmetrical arrangement of polar bonds such as the boron trifluoride (BF_3) refers to non-polar molecules as an exception. The non-polar molecules, on the other hand, share an equal amount of electrons between two different atoms.

The polarity of an organic molecule determines its solubility. The rule of thumb is that organic compounds have the best solubility between molecules with similar molecular structures. For example, molecules with hydrocarbon are highly soluble in solvent assisting of hydrocarbon molecules. In other words, polar solvent dissolves polar solutes and vice versa.

There are a few models have been suggested for describing solubility of organic compounds. Hildebrand solubility parameters, proposed by Joel H. Hildebrand in 1936[39], list its solubility parameters of various materials denoted by δ $(cal/cm^3)^{1/2}$, which corresponds to the square root of the cohesive energy density as follows:

$$\delta = \sqrt{((\Delta H_v - RT)/V_m)} \qquad (3.4)$$

where ΔH_v is the change in enthalpy for one mole of chemical substance on going from the liquid to the gaseous state and V_m is the volume of molecules. RT corresponds to the ideal gas term. It describes the amount of energy required to completely transit a unit volume of molecules from their adjacent molecules into a gaseous phase. A similar approach can be applied for describing dissolution of a material. When solid molecules are dissolved in a solvent, molecules need energy to separate the same interactions as cohesive energy with neighbouring molecules. According to the model, materials have the highest solubility into a solvent with the same solubility parameters. For example, PMMA ($\delta = 9.3$) is well dissolved well in chloroform ($\delta = 9.21$). However, the model is valid only for non-polar materials and slightly polar (less than 2 debyes) that do not undergo hydrogen bonding. It gives a useful prediction for cases in polymer/solvent interactions, especially in solubility and swelling of polymers by solvents. Solubility of polar molecules can instead be explained by Hansen solubility parameters.

The Hansen solubility parameter[40] is an extended version of Hildebrand's model and it estimates solubility which is split into three components as polar (δ_p), non-polar (δ_d), and hydrogen bonding (δ_h). This is why the model is called 3D solubility parameters. The three parameters can be regarded as coordinates for a point in three dimensions space which is known as Hansen space. In the space, solubility of materials are located and if two points of a solute and a solution are positioned close to each other, it is then regarded as they dissolve into each other. On the contrary, if the two points are separated by a long distance in the space, they are not likely to be dissolved into each other. To determine the distance between Hansen parameters in Hansen space, the following formula can be used:

$$(R_a)^2 = 4(\delta_{d2} - \delta_{d1})^2 + (\delta_{p2} - \delta_{p1})^2 + (\delta_{h2} - \delta_{h1})^2 \qquad (3.5)$$

Combining the distance with the interaction radius (R_0), which refers to the range within one substance being dissolved, the relative energy difference (RED) can be written as:

$$RED = R_a / R_0 \qquad (3.6)$$

If the RED is less than unity (<1) the molecules are alike and will dissolve and vice versa. The factor of 4 in front of dispersive (non-polar) component in Equation 3.5 is a correction factor to make ellipsoidal plots look spherical.

3.4 Fluidic Movements inside Ink Formulation

3.4.1 Coffee stain effect

A droplet of coffee liquid creates a ring-like deposition of solutes at the edge of the droplet after complete evaporation of the liquid. The phenomenon is attributed to a geometrical constraint that the free surface, constrained by a pinned contact line, squeezes the fluid outwards to compensate for evaporative losses. Deegan *et al*. first

analysed the phenomena called ‘coffee stain’ effect theoretically.[41] Microscopic image of a coffee stain ring is depicted in Figure 3.17.

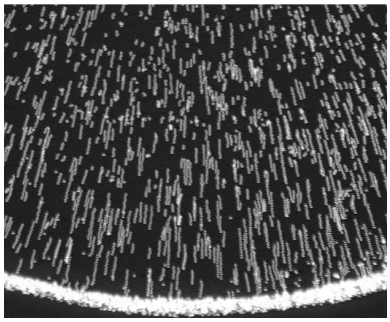


Figure 3.17 A 2-cm-diameter drop of coffee containing 1 wt% solids has dried to form a perimeter ring. Adopted from Ref. [41].

Kajiya *et al*. developed Deegan’s idea that the evaporation process of polymer solution consists of three stages.[42] Firstly, the droplet radius remains constant and the droplet edge is pinned. Secondly, the edge of the droplet recedes with constant velocity with its contact angle constant. Thirdly, the contact line becomes pinned again. The second pinning is thought to be due to deposited polymer concentration, hence it is self pinned. He also suggested that surface morphology of a droplet can be considerably influenced by the concentration of the solution and evaporation speed.

Deegan *et al*. was concerned about evaporation flux distribution with varied time but not with contact angle[43], and he suggested the evaporation flux on the droplet surface as:

$$(\vec{J}\cdot\vec{n}) = J_0\left(1-\frac{r^2}{R}\right)^{-\lambda} \qquad (3.7)$$

where J is the evaporation rate, R is the contact-line radius, r is local position on the droplet surface, and λ is a fitting parameter representing the nonuniformity of the evaporation flux on the droplet surface. Hu *et al*. reported that contact angle changes while a droplet evaporates.[44,45] Figure 3.18 depicts a definition of contact angle which is an angle between solid/ liquid interface. Contact angle from Young’s equation can be defined as:

$$\cos\theta = \frac{\sigma_s - \sigma_{sl}}{\sigma_l} \qquad (3.8)$$

where denoted as s (solid), l (liquid) and s/l is the interface between solid and liquid.

At the first phase, a droplet is pinned at the contact line and the contact angle decreases. In the second phase, the droplet starts to recede from the pinned line while the contact angle remains low. Figure 3.19 describes the two phase processes of solvent evaporation. The critical contact angle for droplet to recede is experimentally observed as around 2~4°.[44] Evaporation flux is much faster at the edge of a droplet than the centre. To compensate the solvent loss, a flow from the centre of droplet should exist. The flow carrying solutes depend on the rate of evaporation and the evaporation-flux distribution over the droplet surface. They fitted contact angle parameter (θ) into the previous Deegan model as Equation 3.9 and it is well approximated.

$$J(r,t) = J_0(\theta)\left(1 - \frac{r}{R}^2\right)^{-\lambda(\theta)} \qquad (3.9)$$

where J(r,t) is the evaporation flux at the surface and $\lambda(\theta) = 1/2-\theta/\pi$. Simulation of fluidic movements in different contact angles of a droplet is described in Figure 3.20.

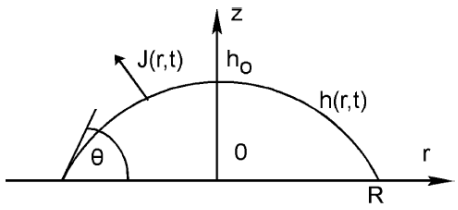


Figure 3.18 A sessile spherical-cap droplet on the substrate in a cylindrical coordinate system. Adopted from Ref. [44].

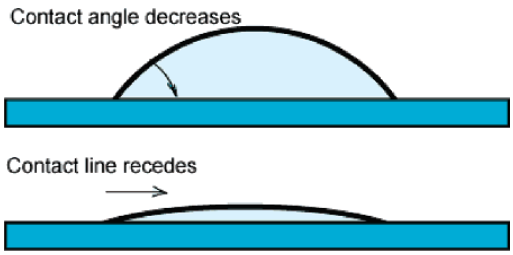


Figure 3.19 A schematic of the droplet-evaporation process. Adopted from Ref. [45].

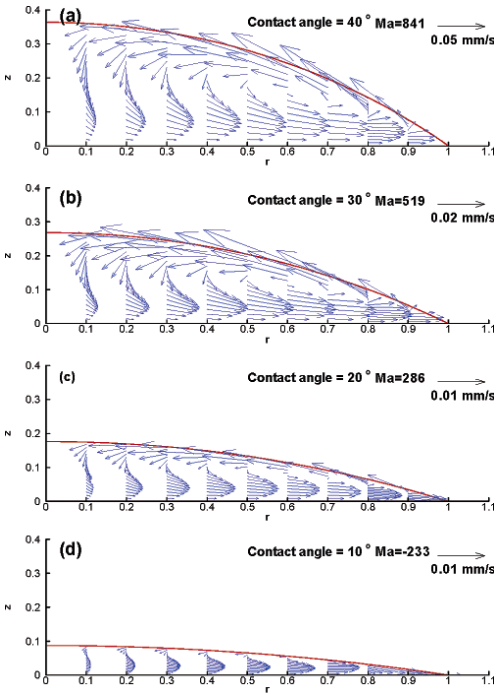


Figure 3.20 The time-dependent velocity fields calculated by the finite element method at different contact angles of 40°, 30°, 20° and 10°. Adopted from Ref. [45].

It is useful to implement the 'coffee stain' phenomena with some interesting applications. DNA mapping method is one of examples using the phenomena, droplet drying is an important for the creation of arrays of DNA spots for gene expression analysis.[46,47] Evaporation induces a microscopic flow which stretches DNA molecules and deposits those molecules onto a substrate where they can be subjected to a restriction digest.

However, many applications related to printing optoelectronics using polymer inks have a serious problem with morphology of thin layer after it is dried. A rough surface can degrade the device operation which consists of stacks of sub-microscale layers. In general, a rough surface generated at the edge of the droplet is formed with a height significantly thicker than the inner area. In order to overcome this unevenness surface profile of the dried film, the evaporation speed can be altered. Deegan *et al*. reported that the morphology of a droplet was improved in a case when the droplet evaporates at slow speed.[43] To control the speed, a droplet was covered by a box with a small hole

located at the centre of the box. The reason for the small hole at the centre of the box is to encourage evaporation occur more at the centre, even though the total evaporation flux is reduced.

Additionally, a droplet, which was placed on a pedestal and surrounded by a bath of water, showed that the level of the bath coincided with the base of the drop. In this case, the evaporation rate was found to be spatially uniform over the droplet surface. They suggested that the evenness of the droplet morphology is dependent with redistribution of the solute. Redistribution of the solute is occurred strongly in a case of fast evaporation rates hence formed a ring at the edge of the droplet. In addition to the slow evaporation, it is also possible to produce a uniform surface from drying droplet by inducing another fluidic movement. This redistributes the solutes uniformly over the surface and will be introduced at the next section.

3.4.2 Surface tension driven Marangoni flow

Marangoni effects, manifested as 'tears of wine', were first observed as early as 1800s by Italian physicist Marangoni. On a surface of a wine glass, the evaporation of alcohol induces surface tension gradient, which produces traction on the wine surface causing the wine to climb up the side of the glass where it forms a thin film. As the particles of wine accumulates, a bulging rim of liquid forms along the top of the film, which eventually pinches into droplets which roll under their own weight, like tears, back into the wine pool. Marangoni described the fluidic movement and suggested that the movement is induced by surface tension gradient, generated either by composition or by temperature variation along the free surface.

In an evaporating liquid, a temperature discontinuity exists at the liquid-vapour interface, and independently of the phase change direction, the temperature is always greater in the vapour. In the liquid phase just below the surface, the temperature is approximately spatially uniform within a depth which depends on the phase change process. Below the uniform temperature zone, the temperature profile in the liquid have a constant gradient, indicating the mode of energy transport, which is thermal conduction. The existence of

the uniform temperature layer and the constant temperature gradient in the subinterface region implies that surface-tension driven convection is present in the liquid near the interface. This convection will result in the circular motion of the liquid during evaporation driven by the need to form a uniform temperature layer. Such convection is called ‘Marangoni flow’.[48-50]

The interfacial vapour temperatures were measured to be greater than that inside the liquid. At the highest evaporation rate of water, the temperature in the vapor was measured and it was 7.8° C higher than that of the liquid side of the interface.[51] Interestingly, reversal formation of temperature gradient was observed from a droplet with a low contact angle (~10°).[50] In general, the high contact angle case showed that its temperature gradient was distributed by temperature which increases from the top to the bottom of the droplet, and from the centre to the edge of the droplet. However, the low contact angle droplet showed that its temperature decreases from the centre to the edge of the droplet attributed to evaporative cooling occurring at the edge of the droplet. It again supports the previous argument that evaporation process of a droplet consists of two phases; i) evaporation while contact line is pinned with contact angle reduced and ii) receding of contact line at fixed contact angle less than 10°. Evaporative cooling starts to be induced at the moment between the two phases. Figure 3.21 and Figure 3.22 describe contour plots of the temperature fields and the temperature profiles along the droplet surface.

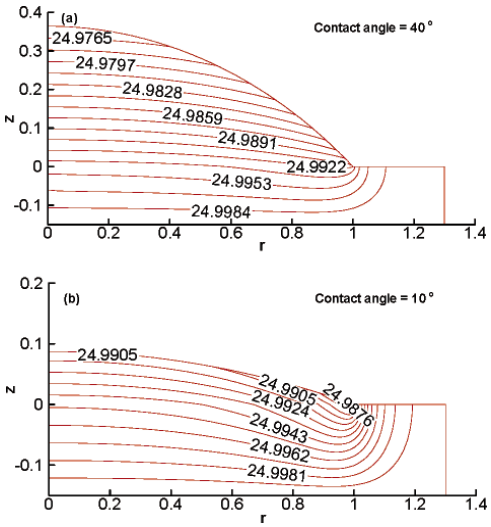


Figure 3.21 Contour plots of the temperature fields in the droplet at two contact angles. Adopted from Ref. [50].

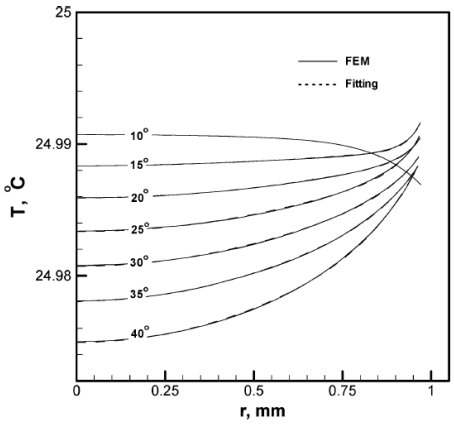


Figure 3.22 The temperature profiles along the droplet surface at various contact angles. Finite element (FEM) results and the fitting results are almost identical. Adopted from Ref. [50].

A mixture of binary solvents can control the direction of the Marangoni flow, so as to either favour or oppose the spreading of the liquid. Pesach *et al*. reported[48] that there exist two possibilities. For a case of two solvents of a and b having a vapour pressure (P_i) of $P_a < P_b$ and $\gamma_a > \gamma_b$, where γ_i corresponds to the surface tension of component i, the removal of component b due to its higher evaporation rate can induce a surface tension gradient. The Marangoni flow will therefore flow from the low evaporation region to the high evaporation region. Hence, the flow will be induced from the centre of the droplet to the edge which is same direction as the spreading of mixtures. On the other hand for a case of $P_a < P_b$ and $\gamma_a < \gamma_b$, a flow will be diffusively induced from the higher surface tension region to the low surface tension region which is a direction opposite to the spreading.

Similarly, a proportion of additive solvents can influence a direction of the Marangoni flow. Lim *et al*. suggested[52] that the Marangoni flow is induced when a solvent was mixed with a higher boiling point, lower surface tension additive solvent. If the amount of the additive solvent is minor compared to the primary solvent, the Marangoni flow with a counter direction to the evaporative convection flow was observed. Alternately, if an additive solvent with low boiling point and high surface tension solvent was mixed as a minor component, an outward spreading can be enhanced. The schematic figure

describing the hydrodynamic movement of the Marangoni flow is depicted in Figure 3.23.

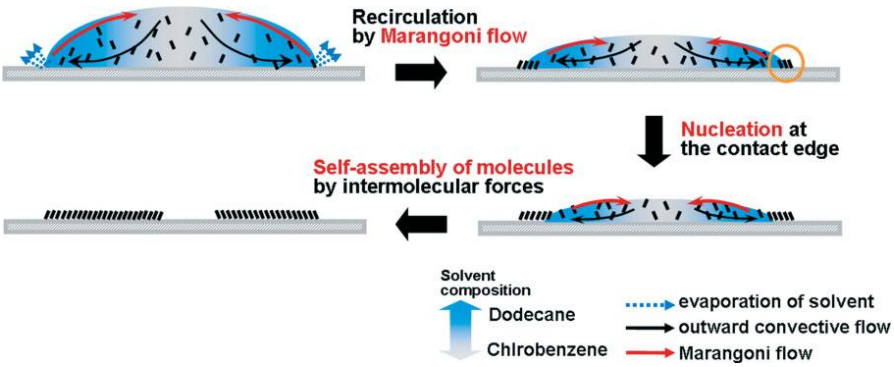


Figure 3.23 Schematic representation of the possible mechanism of the kinetically driven development with Marangoni flow. Adopted from Ref. [52].

The Marangoni flow plays an important role in coating, thin film deposition, crystal growth, and production of photonic structures. Therefore, in-depth understanding of the Marangoni flow in an evaporating droplet will be important subjects of study for both fundamental research and practical applications.

3.5 Hydrodynamics in Printing Process

3.5.1 Application in ink-jet printing

A uniform surface morphology is crucial for the functioning of optoelectronic devices as the thickness range of each layer is typically less than 100 nm, and it is an important issue in printing of optoelectronic devices for both industry and academia. Ink-jet printing, the most advanced type of printing, has been considered to see if it can control fluidic movement of pico-liter droplets while it dries. Typically, the ‘coffee stain effect’ is one of hurdles for the feasibility of the technique, as non-uniformity of the printed surface often results in spatially varied charge injection and high leakage current in the devices.

There have been a number of approaches suggested to remove the coffee stain effect including using a high boiling point solvent as a dissolving solvent and spraying the same solvent used onto the deposited layer to smoothen the surface. The former produces slightly rough surface profile in average owing to the high boiling point solvent evaporates at random speeds at various positions of the surface and the latter requires additional processing step for spraying even though it slightly improves the overall surface roughness. Mixing of high and low boiling point solvents helped with controlling fluidic movements inside printed droplets via inducing the Marangoni flow and resulted in a uniformly deposited thin film.[48, 53-55] Park *et al*. reported that concentration of solutes as well as chemical properties of solvent can influence the surface-tension driven fluidic movement.[56] Marangoni number, denoted as $B = \left[-\frac{\partial \gamma}{\partial T} \cdot \frac{\beta d^2}{\kappa \eta} \right]$, where $\frac{\partial \gamma}{\partial T}$ is the derivative of the surface tension γ with respect to temperature T. β is the base state temperature gradient established by the evaporative flux, η is the viscosity, d is the depth of the fluid, and κ is the thermal diffusivity. The Marangoni number is therefore proportional to the square of the thickness of droplet and the surface tension difference of two solvents, while it is inversely proportional to the viscosity of the liquid and its thermal diffusivity. Figure 3.24 described arrangement of 50 μm size silica particles dispersed in different ink formulations.

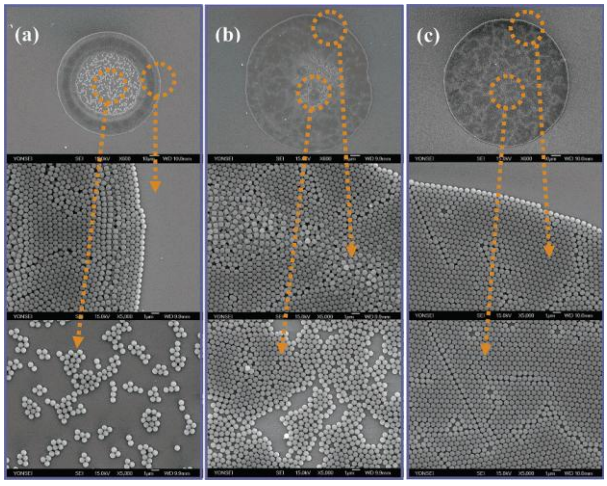


Figure 3.24 SEM images of deposit patterns of silica microspheres with varying of ink compositions: (a) water-based ink, (b) water/diethylene glycol (DEG) – based ink and (c) water/ formamide (FA)-based ink. Adopted from Ref. [56].

Assembly of silica particles is shown in printed droplets of (b) and (c) compared to a water only case (a). The best result was observed from the case of mixing water with formamide (c). The boiling point of diethylene glycol and formamide are 245° C and 210° C respectively. In addition, a large divergence between their viscosity, which is 3.5 mPa.s for formamide and 38.5 mPa.s for diethylene glycol, may be a stronger factor on the effectiveness of the Marangoni flow. The resulting Marangoni number of the mixture of the two formulations with water is 34,725 (water/ diethylene glycol) and 118,094 (water/ formamide).

The concentration of ink formulations affects the viscosity of droplet in non-Newtonian fluid, hence it is also an important parameter for droplet formation.[56] Figure 3.25 describes microscopic images of the dried droplets with variation of its concentration of silica particles. As expected, surface profiles as well as assemble of solute particles are varied even at a small change of its concentration.

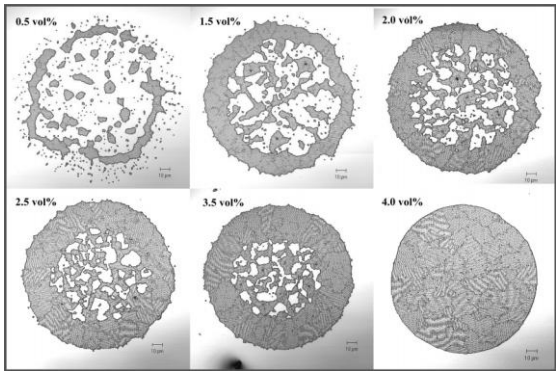


Figure 3.25 Confocal microscope images of deposit patterns composed of the silica microspheres with different concentrations. Adopted from Ref. [56].

Charge carrier transport in an OFET is strongly related to regioregularity of packed chains and crystalline structures of deposited organic semiconducting films. Charge carrier transport in OFETs occurs mainly by hopping process between localized states of the molecules in the disordered structure, and molecular ordering can help to provide a sufficient overlap of the π-π orbitals of conjugated molecules, which enables efficient charge transport between the localized molecular states.[4,57,58] Previous studies already examined the feasibility of the Marangoni flow to create homogeneous thin

films however only few reports have demonstrated functional devices. Lim *et al*. reported that device performance of OFETs based on Tips-pentacene has been improved via inducing the Marangoni flow.[52] Figure 3.26 describes droplet surface profiles after full evaporation of solvents. Compared to pure chlorobenzene (a), the surface characteristics of ink-jet printed chlorobenzene based formulations mixed with hexane (b), *o*-dichlorobenzene (c), and dodacane (d) show that its morphology is again influenced by chemical properties of ink formulations. For example, dodecane with the highest boiling point (216° C) contributed to a large Marangoni number. Interestingly, the formulation mixed with *o*-dichlorobenzene (180° C) results in completely different surface profile to the case of the dodecane mixed formulation in terms of spreading of droplet and pinning of the contact line. They suggested that an inward direction Marangoni flow should be generated to recirculate the outward evaporative convection flow. The Marangoni flow toward the centre of the droplet can only occur if the minority solvent has a higher boiling point, lower surface tension while a higher boiling point, higher surface tension solvent leads the Marangoni flow to flow toward the pinning line which enhances the convection flow even more. A lower boiling point solvent starts to evaporate at the edge of the droplet, which induces a surface tension gradient inside the droplet. Then, the Marangoni flow starts to flow from the higher surface tension region to the lower surface tension region. The direction of the flow can be either inward or outward depending on the surface tension of the additive solvent. Device performance of the OFETs from the different solvent mixtures showed that the formulation mixed with dodecane achieved the highest field-effect mobility of 0.018 cm^2/Vs and an on/off current ratio of 10^6 whereas a slightly poorer performance (field effect mobility - 0.01 cm^2/Vs and on/off current ratio - 10^6) was observed in the case of the formulation mixed with *o*-dichlorobenzene. The authors suggested that it is because higher surface tension of *o*-dichlorobenzene (36.6 dyn/cm) than chlorobenzene (33.6 dyn/cm) while surface tension of dodecane (25.3 dyn/cm) is lower than chlorobenzene. For the case of mixing with hexane, an outward Marangoni flow was induced which reinforced the evaporative convection flow.

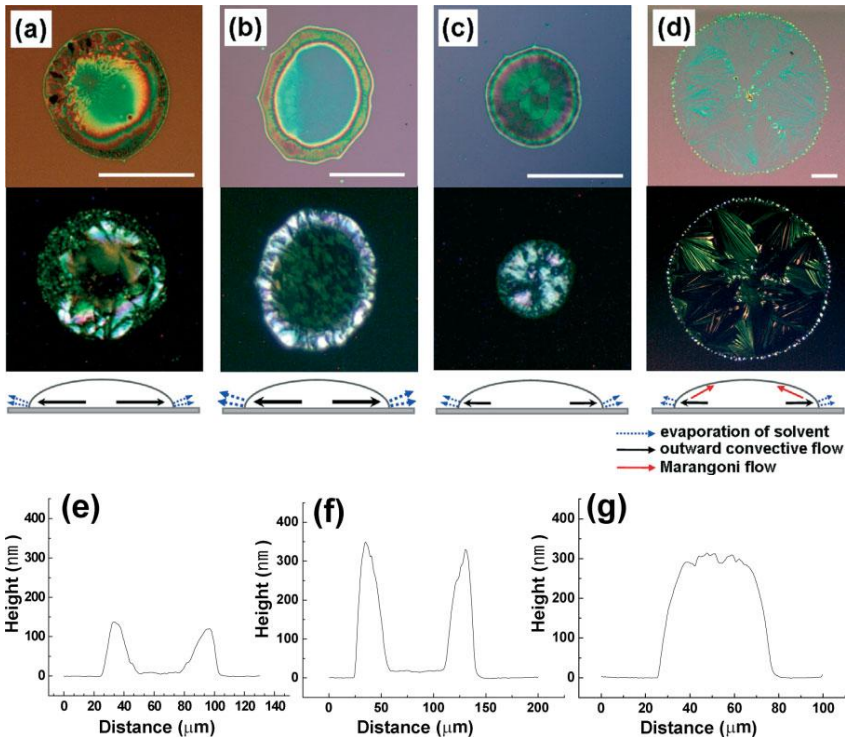


Figure 3.26 Optical microscopic images of ink-jet printed TIPS-Pentacene droplets with various solvent compositions: a) pure chlorobenzene, chlorobenzene is mixed with 25 vol % of b) hexane, c) *o*-dichlorobenzene, and d) dodecane. The height of droplets from e) chlorobenzene and the solvent mixtures with f) hexane, and g) *o*-dichlorobenzene (scale bar = 50 μm). Adopted from Ref. [52].

3.5.2 Application in other printing

Optimizing the orientation of molecular chains is of great interest in the fields of organic optoelectronic devices, especially OFETs, for its potential in significantly enhanced charge carrier transport.[4,57] The improvement in charge carrier transport has been reported from rubbing technique[59,60], mechanical stretching, Langmuir-Blodgett (LB) deposition[61,62], and liquid-crystalline self-organization[63]. Figure 3.27 shows the oriented molecules and crystals parallel to the rubbing direction after rubbing a polyimide dielectric surface and sequentially deposit a thin layer of small molecule semiconducting material. This anisotropic characteristic of the aligned molecules and chains of semiconducting materials enhance charge carrier transport between the molecules. Also, they are particularly useful for polarized light emission in light-emitting diodes and anisotropic charge transport in thin film transistors. These preferential characteristics can be detected via absorption and photoluminescence (PL)

measurements with a comparison of two polarized directions either parallel or perpendicular to the direction of the molecular orientation.

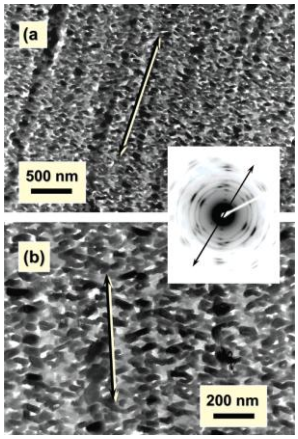


Figure 3.27 Transmission electron micrographs of rubbed α-sexithiophene (6T) films following subsequent sublimation of 50-nm α-6T. Adopted from Ref. [59].

Various deposition methods have also been analysed to observe alignments in molecular and crystal structures. Figure 3.28 describes microscopic images of Tips-pentacene deposited via various methods. It suggests that it is also possible to induce an orientation of molecules by generating hydrodynamic flows during solvent drying as well as by inputting mechanical forces along a preferred direction.

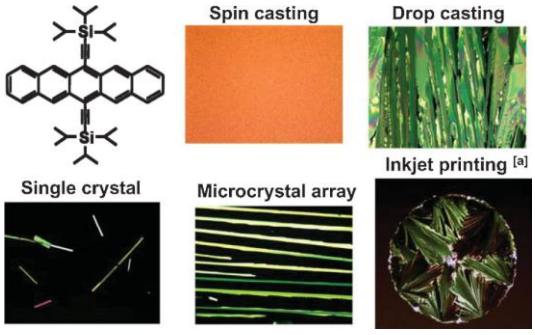


Figure 3.28 Optical microscopic images of Tips-Pentacene thin films with various morphologies and structural developments. Adopted from Ref. [64].

3.5.3 Research work in this Thesis

Gravure contact printing is a preferentially oriented process along the driving direction and may result in oriented conformation of polymer chains in printed thin films. As previously described, preferentially oriented patterns in printed thin films are closely related to fluidic movements inside drying formulations. Controlling such movements together with the single direction driving force in gravure printing has a great potential in aligning chains of polymer molecules parallel to the printing direction. One piece of evidence in the molecular alignment has been observed that polymer solutes were heavily deposited at the edge of the printed pattern attributed to the coffee stain effect when using a low boiling point solvent based formulation. Also, the deposited solutes were aligned parallel to the printing direction. Figure 3.29 depicts gravure printed PEDOT:PSS AI4083 thin film using the formulation mixed with IPA with low boiling point. Contact pinning lines due to the coffee stain effect were found only at the edges of the printed pattern parallel to the printing direction.

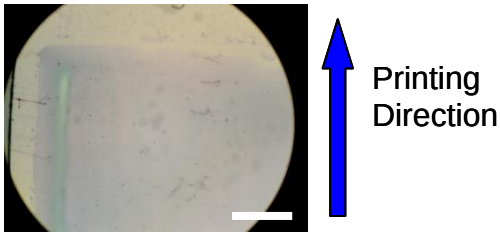


Figure 3.29 Preferentially oriented coffee stain pinning line on gravure printed PEDOT:PSS AI4083 (Scale bar = 1 mm).

The morphology of a thin film surface is also an important parameter for functional devices. Aligned backbone of polymer chains significantly improve the device performance via efficient hopping process, however, non-uniformity of the surface may result in poor operation or device failure. In other words, surface morphology of printed thin film should be controlled prior to enhancement of charge carrier transport throughout aligned π-π stacking chains. Sufficient hydrodynamic movements inside drying ink formulations are mandatory for uniformly distributed thin film surface. It is important to consider both evaporative convection flow and the Marangoni flow in case

of gravure printed ink formulation. A schematic presentation of the hydrodynamic flows in gravure printing is suggested in Figure 3.30. Two cases of ink formulations of *p*-xylene (Bp – 138.3 °C) either mixed with 20% in volume of cyclohexane (B_p – 80.7 °C) or indan (B_p – 177 °C) when printing LG1300 onto PEDOT:PSS surface having a surface energy of 58.21 mN/m (σ_p - 33.52, σ_d - 24.69) showed completely different printing morphology. A detailed experimental procedure is explained in Section 5.4. As previously discussed, the chemical properties of organic solvents such as boiling point, surface tension, and viscosity strongly influence the hydrodynamics of the printed ink formulations. The printing behaviour is also dependent on the surface characteristics of the bottom layer and environmental conditions. In other words, the surface energy and polarity of the substrate as well as humidity and temperature at the moment of printing are important parameters.

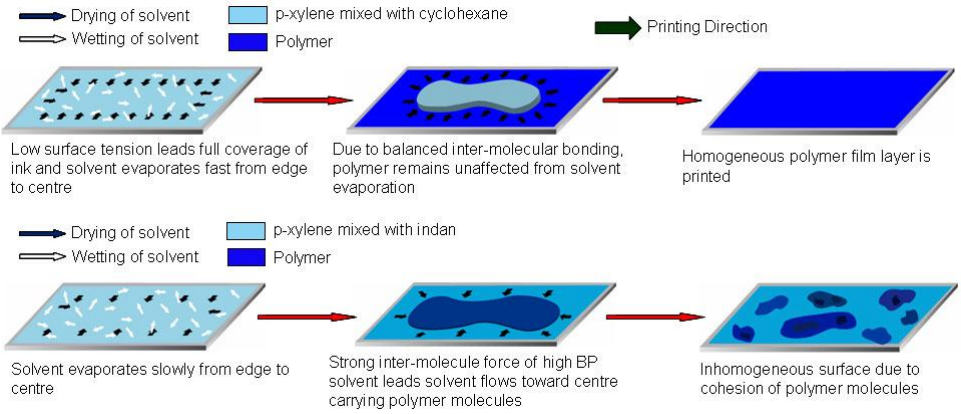


Figure 3.30 Fluidic movements during thin film formation in gravure printing process when printing LG1300 onto PEDOT:PSS surface.

We suggest that thin film formation in gravure printed ink formulations consist of two main hydrodynamic processes, which refer to wetting and drying of ink formulations. A sufficiently low surface tension of ink formulation is a prerequisite for complete wetting of the formulation onto a substrate. The surface tension of the formulation should be smaller than the surface energy of the substrate for good wetting. Plotting a wetting envelope, which graphically indicates a region where specific ink formulations wet onto a substrate, is a useful method to simulate the wetting behaviour of the ink formulation. Also, the drying process is important. If an ink formulation is made of low boiling point

solvent, it is likely to form a non-uniform edge in printed patterns due to the coffee stain effect. On the other hand, if an ink formulation is made of high boiling point solvent, it will remain non-uniform polymer stacks after evaporation is completed. For example, when LG1300 formulation in *p*-xylene was mixed with cyclohexane, a lower boiling point solvent (cyclohexane) starts to flow toward the edge of the droplet due to evaporative convection flow. Cyclohexane has a lower surface tension than *p*-xylene so that the Marangoni flow was induced flowing from the centre of the droplet with a higher surface tension region to the edge with a lower surface tension region. The outward Marangoni flow, hence, planarize the surface of the printed LG1300 (Figure 3.31ii). On the other hand, when the LG1300 formulation in *p*-xylene was mixed with indan having a higher boiling point and lower surface tension, the surface of the printed LG1300 still had stacks of polymer and its surface roughness became worse (Figure 3.31i). We believe that the small deviation in both surface tension and boiling point between *p*-xylene and indan (25.2 mN/m) contributed to the results.

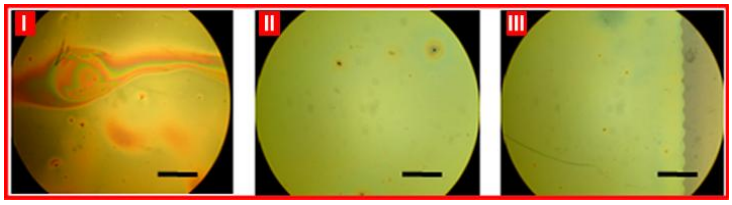


Figure 3.31 Optical microscopic images of printed LG1300 formulations: i, mixed with indan; ii, mixed with cyclohexane; iii, edge of ii; (scale bar indicates 1 mm).

3.6 Conclusion

There have been a lot of effort made to print optoelectronic devices via various techniques. Some of techniques have revealed its potential as a next generation production technique although most of them still showed their performance inferior to the device fabricated by the conventional spin-coating method. Printing of optoelectronic devices using organic semiconducting inks is a complicated process which is completely different from the traditional printing for graphic arts such as newspapers and posters. Printing homogeneous thin films, made of a stack of layers with thickness less than 100 nm, is crucial for the functional devices. Understanding of

hydrodynamic movements inside printed formulations during drying process will lead to realization of mass production of the functional optoelectronic devices using via the printing technology. Experimental Chapters 5-8 will describe in detail about the topics related to gravure printing process for printed thin films in applications of both polymer field-effect transistors (PFETs) and polymer light-emitting diodes (PLEDs).

3.7 Reference

[1] W. C. Wilson, T. Boland, *Anatomical Record Part A-Discoveries in Molecular Cellular and Evolutionary Biology* **2003**, *272A*, 491.

[2] T. Boland, V. Mironov, A. Gutowska, E. A. Roth, R. R. Markwald, *Anatomical Record Part A-Discoveries in Molecular Cellular and Evolutionary Biology* **2003**, *272A*, 497.

[3] V. Mironov, T. Boland, T. Trusk, G. Forgacs, R. R. Markwald, *Trends in Biotechnology* **2003**, *21*, 157.

[4] M. M. Ling, Z. N. Bao, *Chemistry of Materials* **2004**, *16*, 4824.

[5] H. Sirringhaus, N. Tessler, R. H. Friend, *Science* **1998**, *280*, 1741.

[6] Georges Hadziioannou, George G. Malliaras (Eds.), Semiconducting Polymers: Chemistry, Physics and Engineering, Wiley-VCH, **2007**.

[7] D. A. Pardo, G. E. Jabbour, N. Peyghambarian, *Advanced Materials* **2000**, *12*, 1249.

[8] Helmut Kipphan (Eds.), Handbook of Print Media: Technologies and Production Methods, Springer-Verlag, Germany, **2001**.

[9] K. Meerholz, *Nature* **2005**, *437*, 327.

[10] L. Kim, P. O. Anikeeva, S. A. Coe-Sullivan, J. S. Steckel, M. G. Bawendi, V. Bulovic, *Nano Letters* **2008**, *8*, 4513.

[11] H. H. Lee, J. J. Brondjik, N. G. Tassi, S. Mohapatra, M. Grigas, P. Jenkins, K. J. Dimmler, G. B. Blanchet, *Applied Physics Letters* **2007**, *90*.

[12] L. C. Chen, P. Degenaar, D. D. C. Bradley, *Advanced Materials* **2008**, *20*, 1679.

[13] A. Guite, *Transfer Report*, Imperial College London, **2007**.

[14] M. Tuomikoski, R. Suhonen, M. Valimakia, T. Maaninen, A. Maaninen, M. Sauer, P. Rogin, M. Mennig, S. Heusing, J. Puetz, M. A. Aegerter, *Manufacturing of polymer light-emitting device structures - art. no. 619204*, SPIE-INT SOC OPTICAL ENGINEERING, BELLINGHAM **2006**.

[15] P. Kopola, M. Tuomikoski, R. Suhonen, A. Maaninen, *Thin Solid Films* **2009**, *517*, 5757.

[16] A. C. Huebler, F. Doetz, H. Kempa, H. E. Katz, M. Bartzsch, N. Brandt, I. Hennig, U. Fuegmann, S. Vaidyanathan, J. Granstrom, S. Liu, A. Sydorenko, T. Zillger, G. Schmidt, K. Preissler, E. Reichmanis, P. Eckerle, F. Richter, T. Fischer, U. Hahn, *Organic Electronics* **2007**, *8*, 480.

[17] H. Yan, Z. H. Chen, Y. Zheng, C. Newman, J. R. Quinn, F. Dotz, M. Kastler, A. Facchetti, *Nature* **2009**, *457*, 679.

[18] M. M. Voigt, A. Guite, D. Y. Chung, R. U. A. Khan, A. J. Campbell, D. D. C. Bradley, F. S. Meng, J. H. G. Steinke, S. Tierney, I. McCulloch, H. Penxten, L. Lutsen, O. Douheret, J. Manca, U. Brokmann, K. Sonnichsen, D. Hulsenberg, W. Bock, C. Barron, N. Blanckaert, S. Springer, J. Grupp, A. Mosley, *Advanced Functional Materials* **2010**, *20*, 239.

[19] F. C. Krebs, S. A. Gevorgyan, J. Alstrup, *Journal of Materials Chemistry* **2009**, *19*, 5442.

[20] N. J. Kaihovirta, D. Tobjork, T. Makela, R. Osterbacka, *Advanced Engineering Materials* **2008**, *10*, 640.

[21] Z. Y. Fan, J. C. Ho, Z. A. Jacobson, R. Yerushalmi, R. L. Alley, H. Razavi, A. Javey, *Nano Letters* **2008**, *8*, 20.

[22] R. Yerushalmi, Z. A. Jacobson, J. C. Ho, Z. Fan, A. Javey, *Applied Physics Letters* **2007**, *91*.

[23] Z. Y. Fan, J. C. Ho, T. Takahashi, R. Yerushalmi, K. Takei, A. C. Ford, Y. L. Chueh, A. Javey, *Advanced Materials* **2009**, *21*, 3730.

[24] M. Lahti, S. Leppavuori, V. Lantto, *Applied Surface Science* **1999**, *142*, 367.

[25] D. Zielke, A. C. Hubler, U. Hahn, N. Brandt, M. Bartzsch, U. Fugmann, T. Fischer, J. Veres, S. Ogier, *Applied Physics Letters* **2005**, *87*.

[26] H. Sirringhaus, T. Kawase, R. H. Friend, T. Shimoda, M. Inbasekaran, W. Wu, E. P. Woo, *Science* **2000**, *290*, 2123.

[27] J. Bharathan, Y. Yang, *Applied Physics Letters* **1998**, *72*, 2660.

[28] T. R. Hebner, C. C. Wu, D. Marcy, M. H. Lu, J. C. Sturm, *Applied Physics Letters* **1998**, *72*, 519.

[29] H. Sirringhaus, T. Shimoda, *Mrs Bulletin* **2003**, *28*, 802.

[30] T. Kawase, H. Sirringhaus, R. H. Friend, T. Shimoda, *Advanced Materials* **2001**, *13*, 1601.

[31] H. S. Koo, M. Chen, P. C. Pan, L. T. Chou, F. M. Wu, S. J. Chan, T. Kawai, *Displays* **2006**, *27*, 124.

[32] H. S. Koo, M. Chen, P. C. Pan, *Thin Solid Films* **2006**, *515*, 896.

[33] B. J. de Gans, P. C. Duineveld, U. S. Schubert, *Advanced Materials* **2004**, *16*, 203.

[34] S. F. Tedde, J. Kern, T. Sterzl, J. Furst, P. Lugli, O. Hayden, *Nano Letters* **2009**, *9*, 980.

[35] T. Ishikawa, M. Nakamura, K. Fujita, T. Tsutsui, *Applied Physics Letters* **2004**, *84*, 2424.

[36] C. N. Hoth, R. Steim, P. Schilinsky, S. A. Choulis, S. F. Tedde, O. Hayden, C. J. Brabec, *Organic Electronics* **2009**, *10*, 587.

[37] A. Bashir, P. H. Wobkenberg, J. Smith, J. M. Ball, G. Adamopoulos, D. D. C. Bradley, T. D. Anthopoulos, *Advanced Materials* **2009**, *21*, 2226.

[38] S. F. Tedde, J. Kern, T. Sterzl, J. Furst, P. Lugli, O. Hayden, *Nano Letters* **2009**, *9*, 980.

[39] J. H. Hildebrand, The solubility of Non-Electrolytes, New York, Reinhold, **1936**.

[40] C. M. Hansen, *J. Paint Technol.* **1967**, *39*, 511

[41] R. D. Deegan, O. Bakajin, T. F. Dupont, G. Huber, S. R. Nagel, T. A. Witten, *Nature* **1997**, *389*, 827.

[42] T. Kajiya, E. Nishitani, T. Yamaue, M. Doi, *Physical Review e* **2006**, *73*.

[43] R. D. Deegan, O. Bakajin, T. F. Dupont, G. Huber, S. R. Nagel, T. A. Witten, *Physical Review e* **2000**, *62*, 756.

[44] H. Hu, R. G. Larson, *Journal of Physical Chemistry B* **2002**, *106*, 1334.

[45] H. Hu, R. G. Larson, *Langmuir* **2005**, *21*, 3963.

[46] V. Namasivayam, R. G. Larson, D. T. Burke, M. A. Burns, *Analytical Chemistry* **2002**, *74*, 3378.

[47] V. Namasivayam, R. G. Larson, D. Burke, M. A. Burns, *Abstracts of Papers of the American Chemical Society* **2002**, *223*, U632.

[48] D. Pesach, A. Marmur, *Langmuir* **1987**, *3*, 519.

[49] V. X. Nguyen, K. J. Stebe, *Physical Review Letters* **2002**, *88*.

[50] H. Hu, R. G. Larson, *Langmuir* **2005**, *21*, 3972.

[51] C. A. Ward, D. Stanga, *Physical Review e* **2001**, *6405*.

[52] J. A. Lim, W. H. Lee, H. S. Lee, J. H. Lee, Y. D. Park, K. Cho, *Advanced Functional Materials* **2008**, *18*, 229.

[53] B. J. de Gans, U. S. Schubert, *Langmuir* **2004**, *20*, 7789.

[54] E. Tekin, P. J. Smith, S. Hoeppener, A. M. J. van den Berg, A. S. Susha, A. L. Rogach, J. Feldmann, U. S. Schubert, *Advanced Functional Materials* **2007**, *17*, 23.

[55] M. Kaneda, H. Ishizuka, Y. Sakai, J. Fukai, S. Yasutake, *Aiche Journal* **2007**, *53*, 1100.

[56] J. Park, J. Moon, *Langmuir* **2006**, *22*, 3506.

[57] H. Sirringhaus, *Advanced Materials* **2005**, *17*, 2411.

[58] H. Sirringhaus, P. J. Brown, R. H. Friend, M. M. Nielsen, K. Bechgaard, B. M. W. Langeveld-Voss, A. J. H. Spiering, R. A. J. Janssen, E. W. Meijer, P. Herwig, D. M. de Leeuw, *Nature* **1999**, *401*, 685.

[59] X. L. Chen, A. J. Lovinger, Z. N. Bao, J. Sapjeta, *Chemistry of Materials* **2001**, *13*, 1341.

[60] K. S. Whitehead, M. Grell, D. D. C. Bradley, M. Jandke, P. Strohriegl, *Applied Physics Letters* **2000**, *76*, 2946.

[61] B. O. Dabbousi, C. B. Murray, M. F. Rubner, M. G. Bawendi, *Chemistry of Materials* **1994**, *6*, 216.

[62] F. Kim, S. Kwan, J. Akana, P. D. Yang, *Journal of the American Chemical Society* **2001**, *123*, 4360.

[63] L. S. Li, J. Walda, L. Manna, A. P. Alivisatos, *Nano Letters* **2002**, *2*, 557.

[64] J. A. Lim, H. S. Lee, W. H. Lee, K. Cho, *Advanced Functional Materials* **2009**, *19*, 1515.

Chapter IV

Experimental Techniques and Materials

4.1 Organic Materials used in the Thesis

4.1.1 Poly(3,4-ethylenedioxythiophene): poly(styrenesulfonate) (PEDOT: PSS)

Poly(3,4-ethylenedioxythiophene): poly(styrenesulfonate) (PEDOT:PSS) is a conducting polymer comprising of a mixture of two homopolymers. One component in this mixture is a sulfonated polystyrene, which is based on sodium polystyrene sulfonate. The component carries a negative charge. The other component poly(3,4-ethylenedioxythiophene) (PEDOT) is a p-type polythiophene based conjugated polymer. The mixture can be regarded as charged macromolecules forming a macromolecular salt. The chemical structure of PEDOT: PSS is depicted in Figure 4.1.

The material is popular as conducting and hole injecting materials in applications of OLEDs or OPVs. The conductivity of the material can be increased by adding of high boiling point solvents such as methylpyrrolidone, dimethyl sulfoxide or sorbitol with an increase of several orders of magnitude reported.[1-3] The transparency of a PEDOT: PSS thin film is more than 95% at visible wavelengths, hence high conductivity PEDOT: PSS can be used as a transparent electrode. Properties of solution

processability and transparency are particularly useful in flexible and transparent optoelectronic devices.

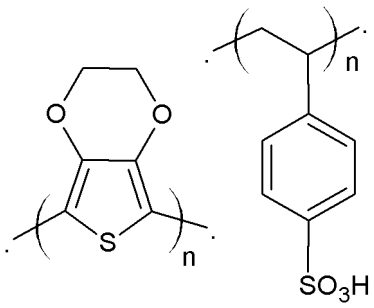


Figure 4.1 The chemical structure of PEDOT: PSS

4.1.2 Poly (9,9-dioctylfluorene-*co*-benzothiadiazole) (F8BT)

Poly (9,9-dioctylfluorene-*co*-benzothiadiazole) (F8BT) is a copolymer, which comprises of alternating benzothiadiazole and 9,9-dioctylfluorene moieties. The chemical structure of F8BT is shown in Figure 4.2. F8BT emits a green luminescence where its main peak in the photoluminescence spectra is around 540 nm. Its absorption spectrum is characterized by two peaks, with the most prominent at 455 nm and a secondary peak at 310 nm.

F8BT is an electron transporting material having its ionized potential (I_p) of 5.9 eV and a relatively high electron affinity (E_a) of 3.3 eV because of the electron-withdrawing properties of the benzothiadiazole group.[4] TOF measurements of F8BT previously showed that its electron mobility reaches around 1×10^{-3} cm^2/Vs at an electric field of 5×10^5 V/cm.[5] Similarly, its mobility measured by TFT recorded electron mobility about 5×10^{-3} cm^2/Vs.[6]

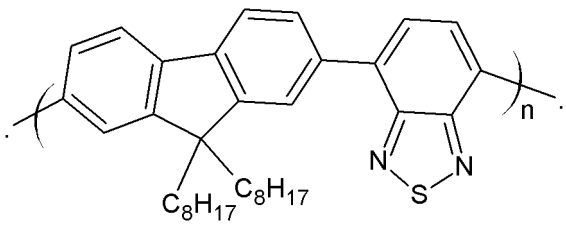


Figure 4.2 The chemical structure of F8BT

4.1.3 Poly (9,9-dioctylfluorene-*co*-N-(4-butylphenyl)-diphenylamine) (TFB)

Poly (9,9-dioctylfluorene-*co*-N-(4-butylphenyl)-diphenylamine) (TFB) is a arylamine-based copolymer. It has an I_p of 5.3 eV and electron affinity of 2.3 eV.[7] It is an efficient hole transporter having its hole mobility around 0.01 cm^2/Vs.[8] TFB can be used as an interlayer between a hole injecting material and a light-emitting polymer to reduce potential barrier for hole transporting, hence the device is required a relatively low applied bias for a certain current density level. TFB has a high solubility in organic solvents such as *p*-xylene or toluene. The high solubility of TFB compared to other polymers such as F8BT or F8T2 enabled a bilayer structure to be built by sequential solution processing where TFB layer is placed on the top of F8BT layer, and detailed procedure can be found in Chapter 6. The chemical structure of TFB is shown in Figure 4.3.

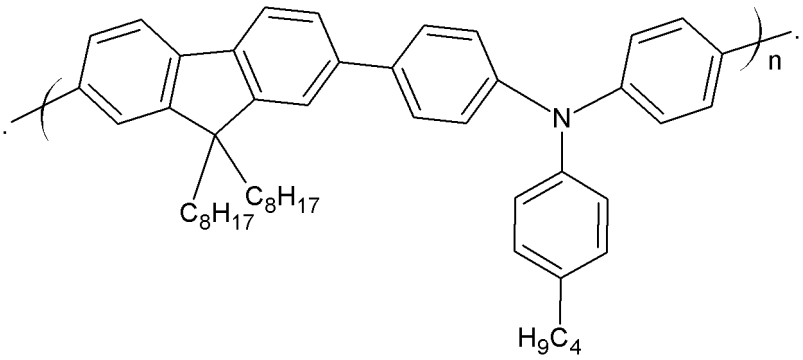


Figure 4.3 The chemical structure of TFB

4.1.4 Poly(9,9-dioctylfluorene-*co*-bithiophene) (F8T2)

Poly(9,9-dioctylfluorene-*co*-bithiophene) (F8T2) is an alternating copolymer of 9,9-dioctylfluorene and bithiophene moieties. The absorption spectrum of the material has a peak at 457 nm with a shoulder at 480 nm. It is a green emitting polymer, which has a photoluminescence with the most prominent peak at 545 nm.[9] F8T2 is less soluble than other polyfluorene derivative polymers, hence its surface profile of thin film is sometimes poor. The chemical structure of F8T2 can be found in Figure 4.4.

F8T2 has an I_p of 5.5 eV and an E_a of 3.2 eV.[10] The bi-thiophene moiety offers good hole transporting properties. The mobility measurement by FET showed that its hole mobility can be reached around 5×10^{-3} cm^2/Vs.[6] If the conformation of polymer backbone of F8T2 is aligned parallel to the direction of charge transport, the hole mobility can be further increased to 0.01-0.02 cm^2/Vs.[11] F8T2 used to be a popular hole transporting material before the advent of poly(3-hexylthiophene)-2,5-diyl (P3HT) for OPVs or OFETs. For example, F8T2 blended with C60, a fullerene with n-type transporting property, is a previous version of an active material in OPVs, and it is now replaced by P3HT:PCBM (C60) blend.

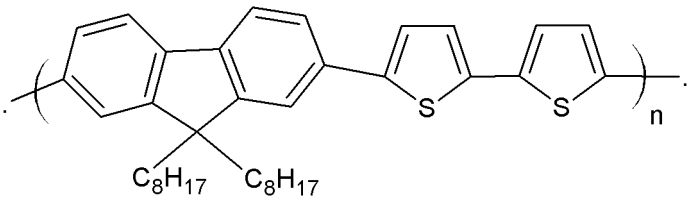


Figure 4.4 The chemical structure of F8T2

4.1.5 Lumation Green (LG)1300

Lumation Green 1300 is a copolymer having a chemical structure undisclosed yet by the manufacturer. It is known that the chemical structure comprises x% mol. of F8BT, y% mol. of a polyfluorene, and z% mol. of adjacent polyfluorene and arylamine units (x + y + z = 100%).[12] It is thought to be a copolymer with both electron (x) and hole transporting (y and z) properties and its balanced charge transporting properties can be adjusted by the proportion of each compound.

The absorption spectrum of Lumation Green 1300 has a peak at 379 nm, which corresponds to the absorption of the polyfluorene groups. It is a green emitting polymer with its main peak of photoluminescence in a broad range between 535-575 nm. Its luminescence is similar to the PL spectrum of F8BT. The function of LG1300 can be similar to a mixture of F8BT and other arylamine based materials such as TFB. In Chapter 7, PLEDs with LG1300 single layer and F8BT/TFB bilayer are compared in terms of device efficiency and luminous property.

4.1.6 Poly(3-hexylthiophene)-2,5-diyl (P3HT)

Polythiophenes are popular materials as an active OSC in OFETs and an electron donor in OPVs. Polythiophenes have been widely studied since regioregular (RR) head to tail poly(3-hexyl-thiophene) (P3HT) transistors achieved an excellent mobility as high as 0.1 cm^2/Vs.[13] It is believed that the high mobility is mainly attributed to the crystalline nature of the films. X-ray diffraction studies have confirmed that charge carrier transport mobility was improved in well ordered lamellae with co-facially stacked polymer backbones. Annealing condition, film deposition techniques of P3HT and boiling point of solvents, in which P3HT is dissolved, are main factors for aligning P3HT polymer backbones. However, a critical disadvantage of P3HT is that it is highly sensitive to ambient dopants such as oxygen and water. Therefore, it is recommended that deposition of P3HT should be fully done in a nitrogen filled glove box. The chemical structure of P3HT is shown in Figure 4.5.

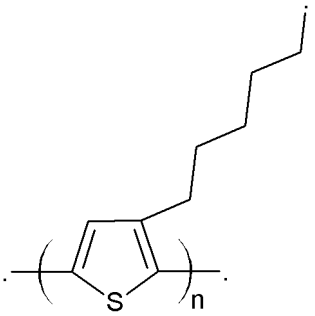


Figure 4.5 The chemical structure of P3HT

4.2 Gravure Contact Printing

Gravure printing, which is conventionally used for graphic arts and media, is one of the contact printing techniques used in roll-to-roll (R2R) type printing. Although there are a couple of drawbacks existing in this technique such as low resolution printing and material weaknesses of organic compounds compared to typical inorganic optoelectronic devices, various research groups are currently attempting to overcome these issues. The gravure printer used in this thesis work is a Labratester I manufactured

by Schlafli Maschinen. An experimental setup of the printing machine is shown in Figure 4.6. The printer is located in a fume hood as most of printing uses toxic organic solvents.

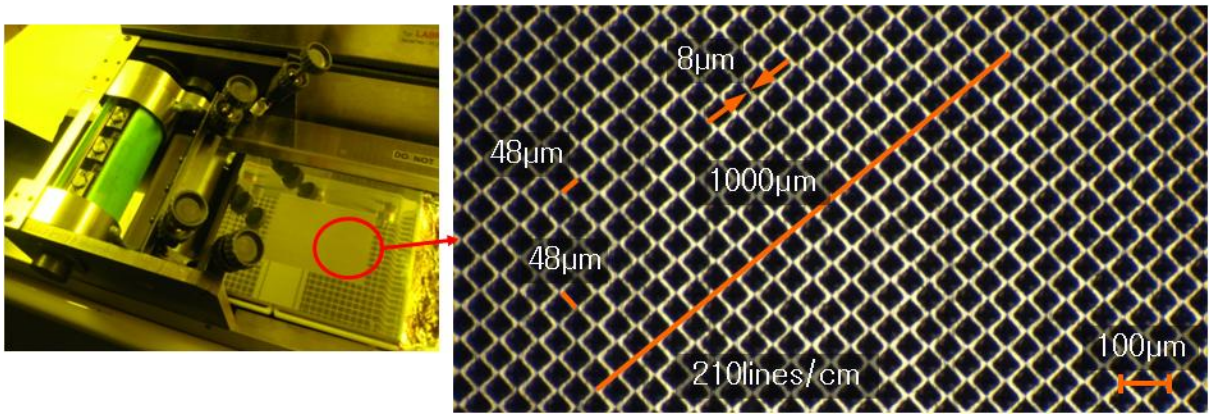


Figure 4.6 Gravure printer at Imperial College London (left) and microscopic image of cliché (210 lines/cm) (right). The microscopic image was taken by M. Voigt.

4.2.1 Printing procedure

The overall gravure printing process is illustrated in Figure 4.7. Unlike spin-coating or ink-jet printing it is a contact technique. The printer configuration used in this thesis (i) consists of a planar cliché (printing plate) and a flexible substrate attached to a freely-rotating cylindrical drum. Upon printing the cliché moves to the left and doctor blade (used to scrape ink into the cliché ink cells (ii)) and substrate drum move to the right. The tetrahedral cells (typical width 50-200 µm) on the cliché surface form the pattern to be printed. The substrate and cliché are then pressed together (iii), the lower surface energy of the substrate relative to the cliché and the shear forces pulling the ink onto the substrate. The ink droplets deposited from the cells then coalesce (iv), form a continuous layer of thickness 5-10 µm (v), the solvents evaporate (vi) depositing a thin film of the solute (vii).

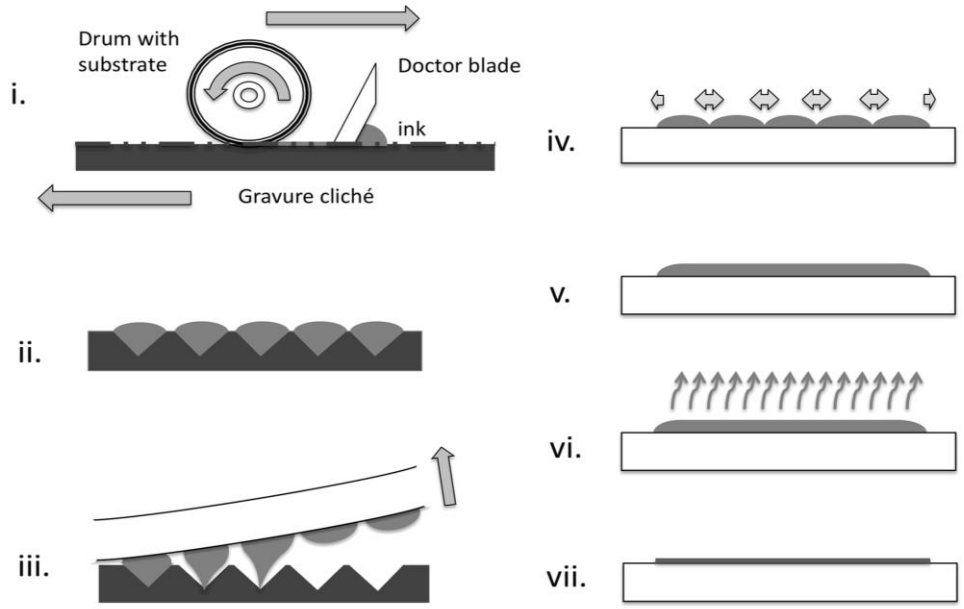


Figure 4.7 Schematic of gravure printing process

4.2.2 Engaged force

In gravure contact printing prosess, both mechanical and fluidic forces are engaged. Understanding of these forces is crucial to realize functional optoelectronic devices with highly uniform printed layers. Controlling parameters related to these forces modifies the characteristics of the printed thin films and the printing behaviour can be optimized for specific applications. For example, printing high resolution patterns requires high pressure forces between the cylindrical roll and the substrate. High viscosity printing inks are more suitable to print highly defined patterns while low viscosity printing inks can achieve highly uniform films over a surface owing to sufficient hydrodynamic movements occuring inside the printed formulation while it dries.

Printing is performed along a single direction. Directionality parallel to the printing direction is different from the forces perpendicular to the printing direction. This asymmetry may help with an orientation of molecular chains along the printing direction.

Fluidic movements are dominant factors determining the homogeneity of printed thin films. Surface tension of ink formulations and surface energy of both cliché and flexible substrate determine the wettability of ink formulations onto the substrate. Normally, it is a rule of thumb that surface tension of an ink formulation should be sufficiently smaller than surface energy of both cliché and substrate for complete transfer of inks and wetting onto the substrate, in other words, surface energy of substrate should be favourable to the printing formulation.

During evaporation of solvents, hydrodynamic movements of solvents can be observed. The 'coffee stain effect' is found when the boiling point of solvent is low, in other words, an outward convection flow is generated more actively as solvent evaporates at the edge of droplet at a faster rate. Also, it should be noted that the surface area at the edge of the droplet is larger than at the centre of the droplet, hence evaporation at the edge is faster although evaporation flux is equal at the whole surface area. After evaporation of the solvent is completed, a line of solute is formed at the edge of the droplet owing to capillary flow inside the droplets to compensate for losses due to fast evaporation at the pinning line. This pinned line is problematic for functional optoelectronic devices as the thickness of the polymer line at the micrometer scale, results in device failure.

4.2.3 Engraved cliché pattern

Copper clichés were designed by Schläfli-Maschinen with machined cells at line densities from 40 to 210 lines/cm. Cells were pyramidal-structures engraved by laser lithography.[14] All clichés were provided from Schläfli-Maschinen. An Xtreme engraved pattern developed by Hell[15], as shown in Figure 4.8a, was used for highly defined resolution of printed patterns. A line pattern in Xtreme engraved cliché is shown in Figure 4.8b.

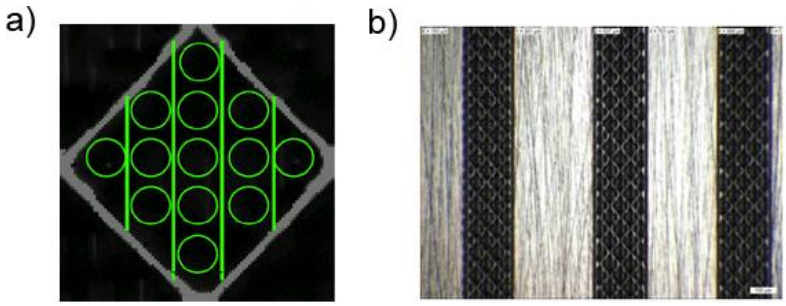


Figure 4.8 a) Schematic of Xtreme engraved pattern, b) Microscopic image of line pattern cliché with Xtreme patterned of line width 206 µm and line gap of 287 µm. The image 4.8b) was taken by M. Voigt.

4.2.4 Control printing parameters

The profiles of printed layers including thickness and uniformity can be controlled by a few factors. Firstly, cell depth of the cliché determines the amount of inks being printed each time. Therefore, a pattern with deeper depth prints thicker layers and vice versa. Secondly, line density of cliché, which is normally denoted as a number of patterned lines per centimetre affects homogeneity of printed thin film. A line density of cliché is related to the cell depth of the cliché. A high density cliché has a small variation of thickness in cell depth and vice versa. Hence, it is generally true that high density patterned cliché can induce improved homogeneity of printed films as a thickness variance in the cell depth is smaller. However, a high density patterned cliché with shallow cell depth transfers a low volume of ink formulation and the effects of fluidic movements such as the coffee stain effect and the Marangoni flow are reduced because of the small volume of the printed formulation. To increase hydrodynamic movements inside the droplet while it dries, a low line density patterned cliché with a deep cell depth can be used. Also, printing speed can control amount of transferred ink formulation. Faster printing speed carries smaller volume of inks but results in improved the surface uniformity of the printed thin films and vice versa.

4.3 Device Characterization

4.3.1 Field-effect transistor (FET) measurement

A Hewlett Packard 4155A semiconductor analyser was used for FET testing. Polymers are highly degraded in air ambient environment so that all measurements were performed inside glove box where filled in nitrogen. Characteristics of FETs are controlled by applied electric fields formed at the interface between semiconductor and dielectric layers, in other words, the operation of FET is voltage dependent. Hence, a bias voltage was applied using 3-probe point station which visualizes transistor characteristics at various input voltages. Three probes are corresponding to either source, drain or gate terminals. It measures the drain current (I_D) at a series of input gate voltage (V_G) with fixed drain voltage (V_D) for transfer characteristic. Output characteristic can be measured with I_D by varying V_D at fixed V_G. Simultaneously, the gate current (I_G) is often measured to quantify how much currents is leaked throughout the gate dielectric layer.

For transfer characteristic measurements, V_G was scanned at between 40V and -80V at a step of 10V for P3HT (p-type) FETs. The measurement was repeated at different V_D between 0V to -50V with an increment of -10V. In case of output characteristic, V_D was recorded between 0 and -20V with a 5V step at V_G of between 0V and -20V with an increment of -5V.

Saturation mobility was calculated from the saturation regime in transfer characteristics at $V_D = -50V = (V_G-V_T)$ using $\partial(I_D)^{1/2} / \partial V_G = (\mu_{SAT})^{1/2} (C_i W/2L)^{1/2}$. V_T was taken as the intercept at $I_D = 0$ of a linear fit to $(I_D)^{1/2}$ versus V_G (where V_G, V_T, I_D, μ_{SAT}, C_i, W and L represent the gate voltage, threshold voltage, drain current, saturation mobility, insulator capacitance per unit area, channel width and channel length, respectively).

4.3.2 Current density – voltage – luminescence (*J-V-L*) characteristic

In PLEDs, it is important to record the amount of current density and luminescence at various applied bias. Efficiency of PLEDs (OLEDs) can be identified as current efficiency (cd/A) and luminous efficiency (lm/W). Current density was measured by using a Keithley 2400 SourceMeter at a series of applied bias. Simultaneously, light output from the transparent electrode of PLEDs was collected by a Minolta LS100 (or Topcon BM-9) luminance meter. The numerical values were recorded by LabVIEW software.

4.4 Spectroscopy and Electroluminescence

4.4.1 Absorption

UV absorption spectroscopy measurement was performed by an ATI Unicam UV-Vis spectrophotometer. Absorption measurement of organic materials in a thin film form, was made on either glass, flexible substrates or quartz. The resulting absorption spectrum quantifies the range of wavelength that an organic film absorbs. For instance, they are useful with investigation of energy transfer between two adjacent fluorescence materials in a bilayer PLED. It is also useful to estimate the thickness of printed layers on a flexible substrate, which is not possible to be measured by common thickness profilers such as alpha-step or dektek as flexible substrates are soft. The intensity of absorption at its peak wavelength is almost proportional to the thickness of organic layers.

The overall process is illustrated in Figure 4.9. Light source from a deuterium (for ultraviolet light) or tungsten halogen lamp (for visible light) is converged into a beam and only selected wavelength of light can be transmitted throughout the monochromator. The monochromator consists of two slits and diffraction gratings between two slits. The first slit controls light intensity from light source so that it keeps the intensity of light identical during the measurement, flowing into the diffraction gratings. The next slit is

positioned where light with the selected wavelength can only travel and it filters out light with other wavelengths. Then, the transmitted beam is split into two beams of light with same intensity and wavelength. One beam passes through the sample and the other through the reference. Two beams are detected to figure out its intensity. The difference of two absorption intensities corresponds to the absorption property of the sample. The measurement is repeated across the entire UV-Vis spectrum which builds up a transmission spectrum for the sample.

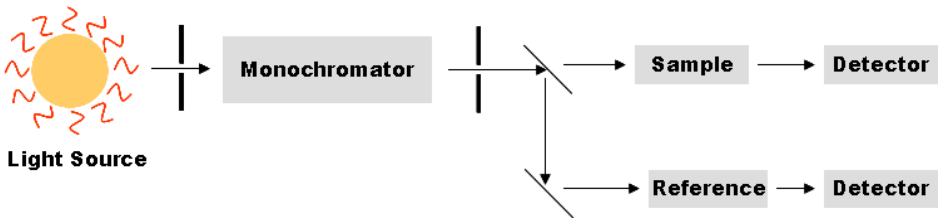


Figure 4.9 Schematic diagram of the measurement of absorption in an organic layer.

4.4.2 Photoluminescence (PL)

Polymer layers with light-emitting property such as polyfluorene based polymers were tested for characterizing its photoluminescence (internal) quantum efficiency (PLQE) and fluorescent emission spectrum. PL measurement can also be applied for analyzing a molecular orientation of polymeric layers.

Photoluminescence (PL) spectra were measured using a Spex FluoroMax-3 Jobin-Yvon spectrometer. The light emitted from a 150 W continuous output xenon arc lamp is transmitted into an excitation monochromator where a reflecting grating inside the monochromator disperses the light into constituent wavelength components via diffraction. The transmitted light passes through adjustable slits that control magnitude and resolution by further limiting the range of transmitted light. The filtered light passes into the sample cell and generates light emission by fluorescent materials within the sample. The emitted light enters the emission monochromator, which is located orthogonal to the light path from the excitation monochromator in order to eliminate background signal and minimize noise due to stray light. Emitted light is again filtered by a narrow range centred about the particular emission wavelength and exits through

adjustable slits and travels into the photomultiplier tube (PMT). Through the PMT, the signal is amplified and creates a voltage that is proportional to the measured emitted intensity. A schematic diagram of PL measurement is described in Figure 4.10.

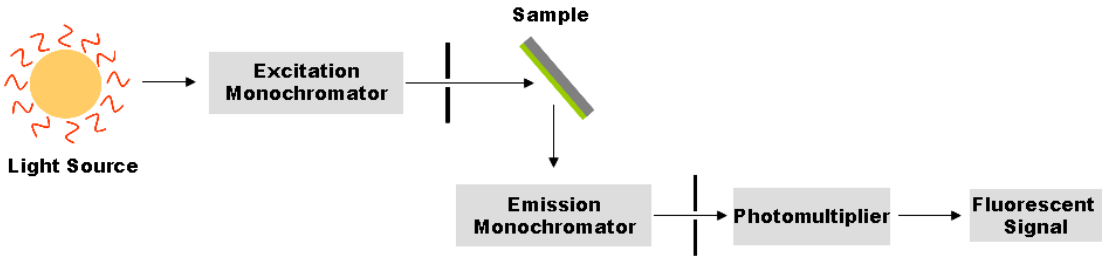


Figure 4.10 Schematic diagram of the measurement of photoluminescence (PL) in a fluorescence layer.

4.4.3 Electroluminescence (EL)

The electroluminescent (EL) spectrum gives the intensity vs wavelength emission from the OLED when a current is passed through the device. The EL efficiency gives the number of photons emitted per electron-hole pair passed through the device. Luminance (cd/m^2), luminous power and current efficiency (lm/W and cd/A respectively) are weighted for the eye response to different wavelengths, which will therefore depend on the EL spectrum of the OLED and the photopic luminousity function. A candle emits light with a luminous intensity, the intensity seen by the eye, of roughly one candela (cd). The unit of candelas is defined as the luminous intensity in a given direction of a source that emits monochromatic radiation of frequency 540×10^{12} Hz with a radiant intensity in that direction of 1/683 W/sr.

In this work, a Keithley 2400 Source Meter was used to apply a bias and supply current to the OLED, which were held in a sample chamber under nitrogen or vacuum. An Ocean Optics USB 2000 CCD spectrophotometer was used to record the EL spectrum. Depending on the device luminance, minimum detectable light output was set as either 1 cd/m^2 or 100 cd/m^2. Luminous intensity was recorded using a calibrated TOPCON luminance meter.

4.5 Contact Angle Measurement

Contact angle measurements were performed with a Krüss DSA 100. It measures the contact angle between a liquid and solid interface in the case of the sessile droplet method, and a droplet shape dangling from a needle in the pendant droplet method. The sessile droplet method is used to measure the surface energy of specific surfaces. The surface energy of a substrate is found by dropping specific test liquids on to its surface. The three probe liquids, namely, water (H_2O), diiodomethane (CH_2I_2) and ethylene glycol ($C_2H_6O_2$) were used to probe and then calculate the surface energy. Liquids with a spread of polar or non-polar (dispersive) properties are chosen for accuracy of the measurement. Contact angles of the three reference liquids on a target surface were visually measured by a CCD camera. If the contact angle is less than 40˚, then it can be said that the liquid wets the surface, and vice versa. The surface with hydrogen bonding is a good example of a hydrophilic surface. Hydrophilicity of a surface can be modified and increased by exposure to an oxygen plasma as hydroxide endgroups are formed at the edge of any surface molecules. A hydrophobic surface repels a water droplet and the contact angle of water on the surface is very high. It is a rule of thumb to estimate surface hydrophilicity that surface energy is large in a hydrophilic surface and low, typically less than 30 mN/m, in a hydrophobic surface. Numerical values of the surface energy can be used to graphically describe the region of good wetting on a polar vs dispersive surface energy plot. The domain is called a 'wetting envelope' which graphically represents a wetting region of a specific surface. If the surface tension of liquid locates inside the wetting envelope, then the liquid is said to wet to the surface. "Wetting" means the attractive forces between a liquid and bonding surface are maximized. For optimum adhesion, a liquid must thoroughly wet the surface. A wetting envelope domain can be calculated using either the Owens and Wendt method or the Fowkes method. The definition of the two methods can be written as Equation 4.1 and 4.2 respectively.

$$\frac{\sigma_L(\cos\theta+1)}{2(\sigma_L^D)^{1/2}} = (\sigma_S^P)^{1/2}\frac{(\sigma_L^P)^{1/2}}{(\sigma_L^D)^{1/2}} + (\sigma_S^D)^{1/2} \qquad (4.1)$$

$$(\sigma_L^D)^{1/2}(\sigma_S^D)^{1/2} + (\sigma_L^P)^{1/2}(\sigma_S^P)^{1/2} = \frac{\sigma_L(\cos\theta + 1)}{2} \quad (4.2)$$

where σ_S is the total surface energy of the solid, σ_S^D and σ_S^P are respectively the dispersive and polar components of the solid surface energy, σ_L is the total surface tension/surface energy of the liquid, and σ_L^D and σ_L^P are respectively the dispersive and polar components of the surface tension. θ is a contact angle of the liquid at the solid/liquid interface. An example of wetting envelope is shown in Figure 4.11.

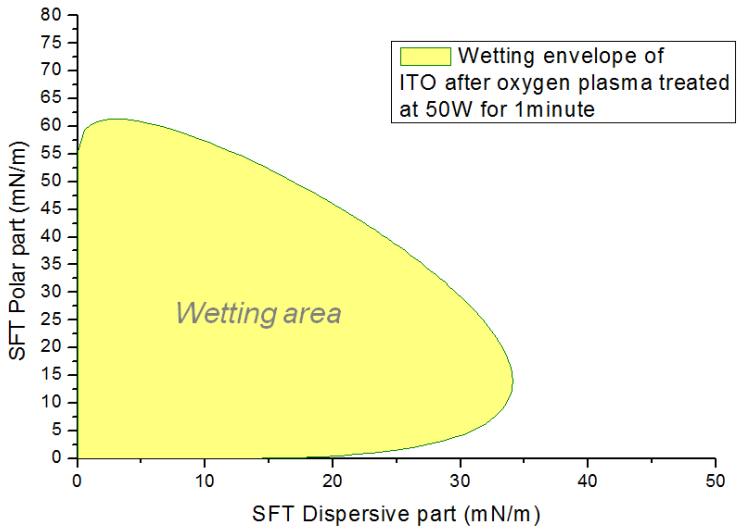


Figure 4.11 Example wetting envelope of ITO substrate indicating a shaded area of wetting region and outside the region denotes dewetting area.

Measuring the surface tension (energy) of a liquid is simple and straightforward. The surface tension of a liquid can be calculated by the pendant method. As the force holding a liquid droplet dangling on the end of a syringe needle is proportional to the surface tension of the liquid, measuring the critical volume of the liquid just before it drops from the needle is a way of measuring its surface tension. The surface tension of a liquid can be either large or small, and also depends on whether the liquid is based on polar or dispersive molecules. To find out the proportion of polar and dispersive components which make up the total surface energy, a contact angle of the liquid on the poly (tetrafluoroethylene) (PTFE), which is assumed to have a surface energy of 18 mN/m and is capable of no polar-type interactions, needs to be obtained. A schematic of measurements of the sessile and pendant droplet methods is depicted in Figure 4.12.

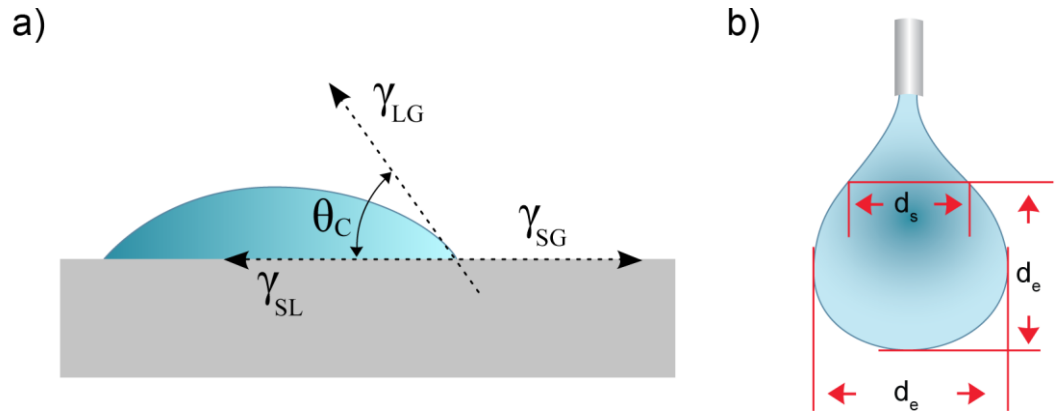


Figure 4.12 Representation of measurement of a) sessile and b) pendant droplets.

As it was mentioned previously, the surface tension is a relative value and it varies with measurement conditions and calculation models. It is important to choose an appropriate model for calculating the surface energy.

Zisman Theory

It is one of the most widely used definitions for surface energy. Zisman defines the surface energy of a solid to be equal to the surface tension of the highest surface tension liquid which completely wets the solid, with contact angle of 0˚. This was experimentally confirmed after measuring contact angle of solids from a large number of liquids with different surface tension values. It showed that contact angle of the solid was decreased as liquid surface tension decreases on the same solid surface. The limitation of this model is that it is only suitable with either purely polar or dispersive materials. As there are no existing pure polar materials (water, the highest polar material, is composed of both polar - 47 mN/m and dispersive - 26 mN/m components), the model fits best for the purely dispersive materials.

Owens/Wendt Theory

The Owens/Wendt theory considers two components, namely dispersive component and polar component. The dispersive component accounts for van der Waals and other non-site specific interactions that a surface is capable of having with applied liquids. The

polar component is engaged for dipole-dipole, dipole-induced dipole, hydrogen bonding, and other site-specific interactions. The theory is based on two well-known equations which describe interactions between solid surfaces and liquids. The equations are as follows:

$$\sigma_{SL} = \sigma_S + \sigma_L - 2(\sigma_L^D \sigma_S^D)^{1/2} - 2(\sigma_L^P \sigma_S^P)^{1/2} \quad \text{(Good's Equation)} \quad (4.3)$$

$$\sigma_S = \sigma_{SL} + \sigma_L \cos\theta \quad \text{(Young's Equation)} \quad (4.4)$$

where σ_S is the total surface energy of the solid, σ_S^D and σ_S^P are respectively the dispersive and polar components of the solid surface energy, σ_L is the total surface tension/surface energy of the liquid, and σ_L^D and σ_L^P are respectively the dispersive and polar components of the surface tension. θ is a contact angle of the liquid at the solid/liquid interface.

Owens and Wendt combined the two equations to produce the following equation:

$$\frac{\sigma_L(\cos\theta + 1)}{2(\sigma_L^D)^{1/2}} = (\sigma_S^P)^{1/2} \frac{(\sigma_L^P)^{1/2}}{(\sigma_L^D)^{1/2}} + (\sigma_S^D)^{1/2} \quad (4.1)$$

In order to determine amount of two components of liquid, the standard reference surface, poly (tetrafluoroethylene) (PTFE), can be used. Pure untreated PTFE has a surface energy of 18 mN/m of purely dispersive component and zero polar type interactions. In other words, σ_S^D is 18 mN/m and σ_S^P is 0 mN/m for PTFE. Substituting these values into the primary Owens/Wendt Equation (4.1) results in the following equation:

$$\sigma_L^D = \frac{\sigma_L^2(\cos\theta_{PTFE} + 1)^2}{72} \quad (4.5)$$

where θ_{PTFE} is the contact angle measured between PTFE and the probe liquid.

Fowkes Theory

The most widely used two component surface energy theory is Fowkes theory. Similar to Owens/Wendt theory, Fowkes theory describes the surface energy of a solid as having two components. Actually, Fowkes theory is mathematically equivalent to Owens/Wendt theory, but is theoretically different.

Fowkes theory is based on three fundamental equations which are as follows:

$$\sigma_S = \sigma_{SL} + \sigma_L \cos\theta \qquad \text{(Young's Equation)} \qquad (4.4)$$

$$I_{SL} = \sigma_S + \sigma_L - \sigma_{SL} \qquad \text{(Dupre's definition of Adhesion Energy)} \qquad (4.6)$$

$$I_{SL} = 2[(\sigma_L^D)^{1/2}(\sigma_S^D)^{1/2} + (\sigma_L^P)^{1/2}(\sigma_S^P)^{1/2}] \qquad (4.7)$$

where I_{SL} is the energy of adhesion per unit area between the liquid and the solid surface. The three equations are combined to derive the governing equation of the Fowke's surface energy theory:

$$(\sigma_L^D)^{1/2}(\sigma_S^D)^{1/2} + (\sigma_L^P)^{1/2}(\sigma_S^P)^{1/2} = \frac{\sigma_L(\cos\theta + 1)}{2} \qquad (4.2)$$

Normally, Fowkes theory is implemented using contact angle data from only two liquids. The recommended liquids are diiodomethane and water. Diiodomethane is purely dispersive liquid with a relatively high surface tension of 50.8 mN/m. A combination of highly polar liquid and non-polar liquid defines a good approximation of the surface energy.

4.6 Atomic Force Microscopy (AFM)

The atomic force microscopy was initially developed to overcome principle drawbacks of scanning tunnelling microscope (STM) which can only visualize atomic scale images

of either conducting or semiconducting surfaces. The AFM, however, has the advantages of imaging almost any type of surface including polymers, ceramics, composites, glass and biological samples.

In this thesis, atomic force microscopy (AFM) measurements were conducted using a Nano-R^{TM} AFM from Pacific Nanotechnology. A schematic illustration of AFM measurements is described in Figure 4.13. The AFM tip is first brought close to the sample surface and finally in contact with the sample surface via careful adjustment. The tip is then scanned across the sample under the action of a piezoelectric actuator, either by moving the sample or the tip. A laser beam targeted at the back of the cantilever-tip reflects off the cantilever surface to a split photodiode detector where collects the small cantilever deflections. A feedback loop maintains constant tip-sample separation by moving the scanner in the z direction to maintain the setpoint deflection. The atomic force relies on the forces between the tip and the sample and obtaining these forces is important for successful imaging. The force is not measured directly, but it can be estimated by measuring the deflection of the lever and the stiffness of the cantilever according to Hooke's law, F = -kz, where F is the force, k is the spring constant of the lever, and z is the cantilever deflection.

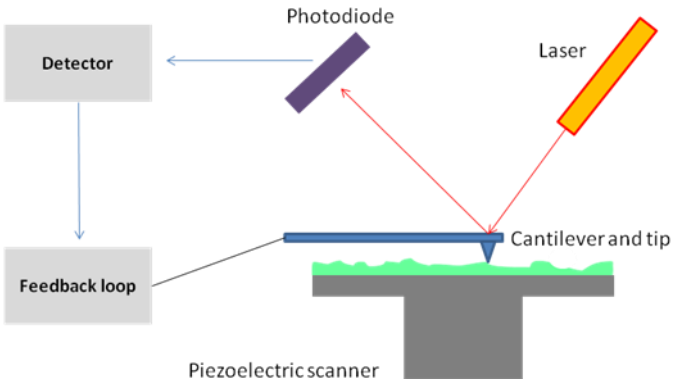


Figure 4.13 Schematic of atomic force microscopic measurement process

There are two types of measurements. In contact mode operation, the static tip deflection is used as a feedback signal. If the tip is very close to the sample surface, attractive forces can be quite strong which may cause the tip to 'snap-in' to the surface.

Therefore, the contact mode AFM is usually preceded in contact with the sample surface under the strong repulsive force. In this mode, the force between the tip and the surface is kept constant during scanning by maintaining a constant deflection. In non-contact mode AFM, the cantilever is externally oscillated at amplitude close to its resonance frequency. When the tip approaches the sample surface, the oscillation amplitude can be attenuated by repulsive van der Waals or electrostatic forces. A feedback loop maintains the degree of this attenuation by controlling the distance between the sample and the tip. The topography of surface can be recorded by calculating the forces deviated from the maintained distance. Phase and resonance frequency are also altered by van der Waals interactions between the tip and the surface. These changes in oscillation provide information about surface profiles. An advantage of non-contact mode over contact mode is that they are suitable with substrates with soft surface while contact mode is only available for rigid surface.

4.7 Reference

[1] S. L. Lai, M. Y. Chan, M. K. Fung, C. S. Lee, and S. T. Lee *Mater. Sci. Eng. B* **2003**, *104*, 26.

[2] S. K. M. Jonsson, J. Birgerson, X. Crispin, G. Greczynski, W. Osikowicz, A. W. Deniervan- der Gon, W. R. Salaneck, and M. Fahlman, *Synth. Met*. **2003**, *139*, 1.

[3] B. D. Martin, N. Nikolov, S. K. Pollack, A. Saprigin, R. Shashidhar, F. Zhang, and P. A. Heiney, *Synth. Met*. **2004**, *142*, 187.

[4] J. Zaumseil, C. L. Donley, J.-S. Kim, R. H. Friend, and H. Sirringhaus, *Adv. Mater*. **2006**, *18*, 2708.

[5] A. J. Campbell, D. D. C. Bradley, and H. Antoniadis, *Appl. Phys. Lett*. **2001**, *79*, 2133.

[6] L.-L. Chua, J. Zaumseil, J.-F. Chang, E. C.-W. Ou, P. K.-H. Ho, H. Sirringhaus, and R. H. Friend, *Nature* **2005**, *434*, 194.

[7] Y. Hou, M. Koeberg, and D. D. C. Bradley, *Synth. Met*. **2003**, *139*, 859.

[8] H. H. Fong, A. Papadimitratos, and G. G. Mallarias, *Appl. Phys. Lett*. **2005**, *89*, 172116.

[9] K. S. Whitehead, *PhD Thesis*, University of Sheffield, **2000**.

[10] L. Burgi, T. J. Richards, R. H. Friend, and H. Sirringhaus, *J. Appl. Phys*. **2002**, *94*, 6129.

[11] H. Sirringhaus, R. J. Wilson, R. H. Friend, M. Inbasekaran, W. Wu, E. P. Woo, M. Grell, and D. D. C. Bradley, *Appl. Phys. Lett*. **2000**, *77*, 3.

[12] P. Levermore, *PhD Thesis*, Imperial College London **2008**.

[13] H. Sirringhaus, N.Tessler, R.H. Friend, *Science* **1998**, *280*, 1741.

[14]G. Henniga, K. H. Selbmann, S. Pfinninger, J. Brendel, S. Bruning, *Large scale laser microstructuring of gravure print rollers - art. no. 68790O*, SPIE-INT SOC OPTICAL ENGINEERING, BELLINGHAM **2008**.
[15] www.hell-gravure-systems.com

Chapter V

High Performance, Flexible Polymer Light-Emitting Diodes (PLEDs) with Gravure Printed Organic Layers

5.1 Introduction

The ultimate approach to organic semiconductor device fabrication is expected to be via high-speed, large area, roll-to-roll (R2R) printing. Gravure contact printing is one of the highest volume potential techniques, operating at speeds of up to 60 m^2/s.[1] There have been already reported organic electronic devices with such fast speed fabrications.[2-4] However, device performance has not yet reached to devices fabricated with conventional spin-coating process.[5-7] Roll-to-roll printing techniques including gravure contact printing was originally invented for the purpose of printing graphic arts and informative media such as newspapers, magazines and books. Not like printing graphic arts where printed letters and figures have a thickness typically in microscale, printing electronic devices comprised of a stack of thin layers with a thickness in tens of nanometres, usually less than 100 nm, is not particularly straightforward and understanding of thin film formation process after ink formulations being printed and evaporated should be fully completed.

In this Chapter, high performance, flexible polymer light-emitting diodes (PLEDs) with gravure contact printed hole injection and emissive layers are reported. High surface tension formulation of poly (3,4-ethylene dioxythiophene): poly (styrene sulfonate) (PEDOT:PSS) needs to be modified with its fluidic parameters for favourable printing. Issues related to printing PEDOT:PSS are described in Section 5.3. Printing of light emitting polymer (LEP) on PEDOT:PSS is explained in Section 5.4. Thin film formation with uniform surface roughness less than RMS of 3 nm confirmed by atomic force microscopy (AFM) measurement is listed in Section 5.5. Finally device performance of printed PLEDs with a comparison of spin-coated PLEDs of the same layers is made in Section 5.6.

A first report of gravure printed PLEDs was published in 2005. Nakajima *et al*. at Dai Nippon Printing reported a flexible OLED panel using a gravure printed light emitting polymer.[8] No formulation details or efficiency values were reported, but the device operated at 100 cd/m^2 for 1,000 hours. Tuomikoski *et al*. reported PLEDs with gravure printed PEDOT:PSS and a polyfluorene light emitting polymer on printed ITO nanoparticles on flexible substrates.[5] The best device showed a maximum electroluminescent quantum efficiency of 0.1% and a luminance of 100 cd/m^2 at a drive bias of 5 V. Recently, PLEDs with printed PEDOT:PSS and an unidentified light emitting polymer have also been reported.[9] Even though no efficiency values were indicated, the devices achieved 100 cd/m^2 at a drive bias of 4.2 V and a maximum luminance of 5,000 cd/m^2.

5.2 Experimental

Materials: The PEDOT:PSS (Baytron Clevios^{TM} AI4083) dispersion was purchased from H. C. Starck GmbH. Triton X-100 and other solvents were obtained from Sigma-Aldrich. Substrates were polyethylene terephthalate (PET) coated in sputtered ITO (R_s = 40-60 Ω/sq) OC50 films from CPFilms Inc. The ITO on PET substrates were first etched by hydrochloric (HCl) acid diluted with DI water at a ratio of 2:1 (HCl:DI water) for 80 seconds to form ITO stripes, defined by acid resistant tape, with a width of 0.8

mm. They were then cleaned with acetone and IPA in an ultrasonic bath and then washed with deionized (DI) water. Oxygen plasma treatment used an Emitech K 1050X plasma asher.

LED preparation and characterization: Printing was with a Labratester I from Norbert Schläfli Maschinen. Cleaned substrates were printed with PEDOT:PSS formulations using a steel cliché with its engraved pattern of a 70 or 90 lines/cm with a cell depth of 35-40 μm at a speed of 35 m/min. After baking at 75 ˚C for 10 minutes in air, the LEP formulations were printed using a cliché with engraved pattern with its cell density of 40 lines/cm and cell depth of 60-70 μm at same speed. Film thicknesses were measured by profileometer-calibrated optical absorption using an ATI Unicam UV-Vis spectrophotometer. For reference devices, 55±5 nm layers of PEDOT:PSS was spin-coated at 2,000 rpm and then baked at 75 ˚C for 10 minutes in air. 75±5 nm layers of LG1300 were deposited by spin-coating at 2,500 rpm a 1.15 wt% LEP in *p*-xylene solution. Layer thicknesses were measured by a Tencor Instruments Alpha Step 200 surface profilometer.

After deposition of LG1300, all samples were transferred to a nitrogen atmosphere glove box (< 2 ppm H_2O, < 0.1 ppm O_2) to anneal at 120 °C for 1 hour. The cathode of 10 nm Ca followed by 100 nm Al was then thermally evaporated (vacuum pressure 4×10^{-6} mbar) with a shadow mask to define electrodes of 4.2 mm^2 (3 mm × 1.2 mm) area which reflects light emission. JVL measurements were performed using a Keithley 2410 Source-Measure Unit and a Topcon BM-9 luminance meter. EL of PLEDs were characterized by using a Keithley 2400 SourceMeter and results were collected from an Ocean Optics USB 2000 charge-coupled device spectrophotometer.

For demonstration of device, fabrications were repeated in the same procedure but it has larger light emission area of 0.42 cm^2 (width: 1.4 cm, height: 0.3 cm).

Contact angle measurement and morphology: Contact angle measurements and wetting envelope calculations were performed with a Krüss DSA 100. Surface energy of substrate was measured by calculating contact angle of sessile droplet when reference

fluids (water, diiodomethane and ethylene glycol) were dropped on a substrate. For a case of surface energy of PEDOT:PSS surface, only diiodomethane and ethylene glycol were used as water is likely to swell the polymer but two fluids have negligible effects on the polymer surface after thermal treatment. Surface tension (SFT) of a fluid was calculated by measuring pendant droplet method. Then, SFT of the fluid was analyzed to obtain its polar and dispersive components by measuring contact angle of the fluid on Teflon substrate using sessile droplet method. Wetting envelope of a substrate was drawn from all the measured surface energy values previously calculated. The tapping mode atomic force microscope (AFM) measurements were done using a Nano-R^{TM} AFM from Pacific Nanotechnology. A Zeiss Axioplan Microscope with a Nikon Coolpix P5100 digital camera was used to capture micron scale surface images.

5.3 Printing of PEDOT:PSS Formulation (high surface tension and polar)

The device structure of a PLED used in this chapter is depicted in Figure 5.1. The device consists of transparent ITO electrode, hole injecting PEDOT:PSS layer, light emitting polymer (LG1300) layer, and calcium as cathode which is capped by aluminium. LG1300 is a copolymer comprising of polyfluorene with doped n-type monomer for balanced mobility and its electric band levels lie in almost identical to the work functions of PEDOT:PSS and calcium.

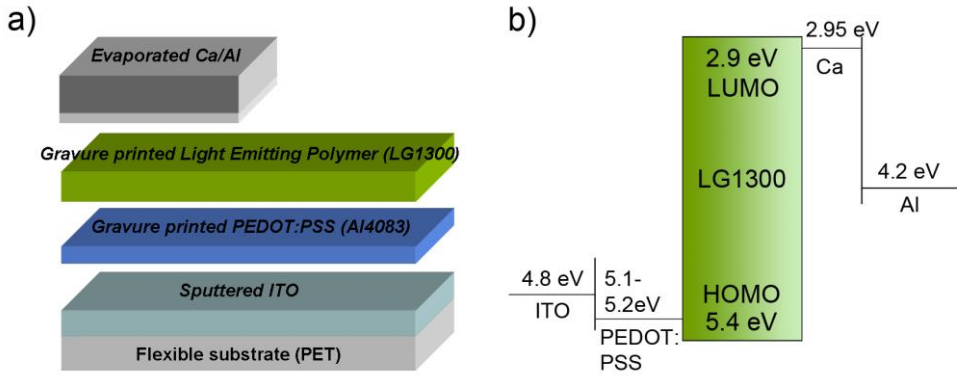


Figure 5.1 a) Structure of gravure printed PLEDs, b) Energy level diagram.

PEDOT:PSS is a standard hole injection layer material used in PLEDs,[10,11] being deposited between the transparent indium-tin oxide (ITO) anode contact and the light emitting polymer (LEP). It planarizes the anode surface, allows better adhesion between anode and LEP, and improves hole injection into the LEP by increasing the anode work function to 5.1-5.2 eV.[12,13]

Commercial PEDOT:PSS formulations are from Baytron and its products are refered to P, AI4083 and CH8000 as defined in Table 5.1. Its chemical and electrical components are different as well as its purpose. Because of high conductivity in Baytron P, it is often used as an organic electrode while Baytron AI4083 and CH8000 have low conductivity and are suitable with a hole injecting layer. Chemical contents, in other words concentrations, are in a similar range for both Baytron P and AI4083 and slightly higher in CH8000. The concentration of formulations is particularly important for printing as it affects both viscosity and layer thickness when it is printed.

	Baytron P	CH8000	AI4083
Resistivity (Ω.cm)	0.05	1-3 M	500-5000
Solid contents	1.2-1.4%	2.5-3%	1.3-1.7%
Application	Anode	Hole injection layer of solar cells or PLEDs	

Table 5.1 Properties of commercial PEDOT:PSS dispersions

Commercial PEDOT:PSS formulations developed for spin-coating are water based with a high surface tension of 70-80 mN/m. Initial attempts to gravure print the unaltered formulations on untreated ITO gave very poor results. First of all, a couple of factors including printing speed and line density of grid (lines/cm) were varied to investigate the reason for the poor printing. These parameters are expected to affect printing behaviour of PEDOT:PSS formulations. The three different formulations were tested and its microscopic images are presented in Figure 5.2-5.4.

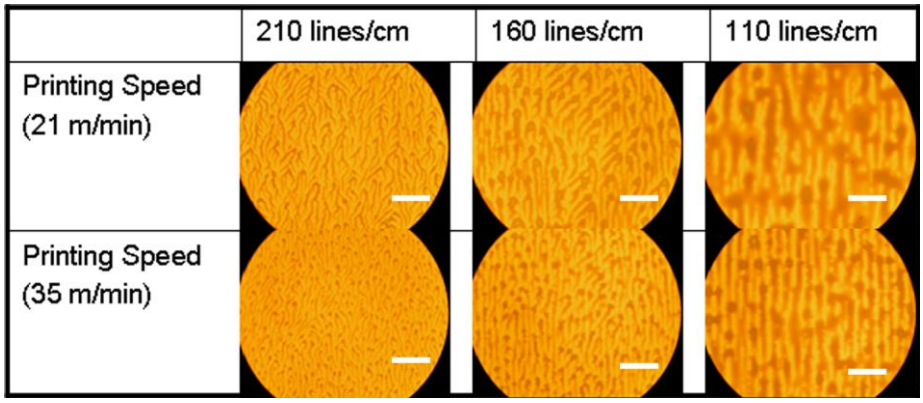


Figure 5.2 Optical microscopic images of printed pristine Baytron P (Scale bar indicates 1 μm).

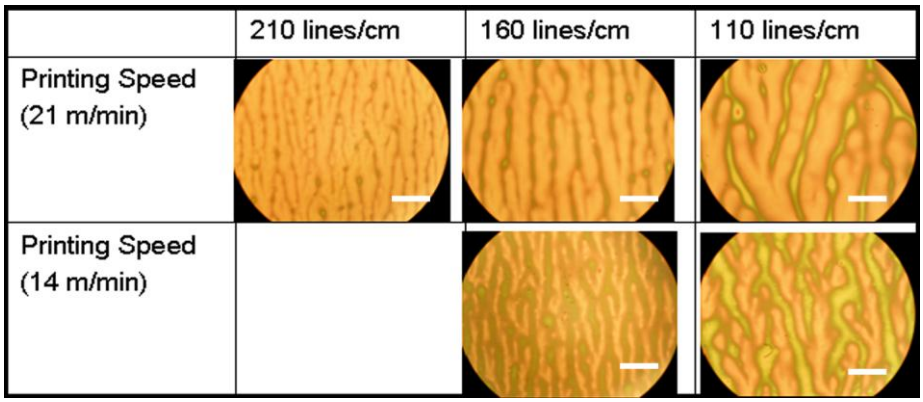


Figure 5.3 Optical microscopic images of printed pristine Baytron AI4083 (scale bar indicates 1 μm).

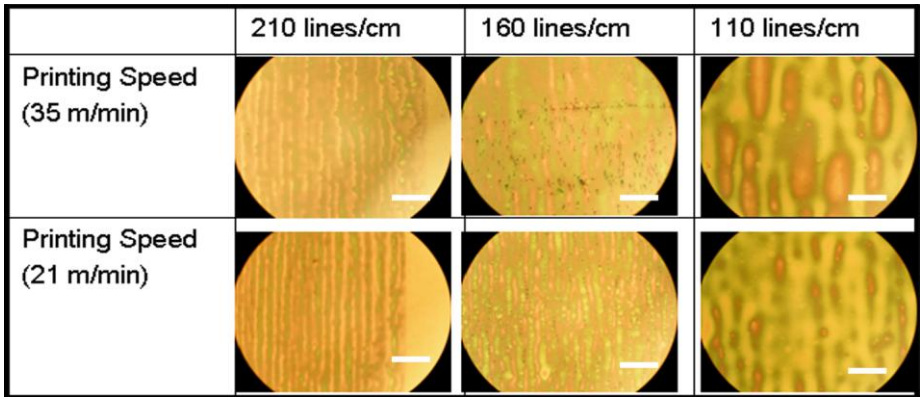


Figure 5.4 Optical microscopic images of printed pristine Baytron CH8000 (scale bar indicates 1 μm).

The printed PEDOT:PSS thin films show that their coverage on the substrate increases for slower printing speeds and lower number of line density of the cliché. Also, the coverage is largely increased in the case of CH8000 because of the higher concentration. Even though a pattern is fully covered, it is also crucial to consider the printed surface

maintains good homogeneity for uniform hole injection into the LEP layer. In Chapter 8, microscopic images of printed patterns (Figure 8.23) of OTFTs are shown that the surface of the printed pattern is slightly rough but they are fully covered on the conducting channel between the pre-patterned ITO source and drain electrodes. Surface homogeneity is particularly important in case of PLEDs for uniform emission while it is not the most important factor in OTFTs. However, maintaining good homogeneity of OTFTs may be preferred as it can affect switching speed of each OTFT at different positions of pixels in an array and also affect transistor yield.

The coverage of a printed pattern is related to spreading of an ink formulation on a substrate. If the surface energy of the substrate is not higher than the surface tension of the formulation, the ink formulation will remain in parts or stripes as it is shown in Figure 5.2-5.4. This can be explained by considering the surface tension (made up of polar σ_p and dispersive σ_d components) of the unaltered PEDOT:PSS formulation (point A) and the surface-energy wetting envelope (calculated using the Fowkes method) of the untreated ITO shown in Figure 5.5. The formulation lies far outside the wetting envelope and as result dewets. To vary the surface energy, the ITO was exposed to an oxygen plasma.[14,15] Figure 5.5 shows the resultant wetting envelopes for 30 and 50 W exposure for 1 minute. The plasma treatment increases the oxygen content of the ITO, greatly increasing its polar component and decreasing its dispersive component. Numerical values of surface energy of ITO according to oxygen plasma treatment are listed in Table 5.2. This increases the surface energy envelope towards the unaltered PEDOT:PSS formulation, but it still lies outside even after its treatment at 50W for 1 minute. Gravure printing the unaltered formulation on oxygen plasma treated ITO is shown in Figure 5.6 (i). The result is very poor with the film breaking up into large non-uniform streaks in the printing direction. Although not as extreme as the untreated ITO, solution surface tension is still too large compared to the substrate surface energy.

Surface	Surface Energy ($\sigma_s = \sigma_p + \sigma_d$) (mN m^{-1})		Total Energy (mN m^{-1})
	Polar component (σ_P) (mN m^{-1})	Dispersive component (σ_d) (mN m^{-1})	
ITO - non treated	1.61	31.83	33.44
ITO - 30W, 1 min	43.06	19.74	62.8
ITO - 50W, 1 min	55.46	11.99	67.45
PEDOT:PSS	33.52	24.69	58.21

Table 5.2 Surface energy of ITO surfaces. All the values were experimentally calculated from sessile droplet method using contact angle measurement.

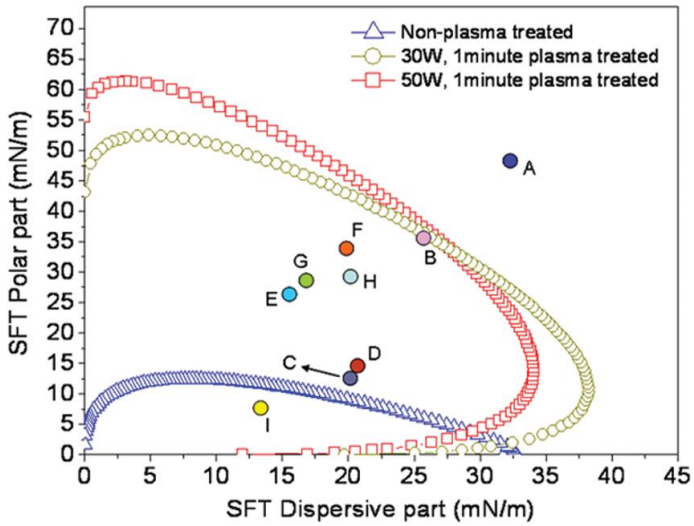


Figure 5.5 Wetting envelopes of oxygen plasma treated ITO on PET substrate with various surface tensions of mixtures: Pristine PEDOT:PSS (AI4083), A; This was modified (vol %) at 5 (PEDOT:PSS) : 1 (solvent) ratio with ethylene glycol, B; Triton X-100, C; IPA, D; ethanol, E; methanol, F; acetone, G; acetonitrile, H; vol % of 10 (PEDOT:PSS) : 5 (IPA) : 1 (Triton X-100) ratio, I.

PLEDs were fabricated with spin-coated films of PEDOT:PSS formulations blended with ethylene glycol.[16,17] PEDOT:PSS mixed with ethylene glycol (5:1 ratio by volume) lies just inside the wetting envelope (see Figure 5.5, point B). The printed formulation (Figure 5.6 (ii)) gives poor coverage and large regions of different thickness. Ethylene glycol has a high boiling point (B_p = 197.3 °C) and will take a long time to evaporate. Mixing a water based formulation with a higher boiling point, lower surface tension solvent is expected to oppose solution spreading due to the Marangoni effect[18] which, especially when combined with de-pinning of the contact line[19] and a slow evaporation rate,[20] will pull the solute inwards during drying.[21] These

effects along with the small difference between surface tension and substrate surface energy are likely to result in this unevenness.

Triton X-100[6,7] is a viscous non-ionic detergent with a high boiling point ($B_p \geq$ 200 °C). It has both hydrophilic and hydrophobic endgroups, which should allow a change in the balance between surface tension and surface energy favouring better wetting. A formulation of PEDOT:PSS mixed with Triton X-100 (5:1 by volume) lies deep within the wetting envelope (Figure 5.5, point C). The printed formulation (Figure 5.6 (iii)) gives good overall coverage, but the film is non-uniform and has broken up into fine interconnected streaks aligned in the printing direction. This is again a high boiling point, low surface tension solvent, which will take a long time to dry and will have the same spreading issues as ethylene glycol.

However, surfactants can disrupt the surface tension driven Marangoni forces at very low concentrations.[22] Certainly the large scale aggregation and poor coverage found for ethylene glycol is not seen here. The fine streaks in Figure 5.6 (iii) are of approximately the same width as the cliché ink cells (200 μm), indicating that it is at the moment of printing where this formulation has failed. This also suggests the role of poor cliché-substrate surface energy differences, solution shear force intermixing and inversion of the droplet surface.

To stay deep within the wetting envelope and also avoid high boiling point solvents, the PEDOT:PSS formulation was blended with IPA (B_p = 82.4 °C). Figure 5.6 (iv) shows a gravure printed film of PEDOT:PSS mixed with IPA (5:1 ratio by volume). This formulation lies within the wetting envelope (Figure 5.5, point D). The printed films are highly uniform and show very good coverage. Similar good printing results were obtained using PEDOT:PSS blended at a 5:1 ratio by volume with low boiling point, low surface tension solvents such as ethanol (B_p = 78.5° C), methanol (64.6° C), acetone (56.2° C) and acetonitrile (81.6° C). These all lie within the wetting envelope (Figure 5.5, points E, F, G and H respectively). Its numerical parameters of the surface energy calculated by pendant droplet are listed in Table 5.3. The use of a lower boiling point, lower surface tension solvent will result in Marangoni forces which favour

spreading and act against aggregation during drying.[16] The faster evaporation rate, which may also result in evaporative cooling and an increase in formulation viscosity,[23] will additionally act against the possibility of formulation flow and aggregation during the later stages of drying. All of these factors should contribute to the observed excellent printing results. All printed PEDOT:PSS films have a thickness of 50-60 nm.

The coffee-stain effect,[24] a major problem found for ink-jet printing,[18,20,25] was observed for some of the above films. This can be ascribed to the capillary forces and Marangoni forces acting in the same direction, depositing solute at the film edge.[25] To avoid this, the above formulations were printed with a small amount of the surfactant. PEDOT:PSS : IPA : Triton X-100 blended at a ratio 10:5:1 volume lies very deep within the wetting envelope (Figure 5.5, point I) and gives a highly uniform printed film (Figure 5.6 (v)). The edge of the gravure printed film is very well defined, the surfactant disrupting enough of the Marangoni flow and lowering the contact angle at the pinning-line to avoid non-uniform deposition. The corner of the film in Figure 5.6 (v) is shown in Figure 5.6 (vi). This exactly follows the cell pattern of the particular plate, consisting of a large uniform area with a thin border of width 200 μm. This demonstrates the ability to print PEDOT:PSS to this resolution.

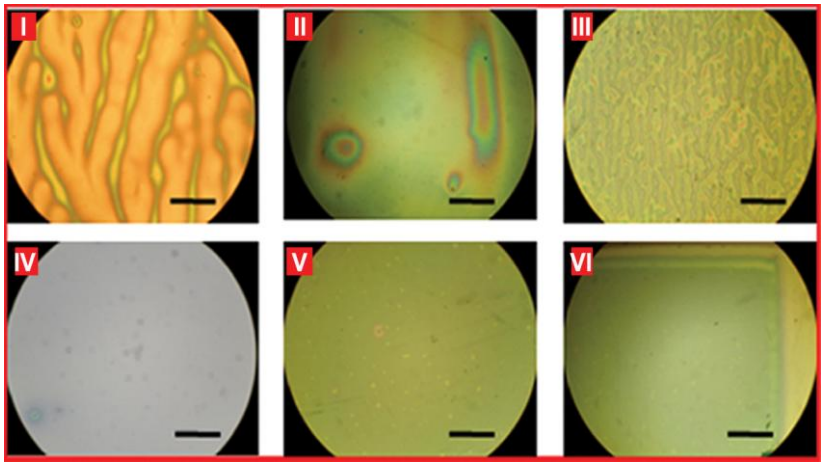


Figure 5.6 Optical microscopic images from these printed PEDOT:PSS formulations: i, A; ii, B; iii, C; iv, D; v, I; vi, edge of I; (scale bar indicates 1 mm).

Ink formulation	Surface Tension ($\sigma_s = \sigma_p + \sigma_d$) (mN/m)		Total Surface Tension
	Polar component (σ_P) (mN/m)	Dispersive component (σ_d) (mN/m)	
A	47.76	32	79.76
B	35.77	26.06	61.78
C	12.74	20.13	32.87
D	14.24	21.2	35.45
E	26.52	15.98	42.5
F	31.87	20.42	52.29
G	27.36	17.73	45.09
H	28.57	20.67	49.24

Table 5.3 Surface tensions of PEDOT:PSS ink formulations. All the values are experimentally calculated from pendant droplet method using contact angle measurement.

Solvent	Chemical formula	Surface Tension ($\sigma_s = \sigma_P + \sigma_d$) (mN/m)		Boiling point (°C)
		Polar component (σ_P) (mN/m)	Dispersive component (σ_d) (mN/m)	
Acetone[b]	C_3H_6O	8	14.7	56.2
Acetonitrile [b]	C_2H_3N	13	15.3	81.6
2-propanol [b]	C_3H_8O	12.6	10.5	82.4
Ethanol[a]	C_2H_6O	14.5	7.6	78.5
Methanol[a]	CH_4O	17.3	5.4	64.6
Ethylene glycol [b]	$C_2H_6O_2$	16.8	30.9	197.3
Water[a]	H_2O	46.8	26	100
Cyclohexane [b]	C_6H_{12}	0	24.6	80.7
p-xylene [b]	C_8H_{10}	2	25.8	138.3
Toluene[a]	C_7H_8	2.3	26.1	110.6
Indan [c]	C_9H_{10}	0	25.2	177

Table 5.4 Chemical properties of solvents used as wetting and bonding balance agents. Surface tension properties of [a] are from Ref. [26] and [b] are from Ref. [27]. Surface tension of Indan[c] was experimentally calculated using contact angle measurement

The gravure printed PEDOT: PSS films were examined in PLEDs with spin-coated LEP layers. The current density – voltage – luminance (*J-V-L*) characteristics are shown in Figure 5.7. All the gravure printed PEDOT:PSS devices compared very favourably against a spin-coated PEDOT:PSS device. The highest current density and luminance values for a given bias were obtained for the IPA formulation (5:1 by volume), this

having the optimum bulk and interfacial morphology. Numerical values of surface tension and boiling point of solvents used in this chapter are listed in Table 5.4.

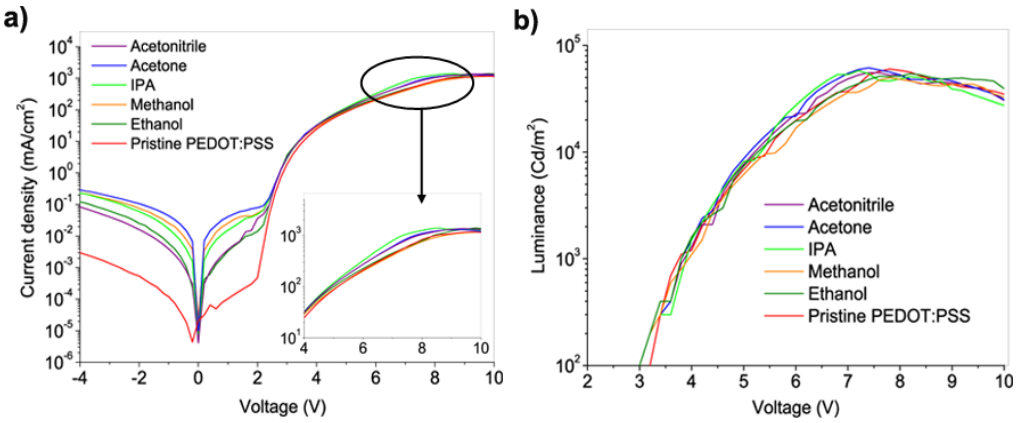


Figure 5.7 Performance of PLEDs with spin-coated and printed PEDOT:PSS (formulations as above) and spin-coated LEP. J-V (a) and L-V (b) characteristics of PLEDs.

5.4 Printing of LG1300 Formulation (low surface tension and dispersive)

Having successfully printed PEDOT:PSS, printing LEP layer is the next. The wetting envelope of the surface of PEDOT:PSS is shown in Figure 5.8. It has a less polar but more dispersive wetting envelope compared to the 50W oxygen plasma treated ITO. This envelope encompasses a broad range of dispersive, non-polar organic solvents. The LEP used in this study was LUMATION Green 1300 (LG1300), a green emitting polyfluorene copolymer.[28-30] The solvents conventionally used for spin-coating LG1300 are *p*-xylene (B_P = 138.3° C) and toluene (B_P = 110.6° C). LG1300 formulations of *p*-xylene and toluene (0.8% by weight) lie close to each other within the PEDOT:PSS wetting envelope (Figure 5.8, points A and B). However, gravure printing of these formulations resulted in non-uniform films attributed to high boiling point of solvents. Large stacks of polymer were observed on printed surface similar to printing of PEDOT:PSS mixed with high boiling point ethylene glycol (Figure 5.6 (ii)) and Triton X-100 (Figure 5.6 (iii)).

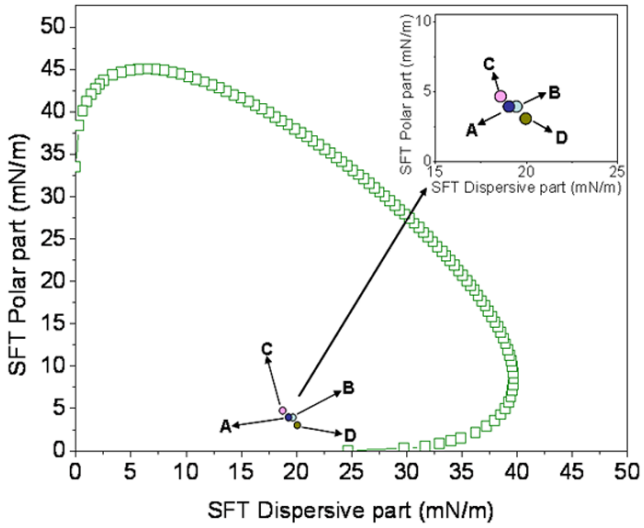


Figure 5.8 Wetting envelope of printed PEDOT:PSS surface with surface tensions of formulations of 0.8 wt% LG1300 in: pure *p*-xylene, A; pure toluene, B; *p*-xylene: indan 5:1 v/v, C; *p*-xylene: cyclohexane 5:1 v/v, D.

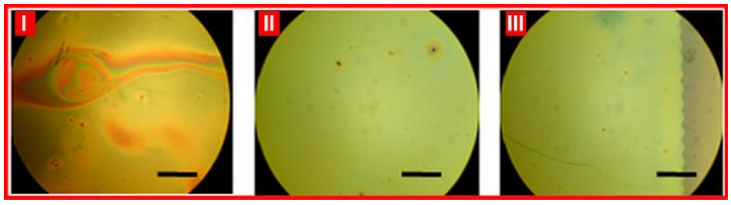


Figure 5.9 Optical microscopic images of printed LG1300 formulations: i, C; ii, D; iii, edge of D; (scale bar indicates 1 mm).

Ink formulation	**Surface Tension ($\sigma_s = \sigma_p + \sigma_d$) (mN m^{-1})**		**Total Surface Tension**
	Polar component (σ_P) (mN m^{-1})	**Dispersive component (σ_d) (mN m^{-1})**	
A	4.3	18.8	23.1
B	4.41	19.72	24.14
C	4.8	18.74	23.53
D	3.64	20.34	23.98

Table 5.5 Surface tensions of LG1300 ink formulations. All the values are experimentally calculated from pendant droplet method using contact angle measurement.

Given the results for PEDOT:PSS, solvent blends were investigated using either high boiling point - indan (B_P = 177° C) or low boiling point - cyclohexane (B_P = 80.7° C). Figure 5.8 shows the position of LG1300 formulations (0.8% by weight) of *p*-xylene

blended with 5:1 ratio by volume of indan and cyclohexane (points C and D respectively). Both lie very close to each other and the *p*-xylene and toluene points within the PEDOT:PSS wetting envelope. Figure 5.9 (i) and (ii) show gravure printed films of the blended formulations. The indan formulation produces a highly uneven, non-uniform film of poor quality. The cyclohexane formulation, however, printed with excellent homogeneity comparable to that of spin-coated films. These again follow the trend found for PEDOT:PSS adding the lower boiling point, lower surface tension solvent (cyclohexane) produces homogeneous printing, whereas adding the higher boiling point, lower surface tension solvent (indan) produces relatively poor printing. However, compared to the successful PEDOT:PSS formulations, the difference in solvent surface energy is nearly an order of magnitude smaller so we expect a smaller Marangoni effect.[21,23] The surface tension values of LG1300 ink formulations are listed in Table 5.5. Other factors such as more rapid drying and evaporative cooling increasing the polymer solution viscosity[23] may contribute to the cyclohexane formulation being favorable. In addition, during drying polymer solutions form surface gels at the solution-air interface.[23,31] Rapid evaporation and evaporative cooling will increase such gelation effects, stabilizing the drying formulation.

Evaporative cooling driven Bénard-Marangoni convection has been observed in evaporating polymer solutions of thickness > 500 µm,[23] but the solution thickness here of 10 µm would give a vertical Marangoni number far below the instability threshold. Vertical solution density driven Rayleigh-Bénard or Rayleigh-Taylor type instabilities[23,32,33] are also precluded by the film thickness and the continuously changing, multi-directional g-forces experienced in this printing method.

We also note that Figure 5.9 (iii) shows the complete absence of any coffee-stain effect, consistent with a relatively low outward Marangoni flow. It means that gravure printing can achieve very well defined pixels with uniform emission over the whole device area. An additional advantage of low boiling point solvent formulations is that residual solvent removal can be done quickly at room temperature. Annealing of PEDOT:PSS film was performed at 75° C for 10 minutes in air. This is vital for high speed, R2R printing on low heat resistance, flexible plastic substrates.

Optimum thickness of LEP for single emissive layer structure PLEDs is known to be between 70-80 nm.[34] All printed LEP films had a thickness of 70-80 nm. Thickness of thin films on flexible substrate such as PET or PEN cannot be measured by conventional alpha-step or dektek measurement tools because smoothness of flexible substrate induces false measurements. Hence, the thickness of a printed layer on a flexible substrate was estimated by absorption intensity using UV-spectroscopic measurement. Pre-developed spin-coated organic films on glass having a thickness, which is already measured, were compared to a printed thin film. The absorption intensity increased linearly with the polymer film thickness. Both printed on ITO and PEDOT:PSS show a linear fit over R^2=0.98 as shown in Figure 5.10 and 5.11. PLEDs were gravure printed using LEP formulations with different fractions of cyclohexane (Figure 5.12). An increased fraction of cyclohexane generally decreases the current and maximum luminance values but increases device efficiency. This indicates a lower hole and/or electron current but a better charge balance and/or recombination zone position.[34] The maximum device efficiency was found to be at a ratio by volume of 10:3.

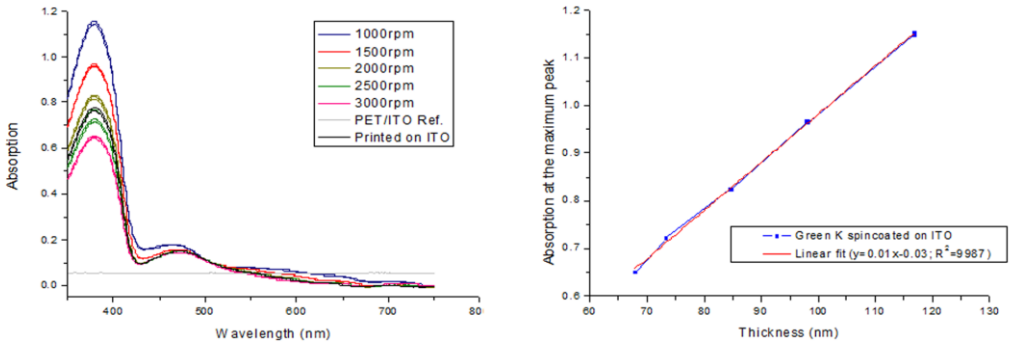


Figure 5.10 UV absorption peaks of LG1300 spin-coated on ITO.

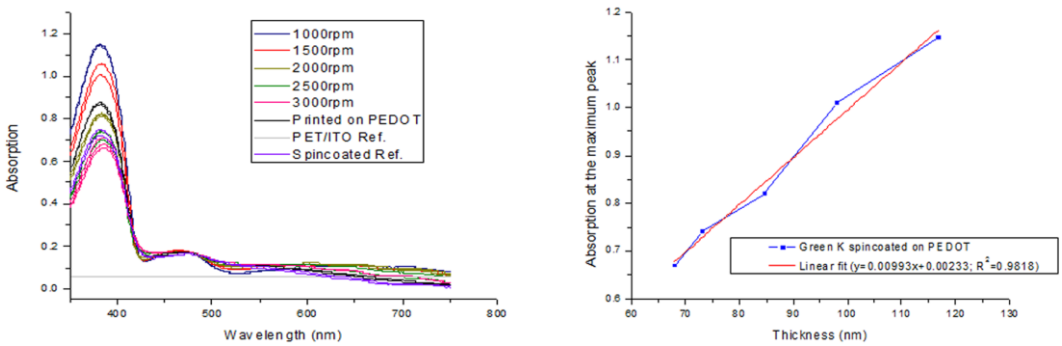


Figure 5.11 UV absorption peaks of LG1300 spin-coated on PEDOT:PSS.

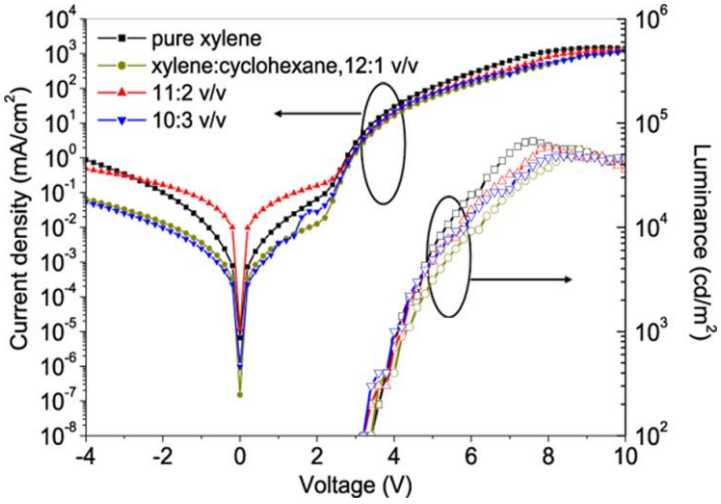


Figure 5.12 Performance of PLEDs with gravure printed LG1300 at different *p*-xylene:cyclohexane volume ratios.

To explain the mechanism by which homogeneously gravure printed thin film are created, we suggest a schematic representation model for describing two main hydrodynamic movements of solvents during thin film deposition ascribed as spreading and drying process of the ink formulation in Figure 5.13. Once an ink formulation is transferred to a flexible substrate, dropped ink formulation is spread over the substrate depending on the surface energy of the substrate and the ink. After spreading of the ink, the solvent of the ink formulation starts to evaporate at all the surface and evaporation seems faster at the edge of the droplet due to larger surface area than the centre. It is usually a case that solvent starts to evaporate after ink formulation is fully spread having a low contact angle onto the substrate. The convection flow toward a pinning line of the ink droplets can be observed when the solvent evaporates at a fast speed to compensate the losses from the solvent evaporation at the pinned line. This outward convection flow carries polymer solutes. If the solvent evaporation occurs too quickly, a large amount of convection flow is generated, and a large number of solutes can be transferred toward the pinning line. As a result, it is likely to observe a 'coffee stain ring' at the edge of the ink droplet. On the other hand, if the evaporation is too slow, polymer solutes will have irregular convection flow which does not occur toward the pinning line of the printed formulation. Instead, solvent evaporation can occur at various points on the surface at random speed so that finally there are many piles of polymer solutes remained after the solvent is fully evaporated. In order to resolve this

unevenness surface problem, it would be useful to mix the formulation with other solvents to recirculate the fluidic movements inside the printed ink formulations by inducing a surface tension driven Marangoni flow.[18]

In our case, a LG1300 formulation dissolved in *p*-xylene showed non-uniform surface characteristics due to a high boiling point of the solvent so that dried polymer solutes are remained as piles. Here is a turning point which determines surface roughness of printed thin films. A LG1300 formulation in *p*-xylene was mixed with either a lower boiling point (cyclohexane) or a higher boiling point (indan) solvents. Both additive solvents have a lower surface tension than *p*-xylene (Table 5.4). A lower boiling point solvent starts to flow toward an edge of a droplet due to a capillary flow. This diverges spatially surface tension inside the printed droplet. If a lower boiling point solvent has a lower surface tension, an outward Marangoni flow can be induced from the centre with a higher surface tension to the edge with a lower surface tension. On the other hand, if a lower boiling point solvent has a higher surface tension, an inward Marangoni flow is induced for the same reason. In our case, cyclohexane has a lower surface tension than *p*-xylene so that an outward Marangoni flow was observed. The flow planarized the unevenness in surface morphology due to the remained stacks of polymer solutes. However, when a higher boiling point, lower surface tension solvent (indan) was mixed, an inward Marangoni flow was induced resulting in the surface unevenness profile being even worse.

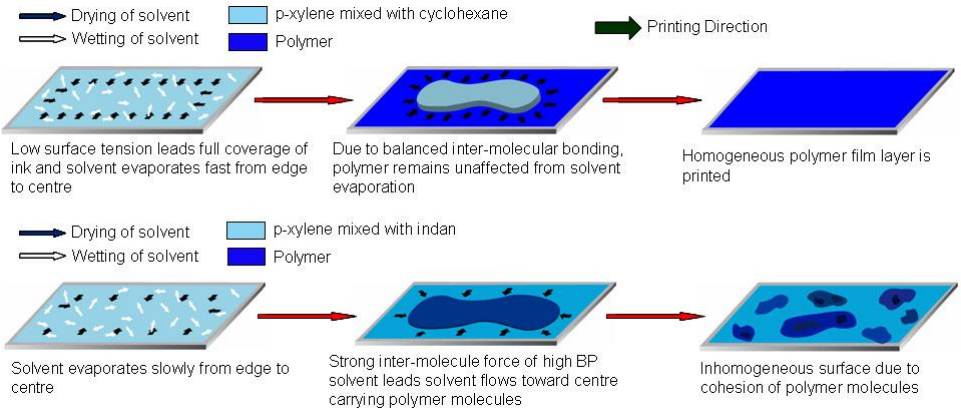


Figure 5.13 Fluidic movements during thin film formation in gravure printing process.

5.5 Morphology in Nanoscale of Printed Layers

It was previously confirmed that appropriately mixed ink formulations can print thin films with surface roughness uniform in microscale. Nanoscale patterns, which are concerned for an arrangement of molecules, are crucially related to device performance as well. A rough surface typically more than RMS value of 3 nm can disrupt charge carrier transport and injection between organic layers, hence it normally results in high leakage currents (low efficiency) or/and non-uniform emission. Printed layers with uniform surface profile are vital for a high efficiency device. Preferentially oriented molecular structure can enhance charge carrier mobility enormously which is an important issue especially in organic transistors using polycrystalline materials.[35-39] In this study, it was only concerned about surface roughness in nanoscale for uniform emission and high efficiency using an amorphous light-emitting polymer. Molecular orientation effects along the printing direction should be negligible as an amorphous polymer has a low crystalinity.

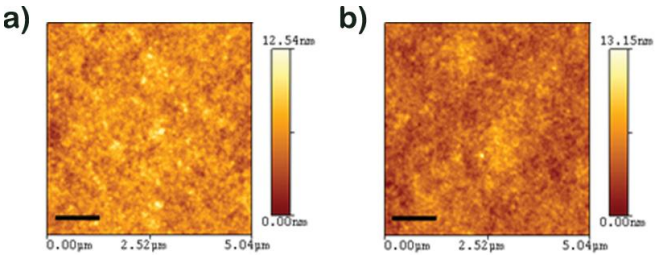


Figure 5.14 Tapping mode AFM images of spin-coated (a) and printed (b) PEDOT:PSS on PET (scale bar indicates 1 μm).

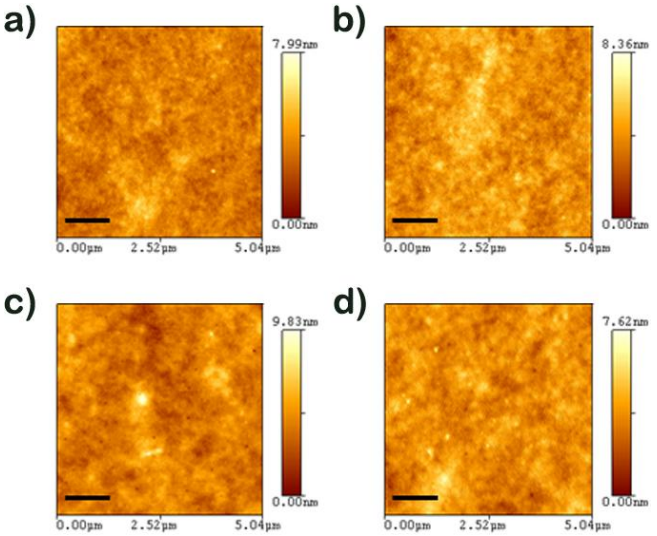


Figure 5.15 Tapping mode AFM images of spin-coated (a) and printed LG1300 with different ink formulations of pure *p*-xylene (b), *p*-xylene:cyclohexane 12:1 (c) and 10:3 v/v (d) on PET (scale bar indicates 1 μm).

Figure 5.14 shows AFM images of spin-coated and gravure printed (5:1 by volume IPA) PEDOT:PSS films. The gravure printed film shows a slightly greater thickness variation over the 5x5 μm^2 area, but the overall RMS roughness of about 1.2 nm is the same for both films. The AFM images of PEDOT:PSS is amorphous and matches to the results previously reported.[10] Figure 5.15 shows AFM images of the surface of LG1300 spin-coated from *p*-xylene (i), printed from *p*-xylene (ii) and printed from *p*-xylene blended with cyclohexane at ratios of 12:1 (iii) and 10:3 (iv) by volume. The RMS surface roughness is 0.73, 0.92, 0.88 and 0.7 nm respectively. As the fraction of cyclohexane is increased, the gravure printed films become increasingly smooth on a sub-micron level, eventually reaching the value found for the spin-coated films. This indicates that the film uniformity and smoothness achieved with these formulations occurs on both large (> 1 mm) and small scales (< 1 μm). It can be also said that the inhomogeneity of printed LG1300 of pure *p*-xylene at the microscale are also observed at the nanoscale indicating that fluidic movements inside the ink formulation also influence arrangement of molecules in nanoscale as well as microscale surface profile.

5.6 Device Performance Compared to Spin-coated Films

Finally, we compare PLEDs with the PEDOT:PSS and the LEP layers either spin-coated or gravure printed using the optimized formulations. Figure 5.16 shows the *J*-*V*-*L* characteristics of both spin-coated and gravure printed devices on flexible PET substrates. All cases resulted in similar characteristics. Table 5.6 lists PLED performance values. The relatively high drive bias for the maximum luminance of the PLEDs can be attributed to the poor conductivity of the ITO on PET substrates (σ = 1,282 S/cm) compared to a reference ITO on glass substrates (σ = 5,000-6,000 S/cm). There is a higher leakage current when gravure printed layers are present, indicating increased surface roughness at the ITO anode. However, the built-in potential just above 2 V is unchanged. When in the on state, the *J*-*V* and *L*-*V* characteristics of all devices

are almost identical across all applied bias values. The PLED performance values in Table 5.6 are also similar. When both layers are spin-coated, at a display brightness of 100 cd/m^2 the devices have luminosity, efficiency and drive bias values of 5.7 lm/W, 5.4 cd/A and 3 V respectively. When both layers are gravure printed, the values are 5.4 lm/W, 5.2 cd/A and 3 V respectively. The maximum luminance values for fully spin-coated and gravure printed are 56,000 and 66,000 cd/m^2 respectively. The values for devices with one layer printed and one layer spin-coated cover a similar range.

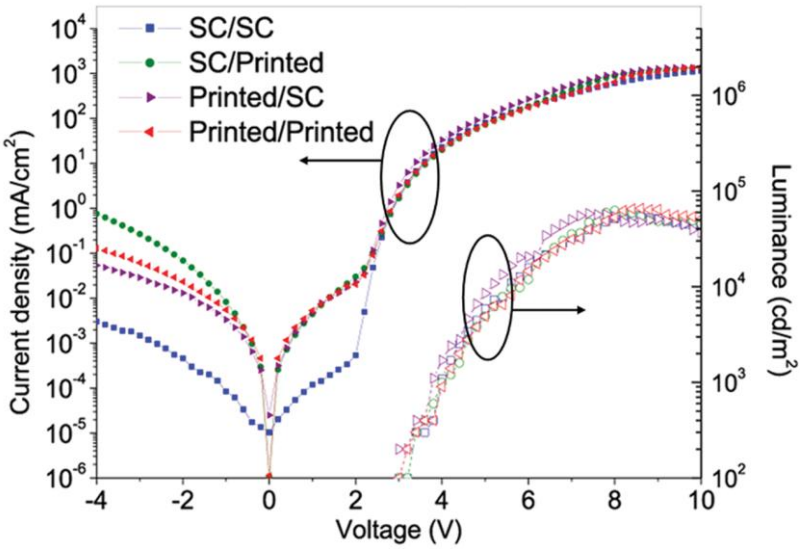


Figure 5.16 Performance of spin-coated and gravure printed PLEDs (PEDOT:PSS/LG1300). The formulations used for gravure printing are PEDOT:PSS (AI4083) mixed with IPA in vol% of 5:1 (AI4083:IPA) and 0.8 wt% of LG1300 in vol% of 10:3 (*p*-xylene:cyclohexane).

State-of-the-art polyfluorene copolymer green-emitting flexible PLEDs have been fabricated on transparent barrier layer substrates with high conductivity anodes.[38] These have achieved a maximum luminosity of 9.9 lm/W, a maximum efficiency of 10 cd/A and a maximum luminance of 20,000 cd/m^2. Our gravure printed devices achieve values of 8.8 lm/W, 5.4 cd/A and 66,000 cd/m^2 respectively. These are very comparable, even though we are using a poorer conductivity anode.

Figure 5.17 also shows light emission from a device where both PEDOT:PSS and LEP layers are gravure printed. The flexible PLED has highly uniform emission over all

drive voltages. The electroluminescence (EL) spectrum is also identical to the spin-coated control device as shown in Figure 5.18.

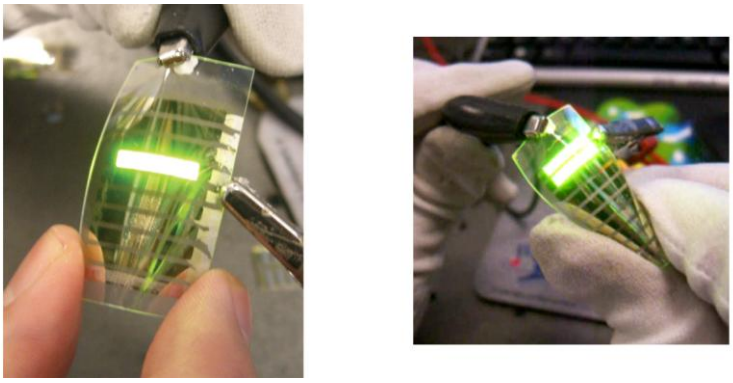


Figure 5.17 Photograph of light emission from a fully printed flexible PLED. The size of the light emission area of each pixel is 0.42 cm^2 (width: 1.4 cm, height: 0.3 cm). Images were captured by H. Yoon.

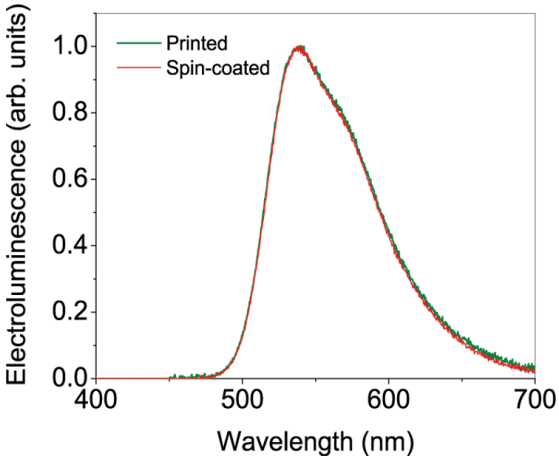


Figure 5.18 Electroluminescence (EL) of spin-coated and printed PLEDs.

PEDOT:PSS	**LG1300**	**L_{max}**	**~100 cd/m^2**		**~1,000 cd/m^2**		**η_{max}**	
		(cd/m^2)	**η_L**	**η_P**	**η_L**	**η_P**	**η_L**	**η_P**
Spin-coating	Spin-coating	55,700 (8.6 V)	5.4 (3 V)	5.7	4.7 (4 V)	3.7	9 (7 V)	5.7 (3 V)
Spin-coating	Printing	62,800 (8 V)	5.9 (3 V)	6.2	4.9 (4 V)	3.9	8.3 (6.6 V)	6.2 (3 V)
Printing	Spin-coating	58,000 (7.4 V)	6.1 (3 V)	6.4	4.5 (3.8 V)	3.7	9.3 (6.4 V)	6.4 (3 V)

Printing	Printing	65,900 (8.6 V)	5.16 (3 V)	5.4	4.4 (4 V)	3.5	8.8 (7 V)	5.4 (3 V)

Table 5.6 Performance parameters of spin-coated and gravure printed PLEDs. The first two columns indicate the deposition methods used for the PEDOT:PSS and LG1300 layers. L_{max} is the maximum luminance achieved. η_L and η_P are the efficiency (cd/A) and luminosity (lm/W) values respectively (reported at representative luminance of 100 and 1,000 cd/m^2; the absolute maxima are also reported). The voltage values (in brackets) indicate the bias voltages applied to the devices for each measurement.

5.7 Conclusion and Future Work

In summary, we demonstrated that gravure contact printing can be used to produce organic layers in high-performance PLEDs. Gravure printing provides a couple of advantages over other printing methods. One is that it is a contact printing method which is relatively convenient to optimize ink formulations for homogeneously printing layers. We showed that a simple modification of spin-coatable formulations can produce inks which are easily printable, achieve complete wetting, and dry to form homogeneous layers with a uniform thickness. Ink preparation in ink-jet printing, one of non-contact printing methods, has been a key limitation factor due to its gravitational force when formulation drops as well as conventional nozzle blockage problem. The other is that shape of a printing pattern follows a pattern of engraved area on a cliché in gravure printing. It allows handful alterations in size and shape of printing patterns. Recently, our group has shown that Ag ink can also be gravure printed to form the gate electrode in multilayer gravure printed polymer field-effect transistors.[41] Development of low work function metal inks or other electron injection materials should allow the PLED cathode to be printed. Suitable flexible barrier-layer substrates can also be used to provide appropriate encapsulation after printing.[42] All the components necessary for the high-speed, mass production of large-area organic electronic displays and lighting are finally coming together.

The chapter demonstrated the feasibility of gravure printing of high performance optoelectronic devices. However, it was limited to printing organic layers only in this chapter. To maximize the advantage of fast and cost effectiveness such a printing

method, the process should be sequentially repeated for all layers including both electrodes. High air reactivity of low work function metals such as Ca or LiF caused a difficulty in ink preparation using the metal particles. Recently, a new device structure has been suggested by Huang *et al*. that anode with a high work function metal can be converted to an electrode with low work function being acceptable as cathode by using of Cs_2CO_3.[43] Hence, a work function shifted metal as cathode can be positioned at the bottom of device and a typical anode with high work function is positioned as a top electrode. The structure is called 'inverted structure', and can be chosen for realization of fully printed PLEDs. The following studies will focus on developing of fully gravure printed PLEDs.

5.8 Reference

[1] G. Hadziioannou, G. G. Malliaras (Eds.), Semiconducting Polymers: Chemistry, Physics and Engineering, Wiley-VCH, **2007**.

[2] S. R. Forrest, *Nature* **2004**, *428*, 911.

[3] D. J. Gundlach, *Nature Materials* **2007**, *6*, 173.

[4] M. Berggren, D. Nilsson, N. D. Robinson, *Nature Materials* **2007**, *6*, 3.

[5] M. Tuomikoski, R. Suhonen, M. Valimakia, T. Maaninen, A. Maaninen, M. Sauer, P. Rogin, M. Mennig, S. Heusing, J. Puetz, M. A. Aegerter, *Manufacturing of polymer light-emitting device structures - art. no. 619204*, SPIE-INT SOC OPTICAL ENGINEERING, BELLINGHAM **2006**.

[6] N. J. Kaihovirta, D. Tobjork, T. Makela, R. Osterbacka, *Advanced Engineering Materials* **2008**, *10*, 640.

[7] D. Tobjork, H. Aarnio, T. Makela, R. Osterbacka, *Mater. Res. Soc. Symp. Proc*. **2008**, 1091-AA05-45.

[8] H. Nakjima, S. Morito, H. Nakajima, T. Takeda, M. Kadowaki, K. Kuba, S. Handa, D. Aoki, *Society Information Display Symposium Digest of Technical Papers*, **2005**, *36*, 1196.

[9] P. Kopola, M. Tuomikoski, R. Suhonen, A. Maaninen, *Thin Solid Films* **2009**, *517*, 5757.

[10] C. S. S. Sangeeth, M. Jaiswal, R. Menon, *Journal of Physics-Condensed Matter* **2009**, *21*.

[11] A. van Dijken, A. Perro, E. A. Meulenkamp, K. Brunner, *Organic Electronics* **2003**, *4*, 131.

[12] R. H. Friend, R. W. Gymer, A. B. Holmes, J. H. Burroughes, R. N. Marks, C. Taliani, D. D. C. Bradley, D. A. dos Santos, J. L. Bredas, M. Logdlund, W. R. Salaneck, *Nature* **1999**, *397*, 121.

[13] J. S. Huang, P. F. Miller, J. S. Wilson, A. J. de Mello, J. C. de Mello, D. D. C. Bradley, *Advanced Functional Materials* **2005**, *15*, 290.

[14] J. Z. Wang, Z. H. Zheng, H. W. Li, W. T. S. Huck, H. Sirringhaus, *Nature Materials* **2004**, *3*, 171.

[15] H. Sirringhaus, T. Kawase, R. H. Friend, T. Shimoda, M. Inbasekaran, W. Wu, E. P. Woo, *Science* **2000**, *290*, 2123.

[16] T. J. Wang, Y. Q. Qi, J. K. Xu, X. J. Hu, P. Chen, *Applied Surface Science* **2005**, *250*, 188.

[17] P. Levermore, *Ph.D. Thesis*, Imperial College London, **2008**.

[18] D. Pesach, A. Marmur, *Langmuir* **1987**, *3*, 519.

[19] T. Kajiya, E. Nishitani, T. Yamaue, M. Doi, *Physical Review e* **2006**, *73*.

[20] M. Kaneda, H. Ishizuka, Y. Sakai, J. Fukai, S. Yasutake, *Aiche Journal* **2007**, *53*, 1100.

[21] J. Park, J. Moon, *Langmuir* **2006**, *22*, 3506.

[22] H. Hu, R. G. Larson, *Langmuir* **2005**, *21*, 3972.

[23] G. Toussaint, H. Bodiguel, F. Doumenc, B. Guerrier, C. Allain, *International Journal of Heat and Mass Transfer* **2008**, *51*, 4228.

[24] R. D. Deegan, O. Bakajin, T. F. Dupont, G. Huber, S. R. Nagel, T. A. Witten, *Nature* **1997**, *389*, 827.

[25] J. A. Lim, W. H. Lee, H. S. Lee, J. H. Lee, Y. D. Park, K. Cho, *Advanced Functional Materials* **2008**, *18*, 229.

[26] Solvent data lists, Krüss DSA 100.

[27] G. W. Kauffman, P. C. Jurs, *Journal of Chemical Information and Computer Sciences* **2001**, *41*, 408.

[28] D. Poplavskyy, W. C. Su, F. So, *Journal of Applied Physics* **2005**, *98*.

[29] P. A. Levermore, R. Jin, X. H. Wang, L. C. Chen, D. D. C. Bradley, J. C. de Mello, *Journal of Materials Chemistry* **2008**, *18*, 4414.

[30] M. J. Harding, D. Poplavskyy, V. E. Choong, A. J. Campbell, F. So, *Organic Electronics* **2008**, *9*, 183.

[31] T. Okuzono, K. Ozawa, M. Doi, *Physical Review Letters* **2006**, *97*.

[32] T. E. Faber, *Fluid Dynamics for Physicists*, Cambridge University Press, Cambridge, **1997**.

[33] S. Chandrasekhar, *Hydrodynamic and Hydromagnetic Stability*, Oxford University Press, Oxford, **1961**.

[34] R. H. Friend, R. W. Gymer, A. B. Holmes, J. H. Burroughes, R. N. Marks, C. Taliani, D. D. C. Bradley, D. A. Dos Santos, J. L. Bredas, M. Logdlund, W. R. Salaneck, *Nature* **1999**, *397*, 121.

[35] N. Tessler, Y. Preezant, N. Rappaport, Y. Roichman, *Advanced Materials* **2009**, *21*, 2741.

[36] H. Sirringhaus, P. J. Brown, R. H. Friend, M. M. Nielsen, K. Bechgaard, B. M. W. Langeveld-Voss, A. J. H. Spiering, R. A. J. Janssen, E. W. Meijer, P. Herwig, D. M. de Leeuw, *Nature* **1999**, *401*, 685.

[37] A. Salleo, *Materials Today* **2007**, *10*, 38.

[38] C. L. Donley, J. Zaumseil, J. W. Andreasen, M. M. Nielsen, H. Sirringhaus, R. H. Friend, J. S. Kim, *Journal of the American Chemical Society* **2005**, *127*, 12890.

[39] H. N. Tsao, W. Pisula, Z. H. Liu, W. Osikowicz, W. R. Salaneck, K. Mullen, *Advanced Materials* **2008**, *20*, 2715.

[40] J. Kanicki, S. J. Lee, Y. Hong, C. C. Su, *Journal of the Society for Information Display* **2005**, *13*, 993.

[41] M. M. Voigt, A. Guite, D. Y. Chung, R. U. A. Khan, A. J. Campbell, D. D. C. Bradley, F. S. Meng, J. H. G. Steinke, S. Tierney, I. McCulloch, H. Penxten, L. Lutsen, O. Douheret, J. Manca, U. Brokmann, K. Sonnichsen, D. Hulsenberg, W. Bock, C. Barron, N. Blanckaert, S. Springer, J. Grupp, A. Mosley, *Advanced Functional Materials* **2010**, *20*, 239.

[42] J. Kanicki, S. J. Lee, Y. Hong, C. C. Su, *Journal of the Society for Information Display* **2005**, *13*, 993.

[43] J. S. Huang, G. Li, E. Wu, Q. F. Xu, Y. Yang, *Advanced Materials* **2006**, *18*, 114.

Chapter VI

Flexible Multilayer Hybrid Polymer Light-Emitting Diodes (PLEDs) with a Gravure Printed Cs_2CO_3 Layer

6.1 Introduction

Optoelectronic devices using solution processable conjugated polymers (CPs) have attracted enormous attention for their reduced costs and ease of fabrication.[1, 2] Since a first polymer light-emitting diodes (PLED) was reported in 1990,[3] various researches have been carried on organic electroluminescent devices in order to improve device performance of PLEDs. However, the performance has not yet reached to vacuum evaporated small molecule OLEDs or displays using inorganic materials so far owing to its inherent material weaknesses. Many groups have been working to improve performance of PLEDs via altering a structural design of a device as well as synthesis of new materials. The main challenges for PLEDs are to achieve long life time and high efficiency.[4] These issues can be resolved by designing novel device structures.

Inverted structure, where a low work function metal as a top electrode is replaced with a stable high work function metal, suggests a way to improve device stability.[5-8] Huang *et al*. reported that a ultra thin layer (~5 nm) of caesium carbonate (Cs_2CO_3) with appropriate annealing conditions can reduce work function of the adjacent metal up to

~3.1 eV.[9] Organic LEDs and photovoltaics (OPVs) using materials in inverted structures have been published elsewhere.[10,11] However, the device performance of PLEDs using inverted structure has not yet reached that of 'normal' structures because of its relatively high driving voltage (5-6 V at 100 cd/m^2) and low efficiency (< 1-2 lm/W) attributed to difficulties in balancing charge carrier injection rates.[6,11,12] As a result, the recombination zone is formed at the edge of the emissive layer inducing high leakage currents, in other words, a large population of injected carriers are quenched into the counter electrode without recombination.

Bilayer structures based on multiple emissive layers offer a solution to create a high efficiency device owing to accumulation of charge carriers within the band energy offset at the interface between two polymers.[13-15] The confined charges at the interface increase the electric field of the oppositely charged layer enhancing injection of charge carriers from the counter electrode.[16] Bilayer structure showed improvement in efficiency and increase in efficiency is consistent with charge confinement density at the interface.[17] Emission of light occurs at or near the interface, and away from the metal electrodes, hence reducing non-radiatively decayed excitons into the electrodes.[17] There have been many reports on vacuum-sublimed small molecules as they are easy to fabricate into multilayer structure but solution processable conjugated polymers have a limitation in material choice owing to chemical similarities between layers, dissolving underlying layers upon deposition of the top layer.

In this Chapter, I report a combination of two novel approaches of bilayer and inverted structure in an application of PLEDs providing both high efficiency and stability in air ambient environment. Structural design of PLEDs using poly (9,9-dioctylfluorene-*alt*-benzothiadiazole) (F8BT) and poly (9,9-dioctylfluorene-*alt*-*N*-(4-butylphenyl)-diphenylamine) (TFB) was sequentially developed by solution processing. Low processing temperatures less than 150° C in PLEDs is suitable for use with plastic substrates in future flexible displays. Also, all sequentially solution processed layers except vacuum evaporated electrodes are expected to benefit of both further reduction in costs and ease of fabrication. An ultra thin layer of Cs_2CO_3 was gravure printed. A

comparison of device performance between PLEDs with spin-coated and gravure printed Cs_2CO_3 layer shows that the device performance with the gravure printed Cs_2CO_3 layer is superior to the spin-coated device. Analysis of surface profile of Cs_2CO_3 layer using AFM is attempted to evaluate the result.

The chapter describes structural design of F8BT/TFB multilayer inverted PLEDs in Section 6.3, related issues about gravure printed Cs_2CO_3 layer in Section 6.4, device performance of F8BT/TFB bilayer inverted PLEDs with Cs_2CO_3 layer deposited by either spin-coating or gravure printing together with a surface homogeneity study of Cs_2CO_3 using AFM measurements in Section 6.5.

6.2 Experimental

Materials: LEP The PEDOT:PSS (Baytron Clevios^{TM} AI4083) dispersion was purchased from H. C. Starck GmbH. Caesium carbonate (Cs_2CO_3) powder, Triton X-100 surfactant and other organic solvents were obtained from Sigma-Aldrich. Substrates were either glass with pre-patterned ITO or polyethylene terephthalate (PET) coated in sputtered ITO (R_s = 40-60 Ω/sq) OC50 films from CPFilms Inc. The ITO on PET substrates were first etched by hydrochloric (HCl) acid diluted with DI water at a ratio of 2:1 (HCl:DI water) for 80 seconds to form ITO stripes, defined by acid resistant tape, with a width of 0.8 mm. Substrates were then cleaned with acetone and IPA in an ultrasonic bath and then washed with deionized (DI) water. Oxygen plasma treatment used an Emitech K 1050X plasma asher.

LED preparation and characterization: Printing of Cs_2CO_3 was with a Labratester I from Norbert Schläfli Maschinen. Cleaned substrates were printed with Cs_2CO_3 formulations (2-ethoxyethanol: Triton X-100 in vol% of 100:1) using a steel cliché with its engraved pattern of a 210 lines/cm with a cell depth of 20 μm at a speed of 35 m/min. After baking at 150 ˚C for 20 minutes in air, the LEP formulations were spin-coated for thickness of 80 nm/ 60 nm (F8BT/TFB). F8BT was prepared as 12 mg/ml in *p*-xylene and spin-coated at 1,500 rpm. After deposition of F8BT, samples were brought into a

nitrogen filled glove box (< 2 ppm H_2O, < 0.1 ppm O_2) to anneal at 150 °C for 1 hour. Then, 1 wt% of TFB was dissolved in cyclohexane and spin-coated at high speed (~4000 rpm) in air-ambient condition. Samples were brought again into the glove box to anneal at 120° C for 30 minutes. PEDOT:PSS solution was prepared as a following recipe: The dispersed PEDOT:PSS (AI4083) was mixed with IPA and Triton X-100 at a vol% of 1: 1: 0.01. PEDOT:PSS formulation was spin-coated at 4,000 rpm in air. Layer thicknesses were measured by a Tencor Instruments Alpha Step 200 surface profilometer.

After deposition of LG1300, all samples were transferred to a nitrogen atmosphere glove box (< 2 ppm H_2O, < 0.1 ppm O_2) to anneal at 120 °C for 1 hour. The anode of 100 nm Au was then thermally evaporated (vacuum pressure 4×10^{-6} mbar) with a shadow mask to define electrodes of 4.2 mm^2 (3 mm × 1.2 mm) area which reflects light emission. *J-V-L* measurements were performed using a Keithley 2410 Source-Measure Unit and a Topcon BM-9 luminance meter. Electroluminescence (EL) of PLEDs was characterized by using a Keithley 2400 SourceMeter and results were collected from an Ocean Optics USB 2000 charge-coupled device spectrophotometer.

Optical Measurement: Photoluminescence (PL) measurements were made using a Jobin-Yvon Fluoromax spectrofluorometer equipped with an integrating sphere. Absorbance measurements were made using an ATI Unicam UV-vis spectrophotometer.

Contact angle measurement and morphology: Contact angle measurements and wetting envelope calculations were performed with a Krüss DSA 100. Surface energy of substrate was measured by calculating contact angle of Sessile droplet when reference fluids (water, diiodomethane and ethylene glycol) were dropped on a substrate. For a case of surface energy of PEDOT:PSS surface, only diiodomethane and ethylene glycol were used as water is likely to swell the polymer but two fluids have negligible effects on the polymer surface after thermal treatment. Surface tension (SFT) of a fluid was calculated by measuring Pendant droplet method. Then, SFT of the fluid was analyzed to obtain its polar and dispersive components by measuring contact angle of the fluid on Teflon substrate using Sessile droplet method. Wetting envelope of a substrate was

drawn from all the measured surface energy values previously calculated. The tapping mode atomic force microscope (AFM) measurements were done using a Nano-R^{TM} AFM from Pacific Nanotechnology. A Zeiss Axioplan Microscope with a Nikon Coolpix P5100 digital camera was used to capture micron scale surface images.

6.3 Structural Design of F8BT/TFB Bilayer

The F8BT/TFB bilayer structure has been studied as a high efficient device structure with a sufficient margin of LUMO and HOMO levels between the two polymers formed at the interface.[18] An energy level diagram of F8BT/TFB bilayer in inverted structure is shown in Figure 6.1a. There are energy band offsets of 1.25 eV and 0.5-6 eV for electron and hole transports layers, respectively. Therefore, charge carriers accumulate at the interface until a sufficient bias voltage is applied. Number of recombination events at the interface for multilayer device is more condensed than average number of events for single layer device and charge carriers form an electron-hole-pair (EHP), an exciton, near the interface. Confined charged carriers redistribute internal electric field crossing the layers and attract the oppositely charged region, therefore, enhancing charge injection from the opposite electrode.

It is possible to design a F8BT/TFB bilayer via a sequential solution processing by modification of the TFB solvent. There are a number of ways that have been already proposed to build such a structure via a 'water-float' method [19], cross-linking of the bottom layer[20,21], using a buffer layer between two layers[22] and stamping process[23]. Using of orthogonal solvents for the top organic layer, altering polarity or solubility of the solvents can also deal with the problem.[24] Recently, it was found that solubility of F8BT is lower than TFB even though they are both polyflourene derivative materials and both can be dissolved in common hydrocarbon solvents. F8BT is not dissolved in cyclohexane while high molecular weight TFB is fully dissolved in the solvent, hence it enables to build a multiple layer by sequential solution processing. In addition, an ink formulation for poly(3,4-ethylenedioxythiophene): poly (styrenesulfonate) (PEDOT:PSS) mixing with a wetting agent and a surfactant was prepared for

reduced surface tension and increased adhesion becoming more favourable to the TFB surface.[25] The surface tension of PEDOT:PSS formulation is reduced to 21.63 mN/m wetting completely onto the TFB having a surface energy of 39.25 mN/m (See Figure 6.2). Contact angle of sessile droplets of both TFB and PEDOT:PSS formulation is shown in Figure 6.1b-c and it proves wetting on the surface (PEDOT:PSS on TFB) and free of dissolution of the surface (TFB on F8BT).

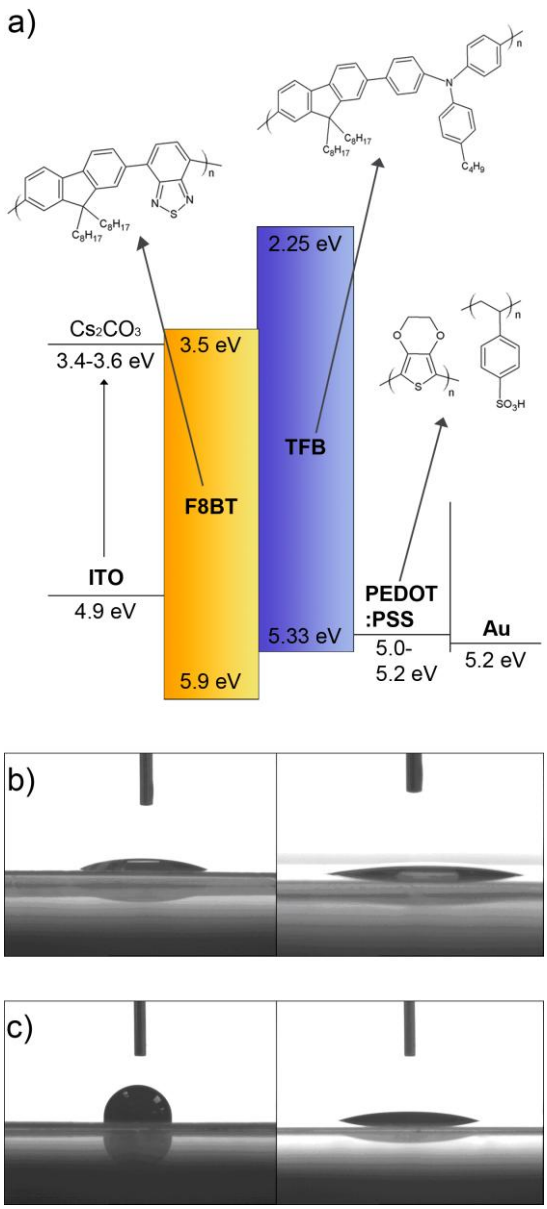


Figure 6.1 a) Energy level diagram. b) Sessile droplets of TFB on F8BT, TFB in *p*-xylene (left, 17.7°) and modified (right, 2°). c) Sessile droplets of PEDOT:PSS on TFB, before (left, 89.4°) and after (right, 8.8°) modification. A nozzle diameter is 1.83 mm.

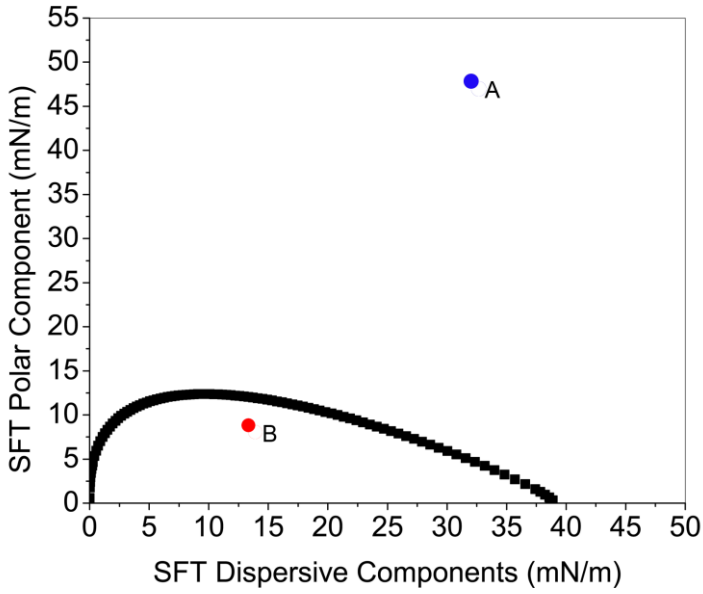


Figure 6.2 Wetting envelope of TFB surface calculated by Fowkes method. Surface tension of PEDOT:PSS formulations (A: Pure AI4083, B: Modified AI4083) and surface energy of TFB are calculated using pendant and sessile droplets, respectively.

Absorption and photoluminescence (PL) spectra of F8BT and TFB together with bilayer and blend structures using the two materials are shown in Figure 6.3-6.4. Figure 6.3 indicates that the modified TFB formulation did not dissolve the underlying F8BT layer during its deposition as a peak of F8BT around 460 nm remained as same intensity after TFB deposition while the intensity of the peak is reduced substantially by TFB formulation in *p*-xylene. Compared to a ratio between peaks of F8BT and TFB in blended layer with a ratio of 1:1 v/v (F8BT:TFB) having a thickness of 80-100 nm, it can be said that most of the F8BT layer was dissolved by the common solvent. Also, thickness measurement by alpha-step confirmed that bilayer structure of F8BT/TFB using the modified TFB formulation was successively built whereas bilayer using TFB dissolved in *p*-xylene showed a thickness reduction after the deposition of TFB layer.

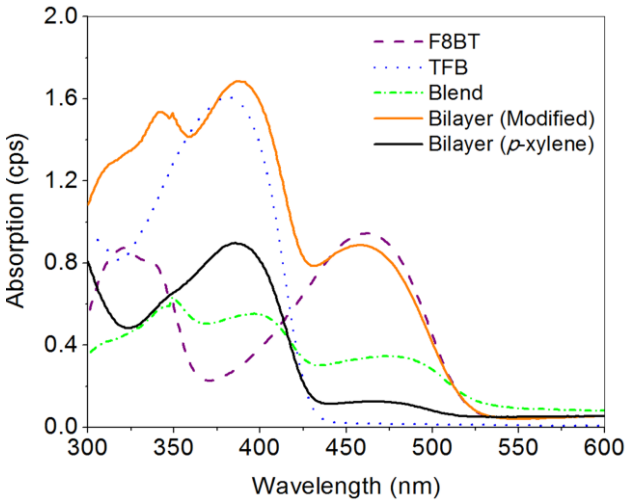


Figure 6.3 Absorption spectra of F8BT and TFB in various device structures

PL spectra of thin films shown in Figure 6.4 suggest that energy transfer between laterally phase separated microscale patterns of F8BT and TFB rich regions in F8BT:TFB blended layer in *p*-xylene produces a blue shifted light with a peak at 540 nm. A case of bilayer of F8BT/TFB, where the energy transfer is limited to the interfacial region of the interface, shows enhanced emission from the F8BT side attributed to emission from the TFB film (455nm) is fully absorbed by the F8BT film. Bilayer in dissolved case resembles the spectrum of the blended structure.

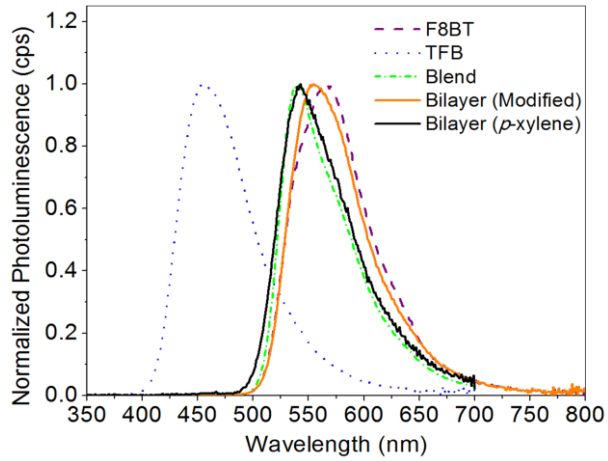


Figure 6.4 Photoluminescence (PL) of F8BT and TFB in various device structures

For simplicity, four different variations in device structure were fabricated: Device A is with a glass substrate and spin-coated Cs_2CO_3; Device B is with a PET substrate and

spin-coated Cs_2CO_3; Device C is with a PET substrate and gravure contact printed Cs_2CO_3; Device A* is the same as A but with the TFB layer spin-coated from toluene instead of cyclohexane.

6.4 Gravure Printing of Cs_2CO_3 Layer

Huang *et al.* reported that deposition of a ultra thin layer of Cs_2CO_3 layer onto a high work function metal such as Ag or ITO can reduce the high work function of the metal by up to ~3.1-3.4 eV.[26] The condition for the conversion is that the thickness of Cs_2CO_3 layer has to be around 5 nm within the tunnelling distance of charged electrons and the layer needs to be thermally treated at 150-170° C in air at which the temperature exerts changes in work function. The advantage of the layer is that it becomes possible to build a device with an air-stable top electrode instead of Ca or LiF, which are highly oxygen reactive, and are called 'inverted structures'. This can, therefore, increase stability and lifetime of a device. Several groups already reported devices with a Cs_2CO_3 layer included[11,27] but solution processing of such a thin layer is problematic as the homogeneity of the layer is a great importance in PLEDs for uniform charge carrier injection and light emission. F8BT/TFB multilayer structures relieve the unbalanced charge carrier density when using Cs_2CO_3 layer. Injected charge carriers are first accumulated at the F8BT/TFB interface instead of travelling throughout the organic layers and passing into the counter electrode. Subsequently light emission is generated once a sufficient bias voltage is applied.

In addition, a Cs_2CO_3 layer can be deposited by different methods. Gravure printing, one of roll-to-roll (R2R) processing methods and it has been typically implemented with printing magazines and newspapers, attracts lots of interests with its potential of fast and cost effective processing for fabrication of optoelectronic devices.[28,29] A semiconducting ink formulation is swept by a doctor blade which spreads the inks onto engraved patterns on a cliché, then it is transferred onto a flexible substrate attached to the cylindrical rubber roll as the cylindrical rubber roll travels and passes by the cliché.

Homogeneity of the printed thin films is determined by balanced fluidic movements inside printed formulations while it dries.[25]

In general, an evaporative convection flow, which moves toward pinning line to compensate energy losses from solvent evaporation, carries polymer chains while it flows and a polymer ring is formed at the pinning line after drying as called the 'coffee stain' effect.[30] In Chapter 5, it was found that an inward fluidic movement, such as 'Marnagoni flow'[31,32] can balance fluidic movements and remain a homogeneous film surface after completed solvent evaporation in a gravure printing process.[25] Cs_2CO_3 powders were dissolved in 2-ethoxyetanol and printing the formulation results in inhomogeneously printed Cs_2CO_3 layer which forms thicker layers at inner parts of the device due to its high boiling point (B_p = 135° C) and lack of convection flow. Hence, light emission was non-uniformly generated, showing brighter emission at outer pixel with thinner Cs_2CO_3 layers. Hu *et al.* suggested that a small amount of surfactant can disrupt solvent fluidic movements.[33] A small amount of Triton X-100 (0.1 vol%) was mixed with the 2-ethoxyetanol Cs_2CO_3 formulation in order to balance fluidic movement as disrupting the inward flow due to high boiling point of 2-ethoxyetanol and to increase adhesion onto the oxygen plasma treated ITO surface.

Interestingly, charge injection from the Cs_2CO_3 treated ITO is influenced by oxygen plasma etching. Oxygen plasma treatment increases polar components of the ITO surface as oxygen doping level increases, hence its total surface energy is increased.[34] The morphology profile of the printed Cs_2CO_3 layer was experimentally probed as best when the ITO surface is oxygen plasma etched at 50 W for 1 minute from evidences of an amount of injected electrons and radiatively decayed excitons (Figure 6.5).

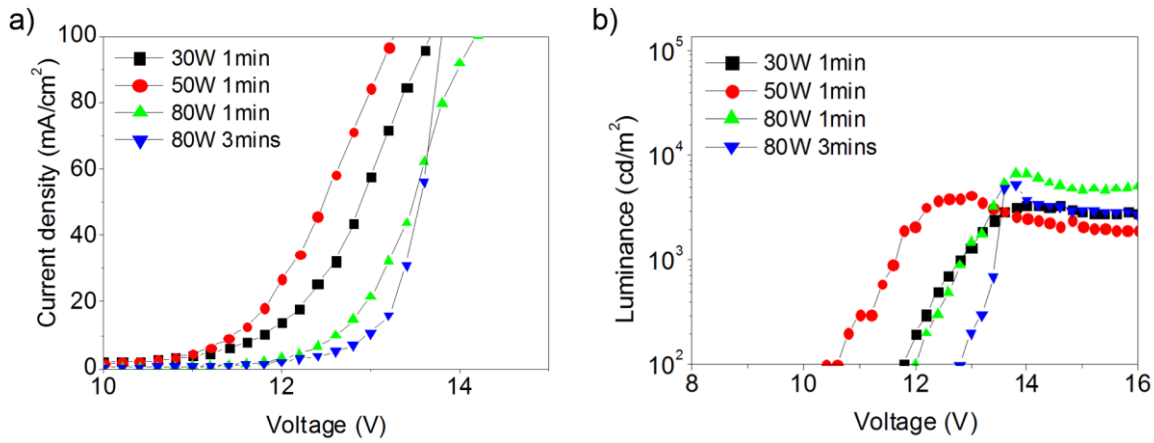


Figure 6.5 Variation of the (a) J-V and (b) V-L characteristics of the inverted PLEDs (Structure C) on ITO with plasma power dissipated.

The thickness of Cs_2CO_3 determines the amount of electron injection as tunnelling range of a charged carrier is limited to ~5-10 nm and thicker layers can hamper efficient charge injection so that the population of the injected electrons can be reduced. Figure 6.6 describes *J-V-L* characteristics of inverted PLEDs with different thicknesses of Cs_2CO_3. As expected, electron injection behaviour was varied with a thickness of Cs_2CO_3 layer, which was controlled by the concentration of Cs_2CO_3 powder dissolved. The concentration was varied between 0.1 wt% and 0.5 wt% in 2-ethoxyethanol. Higher concentration case shows electron injection at lower voltage and the minimum turn-on voltage was 10.4 V for 100 cd/m^2 among the five samples was obtained from the device with the 0.5 wt% concentration. Also, amount of maximum light output was reduced at thicker layers as described in Figure 6.6(b). The highest luminance of 9,900 cd/m^2 was observed for the case of 0.2 wt% while only one-third of the maximum luminance was detected in the device with a 0.5 wt% concentration. The thickness of the Cs_2CO_3 layer printed with the 0.1 wt% concentration is too thin so that less than 100 cd/m^2 luminance was recorded and a control device with no Cs_2CO_3 layer showed no evidence of electron injection attributed to a high potential barrier between the Fermi level of ITO (4.8 eV) and the LUMO level of F8BT (3.5 eV). All formulations were gravure printed using same patterned cliché and the result demonstrates a possibility of an accurate control in thickness of a very thin layer (less than 10 nm) using the printing method via concentration variance.

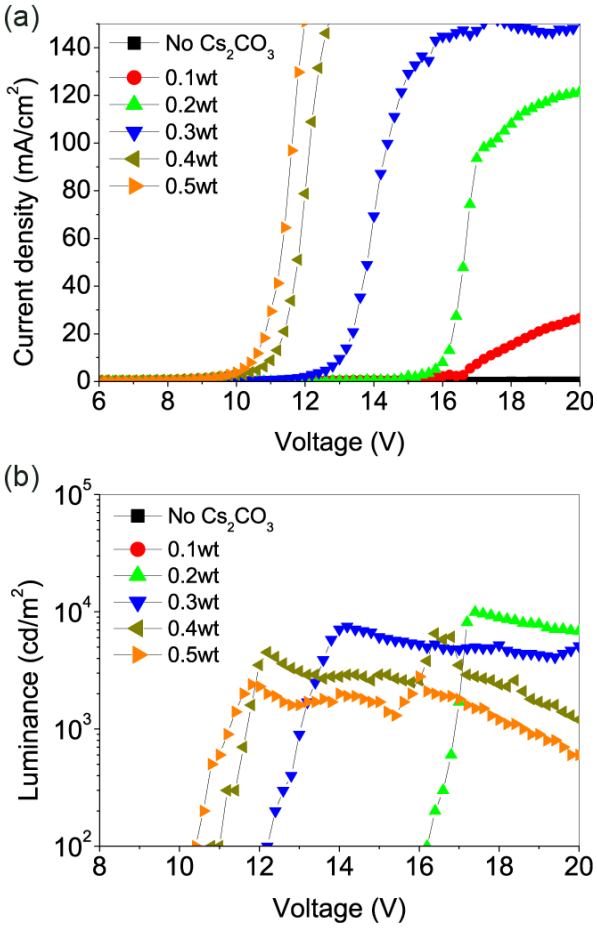


Figure 6.6 Variation of the (a) J-V and (b) L-V characteristics of the inverted PLEDs (Structure C) with gravure printing formulation Cs_2CO_3 concentration

6.5 Device Characteristics of Inverted PLEDs

J-V-L characteristics of F8BT/TFB (80 nm/60 nm) multilayer inverted PLEDs with a Cs_2CO_3 layer spin-coated on either glass or PET substrate are shown in Figure 6.7a and 6.7c, respectively. Both cases show a slow increase of current density with increasing bias voltage. This is attributed to accumulated charge carriers at the F8BT/TFB interface, the current density level at 100 cd/m^2 is low around 8 mA/cm^2 and 6 mA/cm^2 for spin-coated Cs_2CO_3 layers on glass and PET substrates respectively. Device efficiency of the devices, described in Figure 6.8a and 6.8c, implies that the low current density levels owing to the accumulated charged carriers contribute to high efficiency devices. Performance parameters of inverted PLEDs are listed in Table 6.1.

Interestingly, PLEDs with the spin-coated Cs_2CO_3 on the glass substrate recorded efficiency of 3.11 cd/A and 0.94 lm/W, which is lower than 5.8 cd/A and 1.9 lm/W from the spin-coated on the PET flexible substrate. The deviation in efficiency values can be explained by the ITO morphology. In general, the surface morphology of sputtered ITO on PET substrate is more amorphous than ITO on glass due to low heat sustainability of PET.[35] The crystallinity of ITO on glass and PET substrates showed different surface characteristics of a thin Cs_2CO_3 layer. Solution processed TiO_2 layers pick up the underlying structure of the ITO,[36] and it is expected that the same effect for the Cs_2CO_3 layers deposited here. We believe that this is responsible for the improvement in device performance, the decrease in Cs_2CO_3 surface roughness resulting in a more even field distribution and more uniform charge injection. A more amorphous layer may allow multiple, uniform electron injection pathways from the ITO into Cs_2CO_3 and from Cs_2CO_3 into the F8BT. Crystallinity may make injection more difficult if the crystal structure orientation is unfavourable at the ITO/Cs_2CO_3 boundary.

We investigated the physical structure of the spin-coated Cs_2CO_3 on the different substrates. Figure 6.9 shows AFM images of Cs_2CO_3 on (a) ITO on glass and (b) ITO on PET. The Cs_2CO_3 on ITO on glass shows a network of large platelets with typical sizes of order 0.5 µm. The RMS surface roughness is 2.68 nm. The Cs_2CO_3 layer coated onto ITO on PET substrate instead shows a more amorphous, disordered structure with smaller features of order 0.1 µm. The RMS surface roughness of Cs_2CO_3on PET substrate indicated 1.56 nm, which is much lower than on Cs_2CO_3on glass substrate.

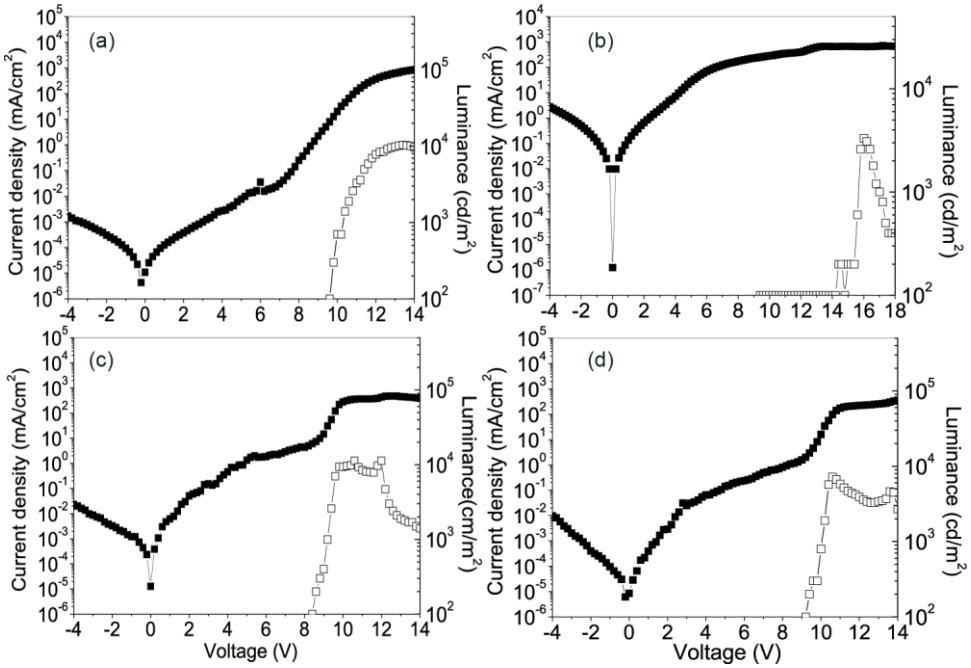


Figure 6.7 J-V-L characteristics of the different substrate/ITO/Cs_2CO_3/F8BT/TFB/PEDOT:PSS/Au inverted PLEDs. (a) is for Device A (spin-coated Cs_2CO_3, glass substrate). (b) is for Device A* (as A but with TFB spin-coated from toluene) [note the change in scale]. (c) is for Device B (spin-coated Cs_2CO_3, PET substrate). (d) is for Device C (gravure printed Cs_2CO_3, PET substrate).

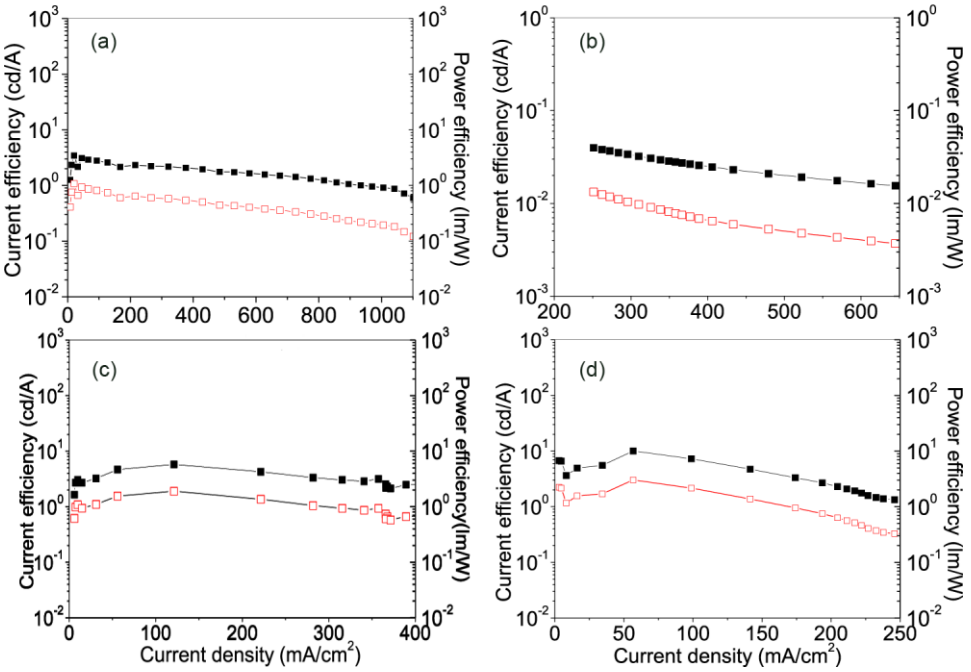


Figure 6.8 Device efficiency of the different substrate/ITO/Cs_2CO_3/F8BT/TFB/PEDOT:PSS/Au inverted PLEDs. (a) is for Device A (spin-coated Cs_2CO_3, glass substrate). (b) is for Device A* (as A but with TFB spin-coated from toluene) [note the change in scale]. (c) is for Device B (spin-coated Cs_2CO_3, PET substrate). (d) is for Device C (gravure printed Cs_2CO_3, PET substrate).

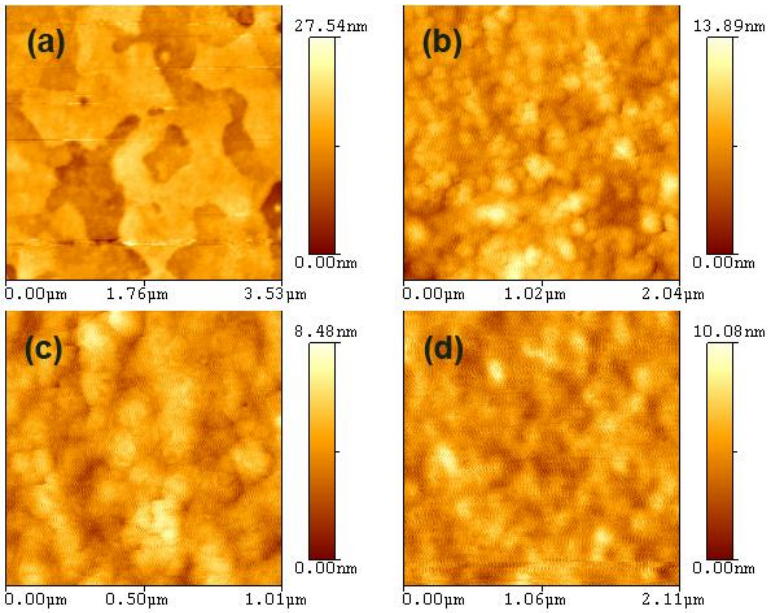


Figure 6.9 Tapping mode AFM images of Cs_2CO_3 (a) spin-coated on to ITO on glass (for Device A), (b) spin-coated on to ITO on PET (for Device B) and (d) gravure printed on to ITO on PET (for Device C). (c) is a higher resolution image of an area of the film in (b).

Also, a Cs_2CO_3 layer was gravure printed on PET flexible substrate. *J-V-L* characteristic of the gravure printed Cs_2CO_3 layer is shown in Figure 6.7d. Surprisingly, the best efficiency of 10.06 cd/A and 3.04 lm/W (Table 6.1) was obtained from the printed Cs_2CO_3 on PET substrate. It is again attributed to the accumulated charge carriers at the interface, which reduces current density, with a current density of only 2 mA/cm^2 recorded from the device. The efficiency is doubled the spin-coated Cs_2CO_3 layer on the same substrate (Figure 6.8d). We suggest that the improvement originates from the reduced voids between Cs_2CO_3 particles inside the layer owing to a pressing force exerted between the cylindrical roll and the patterned cliché when the Cs_2CO_3 ink formulation transfers onto the PET substrate. The pressure may affect the order of Cs_2CO_3 particles and induce improved charge injection. The pressure can be easily controlled by machinery setting and further investigation on printing Cs_2CO_3 is necessary. AFM image of the printed Cs_2CO_3 layer in Figure 6.9d indicates smoothened surface characteristic because of the printing pressure and balanced fluidic movements from the use of the surfactant. The RMS value of gravure printed Cs_2CO_3 layer is further decreased to 1.14 nm.

Device structure	Cs_2CO_3 layer	Substrate	L_{max} (cd/m^2)	~100 cd/m^2		~1000 cd/m^2		η_{max}		CIE (x, y)
				η_L	η_P	η_L	η_P	η_L	η_P	
A	Spin-coated	Glass	10,400 (13.4 V)	1.26 (9.6 V)	0.41	2.6 (10.3 V)	0.8	3.11 (10.4 V)	0.94	(0.47, 0.51)
A* (TFB toluene)	Spin-coated	Glass	3,300 (16 V)	0.04 (9.4 V)	0.013	0.2 (15.6 V)	0.04	0.5 (16 V)	0.99	(0.47, 0.61)
B	Spin-coated	PET	11,300 (10.6 V)	1.65 (8.4 V)	0.62	3.2 (9.2 V)	1.1	5.8 (9.6 V)	1.9	(0.47, 0.61)
C	Gravure printed	PET	7,200 (10.6 V)	6.72 (9.4 V)	2.25	5 (10 V)	1.6	10.06 (10.4 V)	3.04	(0.46, 0.52)

Table 6.1 Performance parameters of Inverted PLEDs. η_L and η_P correspond to current efficiency (cd/A) and power efficiency (lm/W) of devices respectively. Value in brackets indicates drive bias voltage applied to the device.

Also, F8BT/TFB multilayer inverted PLEDs were compared to a case when TFB was in *p*-xylene which dissolves the underlying F8BT layer. A large amount of currents is passed to the counter electrode without recombination and light emission first appears at 9.4 V while its current density level already reaches about 100 mA/cm^2 at the bias voltage as described in Figure 6.7b. This high leakage current contributes to low efficiency of the device. Device efficiency described in Figure 6.8b indicates that both current and power efficiency are less than 0.5 cd/A and 0.1 lm/W and light emission of 100 cd/m^2 was first detected at the current density of 250 mA/cm^2. Also, maximum light emission recorded was 3,300 cd/m^2 at 16 V. The poor performance in the dissolved case can be explained by considering the solubility of the two polymers (F8BT and TFB). Dissolving the underlying F8BT layer while deposition of TFB layer mixes the two polymers then forms a heterogeneous blended layer. Phase separation in blended structure is important for charge carrier transport in the layer and TFB rich zone can be placed at the bottom of the device after deposition of the blended layer as solubility of the TFB is much higher than the F8BT.[37] This is ideal for normal structure PLEDs where anode is placed at the bottom and cathode at the top. The TFB rich zone is formed at the top of the anode and can operate as a good hole transporting layer. However, it is not desirable in inverted structure as a bottom positioned TFB

layer can hamper efficient electron injection and a large amount of holes injected from the top electrode can be quenched across the layer. CIE ordinate values of all cases are similar as listed in Table 6.1.

6.6 Conclusion and Future Work

In conclusion, this chapter demonstrated high efficient F8BT/TFB multilayer inverted PLEDs using Cs_2CO_3 layer deposited either by gravure printing or by spin-coating. Ink modification of both TFB and PEDOT:PSS formulations provided free of swelling of the underlying F8BT layer and lowering surface tension of aqueous PEDOT:PSS solution to make favourable to the non-polar TFB surface. High efficiency of 10.06 cd/A and 3.04 lm/W was obtained from the Cs_2CO_3 layer gravure printed PLEDs because the improvements in surface morphology of the Cs_2CO_3 layer and Cs_2CO_3 particle ordering are in favour of electron injection compared to the spin-coated Cs_2CO_3 layer on either glass or PET. F8BT/TFB multilayer structure is useful in balancing injection rates of charged carriers due to accumulation of both types of carriers at the interface having a large energy offset. Low current density of F8BT/TFB multilayer PLEDs compared to the blended device using the same materials indicates that charge carriers are accumulated at the interface between the two polymeric layers. We showed the feasibility of roll-to-roll (R2R) type printing can be used to deposit a highly uniform ultra thin layer. Together with development of solution processable conductive inks for printing electrodes, all gravure printable optoelectronic devices will be in near future.

It is now confirmed that an ultra thin Cs_2CO_3 layer (~5-10 nm) can be gravure contact printed. As a next step toward fully printing F8BT/TFB multilayer PLEDs, it is recommended to start printing F8BT and TFB polyflourene based light-emitting polymers. Their thicknesses in multilayer structure have not yet reported for highly efficient devices. A thickness study of the two polymers is explained in Chapter 7. Our structural design of F8BT/TFB PLEDs has proven that it can be sequentially gravure printed after modification of TFB and PEDOT:PSS formulations by their solubility difference and investigation through a wetting envelope respectively. A study of

solubility parameters using Hilderbrand and Hansen models for defining solubility ranges of the two polymers should help with a scientific proof of building the bilayer structure. Solubility of a material is varied by its molecular weight, hence molecular weight of polymers could also contribute to modify for appropriate values. A study of effects of molecular weights in solubility and investigation of solubility parameters of various polymers could be interesting research topics for realization of fully solution processable and printable optoelectronic devices.

6.7 Reference

[1] S. R. Forrest, *Nature* **2004**, *428*, 911.

[2] G. P. Collins, *Sci. Am.* **2004**, *291*, 74.

[3] J. H. Burroughes, D. D. C. Bradley, A. R. Brown, R. N. Marks, K. Mackay, R. H. Friend, P. L. Burns, A. B. Holmes, *Nature* **1990**, *347*, 539.

[4] J. R. Sheats, H. Antoniadis, M. Hueschen, W. Leonard, J. Miller, R. Moon, D. Roitman, A. Stocking, *Science* **1996**, *273*, 884.

[5] H. J. Bolink, E. Coronado, D. Repetto, M. Sessolo, *Appl. Phys. Lett.* **2007**, *91*, 223501.

[6] D. Kabra, M. H. Song, B. Wenger, R. H. Friend, H. J. Snaith, *Adv. Mater.* **2008**, *20*, 3447.

[7] H. J. Bolink, E. Coronado, D. Repetto, M. Sessolo, E. M. Barea, J. Bisquert, G. Garcia-Belmonte, J. Prochazka, L. Kavan, *Adv. Funct. Mater.* **2008**, *18*, 145.

[8] N. Tokmoldin, N. Griffiths, D.D.C. Bradley, S.A. Haque, *Adv. Mater.* **2009**, *21*, 3475.

[9] J. S. Huang, G. Li, E. Wu, Q. F. Xu, Y. Yang, *Adv. Mater.* **2006**, *18*, 114.

[10] Z. Xu, L. M. Chen, G. W. Yang, C. H. Huang, J. H. Hou, Y. Wu, G. Li, C. S. Hsu, Y. Yang, *Adv. Funct. Mater.* **2009**, *19*, 1227.

[11] H. J. Bolink, E. Coronado, J. Orozco, M. Sessolo, *Adv. Mater.* **2009**, *21*, 79.

[12] H. J. Bolink, H. Brine, E. Coronado, M. Sessolo, *Adv. Mater.* **2010**, *22*, 2198.

[13] C. W. Tang, S. A. Vanslyke, *Appl. Phys. Lett.* **1987**, *51*, 913.

[14] A. R. Brown, D. D. C. Bradley, J. H. Burroughes, R. H. Friend, N. C. Greenham, P. L. Burn, A. B. Holmes, A. Kraft, *Appl. Phys. Lett.* **1992**, *61*, 2793.

[15] B. K. Crone, P. S. Davids, I. H. Campbell, D. L. Smith, *J. Appl. Phys.* **2000**, *87*, 1974.

[16] D. V. Khramtchenkov, V. I. Arkhipov, H. Bassler, *J. Appl. Phys.* **1997**, *81*, 6954.

[17] N. C. Greenham, S. C. Moratti, D. D. C. Bradley, R. H. Friend, A. B. Holmes, *Nature* **1993**, *365*, 628.

[18] A. C. Morteani, A. S. Dhoot, J. S. Kim, C. Silva, N. C. Greenham, C. Murphy, E. Moons, S. Cina, J. H. Burroughes, R. H. Friend, *Adv. Mater.* **2003**, *15*, 1708.

[19] C. M. Ramsdale, J. A. Barker, A. C. Arias, J. D. MacKenzie, R. H. Friend, N. C. Greenham, *J. Appl. Phys.* **2002**, *92*, 4266.

[20] L. D. Bozano, K. R. Carter, V. Y. Lee, R. D. Miller, R. DiPietro, J. C. Scott, *J. Appl. Phys.* **2003**, *94*, 3061.

[21] S. H. Khong, S. Sivaramakrishnan, R. Q. Png, L. Y. Wong, P. J. Chia, L. L. Chua, P. K. H. Ho, *Adv. Funct. Mater.* **2007**, *17*, 2490.

[22] S. R. Tseng, S. C. Lin, H. F. Meng, H. H. Liao, C. H. Yeh, H. C. Lai, S. F. Horng, C. S. Hsu, *Appl. Phys. Lett.* **2006**, *88*, 163501.

[23] L. C. Chen, P. Degenaar, D. D. C. Bradley, *Adv. Mater.* **2008**, *20*, 1679.

[24] K. Meerholz, *Nature* **2005**, *437*, 327.

[25] D.-Y. Chung, J.S. Huang, D.D.C. Bradley, and A.J. Campbell, *Org. Electron*. **2010**, *11*, 1088.

[26] J. S. Huang, G. Li, E. Wu, Q. F. Xu, and Y. Yang, *Adv. Mater.* **2006**, *18*, 114.

[27] H.–H. Liao, L.–M. Chen, Z. Xu, G. Li, and Y. Yang, *Appl. Phys. Lett*. **2008**, *92*, 173303.

[28] M. Berggren, D. Nilsson, and N. D. Robinson, *Nature* **2007**, *6*, 3.

[29] H. Sirringhaus, *Nature* **2009**, *457*, 667.

[30] R. D. Deegan, O. Bekajin, T. F. Dupont, G. Huber, S. R. Nagel, and T. A. Witten, *Nature* **1997**, *389*, 827.

[31] D. Pesach, and A. Marmur, *Langmuir* **1987**, *3*, 519.

[32] J. A. Lim, W. H. Lee, J. H. Lee, Y. D. Park, and K. Cho, *Adv. Funct. Mater*. **2008**, *18*, 229.

[33] H. Hu, and R. G. Larson, *Langmuir* **2005**, *21*, 3972.

[34] J. Z. Wang, Z. H. Zheng, H. W. Li, W. T. S.Huck, and H. Sirringhaus, *Nature Mater*. **2004**, *3*, 171.

[35] X. Yin, W. Tang, X. Weng, and L. Deng, *J. Phys. D: Appl. Phys*. **2009**, *42*, 225304.

[36] H. J. Bolink, E. Coronado, D. Repetto, M. Sessolo, E. M. Barea, J. Bisquert, G. Garcia-Belmonte, J. Prochazka, and L. Kavan, *Adv. Funct. Mater*. **2008**, *18*, 145.

[37] J.-S. Kim, P. K. H. Ho, C. E. Murphy, and R. H. Friend, *Macromolecules* **2004**, *37*, 2861.

Chapter VII

Air-Stable, Flexible F8BT/TFB PLEDs having High Efficiency

7.1 Introduction

A field of polymer light-emitting diodes (PLEDs) using conjugated polymers (CPs) is growing fast with its processing advantage of solution processability using semiconducting solutions and reduced fabrication costs.[1] Its device performance reported so far is significantly lower than LED using vacuum sublimed small molecules for inherit weaknesses of the materials. Balancing of charge carrier mobility of emissive materials is important to achieve a high performance device as an electron-hole-pair can be formed at the centre of the device in case of single layer PLEDs so that quenching of excitons at the electrodes can be minimized. It is normally true that materials have a biased characteristic with either n-type or p-type properties dependent on the charge carrier mobility of the materials. High performance PLEDs can be obtained using an emissive layer with balanced charge carrier mobility.[2] Using multi-layer emissive layers can also help by balancing both types of carriers by creating energy barriers at the internal interface between the OSC layers. One type of charge carrier, either hole or electron, or both types of charge carriers can be accumulated at the interface which modifies the internal field distribution within the device. Charge carrier movements such as tunnelling, thermionic injection of carriers across internal heterojunction and energy transfer process at the interface need to be investigated.

A bilayer PLED was first suggested by Greenham *et al*. from Cavendish Laboratory in Cambridge University in 1993[3] after a first bilayer SM-OLED reported by Tang *et al*. in 1987.[4] The researchers from Cavendish Laboratory reported a bilayer of poly (*p*-phenylenevinylene) (PPV) and a red luminescent polymer, called polymer 3. The first bilayer PLED showed a uniform red electroluminescence (EL) which is identical to the photoluminescence (PL) of polymer 3. A decrease in the field requirement for the device operation compared to the single layer device was observed owing to significant charge confinement at the interface between PPV and polymer 3 layers. Inverted structure PLEDs comprising of bilayer polymers have been reported by several groups.[5-8] In 2007, Haque *et al*. from Imperial College reported a large area nanostructured electrode using TiO_2 nanoparticle on ITO in inverted bilayer PLEDs.[7] Later, the same group reported inverted PLEDs using Zirconium dioxide (ZrO_2) as an electron transporting layer instead of TiO_2.[9] They suggested that ZrO_2 device showed a higher device performance than TiO_2 device in a F8BT single layer structure. The possible reasons can be a superior hole blocking property of ZrO_2 layer due to i) larger energy band offsets between the HOMO level of F8BT (5.9 eV) and ZrO_2 (8.7 eV) or TiO_2 (7 eV) and ii) poor electron transport in TiO_2. The device with ZrO_2 showed 2.71 cd/A at 22,800 cd/m^2 of brightness, which is higher than TiO_2 device showing 0.03 cd/A at 787 cd/m^2 of brightness.

Bolink *et al*. reported in 2008 that performance of hybrid organic-inorganic light-emitting diodes (HyLEDs) using inverted structure with TiO_2 as an electron transporter and a single light-emitting polymer layer was further improved by using a caesium carbonate (Cs_2CO_3) layer.[6] The maximum efficiency recorded was 8 cd/A with a maximum brightness of 12,000 cd/m^2.

The thickness of emissive layer in a single layer structure has been experimentally optimized to be 70-80 nm.[1] A thin emissive layer increases quenching rates of quasi-particles and a thick layer is required a higher drive bias to turn on. Very recently, Kabra *et al*. reported that a thick single emissive F8BT layer can dramatically improve device performance of PLEDs reaching 23 cd/A from 1.2 μm thick F8BT film.[10]

However, the device needed a high drive bias of 10 V for 1,000 cd/m^2. A thickness variation in multi-layered PLEDs using F8BT and TFB polymers has not yet reported. Varying the layer thickness will change injected current density and internal fields. Thicker layer increases a drive bias required for tunnelling so that a high concentration of charged carriers can be resided at the interface of multilayer structure PLEDs with thicker layers. Both positively and negatively charged regions at the interface will strongly attract the opposite type of carriers so that charge carrier recombination can actively occur throughout tunnelling at the interface.

This Chapter reports a combination of two novel approaches of bilayer and inverted structures in an application of PLEDs providing both high efficiency and stability in an air ambient environment. Structural design of our PLEDs using poly (9,9-dioctylfluorene-*alt*-benzothiadiazole) (F8BT) and poly (9,9-dioctylfluorene-*alt*-*N*-(4-butylphenyl)-diphenylamine) (TFB) focused on either low turn on voltage device (2.6 V at 100 cd/m) or a super efficient device (34.86 cd/A and 22.8 lm/W). This efficiency is the highest efficiency to the best of our knowledge using fluorescence polymer materials. A thickness variation of the two polymer layers with a large energy offset adjacent to the interface can control a net current density as well as turn on voltage. We believe substantially reduced current density at thicker layers with a high rate of recombination events improves device efficiency. We clarify the condition for each case of either fast turn on or high efficiency PLEDs and explain charge carrier movements and recombination zone shifts in that structure. Emission of F8BT/TFB bilayer structure occurs via exciton formation and radiative decay in the F8BT layer or excitons formed on the TFB side tunnels to a lower energy band gap material (F8BT) via energy transfer and decay radiatively there[3]. A recombination zone can be formed either in F8BT bulk or near the interface. We find this zone can be moved toward the interface where a large number of energy transfer (Förster transfer process) and tunnelling occur by thickness variation of F8BT and TFB layers and it is shown that quantum efficiency is maximized in the zone close to the TFB side. Also, a comparison with other light emitting polymers (LEPs) and structures (single, multilayer and blend) showed that a bilayer is an efficient way for designing an inverted PLED. A low processing temperature less than 150° C in our PLEDs is suitable with plastic substrates for future

flexible displays. Also, all sequentially solution processed layers, attributed to appropriate ink modifications, except vacuum evaporated electrodes expect to benefit of both further reduction in costs and ease of fabrication.

This Chapter describes a comparative study using various polyfluorene derivative light-emitting materials and device structures in case of inverted PLEDs in Section 7.3, influence of a thickness variation of both F8BT and TFB layers is explained in Section 7.4, a quantum mechanic process happening at the F8BT/TFB interface is suggested in Section 7.5 and finally device characteristics of F8BT/TFB multilayer PLEDs and its demonstration on a flexible PET substrate are discussed in Section 7.6.

7.2 Experimental

Materials: LEP materials used in this work including LUMATION^{TM} Green 1300, F8BT, F8T2 and TFB are from the Sumitomo Chemical Company, Ltd. The PEDOT:PSS (Baytron Clevios^{TM} AI4083) dispersion was purchased from H. C. Starck GmbH. Cesium carbonate (Cs_2CO_3), Triton X-100 and other organic solvents were obtained from Sigma-Aldrich. Substrates were either glass with pre-patterned ITO or polyethylene terephthalate (PET) coated in sputtered ITO (R_s = 40-60 Ω/sq) OC50 films from CPFilms Inc. Substrates were cleaned with acetone and IPA in an ultrasonic bath and then washed with deionized (DI) water. Oxygen plasma treatment used an Emitech K 1050X plasma asher.

LED preparation and characterization: Cs_2CO_3 was dissolved in 2-ethoxyethanol solvent at 0.3 wt% concentration and spin-coated at 3000 rpm. Then, samples were thermally treated at 150 °C for 20 minutes in air for converting work function of ITO to 3.1-3.4 eV. Light-emitting layer of F8BT in *p*-xylene was spin-coated then it was brought to glove box (< 2 ppm H_2O, < 0.1 ppm O_2) in nitrogen to anneal at 150 °C for 1 hour to enhance packing of polymer chains and remove any residual solvent and oxygen dopants. Then, TFB in cyclohexane was spin-coated on F8BT layer. TFB has much higher solubility than F8BT and it was experimentally observed that cyclohexane only

dissolves TFB. TFB coated samples were again brought to glove box to anneal at 120 °C for 30 minutes. Next, modified PEDOT:PSS dispersion was spin-coated on TFB surface for a thickness of 50-60 nm. IPA and Triton X-100 were mixed in commercial PEDOT:PSS dispersion with a volume ratio of PEDOT:PSS : IPA : Triton X-100 (1 : 1 : 0.01). Samples were again thermally treated on hot plate at 110 °C for 5 minutes in air. Blend of F8BT:TFB w/w (1:1) was spin-coated from a 18 mg/ml *p*-xylene solution for a thickness 80-100 nm.

Finally, the top electrode of 100 nm Au was thermally evaporated (vacuum pressure 4×10^{-6} mbar) with a shadow mask to define electrodes of 4.2 mm^2 (3 mm × 1.2 mm) area which reflects light emission. *J-V-L* measurements were performed using a Keithley 2410 Source-Measure Unit and a Topcon BM-9 luminance meter. Electroluminescence (EL) of PLEDs were characterized by using a Keithley 2400 SourceMeter and results were collected from an Ocean Optics USB 2000 charge-coupled device spectrophotometer. For demonstration of device, fabrications were repeated in the same procedure but it has larger light emission area of 0.42 cm^2 (width: 1.4 cm, height: 0.3 cm).

Optical Measurement: Photoluminescence (PL) measurements were made using a Jobin-Yvon Fluoromax spectrofluorometer equipped with an integrating sphere. Absorbance measureme-nts were made using an ATI Unicam UV-vis spectrophotometer

7.3 Comparison of Structural and Material Type

Relatively low efficiency and poor stability are problematic issues in PLEDs. These problems must be overcome in order to replace conventional successively vacuum sublimed OLEDs using small molecules where relatively high purification is available. Some groups have suggested that using highly stable metals as a top electrode should compensate these intrinsic problems, which is known as ‘inverted structure’[5,9,11,12]. However, PLEDs in inverted structure showed that its imbalance of charge carrier

injection results in both low efficiency and high driving voltage[5,6,8]. In this Section, various types of device structures in emissive layers (single, multilayer and blend) and various light-emissive materials are compared to find out its influence on device performance in inverted PLED structures. Different LUMO levels of polymers were investigated to analyse electron injection behaviour by considering the barrier height between Cs_2CO_3 treated ITO and the LUMO levels of the polymers. For hole injection and transport, we assumed that they are in ohmic contact from a fact that an energy barrier for hole injection/transport is less than 0.3 eV. Three device structures of single, bilayer and blended using F8BT, poly (9,9-dioclyfluorene-*co*-bithiophene) (F8T2) and LUMATION Green 1300 were examined to see a charge recombination balance in the devices. Energetic diagrams of single and multilayer structures with various materials are depicted in Figure 7.1. We measured current density – voltage – luminance (*J-V-L*) characteristics of inverted PLEDs with different types of structures and materials. *J-V* and *L-V* characteristics are shown in Figure 7.2 and 7.3 respectively. Current and power efficiency versus current density are shown in Figure 7.4 and 7.5 respectively. Also, the performance parameters of all devices are listed in Table 7.1.

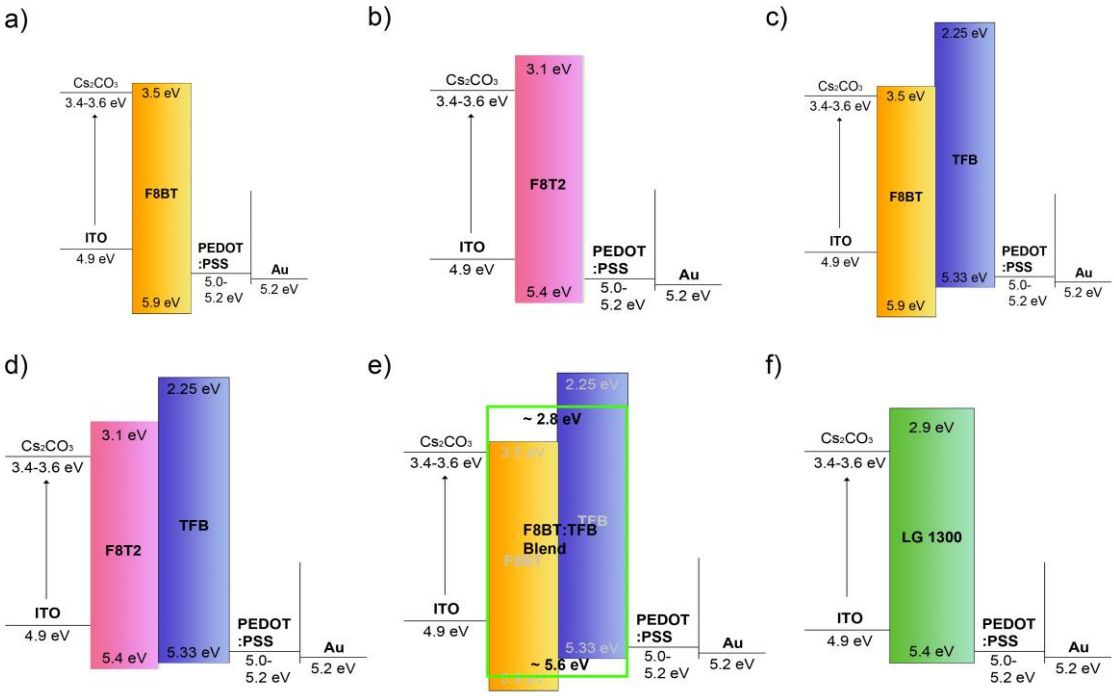


Figure 7.1 Energy level diagrams of Inverted PLEDs with different types of materials and structures. a) F8BT single layer, b) F8T2 single layer, c) F8BT/TFB bilayer, d) F8T2/TFB bilayer, e) F8BT:TFB blend, and f) LG1300 single layer PLEDs.

First we consider single layer structures using F8BT and F8T2. For the F8BT single layer PLEDs, very low efficiency values of 0.2 cd/A and lm/W at 100 cd/m^2 show that a large proportion of charge carriers travel through the device without recombination. F8BT is an electron transporting copolymer having an electron mobility of 4-5 × 10^{-3} cm^2/Vs.[13] We expect that electron injection to be in the space charge limited regime as the energy level difference of Cs_2CO_3 treated ITO and LUMO of F8BT is less than 0.3 eV while injection of holes into F8BT is limited as its HOMO level is relatively too high. As a result, most of recombination events can be observed at the edge of the F8BT near PEDOT:PSS layer, hence a large portion of injected electrons and excitons are quenched. Faster electron mobility of F8BT reinforces the imbalance charge carrier recombination.

A single layer PLED using F8T2 showed even lower efficiency of 0.2 cd/A and 0.06 lm/W. F8T2 has energy band gaps of 3.1 eV and 5.4 eV for LUMO and HOMO levels respectively (See Figure 7.1b). The higher energy barrier (~0.5 eV) for electron injection from Cs_2CO_3 into F8T2 makes the device to be electron injection limited. On the other hand, holes are injected in space charge limited regime for its low energy potential barrier which is opposite to the single F8BT case, hence a recombination zone is formed at F8T2 near Cs_2CO_3 treated ITO electrode.

In order to tackle the problem of low efficiency, it is possible to introduce a well-known method using multiple emissive layers to block quenching of excess carriers by inserting an additional layer at the interface between two polymeric layers. Tang *et al*. first reported in 1987 that multilayer structure of OLEDs can dramatically improve device efficiency[4]. Since that report, there have been various approaches to improve device efficiency of PLEDs using a multilayer structure, however no one yet demonstrated the feasibility of inverted PLEDs with high performance using a multilayer structure.

To do that, an additional TFB layer is positioned between PEDOT:PSS and F8BT or F8T2 layers to reduce any efficiency losses. A thickness of TFB should be sufficiently thick to prevent tunnelling of electrons throughout the layer and being quenched. Instead, it can confine them at the heterojunction at the interface[5]. Contributed to charge carrier confinement at the interface between F8BT (or F8T2) and TFB layers, the device performance is surprisingly improved. A large number of recombination events were observed at the F8BT/TFB interface achieving 28,500 cd/m^2 compared to 1,700 cd/m^2 in the single F8BT layer. Attributed to the increased light output, the device efficiency was improved as well showing its peak values of 5.5 cd/A and 4 lm/W. These values are the highest in inverted PLEDs with a F8BT/TFB multilayer structure reported so far. Similarly, the device efficiency of F8T2/TFB multilayer PLEDs achieved 0.8 cd/A and 0.21 lm/W. A maximum output luminance is also increased from 700 cd/m^2 to 2,500 cd/m^2. In addition, an operating voltage of F8BT/TFB is reduced to 2.6 V for 100 cd/m^2 due to either confined electrons contributed to a high chance of charge carrier recombination or increased local field at the heterojunction interface attracting larger number of holes to be injected. However, this multilayer structure using solution processable polyfluorene derivative polymers is only compatible for cases where modifications of ink formulations for the top layer or crosslinking of the bottom layer are made. Another approach has been suggested to relieve this process limitation in a multilayer structure by de-mixing of two materials[14-16].

Structure	**LEP**	**L_{max} (cd/m^2)**	**~100 cd/m^2**		**~1,000 cd/m^2**		**η_{max}**	
			η_L	**η_P**	**η_L**	**η_P**	**η_L**	**η_P**
Single layer	LG 1300	8,700 (15.2 V)	0.99 (6.8 V)	0.455	1.52 (10 V)	0.48	1.855 (10.8 V)	0.54
	F8T2	700 (12.2 V)	0.1 (10.2 V)	0.033	- -		0.213 (11.8 V)	0.06
	F8BT	1,700 (7.4 V)	0.19 (3.4 V)	0.17	0.25 (6.1 V)	0.13	0.27 (6.6 V)	0.29 (4 V)

Bilayer	F8T2/TFB	2,500 (16.6 V)	0.72 (10.6 V)	0.21	0.65 (14.8 V)	0.14	0.8 (15.2V)	0.21 (10.6V)
	F8BT/TFB (Thin)	28,500 (10.6 V)	3.45 (2.6 V)	3.9	4.6 (3.6 V)	4	5.5 (5 V)	4 (3.6V)
	F8BT/TFB (Thick)	51,200 (15.2 V)	27.42 (4.2 V)	20.51	25.53 (5.8 V)	13.83	34.86 (4.8 V)	22.8
Blend	F8BT:TFB	1,500 (13 V)	1.88 (8.4 V)	0.7	0.72 (12.6 V)	0.18	1.88 (8.4 V)	0.7

Table 7.1 Performance parameters of various PLEDs. Thickness of emissive layers for single layer structure is 70-80 nm, for bilayer structures are F8T2 (115 nm): TFB (30nm), F8BT (75 nm): TFB (25nm) (Thin) and F8BT (115 nm): TFB (140 nm) (Thick), for blend structure of F8BT:TFB is 80-100 nm. L_{max}, η_L and η_P correspond to maximum luminance, current efficiency and luminous efficacy, respectively. Voltage values in blanket indicates a bias voltage applied.

Blending of hole-accepting and electron-accepting materials forming heterogeneous structures, which are vertically distributed throughout the blended layer, has been suggested to increase device performance[17]. A blend of F8BT:TFB shows that its device efficiency can achieve up to 19 lm/W for a green light emission[14]. Distributed heterojunctions so called 'exciplex' in the blended layer using the two polymers can be generated and its lateral phase separation width can be formed in either microscale or nanoscale so that charge transfer in this structure is a very efficient and barrier free process[14,18]. We dissolved the two polymers in *p*-xylene for microscale phase separation to form. Completely mixed patterns in nanoscale were observed in case of dissolving the two materials in chloroform which is ideal for PV diodes for efficient charge separation but not for PLEDs as excitons diffused to the bulk of F8BT can be retrapped because of its narrow width of lateral phase separation[19]. Attributed to the efficient charge transfer, a driving voltage is decreased to 2.1 V for 100 cd/m^2[14]. Vertically phase separated patterns along with lateral phase separation critically influence charge carrier transport inside the layer[16]. Solubility of two polymers in a common organic solvent and surface energy of a substrate are main factors determining a morphology of phase separation patterns and hence efficient charge carrier

transport[16]. Relatively high solubility of TFB compared to F8BT in either *p*-xylene or chloroform deposits TFB heavily at the bottom side after solvent evaporation[15,16]. Hence, normal structure (anode – bottom and cathode – top) PLEDs using F8BT:TFB blend show an efficient charge injection and transport throughout the blending layer. In our case, the result is surprising in inverted structure with the F8BT:TFB blended layer. A driving voltage is four times higher than the normal structure recording 8.4 V at 100 cd/m^2. It is attributed to limited injection of either holes or electrons. For example, a thin polymer layer of TFB formed on the top of Cs_2CO_3 layer blocks injection of electrons into the F8BT so that the device becomes electron limited. The device showed increased efficiency reaching 1.88 cd/A and 0.7 lm/W compared to the single F8BT structure but they rapidly decreased at higher voltages (Figure 7.4-7.5).

It is possible to design a material with balanced charge carrier mobility by modification of chemical compounds of polyfluorene derivative polymers. An advanced material type with balanced hole and electron mobility has been evaluated for replacing the multiple emissive layers to a single emission layer or for avoiding phase separation in the blended case. LUMATION Green 1300[20] has a LUMO level of 2.9 eV and HOMO level of 5.4 eV. The energy band levels (Figure 7.1f) permit charge injection for both holes and electrons using ITO or Au as the anode and Ca as the cathode, which have energy band levels of around 5.2 eV and 2.95 eV respectively. In our case, the Cs_2CO_3 treated ITO after thermal treatment at 150 °C converted energy band level of the ITO to ~3.4 eV[12]. Electrons may face too high energy barrier to be injected and the device may become electron injection limited. A drive voltage at 100 cd/m^2 recorded at 6.8 V proves that the energy band engineering is not optimized for charge injection in the space charge limited regime.

Figure 7.2 and 7.3 describe current density – voltage – luminance (*J-V-L*) characteristics for inverted PLEDs with different material types and structures. As discussed previously the F8BT/TFB multilayer reaches a brightness of 100 cd/m^2 at a driving voltage of 2.6 V indicating charge carrier injection is probably space-charge limited. Compared to the F8BT single layer, a number of recombination events in the emissive layer are huge attributed to charge confinement at the energy band offsets between

F8BT and TFB layers even though current density at the F8BT single layer is higher. A large proportion of currents is quenched into the opposite electrodes without recombination. The PLEDs with using F8T2, F8BT:TFB blend and LG1300 all show similar characteristics of a high drive voltage and low current density supporting again that electron injection is limited due to a large energy barrier. Compared to the F8BT/TFB bilayer, the F8T2/TFB bilayer showed significantly lower efficiency and a high driving voltage. It derives that efficient electron injection is a governing factor for high efficiency in inverted PLEDs with a Cs_2CO_3 layer. Vertically phase separated F8BT and TFB layers in the blended case showed a poor charge injection as TFB rich zone is formed on the Cs_2CO_3 treated ITO, which hampers efficient electron injection.

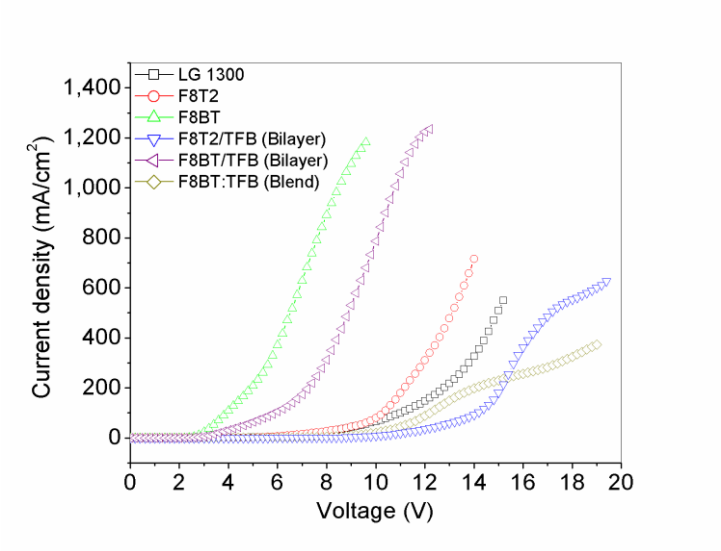


Figure 7.2 Comparison of current density, J – voltage, V (J-V) characteristic for different LEPs and structures.

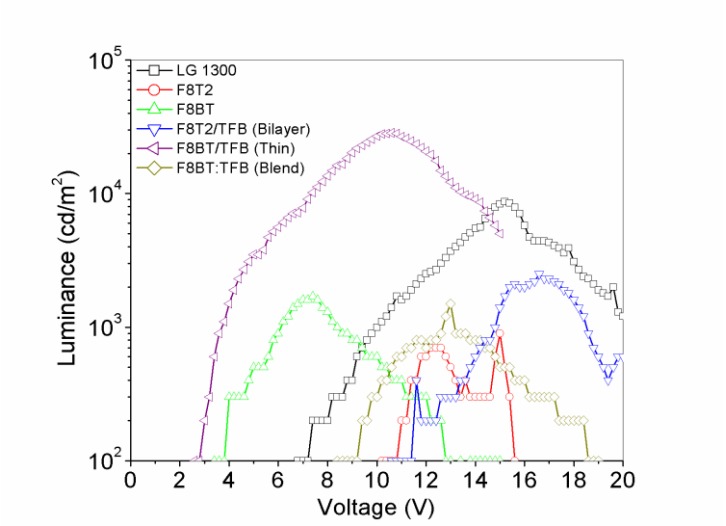


Figure 7.3 Comparison of voltage, V – Luminance, L (V-L) characteristic for different LEPs and structures.

Device efficiency, which describes how much injected charge carriers recombine with an opposite type of carrier and electrically excited, depicted in Figure 7.4-7.5, show that the multilayer of F8BT/TFB has consistent values at all applied bias voltages. Even though amount of current density increases, the efficiencies were maintained as around 5 cd/A and 4 lm/W which are state-of-the-art performance in the F8BT/TFB multilayer inverted PLEDs. The LG1300 single layer recorded lower efficiency than the F8BT/TFB multilayer around 1.8 cd/A and 0.5 lm/W but was kept at consistent values. The consistency in device efficiency in a case of the F8BT/TFB bilayer suggests that electron and hole carrier mobility are balanced in the device, which is similar with the LG1300 copolymer PLEDs having a balanced charge carrier mobility. The F8BT single layer has efficiency of less than unity for both current and power conversion efficiencies owing to a large amount injected holes that traverse into the cathode without recombination as the device is electron injection limited. The F8BT:TFB blended inverted PLEDs showed efficiencies of 1.9 cd/A and 0.7 lm/W at a drive bias of 8.4 V. Interestingly, the efficiency showed a rapid decay at higher driving bias compared to the other cases (Figure 7.4-7.5) which agrees to the previous results in Ref. 16. This may be attributed to quenched charge carriers throughout via either F8BT or TFB rich zones randomly distributed in a vertical direction. The PLEDs using F8T2 recorded efficiencies less than 1 cd/A and 0.3 lm/W from both single and multilayer structures.

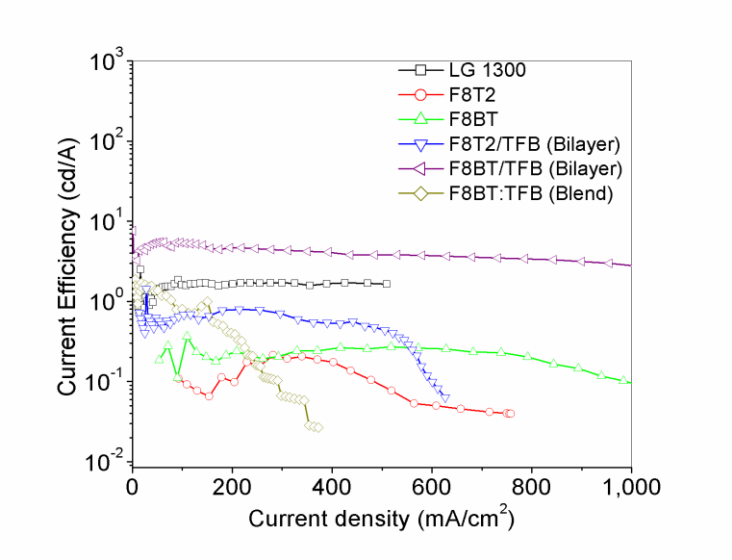


Figure 7.4 Comparison of current efficiency for different LEPs and structures.

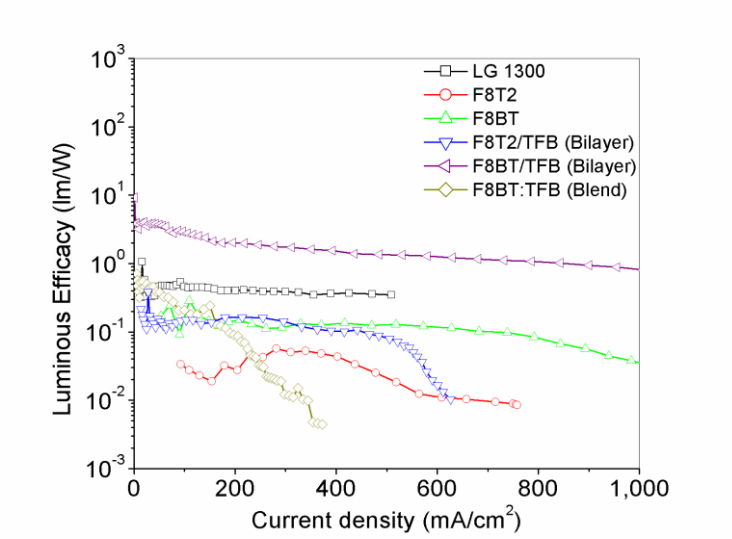


Figure 7.5 Comparison of power efficiency for different LEPs and structures.

7.4 Thickness Variation of F8BT and TFB Layers

For efficient PLEDs, holes and electrons should be captured at the centre of an emissive layer so that excited states do not quench into the electrodes in case of a single layer device. Typical thickness for experimentally optimized condition in a single layer structure is around 70-80 nm[1]. For a multilayer structure, a recombination zone can be formed at the interface between two polymer layers[3,21,22] or carriers can be confined

in an emissive layer for a heterojunction structure[23,24]. Charge carriers are mainly confined at the interface and a recombination zone can be formed in a lower energy gap polymer layer near the interface within a distance of about 30 nm[4].

F8BT and TFB are copolymers with biased n- and p- type electrical property respectively. F8BT is an popular electron transporting material with an electron mobility (μ_e) of 4-5 × 10^{-3} cm^2/Vs while TFB is a hole transporter with a mobility (μ_h) of 1 × 10^{-3} cm^2/Vs.[25] In a multilayer structure, thicknesses of emissive layers are very closely related to performance of a device in terms of operating voltage, the number of exciton generated and efficiency[26, 27]. For example, if a thickness of a layer is less than 20 nm, the excitons can decay non-radiatively into an adjacent metal electrode which acts as quenching sites for singlet excitons[28] and thicker polymer layers can achieve high electroluminescence (EL) efficiency but the light output in an applied electric field can be decreased[27].

First of all, the thickness of an F8BT layer was varied from 20-240 nm with a different concentration of F8BT in *p*-xylene and spin-coating speeds. Changes of performance parameters including maximum luminance, current efficiency and luminous efficacy at 1,000 cd/m^2 with a variation of F8BT thickness at a fixed thickness of TFB at 25 nm are shown in Figure 7.6a. For thickness less than 30 nm, only a small amount of exciton radiative decay was observed (less than 1,000 cd/m^2). This is attributed to quenched excited states in the F8BT into the adjacent Cs_2CO_3 treated indium-tin-oxide (ITO) electrode. A drive voltage at 100 cd/m^2 decreased until thickness of 75 nm, where indicates a minimum voltage (3.2 V), and starts to increase consistently. Electrons are accumulated at the interface for thicker F8BT layers above 45 nm, showing significantly improved light output and reduced driving voltage. It can be said that the device becomes free of quenching effects, involving non-radiatively decayed excitons and electrons, from a F8BT thickness around 120 nm showing a stabilized maximum luminance (~42,000 cd/m^2).

The current efficiency increases with thicker F8BT layers reaching 9.55 cd/A at a thickness of 215 nm. The improved efficiency is occurred by a high concentration of

confined charge carriers at the interface inducing tunnelling of more holes into the F8BT and a large number of recombination events. EL spectra of the device in this range all showed similar to PL spectrum of F8BT (See Figure 7.7), suggesting that an emission broadly occurs in the F8BT bulk side. Luminous efficacy, however, remained rather stable owing to an increased drive voltage as the thickness increases.

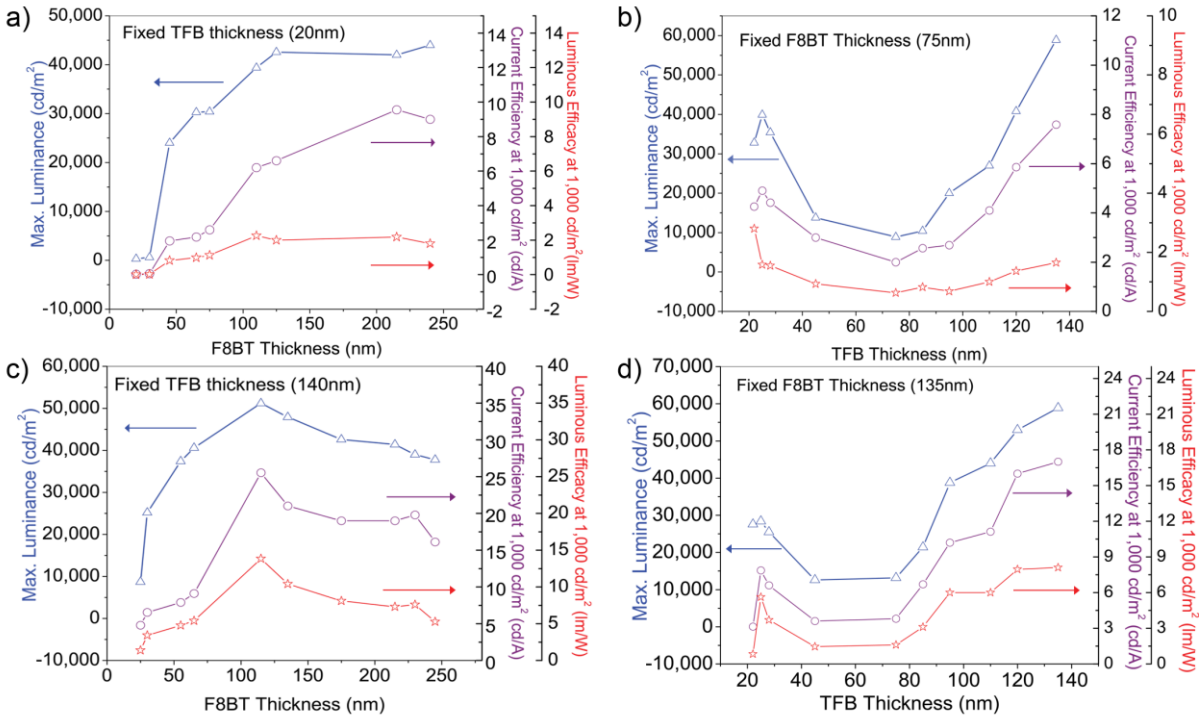


Figure 7.6 a) F8BT thickness variation at 20nm of TFB. b) TFB thickness variation at 75nm of F8BT. c) F8BT thickness variation at 140nm of TFB. d) TFB thickness variation at 135nm of F8BT.

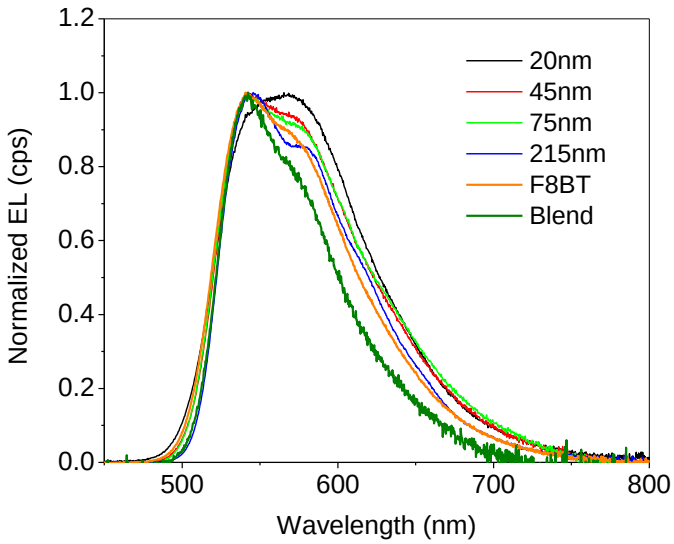


Figure 7.7 EL spectra of different thickness of F8BT layers for a fixed thickness of TFB at 20 nm.

A TFB layer is positioned between F8BT and PEDOT:PSS layer and acts as a hole transporting layer relieving the energy barrier between HOMO of the F8BT and work function of the PEDOT:PSS as well as blocking of injected electrons travelling from the F8BT layer. With a fixed thickness at 80 nm of F8BT layer, the thickness of the TFB layer was varied from 20-135 nm (Figure 7.6b). A drive voltage for 100 cd/m^2 increases for thicker layers recording its minimum value at 20 nm (3 V). It does not show quenched excited states at thin layers (< 30 nm) and it again supports a recombination zone in the bulk of F8BT layer according to its EL spectra similar to the PL spectrum of F8BT single layer (See Figure 7.8). F8BT is a lower-energy gap polymer (2.4 ev) than TFB (3.08 eV) and emission occurs either when a hole tunnels through into the F8BT layer forming an exciton then decay radiatively or when an electron tunnels through into TFB layer and generates an exciton which diffuses into the lower energy polymer layer (F8BT) and decays there[3]. Light output decreases as a thickness of TFB layer increases up to 75 nm as hole concentration at the interface is related to TFB thickness, which agrees to the results from Ref. 29 that device efficiency decreases at TFB thicknesses of thicker than ~20 nm with fixed F8BT thickness of 70 nm. A slightly thicker TFB layer (~25-30 nm) in our case (Figure 7.6a) at which starts to show decrease of performance than from Ref. 29 is attributed to thicker F8BT thickness (80

nm) influences charge carrier density in the F8BT layer together with different device structure and materials used.

Device performance starts to rapidly increase for thicker TFB layers reaching 58,900 cd/m^2 at 135 nm. TFB thicknesses in that range (75-135 nm) induce a strongly charged region attracting more electrons from the F8BT layer to reside near the interface. As tunnelling of holes and energy transfer of excitons into F8BT occurs within a short distance (~5-10 nm) limited by a lifetime of charged carriers or neutralized states, more emission occurs at the vicinity to the interface than from the bulk of F8BT. Blue shifted EL spectra with a reduction of its right shoulder in thicker TFB layers (See Figure 7.8) indicate a shift of recombination zone more toward the interface. A large population of accumulated charge carriers at the interface due to the Coulombic attraction from the oppositely charged TFB region contributed to this enhanced light output. Current efficiency follows a similar pattern with a maximum luminance curve having a maximum value of 7.58 cd/A at TFB layer of 135 nm. Accumulated charge density increases at thicker layers. It is expected that maximum luminance and current efficiency continues to increase with thicker F8BT and TFB layers.

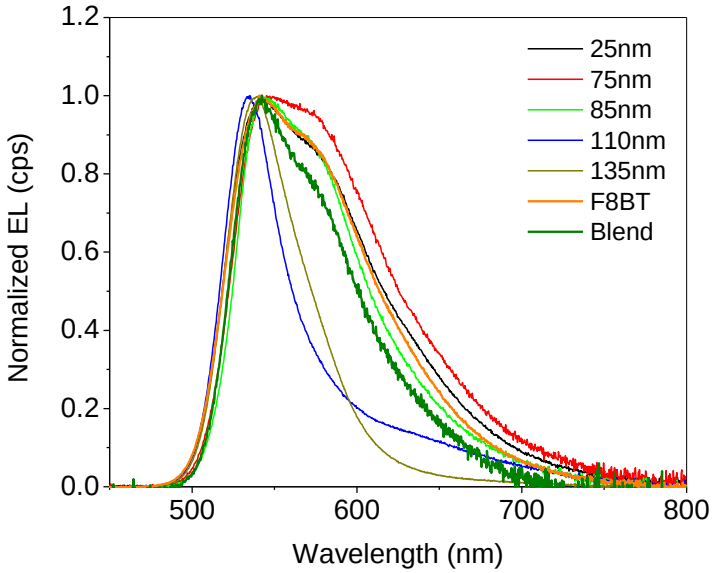


Figure 7.8 EL spectra of different thickness of TFB layers for a fixed thickness of F8BT at 75 nm.

For thicker F8BT and TFB layers, the total current density level is reduced owing to decreased internal electric field (bias voltage / total polymer layer thickness). Thicker layers should have a higher concentration of confined charged carriers attracting a large concentration of oppositely charged carriers to exist at the vicinity of the interface. Thick layers with accumulated charged carriers at the interface strongly increase local fields of both positively and negatively charged regions near the interface. Then, the strongly charged regions will attract opponent type of carriers near the interface owing to the Coulombic attraction. Hence, the confined charge carriers reside very close to the interface and tunnelling of both types of carriers can be efficient increasing a number of electron-hole recombinations. Both increasing a number of recombination events at the interface and lowering the total current density level enhances efficiency of the devices. Figure 7.6c-d represent performance parameters with variations of F8BT and TFB layers at fixed thickness of thicker F8BT (135 nm) and TFB (140 nm) layers.

In a F8BT thickness variation, a maximum luminance of each case increases and reaches to a maximum value at F8BT thickness of 115 nm (51,200 cd/m^2), then it starts to either decrease when TFB layer is thick or stabilize when TFB layer is thin with thick F8BT layers. This divergence can be explained by considering the position of capturing an electron and hole pair. In the case of the thick TFB layer, the strongly attracted F8BT region, due to the confined holes in the TFB region, contains a large number of electrons at the interface. As F8BT layer gets thicker than the thick TFB layer, it slowly becomes free of influence from the positive charges in the TFB region and the emission zone starts to be randomly distributed within the F8BT bulk. In the case of the thin TFB layer, on the other hand, an emission zone is positioned in a wide range of the F8BT layer as a relatively small number of confined holes are resided in the thin TFB layer with lower concentration of confined electrons and the recombination zone is still remained in a similar position as the F8BT layer becomes thicker. A slightly higher luminance for the case of thicker TFB is due to the recombination zone is shifted more closely to the interface where a larger population of excitons exist. A population of the confined charged carriers at the interface is reduced as charge intensity in the F8BT side gets stronger. Light emission occurs within a recombination zone which is widely distributed in the bulk of F8BT layer supported from EL spectra shift and becomes

similar to the PL spectrum of F8BT at thicker F8BT layers (See Figure 7.9), and its shoulder at 600 nm starts to appear in thicker F8BT layers. As a result, the quantum efficiency of the devices decreases for a less number of radiative decay of excitons.

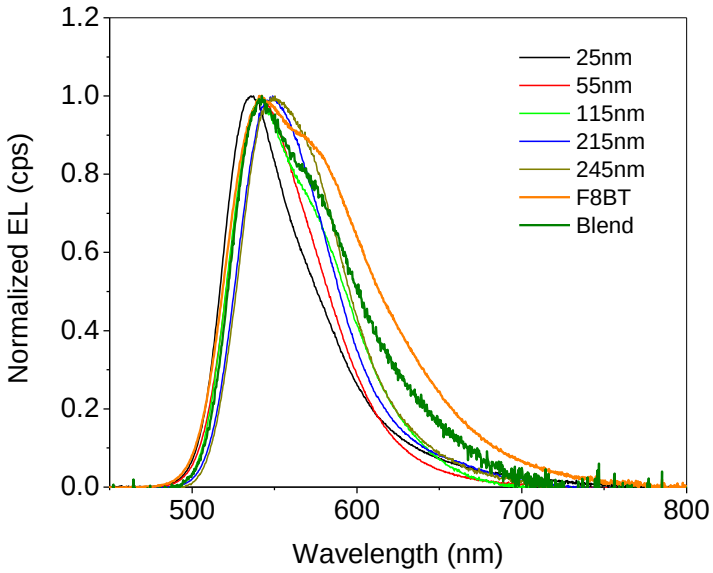


Figure 7.9 EL spectra of different thickness of F8BT layers for a fixed thickness of TFB at 140 nm.

A sufficiently thick F8BT layer is necessary for confining charge carriers and excitons, hence becoming free of quenching effects. It showed a maximum luminance at a thickness of F8BT layer around 100-125 nm for both cases of thin and thick TFB layers (Figure 7.6a and 7.6c). For high efficiency, both regions should be highly concentrated with injected charged carriers. Reduced net current density together with a larger number of recombination events at the interface between the two oppositely charged regions contribute to high device efficiency achieving a maximum value of 25.53 cd/A and 13.83 lm/W at 1,000 cd/m^2 for a F8BT thickness of 115 nm with a fixed TFB thickness at 140 nm.

A TFB thickness variation with a fixed F8BT thickness at 135 nm (Figure 7.6d) follows similar patterns of maximum luminance and device efficiencies to the case of the thin F8BT layer (Figure 7.6b and 7.6d). TFB thicknesses up to 30 nm show a yellow-green emission confirming electrons randomly distributed at the F8BT bulk (See Figure 7.10). A thick F8BT layer enhances hole injection into the TFB layer so that emission from the

interface starts to dominate from a TFB thickness of 45 nm (See Figure 7.10) which is earlier than the case of the thin F8BT layer (Figure 7.8) where a recombination zone starts to form at the interface from a TFB thickness of 80 nm. A maximum luminance starts to increase from the thicknesses as the zone is concentrated more closely to the TFB layer so energy transfer can be effectively generated. A driving voltage at 100 cd/m^2 remained constantly (4-6 V for all cases) showing a slight increase with the thicker layers. A relatively small increase of driving voltage, compared to increase of device thickness, is attributed to the confined charges of both types redistributing the internal electric field of the devices and enhances charge carrier injection of both types simultaneously.

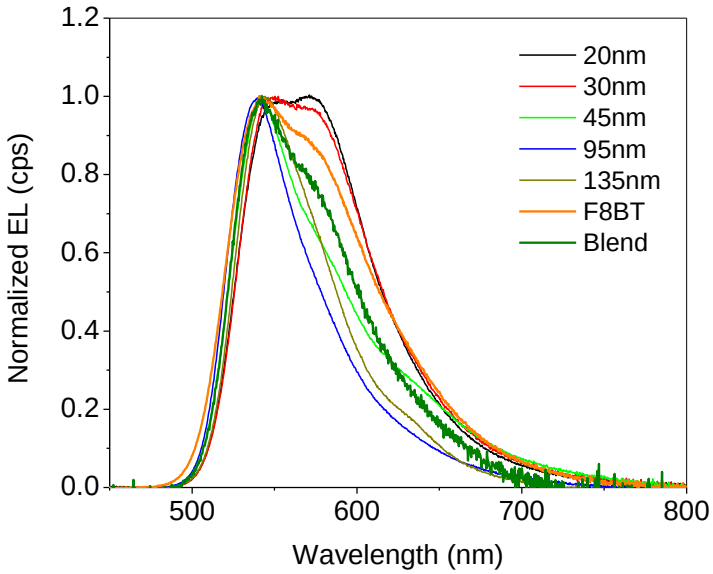


Figure 7.10 EL spectra of different thickness of TFB layers for a fixed thickness of F8BT at 135 nm.

7.5 Exciton Formation and Decay

We propose a simple graphical representation for exciton formation and decay in our F8BT/TFB bilayer PLEDs with different thicknesses of the two polymer layers as described in Figure 7.11. It depicts tunnelling of charge carriers, exciton diffusion, and exciton decay at the F8BT/TFB interface. Four different regimes are demonstrated with different thicknesses of F8BT (L_e) and TFB (L_h) layers: a) both layers are thin (less than

30-40 nm), b) F8BT layer is thicker than thin TFB layer ($L_e > L_h$), c) TFB layer is thicker than thin F8BT layer ($L_h > L_e$), d) both layers are thick (more than 100-120 nm). As mentioned in the previous sections, there are large energy band offsets existing at the interface between the two polymer layers (more than 0.5-0.6 eV) and these large offsets enable charge carrier confinement at the interface, even at a high applied bias.

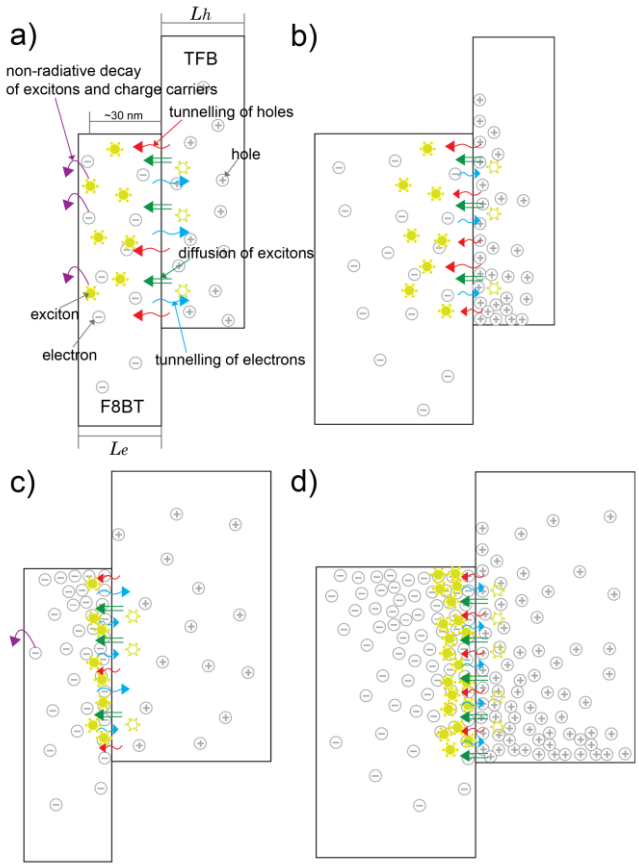


Figure 7.11 Exciton diffusion and decay process in F8BT/TFB bilayer PLEDs when a) both F8BT and TFB layers are thin (< 30-40 nm). b) of thick F8BT and thin TFB. c) of thin F8BT and thick TFB. d) both F8BT and TFB layers are thick (> 100-120 nm).

The overall device thickness determines the drive voltage to achieve a given current. Hence, the drive bias, adjusted for the built-in potential, is expected to be perhaps four times as large in d) as it is in a) to achieve the same current density, potentially decreasing the luminous power efficiency. Varying the relative thicknesses of the F8BT and TFB layers will vary the current balance, depending on the electron and hole injection barriers respectively at the cathode and anode, the electron and hole mobility

respectively in F8BT and TFB, and the electron and hole tunnelling barriers at the internal interface. Hence, compared to a) and d), device b) should have an increased hole to electron current ratio, whilst device c) should have an increased electron to hole current ratio. This will allow the current ratio to be tuned towards one to maximise the device efficiency. In addition, if the layers are thin, excitons may diffuse towards the contacts and be quenched. If charge carrier balance is very poor, carriers may flow through the device and the recombination zone could be shifted away from the internal heterojunction, again leading to quenching at the electrodes. Excitons can be generated either in F8BT or TFB at the interface, but those in TFB undergo Förster resonant energy transfer to the smaller energy gap F8BT chains. As emission is from F8BT, the thickness of 30 nm in a) and c) may lead to quenching at the cathode, reducing the device efficiency. If the electron current is dominant and the recombination zone is shifted into the TFB layer, some of the excitons may not be able to diffuse to the internal interface, resulting in blue shifted emission from TFB itself. In the blend case, energy transfer process can be extremely efficient as the exciton diffusion distance from TFB to F8BT is minimised.

7.6 Device Characterization of F8BT/TFB Multilayer

As previously mentioned, we have experimentally clarified a multilayer structure using F8BT and TFB polymers is more efficient than other structures including single and blended structures in inverted PLEDs with a Cs_2CO_3 layer. Also, thicknesses of the two layers play an important role which directly influences light emission and device efficiency. A case with thicknesses of F8BT and TFB are 75 nm and 25 nm respectively achieved its turn on at a low voltage around 2.6 V for 100 cd/m^2 (See Figure 7.3). This is comparable to state-of-the-art PLEDs. For thicker layers of F8BT/TFB, device efficiency and total light emission have been dramatically improved reaching up to 35.86 cd/A and 22.8 lm/W although its driving voltage at 100 cd/m^2 is slightly increased to 4.2 V due to required electric field is higher at the increased thicknesses as listed in Table 7.1. Figure 7.12 compares the *J-V-L* characteristics of inverted PLEDs between single F8BT, thin and thick F8BT/TFB multilayer structures. Quenched

excitons and traversed charge carriers in the F8BT single structure significantly reduced device efficiency but a blocking functionality of the TFB layer resolved the problem and recorded high efficiency in the F8BT/TFB multilayer structure. The total current density is reduced at thicker layers of PLEDs but the overall light output increases. Our inverted PLEDs with a multilayer of thin F8BT and TFB layers show that the total current density at a low bias voltage is 1.5 order of magnitude lower than the single F8BT PLED (Figure 7.12). Required electric field at current density of 5 mA/cm^2 is similar for all cases within 1.6-1.7 × 10^5 V/cm. A maximum luminance is obtained at a higher voltage than the single layer which suggests the confinement of the charge carriers at the interface. Luminance degradation at high voltages is observed in single F8BT layer and thin F8BT/TFB bilayer cases as shown in Figure 7.12. Electric fields applied into the device became too high and exceeded its capacity so that the devices started to burn.

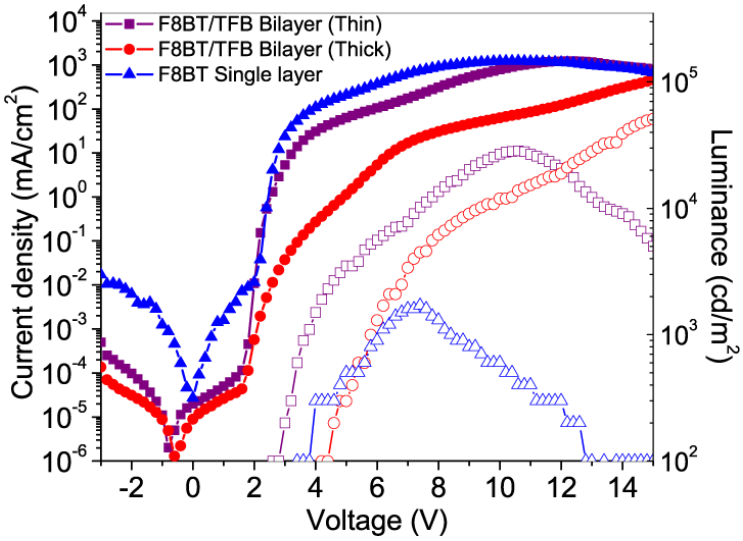


Figure 7.12 Current density, J (left ordinate, filled) and luminance, L (right ordinate, open) versus voltage, V characteristics.

Thicker layers of F8BT (115 nm)/ TFB (140 nm) achieves the highest device efficiency which refers to a higher probability of recombination as described in Figure 7.12. A maximum luminous output records at 51,200 cd/m^2. Device efficiency of both thin and thick F8BT/TFB multilayer cases show that their values consistently maintained over increased luminance values (Figure 7.13). Hence, it can be said that the F8BT/TFB

multilayer inverted PLEDs has a consistent efficiency at all ranges of both current density (Figure 7.4-7.5) and light output (Figure 7.13). Electrically excited emission spectrum of inverted PLEDs shown in Figure 7.14 describe that light emission from the F8BT/TFB bilayer with thinner layers resembles to the F8BT single layer structure case which insists that light emission mainly occurs in the F8BT layer after energy transfer of excitons from the TFB layer. However, it was surprising that light emission from the thicker F8BT/TFB layer inverted PLEDs shows its emission spectrum becomes blue-shifted similar to the case of the F8BT:TFB blend structure. It again supports that light emission from the thicker layers of the F8BT/TFB bilayer structure have a similar energy transfer mechanism to the F8BT:TFB blended case where a barrier free electron-hole capture is dominated. The emission colour can be shifted via thickness variation of emissive layers if their energy band gaps are similar[24]. Large offsets at the interface in our PLEDs constrain the peak of EL wavelength to be around 540 nm. There was no shifts of colour of emission observed during the device operation.

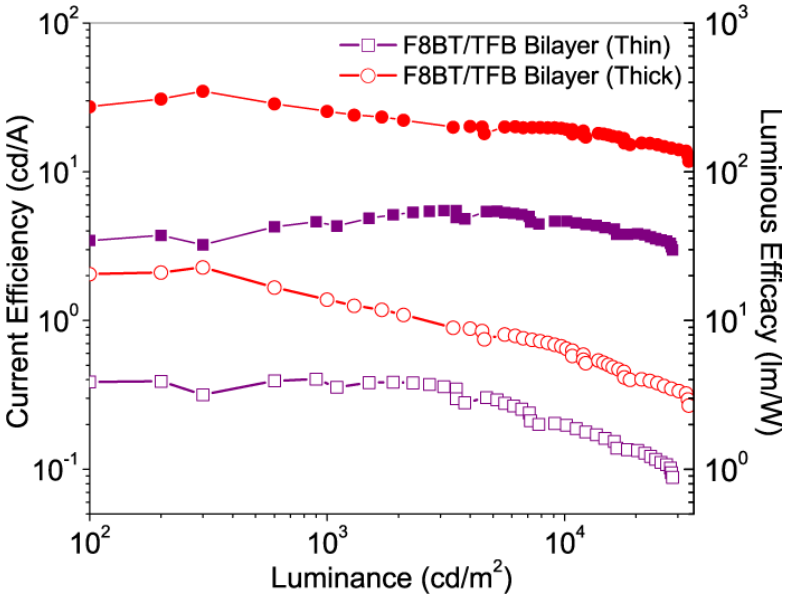


Figure 7.13 Current efficiency (left ordinate, filled) and luminous efficacy (right ordinate, open).

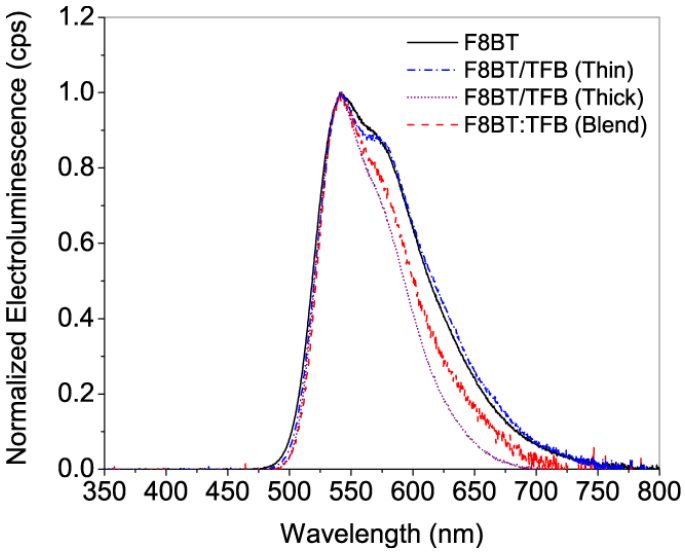


Figure 7.14 EL spectra of F8BT/TFB inverted PLEDs.

In addition, low processing temperature of our PLEDs, less than 150° C, enabled to build such devices on flexible PET substrates as shown in Figure 7.15. A future type of LEDs shall be low cost, adaptable in broad applications as well as with both high efficiency and stability. Flexible display has a great potential that will innovate a new processing methods such as roll-to-roll (R2R) printing and create lots of interesting applications.

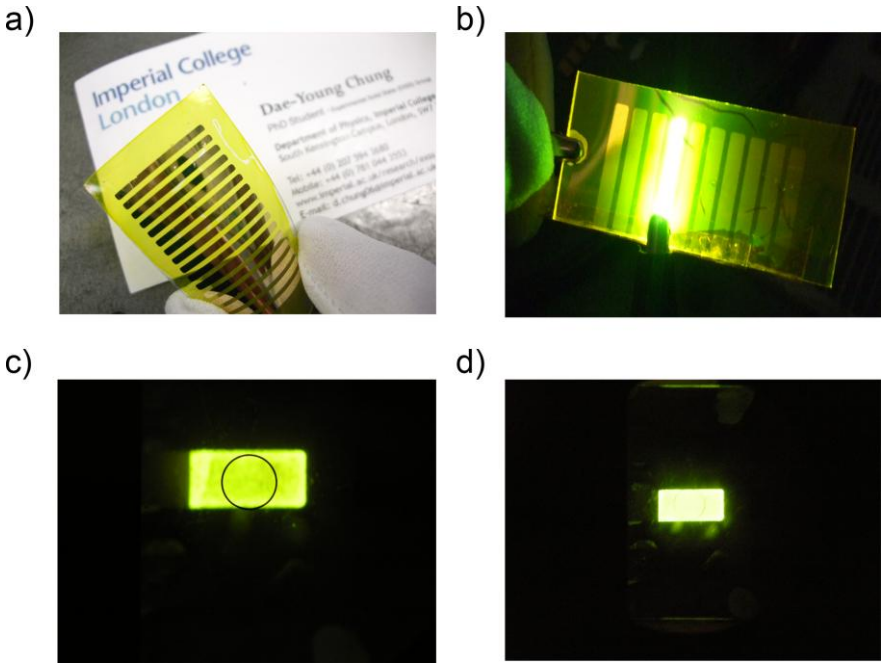


Figure 7.15 Demonstration of Inverted PLEDs with F8BT/TFB Multilayer on flexible PET or glass substrate. a) as prepared and b) with light emission. Light emission area (right) is 0.42 cm^2 (width: 1.4 cm, height: 0.3 cm). c) a light emitting pixel on glass substrate. d) a light emitting pixel with uniform emission. Light emission area on glass substrate is defined as 4.2 mm^2 (width: 3 mm, height: 1.2 mm). Images were captured by D. Leem.

7.7 Conclusion and Future Work

To conclude with a brief discussion, we experimentally examined that a bilayer is an efficient way for designing a PLED with both high efficiency and reduced leakage currents. However, it is not easy to build such a structure due to similar solubility of common polymers and as a result solvent used for a top layer often dissolves a bottom layer during its deposition. Finding an appropriate solvent is not easy due to a limitation in solvent choice and similar solubility between popular organic materials. Recently, alcohol or water soluble semiconducting materials have been reported[30-33] and invention of these materials is expected to relieve the limitation.

We demonstrated efficient inverted PLEDs with a highly stable top electrode. A device for low voltage turn-on requires relatively thin both F8BT (~75 nm) and TFB (~25 nm) layers which achieves 100 cd/m^2 at a drive bias of 2.6 V. Energy band offsets of more than 0.5 eV between the two polymers are enough for confinement of charge carriers at the interface. We showed a shifted recombination zone close to the interface between the two highly concentrated regions with thicker layers that was attributed to excellent efficiency (34.86 cd/A and 22.8 lm/W at 4.8 V). For a high recombination yield, both F8BT and TFB layer should be sufficiently thick for a high charge concentration at the interface and the recombination zone should be positioned in the F8BT side near the interface within a tunnelling distance for effective tunnelling of charge carriers and diffusion of excitons from the TFB layer. Thicker layers required a slightly higher drive bias of 4.2 V for 100 cd/m^2 and 5.8 V for 1,000 cd/m^2. There is a trade-off between high efficiency and low voltage operating devices. Device performance of both cases are comparable to ‘normal’ structure PLEDs. Our PLEDs are all solution processed except for vacuum evaporated electrodes. Researches on high conductive polymers showed

that they can be applied as conductive electrodes[34-36]. Enhanced stability and efficiency together with all solution processed PLEDs at low temperature will realize a future display on a flexible substrate using printing technology with a fast line production.

It has been demonstrated that PLEDs with both high efficiency and long lifetime can be developed by using a multilayer structure in inverted PLEDs. It will be an interesting study to investigate the interface state between the F8BT/TFB polymeric layers which can be sequentially solution processed followed by a given experimental procedure. The interface state should be very much strongly linked with the injected charge carriers and excitons. In addition, PLEDs can now be all solution processed including electrodes using a high work function metal as a top electrode. In Chapter 8, we demonstrate that Ag nano particle ink can be roll-to-roll printed. Using of Ag bottom electrode as a reflective layer and a semi-transparent top electrode such as carbon nanotube[37], VPP-PEDOT[34, 38] or graphene[39, 40] is a very promising way to develop a device via all solution processing.

7.8 Reference

[1] R. H. Friend, R. W. Gymer, A. B. Holmes, J. H. Burroughes, R. N. Marks, C. Taliani, D. D. C. Bradley, D. A. dos Santos, J. L. Bredas, M. Logdlund, W. R. Salaneck, *Nature* **1999**, *397*, 121.

[2] P. L. Burn, A. B. Holmes, A. Kraft, D. D. C. Bradley, A. R. Brown, R. H. Friend, R. W. Gymer, *Nature* **1992**, *356*, 47.

[3] N. C. Greenham, S. C. Moratti, D. D. C. Bradley, R. H. Friend, A. B. Holmes, *Nature* **1993**, *365*, 628.

[4] C. W. Tang, S. A. Vanslyke, *Appl. Phys. Lett.* **1987**, *51*, 913.

[5] D. Kabra, M. H. Song, B. Wenger, R. H. Friend, H. J. Snaith, *Adv. Mater.* **2008**, *20*, 3447.

[6] H. J. Bolink, E. Coronado, J. Orozco, M. Sessolo, *Adv. Mater.* **2009**, *21*, 79.

[7] S. A. Haque, S. Koops, N. Tokmoldin, J. R. Durrant, J. Huang, D. D. C. Bradley, E. Palimares, Adv. Mater. 2007, 19, 683.

[8] H. J. Bolink, H. Brine, E. Coronado, M. Sessolo, *Adv. Mater.* **2010**, *22*, 2198.

[9] N. Tokmoldin, N. Griffiths, D.D.C. Bradley, S.A. Haque, *Adv. Mater.* **2009**, *21*, 3475.

[10] D. Kabra, L. P. Lu, M. H. Song, H. J. Snaith, R. H. Friend, *Adv. Mater.* **2010**, *22*, 3194.

[11] H. J. Bolink, E. Coronado, D. Repetto, M. Sessolo, E. M. Barea, J. Bisquert, G. Garcia-Belmonte, J. Prochazka, L. Kavan, *Adv. Funct. Mater.* **2008**, *18*, 145.

[12] J. S. Huang, G. Li, E. Wu, Q. F. Xu, Y. Yang, *Adv. Mater.* **2006**, *18*, 114.

[13] A. J. Campbell, D. D. C. Bradley, and H. Antoniadis, *Appl. Phys. Lett*. **2001**, *79*, 2133.

[14] A. C. Morteani, A. S. Dhoot, J. S. Kim, C. Silva, N. C. Greenham, C. Murphy, E. Moons, S. Cina, J. H. Burroughes, R. H. Friend, *Adv. Mater.* **2003**, *15*, 1708.

[15] Y. J. Xia, R. H. Friend, *Adv. Mater.* **2006**, *18*, 1371.

[16] J.-S. Kim, P. K. H. Ho, C. E. Murphy, R. H. Friend, *Macromolecules* **2004**, *37*, 2861.

[17] J. J. M. Halls, J. Cornil, D. A. dos Santos, R. Silbey, D. H. Hwang, A. B. Holmes, J. L. Bredas, R. H. Friend, *Phys. Rev. B* **1999**, *60*, 5721.

[18] Y.-S. Huang, S. Westenhoff, I. Avilov, P. Sreearunothai, J. M. Hodgkiss, C. Deleener, R. H. Friend, D. Beljonne, *Nat. Mater*. **2008**, *7*, 483.

[19] *Organic Light-Emitting Devices*, ed. Klaus Müllen and Ullrich Scherf, Wiley-VCH, Weinheim **2006**.

[20] D.-Y. Chung, J.S. Huang, D.D.C. Bradley, A.J. Campbell, *Org. Electron.* **2010**, *11*, 1088.

[21] K. S. Cho, E. K. Lee, W. J. Joo, E. Jang, T. H. Kim, S. J. Lee, S. J. Kwon, J. Y. Han, B. K. Kim, B. L. Choi, J. M. Kim, *Nat. Photonics* **2009**, *3*, 341.

[22] S. R. Tseng, S. Y. Li, H. F. Meng, Y. H. Yu, C. M. Yang, H. H. Liao, S. F. Horng, C. S. Hsu, *J. Appl. Phys.* **2007**, *101*, 084510.

[23] D. OBrien, A. Bleyer, D. G. Lidzey, D. D. C. Bradley, T. Tsutsui, *J. Appl. Phys.* **1997**, *82*, 2662.

[24] A. R. Brown, N. C. Greenham, J. H. Burroughes, D. D. C. Bradley, R. H. Friend, P. L. Burn, A. Kraft, A. B. Holmes, *Chem. Phys. Lett.* **1992**, *200*, 46.

[25] H. H. Fong, A. Papadimitratos, and G. G. Mallarias, *Appl. Phys. Lett*. **2005**, *89*, 172116.

[26] P. E. Burrows, S. R. Forrest, *Appl. Phys. Lett.* **1994**, *64*, 2285.

[27] Y. H. Tak, H. Bassler, *J. Appl. Phys.* **1997**, *81*, 6963.

[28] H. Vestweber, H. Bassler, J. Gruner, R. H. Friend, *Chem. Phys. Lett.* **1996**, *256*, 37.

[29] R-.Q. Png *et al*, *Nat. Mater*. **2010**, *9*, 152.

[30] F. Huang, Y. Zhang, M.S. Liu, A.K.-Y. Jen, *Adv. Funct. Mater.* **2009**, *19*, 2457.

[31] S. Sax, N. Rugen-Penkalla, A. Neuhold, S. Schuh, E. Zojer, E. J. W. List, K. Müllen, *Adv. Mater*. **2010**, *22*, 2087.

[32] W. L. Ma, P. K. Iyer, X. Gong, B. Liu, D. Moses, G. C. Bazan, A. J. Heeger, *Advanced Materials* **2005**, *17*, 274.

[33] G. Gustafsson, Y. Cao, G. M. Treacy, F. Klavetter, N. Colaneri, A. J. Heeger, *Nature* **1992**, *357*, 477.

[34] P. A. Levermore, L. C. Chen, X. H. Wang, R. Das, D. D. C. Bradley, *Adv. Mater.* **2007**, *19*, 2379.

[35] A. Gadisa, K. Tvingstedt, S. Admassie, L. Lindell, X. Crispin, M. R. Andersson, W. R. Salaneck, O. Inganas, *Synthetic Met.* **2006**, *156*, 1102.

[36] K. Fehse, K. Walzer, K. Leo, W. Lovenich, A. Elschner, *Advanced Materials* **2007**, *19*, 441.

[37] S. Iijima, *Nature* **1991**, *354*, 56.

[38] P. A. Levermore, R. Jin, X. H. Wang, L. C. Chen, D. D. C. Bradley, J. C. de Mello, *Journal of Materials Chemistry* **2008**, *18*, 4414.

[39] K. S. Novoselov, A. K. Geim, S. V. Morozov, D. Jiang, Y. Zhang, S. V. Dubonos, I. V. Grigorieva, A. A. Firsov, *Science* **2004**, *306*, 666.
[40] C. Di, D. Wei, G. Yu, Y. Liu, Y. Guo, D. Zhu, *Adv. Mater*. **2008**, *20*, 3289.

Chapter VIII

Developing Gravure Contact Printed Flexible Polythiophene Thin-Film Transistors (TFTs)

8.1 Introduction

So far, organic semiconducting materials, including small molecules and long chain polymers, have been inferior to the solid-state inorganic semiconducting materials such as Si and GaAs in terms of electrical property and stability. During the last decade for applications in TFTs, where a fast speed of charge carrier transport is critical, various ways of enhancing mobility of devices were reported. Larger grain sizes of polycrystalline thiophene occurred by a slow formation of crystalline structure and surface treatments for favoured crystal growth using of self-assembled monolayers (SAMs) have been reported.[1-4] Also, aligning π-π molecular chains with a preferred direction for an efficient 1D charge transport has a similar effect on polycrystalline thin films, for example, using rubbing techniques[5,6]. Despite these innovative fabrication processes and numerous efforts, organic transistors still suffer from its inherent material weaknesses. Printing of semiconducting polymer inks using popular existing techniques such as ink-jet printing,[7] screen printing[8], and gravure printing[9-11] have attracted optoelectronic industry for its fast production and reduced costs for large area

displays.[12-14] Printing techniques are rapidly developing and it is expected to overcome some of the weaknesses of organic materials.

One advantage of organic materials is relatively easy to develop a new material via chemical modifications of polymer compositions or doping for a specific purpose. Also, performance of these materials can be conveniently improved using thermal treatment after being deposited[15-17], increasing of molecular weight of polymer[18], and use of high boiling point solvent[19]. In OTFTs, device structure and geometry are crucial for high performance as well as fabrication processes. A choice of gate insulator, for example, critically influences device performance owing to an energetic disorder at the interface of organic semiconductor (OSC)/insulator as well as its capacity to act as an insulator.[20]

In this Chapter, optimization of fabrication process of poly (3-hexylthiophene)-2,5-diyl (P3HT) including annealing conditions in the top gate and bottom contact OTFT is evaluated in Section 8.3. Dielectric materials of polymethylmethacrylate (PMMA), poly (2-hydroxyethyl methacrylate) (PHEMA), and crosslinkable PHEMA (X-PHEMA) with dielectric constants of 3.2, 7.95, and 5.3 respectively[37] are implemented in our OTFTs to study how important a choice of dielectric layer is in Section 8.4. A dedoping process using tetrakisdimethylaminoethylene (TDAE) is introduced and attempted in our OFET in Section 8.5. P3HT with different polymer chain lengths were printed onto ITO source/drain contact and its device performance is compared to conventional spin-coated device. Also, field-effect mobility measurement of P3HT throughout atomic force microscopy (AFM) with a variation of solvents used for dissolving P3HT and molecular weights of P3HT is discussed in Section 8.6. Finally, developing of fully printed OTFTs including an active layer, two dielectric layers and Ag gate electrode is demonstrated in Section 8.7 and 8.8.

8.2 Experimental

Materials: P3HT in five different molecular weights (M_w = 25,300, 32,000, 32,500, 34,500 and 158,000 Da) were purchased from Merck Chemicals. All organic solvents were obtained from Sigma-Aldrich. PHEMA (M_n = 16 kDa) and other insulators were obtained from Sigma-Aldrich. PHEMA with a range of molecular weights (M_n = 17-64 kDa) and narrow molecular distributions were synthesized via ATRP at Imperial College. To make X-PHEMA, PHEMA was blended with an aminal/acetal crosslinker poly(melamine-*co*-formaldehyde) (PMF; M_n~ 432/84 wt%) in *n*-butanol, isopropanol or trifluoroethanol at concentrations up to 40% by volume. For gate electrode, silver ink from Cabot and an in-house developed nanocolloid silver ink were used. The synthesized Ag ink was formulated at concentrations of 20-30 wt%. PES substrates with pre-patterned ITO electrodes were used (Figure 8.1). Either dimensions of I. length: 50 µm, width: 1300 µm or II. length: 30 µm, width: 1180 µm channels were used.

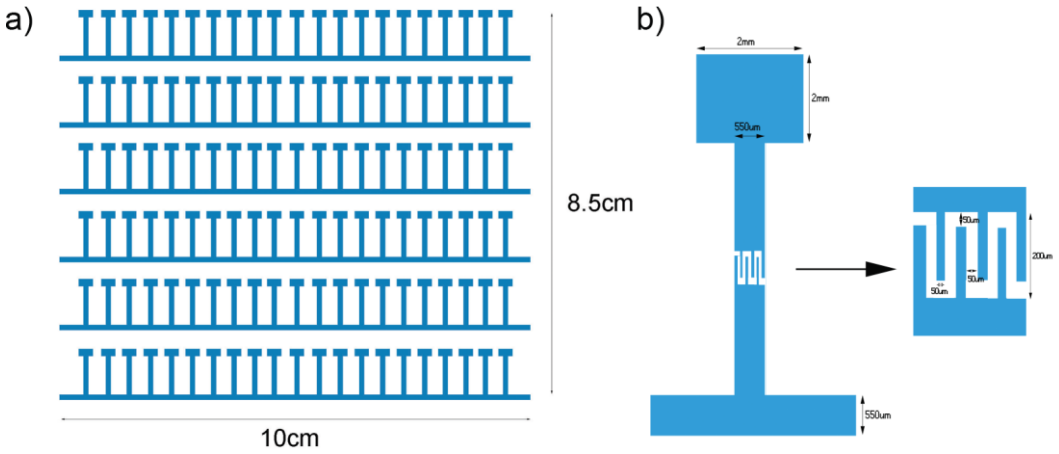


Figure 8.1 a) A schematic view of PES substrate with ITO pre-patterned. This includes 126 transistors in six columns of 21 transistors. The shaded area indicates patterned ITO. b) Dimensions of interdigitated channel between source and drain electrodes. The channel length and width of the active channel are 50µm and 1300µm respectively.

FET Preparation:

1) Spin-coating: The spin-coated devices were made using 3% by wt P3HT in chlorobenzene at 2,000 rpm for 1 min. Spin-coated dielectric layers were 7% by wt

PHEMA in IPA at 2,500 rpm for 1 min, 8% by wt X-PHEMA in TFE at 4,000 rpm for 1 min and 5% by wt PMMA in MEK at 2,000 rpm for 1 min.

2) Gravure printing: A Labratester I test printer from Schläfli-Maschinen was used to print all layers. The printing speed was 40m/min. Copper clichés were designed by Schläfli-Maschinen with machined cells at line densities from 40 to 210 lines/cm. Cells were pyramidal structures of about 20 μm in width and length and 25 μm in depth. The semiconductor cliché was designed to produce 1 mm × 2 mm rectangles. The gate cliché had 0.5 mm wide drive lines connected to 0.8 mm × 3 mm rectangular gates.

3) Al evaporation: For deposition of Al electrode, samples were transferred to a nitrogen atmosphere glove box (< 2 ppm H_2O, < 0.1 ppm O_2) to anneal at 150° C for 4 hours. The gate electrode of Al was then thermally evaporated (vacuum pressure 4×10^{-6} mbar) with a shadow mask.

Thickness Measurement: Layer thickness was measured with a Dektak profilometer from Veeco Metrology Group and α-step 200 from Tencor Instruments. The surface investigations and examination of the wetting behaviour were studied using a Zeiss Axioplan microscope with attached digital camera or the digital camera from the Dektak. Capacitance measurements of the insulators were conducted between 10 and 10^6 Hz using a Schlumberger Solartron 1260 Impedence Analyzer.

FET Characteristics: FETs characteristics were measured using an Agilent 4156C semiconductor parameter analyzer. Saturation mobility was calculated from the saturation regime in transfer characteristics at $V_D = -30V = (V_G - V_T)$ using $\partial(I_D)^{1/2} / \partial V_G = (\mu_{SAT})^{1/2} (C_i W/2L)^{1/2}$. V_T was taken as the intercept at $I_D = 0$ of a linear fit to $(I_D)^{1/2}$ versus V_G (where V_G, V_T, I_D, μ_{SAT}, C_i, W and L represent the gate voltage, threshold voltage, drain current, saturation mobility, insulator capacitance per unit area, channel width and channel length, respectively).

8.3 Annealing Effects on P3HT OFETs

An annealing process is particularly important in fabrication of organic optoelectronic devices.[21,22] The process helps to remove residual solvent being used as well as to enhance crystallinity of polymers. Enhanced mobility is often observed in materials with high crystallinity rather than disordered amorphous materials. P3HT is a p-type polycrystalline material having a field-effect mobility of between 10^{-4} to over 10^{-1} cm^2/Vs dependent on processing conditions.[21] Residual solvents hamper charge carrier transport acting as a charge trap and devices should be annealed at temperature sufficiently higher than a boiling point (BP) of a solvent used for complete removal of residual solvents.

The schematic structure of our top gate, bottom contact OFETs and the chemical structure of materials used in this chapter are provided in Figure 8.2. P3HT with 0.3 wt% in chlorobenzene was deposited onto the pre-patterned ITO source and drain electrodes defining an interdigitated channel between the two electrodes with a distance of either 30 or 50 μm.

The effects of annealing temperature and time on P3HT OFET performance were investigated in fully spin-coated devices with a channel length of 50 μm. Annealing temperature was varied from 100° C to 150° C under a melting point (T_m) of P3HT (178° C). A BP of chlorobenzene is 130° C, hence solvent removal should be completed in temperatures around 130-150° C. Transfer characteristics of OFETs with an annealing temperature variation are shown in Figure 8.3a. It shows that off-current is reduced as temperature increases and a significant reduction in the off-current was observed at temperatures between 100 and 140° C. The high off-current from the samples annealed at 100° C is attributed to a lower crystallinity degree as well as residual chlorobenzene solvents. Accordingly, an on/off current ratio is improved as temperature increases reaching $10^{4.1}$ for 150° C annealed OFETs as listed in Table 8.1. Both on-current and off-current reduced for case of annealing at 150° C, hence maintaining its overall on-off current ratio similar to the 140° C annealed device. Field-

effect mobility, however, shows only a small variance maintaining a constant saturated mobility of 3.7 × 10^{-3} cm^2/Vs for all cases. It suggests that annealing temperature between 100°C and 150°C is relatively independent of the conformation of the polymer backbone.

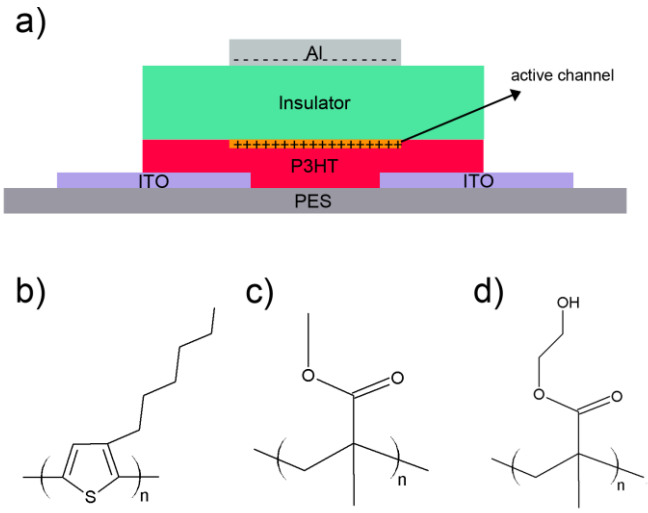


Figure 8.2 a) Device structure of OFET and the chemical structures of materials used in this chapter: b) P3HT, c) PMMA, d) PHEMA.

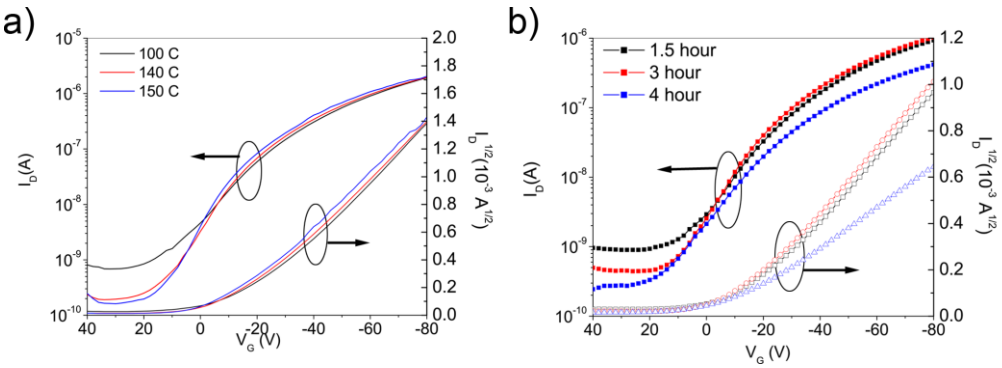


Figure 8.3 OTFT performance with a variation of a) annealing temperature (done for 4 hours) and b) annealing duration (annealed at 120° C).

Annealing condition	V_T (V)	Linear Mobility (cm^2/Vs)	Saturation Mobility (cm^2/Vs)	On-current (A)	Off-current (A)	On-off ratio
100° C, 4 hours	-13	2.5×10^{-3}	3.7×10^{-3}	1.9×10^{-6}	6.9×10^{-10}	$10^{3.45}$
140° C, 4 hours	-12	3.5×10^{-3}	3.7×10^{-3}	2.0×10^{-6}	2.0×10^{-10}	10^{4}

150° C, 4 hours	-10	3.5×10^{-3}	3.7×10^{-3}	2.05×10^{-6}	1.6×10^{-10}	$10^{4.1}$
120° C, 1 and ½ hours	-12	2.5×10^{-3}	2.7×10^{-3}	9.3×10^{-7}	9×10^{-10}	10^{3}
120° C, 3 hours	-10	2.6×10^{-3}	2.83×10^{-3}	1×10^{-6}	4.4×10^{-10}	$10^{3.36}$
120° C, 4 hours	-8	1×10^{-3}	1.1×10^{-3}	4.2×10^{-7}	2.35×10^{-10}	$10^{3.24}$

Table 8.1 OTFT performances with variations of channel length and annealing conditions. Field-effect mobility was extracted with capacitance per unit area of PMMA (C_i = 5.8 nF) at V_D= -50V (saturation) and -20V (linear) in transfer characteristic.

It also shows that off-current was reduced with an increase of annealing duration as depicted in Figure 8.3b) at about 30 V of V_G. Threshold voltage, which is determined by extrapolation of the $I_D^{1/2}$ – V_G lines, approached close to zero voltage at higher temperatures and longer duration of annealing. It means that trap sites at the interface of P3HT/insulator have been removed at the temperature. Annealing is crucial for organic FETs for removing residual solvents and trapped oxygen and moisture dopants within its molecule chains, and is especially important for thiophene polymers because of its high susceptibility against water molecules,[23] enhancing a charge carrier mobility and an on/off current ratio by reducing off-current. Zen *et al*. reported that annealing can also improve crystallinity of P3HT, and its degree of crystalline can vary with solvents used.[22, 24] Figure 8.4 shows annealing effect on crystallinity of P3HT using AFM measurement. P3HT with fabrillar structures is observed (Figure 8.4a) and it becomes more packed (Figure 8.4b) via thermal treatment. Fabrillar structure is more favourable in charge transport than grainlike morphology.[25] Cho *et al*. reported that this transition in P3HT abruptly occur above 150° C.[16] We could not increase annealing temperature above 150° C as our polyethersulphone (PES) flexible substrate underwent degradation. However, fabrillar structures were observed in the samples annealed at 150° C. Also, pin-holes, which may hamper charge carrier transport by forming a direct conducting channel between electrode and organic layers, were observed in the pre-annealed samples while they were all filled after an annealing process. Enhanced packing of chains promotes hopping of charge carriers, hence a field-effect mobility could be improved. Output characteristics of OFETs shown in Figure 8.5 indicate a better modulation of I_D due to improved charge transport and injection in P3HT.

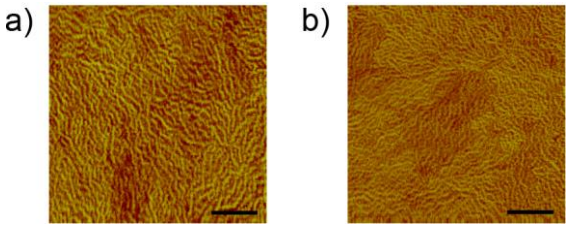


Figure 8.4 AFM images of P3HT in chlorobenzene a) as-prepared b) after annealing at 150° C for 4 hours. AFM measurements were recorded at IMEC by Oliver Douheret. Images are 1µm × 1µm size. A scale bar indicates 200 nm.

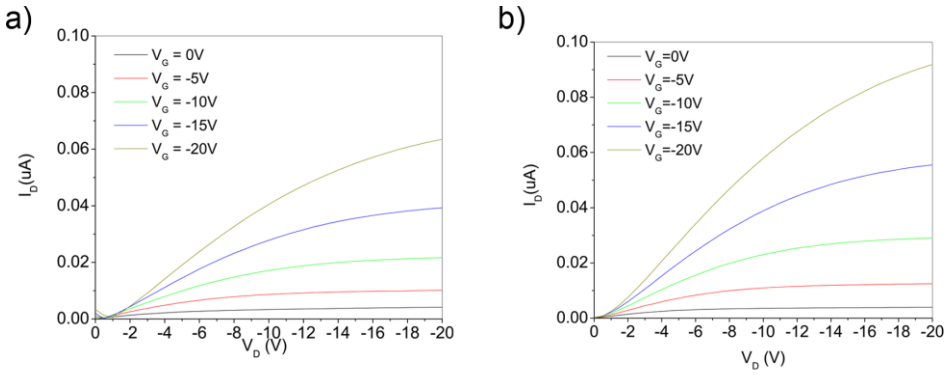


Figure 8.5 Output characteristics of P3HT OFETs a) annealed at 100° C and b) annealed at 140° C.

8.4 Gate Insulators with Different Dielectric Constant k

As mentioned earlier, a gate insulating layer in OFETs is crucially important for device operation and achieving high performance. The layer acts as a capacitor between two conducting channels, one is the gate electrode and the other is the semiconducting layer. Depending on the capacity of the layer and its thickness, a device can be switched at high speed with a low turn on voltage operation. Organic FETs have a limited choice of insulating materials with a low dielectric constant while SiO_2 (κ=3.9) is a popular insulator for inorganic FETs. Recently, a hybrid structure of using inorganic oxide layers as a gate insulator have become popular in OFETs for its high capacity and stability in air ambient atmosphere.[30-32] Also, use of self-assembled monolayers (SAMs) as a gate dielectric layer is another interesting trend for high performance OFETs.[33]

Susceptibility of organic materials against oxygen and moisture dopants should be minimized as molecules can be trapped inside a network of molecular structures in an active layer and become conducting dopants causing serious leakage currents and high off-current. Hysteresis in device operation is more dependent on the bulk property of the active layer than the interface with the insulating layer.[34] Therefore, thermal annealing after deposition of a dielectric layer or use of materials with low solubility in water (non polar – low-κ[35]) can help with avoiding doping by oxygen and moisture. In top gate OTFTs, a gate dielectric layer is significantly important as it covers the active layer and protects from doping by oxygen and moisture.

Three different insulators, namely poly (methylmethacrylate) (PMMA), poly (2-hydroxyethyl methacrylate) (PHEMA), and crosslinkable PHEMA (X-PHEMA) are analyzed to examine its feasibility as a gate dielectric layer in our OFETs. Dielectric properties of the insulators are listed in Table 8.2. The capacitance per unit area, C_i, determines a material property and E_B is the breakdown voltage of dielectric materials at high fields, which is a similar concept to electric displacement, D_{max}. In order to achieve high capacitance for effective switching of OFETs, either a relative dielectric constant (ε_r) should be high or a thickness of the layer need to be reduced. Organic materials, however, are susceptible in air ambient atmosphere to doping. Also, pin-holes can be easily formed and it becomes a conducting channel between the gate electrode and the active layer, where the current flowing through is called a leakage current. For effective switching of OFETs, the formation of pin-holes should be avoided, hence building of a thick insulating layer can be a useful way for protecting the underlying OSC. PMMA has the lowest κ (3.25) among the insulators used in the experiments, which is slightly less than a value (3.5) from Ref. [36]. For its high breakdown voltage, it is expected that OFETs with PMMA will achieve enhanced insulating property and produce low leakage currents.

Insulator	$\varepsilon_r(\kappa)$	C_i (nF/cm^2)	Breakdown field, E_B (V/cm)	Breakdown voltage at 500 nm (V)
PMMA	3.25	5.8	4.6×10^6	230
PHEMA	7.95	14.1	2.3×10^6	115
X-PHEMA	5.3	9.5	2.8×10^6	140

Table 8.2 Values of measured relative permittivity, ε_r, and capacitance per unit area, C_i from metal-insulator-metal (MIM) structure. Capacitance was obtained for thickness of 500 nm from its relation of $C_i = \varepsilon_0\varepsilon_r / d$. These values were obtained by A. Guite[37].

Figure 8.6 shows transfer characteristics of P3HT OFETs with different gate insulators. All experimental conditions were fixed identically including channel dimension, layer thickness, and annealing condition for P3HT. A serious hysteresis was observed in OFET with PMMA while it was relatively small from OFETs with the other insulators. PHEMA showed the minimum degree of a deviation between forward and reverse scans among the insulators. A hysteresis can be attributed to oxygen and moisture dopants trapped in the insulating layer[34] or a large energetic disorder at the interface between an organic semiconductor (OSC) and an insulator[35]. Park *et al*. suggested that a hysteresis in a dielectric layer is more bulk related than interface related as they showed that the hysteresis in a dielectric material of high susceptibility against water and oxygen was dramatically reduced by capping the layer with a thick low susceptibility (low κ) dielectric layer forming a multiple insulating layer structure.[38] Our OFETs are top gate structure and device performance is strongly influenced by a choice of insulator (and solvents). In our case, a high degree of hysteresis in PMMA can be ascribed to trapped oxygen and water in either/both interface or/and bulk of the insulator. A main difference between PMMA and the other insulators is that PMMA has a relatively low κ (3.25) referring that it has a low susceptibility against water and oxygen. It may be true that the trapped oxygen and water dopants in the bulk of P3HT layer during deposition of PMMA could not be removed completely despite a thermal annealing process in nitrogen, which was carried after the PMMA deposition. The dopants are still trapped at the interface because P3HT was deposited and annealed in ambient conditions. Printing of P3HT will be carried in ambient conditions so that the fabrication conditions were kept identical for a comparison.

Figure 8.7 shows the output characteristics of OFETs with different insulating layers. A modulation of I_D reached its saturation regime in cases of PMMA and X-PHEMA while the drain current increased linearly similar to an ohmic response curve in case of PHEMA. This may originate from the leakage currents flowing through the insulating

layer. High κ value of PHEMA (κ = 8) has a high polar property and it may contain a large amount of oxygen and water inside the PHEMA layer. Compared to the PMMA case where hysteresis in transfer curve is the highest among the insulators, the PHEMA has a little hysteresis proposing that the hysteresis was mainly caused by trapped extrinsic dopants at the interface rather than from the bulk of insulator. The X-PHEMA layer modulates less net currents than the PMMA but it shows a pronounced field-effect modulation of I_D.

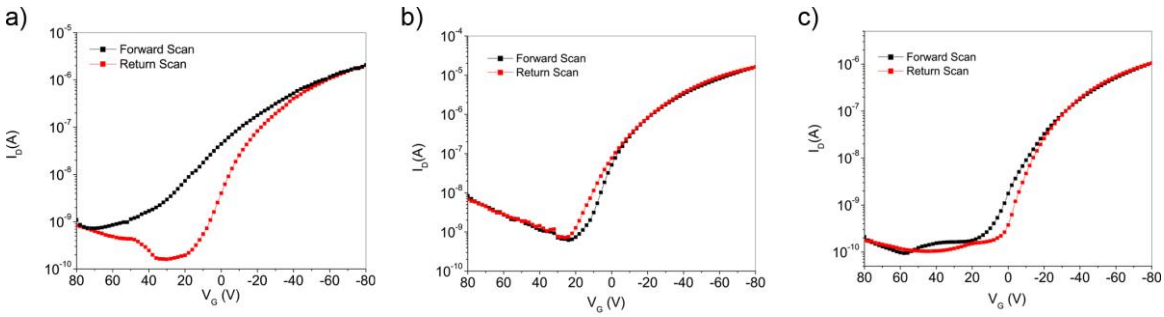


Figure 8.6 Transfer characteristics of OFETs with insulators a) PMMA, b) PHEMA, c) X-PHEMA.

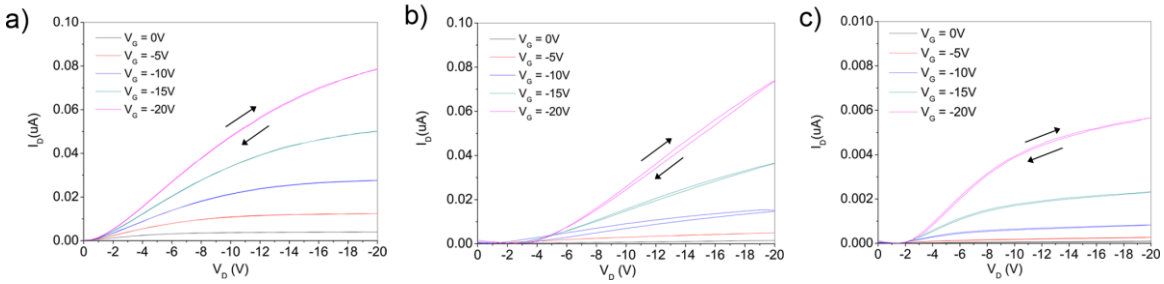


Figure 8.7 Output characteristics of OFETs with insulators a) PMMA, b) PHEMA, c) X-PHEMA.

Performance parameters of OFETs with the three insulating layers are listed in Table 8.3. OFETs with PHEMA as an insulating layer showed the best performance in terms of low threshold voltage (-2 V) and high on/off current ratio ($10^{4.93}$) attributed to the increased on-current and reduced off-current. Mobilities were increased slightly due to the minimized charge trap densities at the interface. Leakage currents, however, showed that the PMMA case has the lowest level of leakage currents having its ratio I_D/I_G at V_G of -80 V as 206 whilst PHEMA and X-PHEMA recorded 7 and 13 respectively. It again appears that a low κ value of PMMA with a relatively non-polar property enhances its insulating functionality as it is less susceptible against the extrinsic dopants. In other

words, device performance such as an on/off current ratio and a field-effect mobility is more related to the interface state between OSC/insulator where the conducting channel is formed. On the other hand, the leakage currents is strongly related to the dielectric constant of the insulator and the insulator should have a low susceptibility against the extrinsic dopants for a low level of leakage currents.

Gate Insulators	Linear Mobility (cm^2/Vs)	Saturation Mobility (cm^2/Vs)	V_T (V)	On-current (A)	Off-current (A)	On-off ratio	I_D / I_G (V_G = -80V)
PMMA	3.5×10^{-3}	3.7×10^{-3}	-10	2.05×10^{-6}	1.6×10^{-10}	$10^{4.1}$	206
PHEMA	5×10^{-3}	5.5×10^{-3}	-2	7.0×10^{-6}	8.1×10^{-11}	$10^{4.93}$	7
X-PHEMA	1.5×10^{-3}	1.7×10^{-3}	-23	1.06×10^{-6}	1.04×10^{-10}	10^{4}	13

Table 8.3 Device performance of OFETs with different gate insulators. Field-effect mobility was extracted at V_D= -50V (saturation) and -20V (linear) in transfer characteristic. Leakage current was extracted when it is in maximum (V_G = -80 V). Channel length and width are 30 μm and 1,180 μm respectively.

8.5 Dedoping Treatment

As P3HT is known to be highly reactive with ambient dopants such as oxygen and moisture, it is always important to process in air-free atmosphere during fabrication of devices using P3HT. Once, doping into P3HT layer has happened owing to a slow diffusion of oxygen through the polycrystalline film, the bulk conductivity of P3HT is increased. The trapped extrinsic dopants inside organic layers can be removed effectively using a tetrakisdimethylaminoethylene (TDAE, $(Me_2N)_2C=C(NMe_2)_2$) treatment. [39] The chemical structure of TDAE is shown in Figure 8.8. TDAE molecules transfer negative charge to the initially p-doped P3HT polymer, which then results in the formation of neutral P3HT.

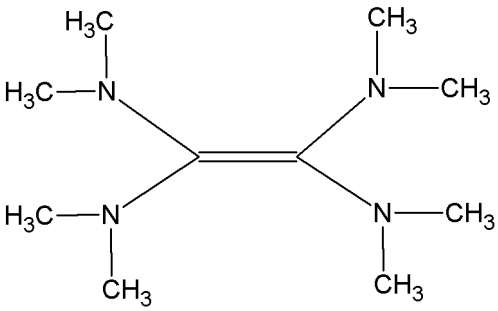


Figure 8.8 The chemical structure of TDAE

We have tried TDAE treatment to dedope any extrinsic dopants diffused into the P3HT organic molecules. Figure 8.9-8.10 describe OFETs characteristic after the TDAE treatment. Compared to a device fabricated and post-measured after preserving in nitrogen for 40 days, a device with the TDAE treatment done after preserved in the same duration in nitrogen filled atmosphere achieves an increase of an order of magnitude of on-current with a sacrifice of an order of magnitude higher off-current, hence maintain a similar total on/off current ratio. It is difficult to observe any significant symptoms of dedoping of extrinsic dopants. The increased off-current suggests doping of moisture and oxygen still exist and the hysteresis becomes even wider and deeper. A reason for less effectiveness after the TDAE treatment in our OFETs may be attributed to the device performance of the OFETs showed a clear transistor characteristics with saturated I_D at high V_D and a high on/off current ratio even before the treatment. The effect of the TDAE treatment can be more pronounced for a device with very low performance.[39]

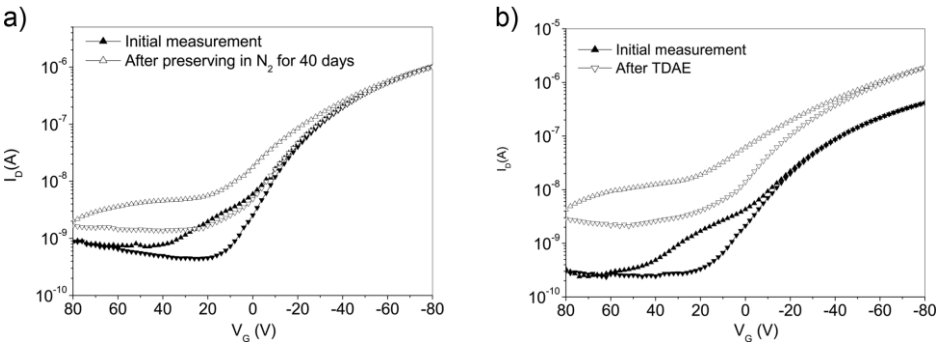


Figure 8.9 Transfer characteristics of OFETs a) without TDAE treatment b) with TDAE treatment. Upper and lower triangle at each graph indicates forward and return scan respectively. The TDAE treatment was done by F. Meng.

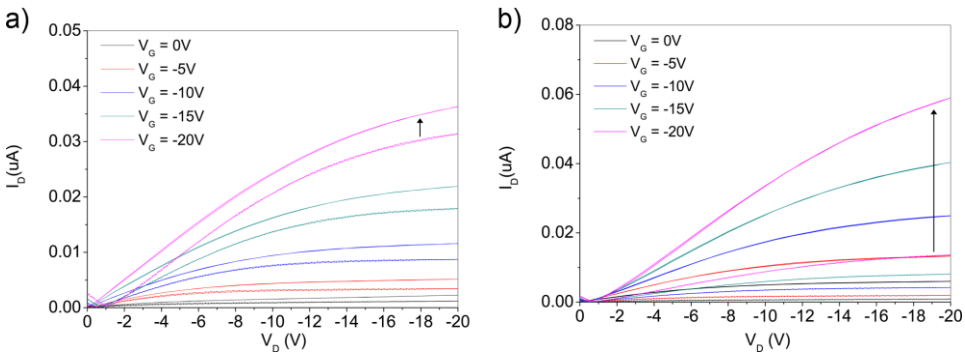


Figure 8.10 Output characteristics of OFETs a) without TDAE treatment b) with TDAE treatment. Lines in upper range indicate initial measurement while in lower range indicate post-measurement. The TDAE treatment was carried by F. Meng.

8.6 Printed P3HT and Related Issues in OFETs

Organic semiconducting (OSC) materials will achieve its full societal impacts by introducing fast speed printing technologies.[12-14, 40] Gravure printing, which is one of traditional roll-to-roll (R2R) printing methods typically used for newspaper and package of products, has one of its fastest speeds reaching maximum speeds up to 60 m^2/s.[41] Recently, high performance p- and n-type transistors were fabricated by gravure printing.[42,43] In the past, various printing methods were implemented for printing of electronic OSC materials. Ink-jet printing is one of the most famous and advanced printing methods among them.[44] A high resolution pattern with around ~1 μm size could be developed.[45-49]

At the same time, aligning of crystal or polycrystalline molecules is important for achieving high charge carrier mobilities.[50-53] Grain boundaries of polycrystalline thiophene are closely related to the charge carrier mobility as a large grain size has less grain boundary regions which can act as a trap for charge carriers.[54] A number of methods have been investigated to increase a grain size. High molecular weight materials with long molecular lengths can achieve hopping of charge carrier furthers before they hop to another chain and longer chains provide charge carriers more opportunities for hopping to neighbouring chains.[55-58] Also, it was reported that the grain size of crystals is dependent on the speed of formation.[59] The boiling point of

solvents and deposition methods can control the crystal formation speed, therefore, a crystal with higher grain size was observed from using either/both high boiling point solvents[19] or/and deposition method with a slow evaporation speed[59-61]. Also, a surface treatment of a substrate using low surface energy materials such as HMDS[62] or self-assembled monolayer (SAMs)[1,4,24,63] can increase charge carrier mobility because the molecular orientation on the treated surface becomes more favour able to charge carrier transport.

In this Section, gravure printed P3HT films and related issues in field-effect mobility are discussed. Before looking into printing issues, bulk mobility of P3HT film was measured to find out changes in mobility with variations of molecular weight of P3HT and boiling point of solvents used for P3HT dissolution. To investigate the correlation between molecular weight and field-effect mobility, bulk mobilities of different molecular weights of P3HT were analyzed by C-AFM at IMEC. In this experiment, the bulk mobility could be calculated by space-charge limited current (SCLC) defining local charge density in the P3HT molecules using the following equation (8.1):

$$I = \frac{3\pi}{4} \cdot \mu \varepsilon_r \varepsilon_0 \cdot \frac{V^2}{r} \qquad (8.1)$$

where r is the tip radius. Figure 8.11 shows AFM images of P3HT with different molecular weights. Density of fabrils is larger in lower molecular weight P3HT and vice versa. High molecular weight P3HT has a longer chain length than the lower molecular weight material hence it should have better connectivity between fabrillar rods inducing improved charge carrier mobility.[58] The bulk charge carrier mobility measured by C-AFM indicates a tendency that mobility is generally improved in the higher molecular weight polymers(Figure 8.12).

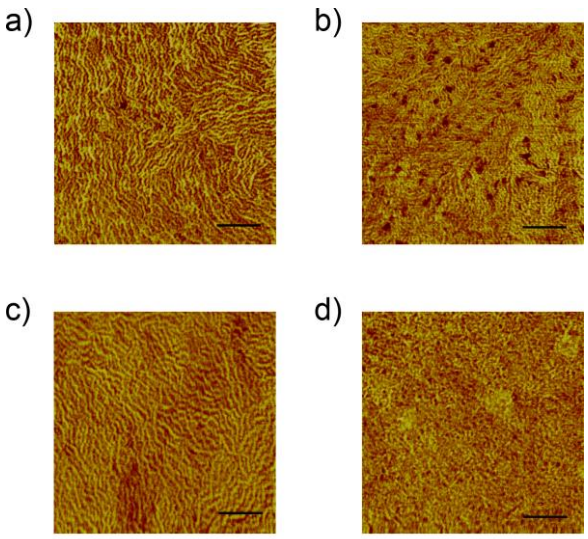


Figure 8.11 AFM images of different molecular weight of P3HT with M_n of a) 12,800, b) 16,250, c) 18,650 and d) 56,000 g/mol. A scale bar indicates 200 nm. AFM images were recorded at IMEC by Oliver Doucheret.

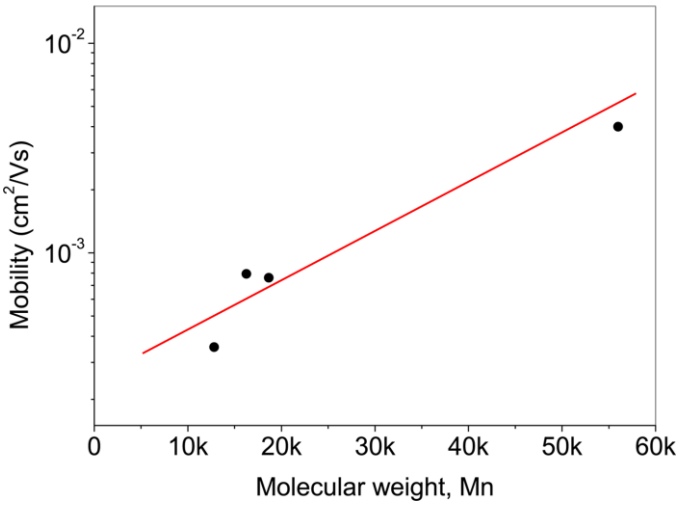


Figure 8.12 Molecular weight dependency of charge carrier mobility in polycrystalline P3HT. The mobility was measured by C-AFM at IMEC by Oliver Douheret.

A slow evaporation of solvents causing a slow formation of crystalline structures can be induced by using high boiling point solvents. A common solvent for P3HT is chlorobenzene but solvents with a higher boiling point than chlorobenzene such as dichlorobenzene, tetrahydronaphtalene, and indan were introduced and field-effect mobility was improved in the deposited P3HT thin films using the high boiling point solvents. AFM images of P3HT spin-coated with different boiling point solvents are

given in Figure 8.13. P3HT in chlorobenzene (Figure 8.13a) showed clearly defined fabrillar structures which becomes more grain-like as the boiling point of solvents increases. Hence, it can be said that the formation of crystalline structures is therefore closely related to evaporation speed of solvents. Also, more improved bulk charge carrier mobilities were observed in OFETs with higher boiling point solvent used for P3HT dissolution as shown in Figure 8.14. The P3HT in indan indicates a very low mobility even though its high boiling point (177° C). The high performance P3HT OFETs using chloroform with a low boiling point was observed (61.2° C) with a field-effect mobility up to 4.2×10^{-3} cm^2/Vs and an on/off current ratio of 8.0×10^4.[64] There may be other factors affecting orientation of molecules such as polarity of solvents, solubility and so on. Chemical properties of indan may differ from the other solvents although their boiling points are in a similar range.

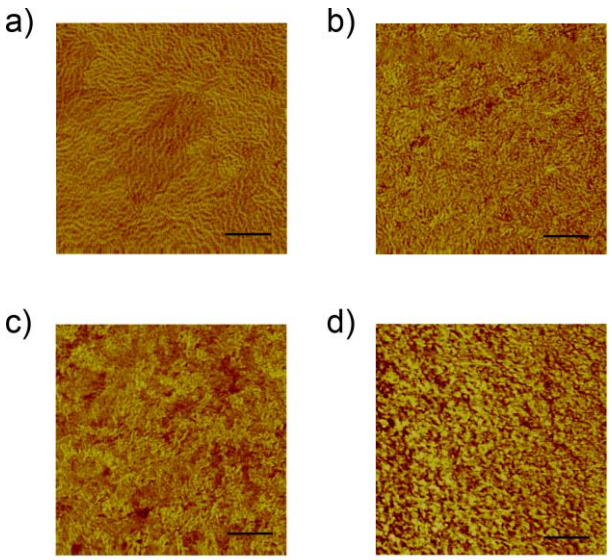


Figure 8.13 AFM images of P3HT deposited in different boiling points of solvents as a) chlorobenzene (131° C), b) indan (177° C), dichlorobenzene (DCB) (180° C), and d) tetrahydronaphtalnene (THN) (208° C). P3HT film was annealed at 150° C for 4 hours before the measurement. A scale bar indicates 200 nm. AFM images were recorded at IMEC by Oliver Douheret.

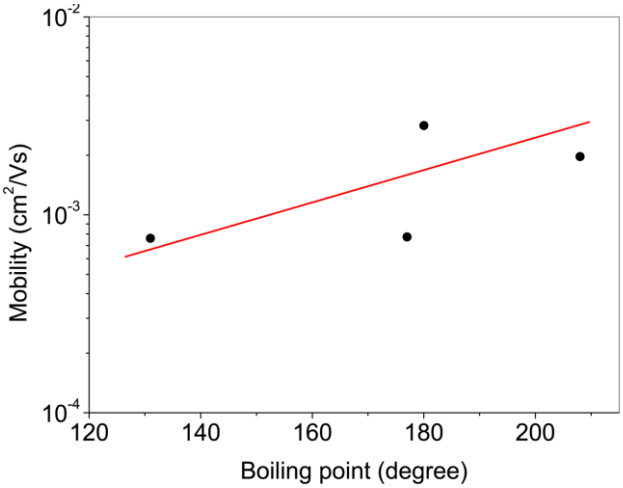


Figure 8.14 Boiling point dependency of bulk charge carrier mobility measured by C-AFM. C-AFM was recorded at IMEC by Oliver Douheret.

Next, we consider printing behaviour of P3HT formulations. P3HT ink formulations were gravure contact printed using different molecular weights of P3HT and boiling point of solvents. Figure 8.15 shows microscale images of printed P3HT thin films on the patterned source/drain ITO electrodes on a PES substrate. An homogeneous film surface can be achieved by appropriate molecular weight of P3HT and boiling point of solvents. From series of printing P3HT, we found that P3HT was printed with excellent homogeneity by using P3HT molecular weights around M_n of 16,000-19,000 g/mol and high boiling point solvents such as tetrahydronaphtalene (THN) or indan. The thicknesses of printed thin films can be controlled by the depth of the engraved cells on the cliché (10-70 μm) and line density of the engraved patterns (number of lines/cm). A mechanism of thin film formation here for printing P3HT is done using of relatively high viscosity inks which constrain movements of ink formulation during the evaporation hence it is ideal for printing high resolution patterns and removal of the coffee stain effect.[65] However, it may cause a rough surface at the μm scale owing to high intermolecular forces between solvent molecules during the evaporation.[66] In this experiment, printing P3HT was mainly concerned for a high resolution printing, and the other printing mechanism for inducing uniform surfaces is discussed in Chapter 6.

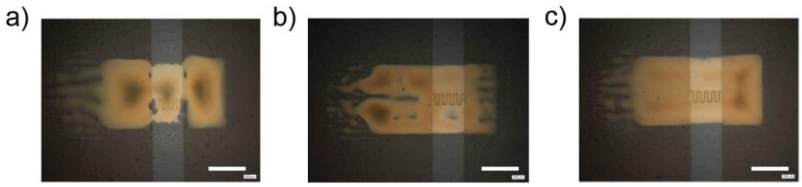


Figure 8.15 Microscopic images of printed P3HT on the pre-patterned source/drain ITO electrode (channel length = 50μm): a) M_n: 16,250 g/mol, THN, b) M_n: 18,650 g/mol, Indan, c) M_n: 18,650 g/mol, THN. A scale bar indicates 500 μm. Films were printed and optical images were recorded at Asulab by M. Voigt.

Figure 8.16 presents transfer characteristics of OFETs with a gravure printed P3HT films with a variation of molecular weights and solvents which were performed at Asulab by Monika Voigt. PHEMA was spin-coated on the top of the P3HT layer as a dielectric layer and the Al gate electrode was thermally evaporated. Both higher on-currents and off-currents were observed in the printed P3HT with M_n of 18,650 g/mol. It may be attributed to doping of extrinsic oxygen and water molecules during transportation from Asulab in Switzerland to Imperial College in London even though the P3HT printed samples were annealed at 150° C for 4 hours prior to the deposition of the top insulating layer. A good modulation of I_D was observed in the P3HT with M_n of 18,650 g/mol printed devices reaching more than 1.5 μA at an applied V_G of -50 V (Figure 8.17). This is an order of magnitude higher than the other molecular weight P3HT devices (Figure 8.17a-b). The printed P3HT with M_n of 18,650 g/mol devices showed an excellent surface profile attributed to the molecular weight of P3HT is in a range for printing a smooth surface as described in Figure 8.15. Homogeneity of the printed P3HT surface can be related to the assemblage of the P3HT molecules during the deposition. Charge carrier transport is at least an order of magnitude faster in M_n of 18,650 g/mol than the other P3HT batches as listed in Table 8.4. It again supports that there exists a strong correlation between the molecular weight and the homogeneity of the printed thin film. Nanoscale analysis is necessary for further investigations on crystalline structures of P3HT molecules. Also, the OFETs with high molecular weight P3HT of 56,000 g/mol achieved a higher on/off ratio attributed to higher on-current. It is true that a higher molecular weight polymer has more condensed percolated structures, which result in higher rates of charge transport between the molecular chains, but it may

be also dependent on a doping level of extrinsic dopants which can vary with the printing condition.

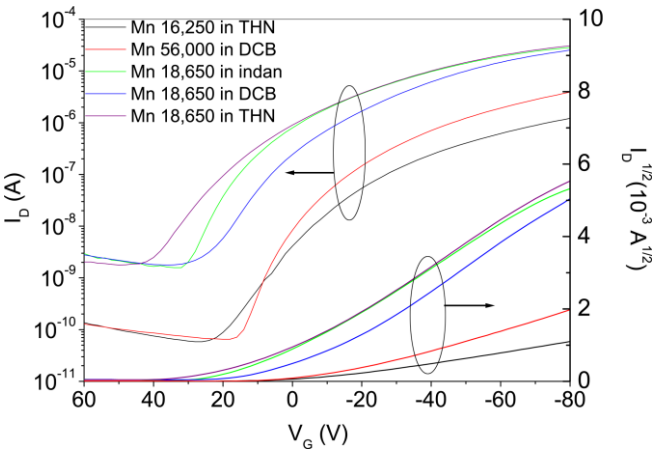


Figure 8.16 Transfer characteristic of P3HT printed OFETs with different M_w and BP.

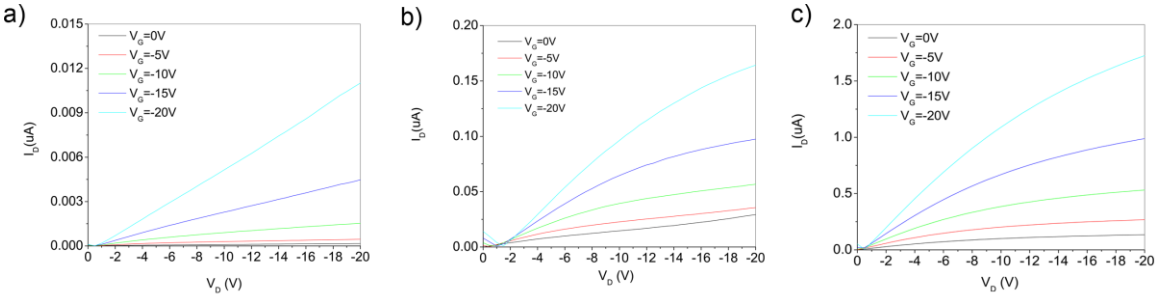


Figure 8.17 Output characteristic of P3HT printed OFETs with different M_n and BP: a) M_n: 16,250 g/mol, THN, b) M_n: 56,000 g/mol, DCB, c) M_n: 18,650 g/mol, DCB.

P3HT formulation	Linear Mobility (cm^2/Vs)	Saturation Mobility (cm^2/Vs)	V_T (V)	On-current (A)	Off-current (A)	On-off ratio
M_n: 16,250 g/mol, THN	5.3×10^{-4}	8.4×10^{-4}	-8	1.2×10^{-6}	5.9×10^{-11}	$10^{4.3}$
M_n: 56,000 g/mol, DCB	1.7×10^{-3}	2.9×10^{-3}	-10	3.9×10^{-6}	6.5×10^{-11}	$10^{4.8}$
M_n: 18,650 g/mol, indan	1.35×10^{-2}	1.4×10^{-2}	10	2.8×10^{-5}	1.6×10^{-9}	$10^{4.25}$
M_n: 18,650 g/mol, DCB	1.6×10^{-2}	1.7×10^{-2}	-4	2.5×10^{-5}	1.8×10^{-9}	$10^{4.15}$
M_n: 18,650 g/mol, THN	1.5×10^{-2}	1.8×10^{-2}	5	3×10^{-5}	1.8×10^{-9}	$10^{4.23}$

Table 8.4 Transistor performance of P3HT printed with 7wt% PHEMA spin-coated OTFTs. Field-effect mobility was extracted with capacitance per unit area of PHEMA (C_i=14.1nF) at V_D= -50V (saturation) and -20V (linear) in transfer characteristic.

8.7 Fully Gravure Printed P3HT OFETs

Having investigated printing of P3HT and its dependency with molecular weight, evaporation speed of solvents, and deposition method, we now move onto printing the rest of layers for realization of fully gravure printed OFETs. Gate dielectric layers such as PMMA, PHEMA, and X-PHEMA can be gravure printed and their electric properties involving leakage current blockage and dielectric constant were already analyzed in Section 8.4. The PMMA was found to produce the most efficient blocking of leakage current from the gate electrode for its low κ value (less polar), which is less susceptible against moisture and oxygen molecules, but it showed a very high hysteresis on the transfer characteristic (Figure 8.6). The PHEMA, on the other hand, recorded less hysteresis owing to its relatively high κ value (κ = 8) so that most of the trapped extrinsic dopants inside or on the surface of P3HT layer can be extracted during an annealing process throughout the PHEMA layer but a high level of dopants trapped inside either/both the insulating or/and the P3HT layers caused an ohmic like behaviour in the output characteristic.[39,67,68] Park *et al*. suggested that a bilayer structure of insulating layers comprising of an insulating layer, which has non-polar property and induces high electrical modulation, adjacent to an active layer and another insulating layer with high air stability as a capping layer can be used to perform both high insulating and high capacitance characteristics simultaneously.[38]

For our printed insulating layer, we examined a multilayer structure of two insulating layers with a thickness of 300 nm for each layer. The PHEMA induced good modulation of I_{DS} achieving $10^{4.92}$ and 5.5×10^{-3} cm^2/Vs, which is the best among the three insulating layers for the spin-coated OFETs. The PHEMA layer was printed as the bottom insulating layer for high performance and prior to the deposition of the crosslinked PHEMA (X-PHEMA). The X-PHEMA was chemically modified (crosslinking) to increase the bonding strength of the molecules to protect from dissolution against upper liquid crystal (LC) molecules by F. Meng in the Chemistry Department at Imperial College London. Another benefit of using the layer is encapsulation of the underlying PHEMA and the P3HT against extrinsic dopants. The

schematic of the fully printed OFETs is presented in Figure 8.18. With the X-PHEMA fixed as the top insulating layer as the X-PHEMA is the only material which is not dissolved against the LC molecules, the bottom insulating layer was varied by the three insulating layers. Figure 8.19 describes transfer characteristics of the OFETs with a performance comparison from the insulating layers. As expected the PHEMA/X-PHEMA case showed the minimum hysteresis and good transistor performance among the insulating layers (Figure 8.19b). The highest level of hysteresis is observed in the case of PMMA/X-PHEMA (Figure 8.19a) which follows a trend in the spin-coated OFETs. The output characteristics of the same structures are shown in Figure 8.20. In the case of PHEMA/X-PHEMA OFETs, the I_{DS} current reaches to the saturation regime at high V_{GS} while I_{DS} linearly increases at higher V_{GS} for the spin-coated single PHEMA layer OFETs (Figure 8.7b). The relatively high insulating property of the X-PHEMA than the PHEMA induces this saturation of I_{DS}. The capacitance of double insulating layers for the total thickness of 600 nm is 6.8, 9.8, and 7.8 nF/cm^2 for PMMA, PHEMA, and X-PHEMA respectively, with a combination of the top X-PHEMA layer.

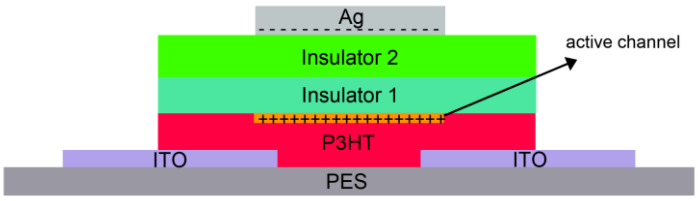


Figure 8.18 Device structure of OFETs with double insulating layer structure.

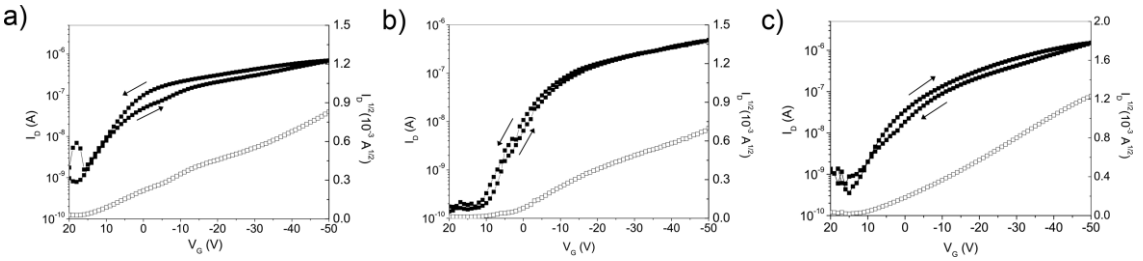


Figure 8.19 Transfer characteristics of double insulating structures of a) PMMA, b) PHEMA, c) X-PHEMA with X-PHEMA as the top insulating layer. Filled and empty symbols refer to left and right axis respectively. The devices were printed by M. Voigt and measured by A. Guite.

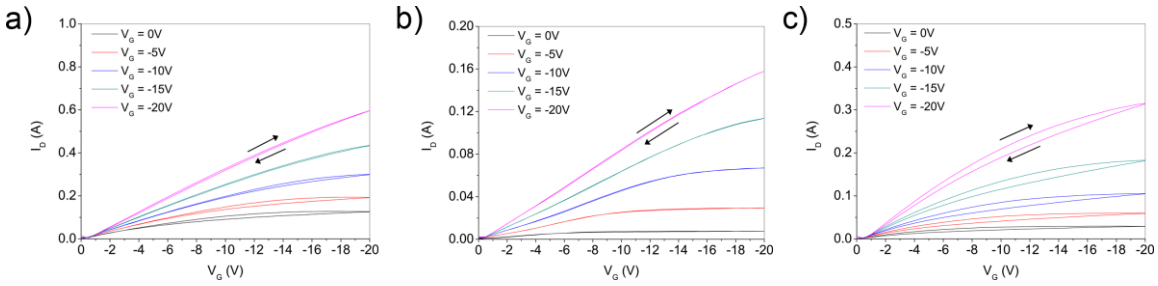


Figure 8.20 Output characteristics of double insulating structures of a) PMMA, b) PHEMA, c) X-PHEMA with X-PHEMA as the top insulating layer. The devices were printed by M. Voigt and measured by A. Guite.

The performance values for the OFETs with a double insulating layer structure are listed in Table 8.5. The mobilities and on/off current ratios of the OFETs lay in the range between 1-5×10^{-3} cm^2/Vs and 10^{3-4}. The reason of having the similar performance between the OFETs is attributed to the identical structural and fabrication conditions except the deposition of the bottom insulating layer. Interestingly, the high insulating property of PMMA (I_{DS} / I_{GS} ~ 200) in the single insulating layer OFET is reduced to less than 10, which is similar to the other two cases. This suggests that the top insulating layer has a strong influence on device stability because the bottom PMMA layer is not thick enough (300 nm) to give a good insulating functionality.

P3HT formulation	Linear Mobility (cm^2/Vs)	Saturation Mobility (cm^2/Vs)	V_T (V)	On-current (A)	Off-current (A)	On-off ratio	I_{DS}/I_{GS} ratio (at V_{GS} = -50V)
PMMA/X-PHEMA	1.7×10^{-3}	1.9×10^{-3}	16	6.9×10^{-7}	7.9×10^{-10}	$10^{2.94}$	4
PHEMA/X-PHEMA	1.2×10^{-3}	1.3×10^{-3}	4	4.9×10^{-7}	1.46×10^{-10}	$10^{3.5}$	11.5
X-PHEMA/X-PHEMA	4.7×10^{-3}	5.4×10^{-3}	4	1.5×10^{-6}	3.5×10^{-10}	$10^{3.6}$	5

Table 8.5 Performance parameters of gravure printed OFETs with Al evaporated gate electrode. A double insulating structure was applied and P3HT batch used here is 4% by weight (M_n: 18,650 g/mol) in indan. Channel length and width are 50 and 1,300 µm respectively. Field-effect mobility was extracted at V_D= -50V (saturation) and -20V (linear) in transfer characteristic.

8.8 Printed Ag Metal Inks

Solution processable metal inks can be used as a gate electrode in OFETs.[69-71] A main advantage of this type of ink is that it reaches to the conductivity of bulk metal after a sintering process at relatively low temperature between 125-200° C. Applying a conductive ink as a gate electrode completes our fully printed OFET structure. The Chemistry Department at Imperial College has succeeded in synthesizing a high conductive Ag nanoparticle ink having a resistance of 0.43 Ω/sq for spin-coated on glass substrate and increased resistance of 9 Ω/sq for gravure printed formulation on PES flexible substrate. This value is comparable to commercial state-of-the-art Ag conductive ink with a sheet resistance normally between 200-500 mΩ/sq on glass[72]. Similarly, another version of Ag conductive ink was developed by Asulab which recorded a relatively high sheet resistance of 10.55 Ω/sq for a spin-coated film on glass substrate and 1.25×10^4 Ω/sq for gravure printed film on a PES flexible substrate. A large variance of conductivity between spin-coated on glass and gravure printed on PES may be attributed to the wetting behaviour of the conductive inks and the homogeneity of the substrates. A comparison of the Ag conductive inks is listed in Table 8.6.

Ag conductive ink	Sheet resistance of spin-coated on glass substrate (Ω/sq)	Sheet resistance of gravure printed on PES substrate (Ω/sq)
Asulab (conc. of 30 %)	10.55	1.25×10^4
Imperial College (conc. of 25 %)	3.66	15
Imperial College (conc. of 30 %)	0.43	9

Table 8.6 Comparison of Ag conductive inks developed by either Asulab or Imperial College. A thickness of Ag layer is 120 nm. The conductivity measurement was done by M. Voigt.

A comparison of device performance using different Ag conductive inks is shown in Figure 8.21 for transfer characteristics and Figure 8.22 for output characteristics. The Ag nanoparticle ink developed by Imperial College (IC) with concentration of 30% recorded a high performance transistor with a on/off ratio of $10^{4.62}$ and a field-effect mobility around 3×10^{-2} cm^2/Vs (Table 8.7) while other Ag inks reached an on-current about three orders of magnitude lower than the IC ink (conc. 30%), which becomes a

primary reason for the low performance. Conductivity of an Ag ink can be varied by wetting of an Ag ink onto a substrate and homogeneity of an Ag layer. Using of appropriate solvents for the Ag ink formulation which do not dissolve the underlying layer and good adhesion between the Ag layer and the underlying insulating layer are important for achieving high performance printed OFETs with the printed Ag ink electrode. High mobility of fully printed OFETs around 3×10^{-2} cm^2/Vs, which is even higher than the gravure printed P3HT with spin-coated insulator OFETs (Section 8.4) having a single dielectric layer ($1.3\text{-}1.8 \times 10^{-2}$ cm^2/Vs), can be explained by the enhanced insulating functionality from the double-layer insulating structure.

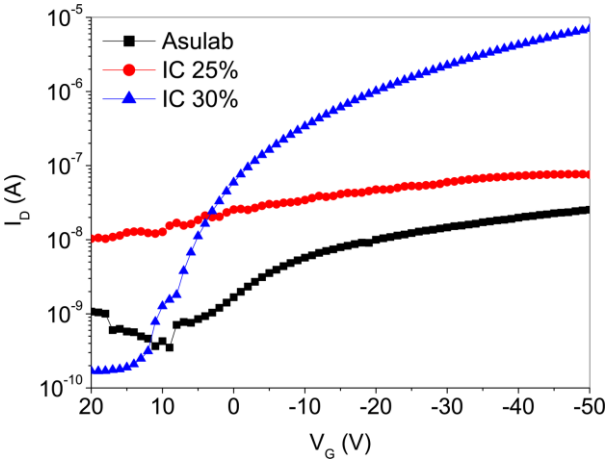


Figure 8.21 Transfer characteristics of OFETs with a variation of Ag nanoparticle inks. The devices were printed by M. Voigt and measured by A. Guite.

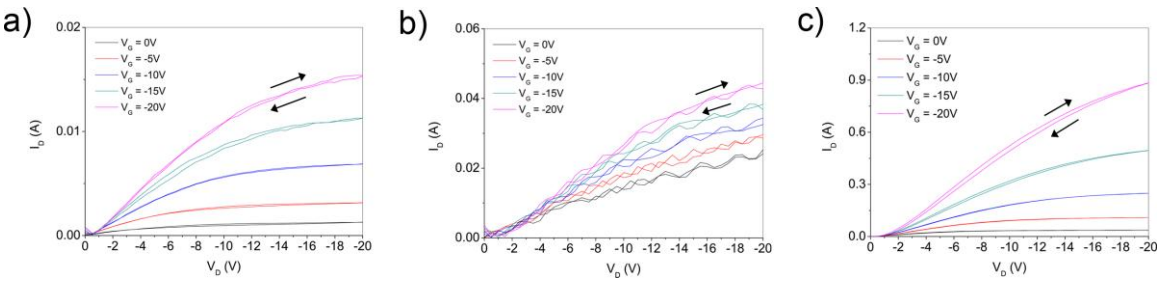


Figure 8.22 Output characteristics of OFETs with a variation of Ag nanoparticle inks: a) Asulab, b) Imperial College (conc. 25%), c) Imperial College (conc. 30%). The devices were printed by M. Voigt and measured by A. Guite.

Ag conductive ink	Linear Mobility (cm^2/Vs)	Saturation Mobility (cm^2/Vs)	V_T (V)	On-current (A)	Off-current (A)	On-off ratio	I_D/I_G ratio (at V_G = -50 V)
Asulab	7×10^{-5}	7×10^{-5}	12	2.5×10^{-8}	3.5×10^{-10}	$10^{1.86}$	< 1
Imperial College 25%	1.5×10^{-4}	1.5×10^{-4}	>20	7.7×10^{-8}	1×10^{-8}	$10^{0.86}$	4.3
Imperial College 30%	3×10^{-2}	3.3×10^{-2}	-8	7×10^{-6}	1.68×10^{-10}	$10^{4.62}$	21

Table 8.7 Performance parameters of fully gravure printed OFETs with a variation of Ag nanoparticle inks. The field-effect mobility was extracted at V_D= -50V (saturation) and -20V (linear) in transfer characteristic.

Finally, we demonstrate a high performance fully gravure printed OFET with a structure as ITO/P3HT/PHEMA/X-PHEMA/Ag. Microscopic images of sequential printing steps are depicted in Figure 8.23. In general, all the images show a good homogeneity in microscale with a small variation in surface roughness. This unevenness may reduce a yield rate of the printed OFETs and induce non-uniform transistor performance in each pixel in an array. As previously mentioned in Section 8.6, an ink formulation with high viscosity and concentration properties form well defined printed patterns while the roughness is relatively poor. For ink formulations in an application of OFETs, the resolution may be more important than the uniformity of printed patterns.

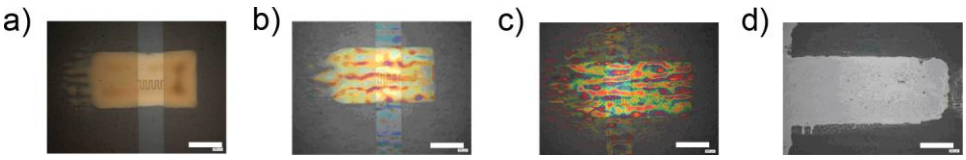


Figure 8.23 Microscopic images of fully printed OFETs sequentially as a) P3HT, b) PHEMA, c) X-PHEMA, d) Ag ink. A scale bar indicates 500 μm. The devices were printed and images were taken by M. Voigt.

Fully gravure printed a top gate-bottom contact OFETs on the pre-patterned ITO source/drain electrodes were successfully developed (Figure 8.24). The device performance is listed in Table 8.7 denoted as Imperial College 30%. Gate voltage dependence of field-effect mobility is observed in our fully printed OFETs (Figure 8.25). It turns into the saturation regime around V_G of -20 V with its consistent mobility around 0.03 cm^2/Vs at higher V_G. Output characteristic of the OFET can be found in

Figure 8.22c. It shows a good modulation of I_D and it is clearly saturated indicating a low level of extrinsic dopants residing in layers and at the interfaces.

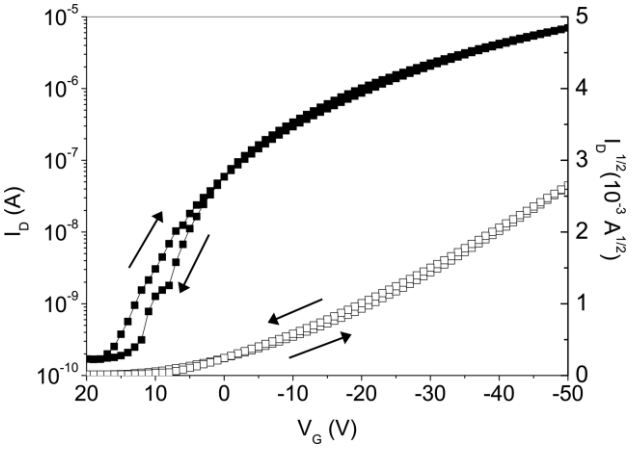


Figure 8.24 Fully gravure printed OFETs. Transfer characteristic (left ordinate, solid) and $I_D^{1/2}$ (right ordinate, open). Channel width and length are 1,300 and 50 µm respectively. Filled and empty symbols refer to left and right axis respectively. The device was printed by M. Voigt and measured by A. Guite.

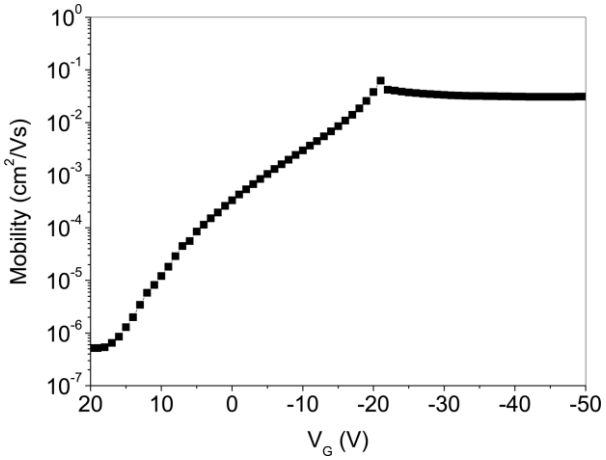


Figure 8.25 Gate voltage dependent mobility of fully gravure printed OFETs. Linear regime (V_G > -20 V) and saturation regime (V_G < -20 V). The device was printed by M. Voigt and measured by A. Guite.

8.9 Conclusion and Future Work

In summary, fully gravure printed OFETs on pre-patterned source/drain ITO electrodes were successfully developed. Fast processing speeds of gravure printing around 60 m^2/s are expected to compensate inherent weaknesses of organic materials. Polycrystalline

materials are versatile for OFETs with a high mobility up to 0.1 cm^2/Vs and its performance is strongly dependent with fabrication processes such as annealing and orientation of molecules. Our fully gravure printed P3HT showed enhanced mobility recorded 0.03 cm^2/Vs, which is about a magnitude order higher than the spin-coated OFETs ($3\text{-}5 \times 10^{-3}$ cm^2/Vs). It may be attributed to enhanced charge carrier mobility in the gravure printed P3HT with the preferentially aligned molecules or chains as well as the improved insulating property and reduced doping levels of impurity molecules. We have not confirmed any clear evidences for the oriented P3HT chains from our gravure printed films but it may have a tendency to align parallel to the printing direction with an applied external driving force. Unevenness in surface profile from the printed films in microscale was observed. Organic electronic devices have a thickness of a stack of layers usually less than 1 μm and its homogeneity critically affects the device operation. As a result, a low yield rate of gravure printed OFETs occurred. For application in OFETs, a high definition of pixels may be more important than uniformity as its pattern size is quite small generally less than 1 μm. We, therefore, introduced ink formulations with high viscosity and concentration even though it likely produces unevenness in surface morphology. Improvements in ink formulation and printing machine for uniform film surface are necessary.

To develop the current stage of gravure printing OFETs, investigation of molecular orientation in printed films using techniques such as GIWAXS is very promising for fruitful outcomes. Also, introducing SAMs, as surface treatment for favoured growth of crystals or a gate dielectric layer, should be useful in order to improve field-effect mobility together with lowered threshold voltage. Development of high resolution cliché pattern is vital for printing arrays of transistors, whose size is currently limited to around 100-200 μm. In addition, a complementary metal-oxide-semiconductor (CMOS) can be printed by developing of printable n-type materials such as poly (9,9-dioctylfluorene-*alt*-benzothiadiazole) (F8BT) and fullerene, C_{60}.

8.10 Reference

[1] A. Salleo, M. L. Chabinyc, M. S. Yang, R. A. Street, *Applied Physics Letters* **2002**, *81*, 4383.

[2] G. E. Poirier, E. D. Pylant, *Science* **1996**, *272*, 1145.

[3] A. Cossaro, R. Mazzarello, R. Rousseau, L. Casalis, A. Verdini, A. Kohlmeyer, L. Floreano, S. Scandolo, A. Morgante, M. L. Klein, G. Scoles, *Science* **2008**, *321*, 943.

[4] R. J. Kline, M. D. McGehee, M. F. Toney, *Nature Materials* **2006**, *5*, 222.

[5] H. Sirringhaus, R. J. Wilson, R. H. Friend, M. Inbasekaran, W. Wu, E. P. Woo, M. Grell, D. D. C. Bradley, *Applied Physics Letters* **2000**, *77*, 406.

[6] K. S. Whitehead, M. Grell, D. D. C. Bradley, M. Jandke, P. Strohriegl, *Applied Physics Letters* **2000**, *76*, 2946.

[7] H. Sirringhaus, T. Kawase, R. H. Friend, T. Shimoda, M. Inbasekaran, W. Wu, E. P. Woo, *Science* **2000**, *290*, 2123.

[8] D. A. Pardo, G. E. Jabbour, N. Peyghambarian, *Advanced Materials* **2000**, *12*, 1249.

[9] H. Yan, Z. H. Chen, Y. Zheng, C. Newman, J. R. Quinn, F. Dotz, M. Kastler, A. Facchetti, *Nature* **2009**, *457*, 679.

[10] D. Tobjork, N. J. Kalihovirta, T. Makela, F. S. Pettersson, R. Osterbackaa, *Organic Electronics* **2008**, *9*, 931.

[11] N. J. Kaihovirta, D. Tobjork, T. Makela, R. Osterbacka, *Advanced Engineering Materials* **2008**, *10*, 640.

[12] H. Sirringhaus, *Nature* **2009**, *457*, 667.

[13] S. R. Forrest, *Nature* **2004**, *428*, 911.

[14] G. P. Collins, *Scientific American* **2004**, *291*, 74.

[15] Y. Kim, S. A. Choulis, J. Nelson, D. D. C. Bradley, S. Cook, J. R. Durrant, *Applied Physics Letters* **2005**, *86*.

[16] S. Cho, K. Lee, J. Yuen, G. M. Wang, D. Moses, A. J. Heeger, M. Surin, R. Lazzaroni, *Journal of Applied Physics* **2006**, *100*.

[17] W. L. Ma, C. Y. Yang, X. Gong, K. Lee, A. J. Heeger, *Advanced Functional Materials* **2005**, *15*, 1617.

[18] J. F. Chang, J. Clark, N. Zhao, H. Sirringhaus, D. W. Breiby, J. W. Andreasen, M. M. Nielsen, M. Giles, M. Heeney, I. McCulloch, *Physical Review B* **2006**, *74*.

[19] J. F. Chang, B. Q. Sun, D. W. Breiby, M. M. Nielsen, T. I. Solling, M. Giles, I. McCulloch, H. Sirringhaus, *Chemistry of Materials* **2004**, *16*, 4772.

[20] J. Veres, S. Ogier, G. Lloyd, D. de Leeuw, *Chemistry of Materials* **2004**, *16*, 4543.

[21] L. A. Majewski, J. W. Kingsley, C. Balocco, A. M. Song, *Applied Physics Letters* **2006**, *88*.

[22] A. Zen, J. Pflaum, S. Hirschmann, W. Zhuang, F. Jaiser, U. Asawapirom, J. P. Rabe, U. Scherf, D. Neher, *Advanced Functional Materials* **2004**, *14*, 757.

[23] S. Hoshino, M. Yoshida, S. Uemura, T. Kodzasa, N. Takada, T. Kamata, K. Yase, *Journal of Applied Physics* **2004**, *95*, 5088.

[24] L. A. Majewski, J. W. Kingsley, C. Balocco, A. M. Song, *Applied Physics Letters* **2006**, *88*.

[25] G. Horowitz, M. E. Hajlaoui, *Advanced Materials* **2000**, *12*, 1046.

[26] G. M. Wang, J. Swensen, D. Moses, A. J. Heeger, *Journal of Applied Physics* **2003**, *93*, 6137.

[27] D. J. Gundlach, L. Zhou, J. A. Nichols, T. N. Jackson, P. V. Necliudov, M. S. Shur, *Journal of Applied Physics* **2006**, *100*.

[28] M. L. Chabinyc, J. P. Lu, R. A. Street, Y. L. Wu, P. Liu, B. S. Ong, *Journal of Applied Physics* **2004**, *96*, 2063.

[29] D. J. Gundlach, J. E. Royer, S. K. Park, S. Subramanian, O. D. Jurchescu, B. H. Hamadani, A. J. Moad, R. J. Kline, L. C. Teague, O. Kirillov, C. A. Richter, J. G. Kushmerick, L. J. Richter, S. R. Parkin, T. N. Jackson, J. E. Anthony, *Nature Materials* **2008**, *7*, 216.

[30] A. Bashir, P. H. Wobkenberg, J. Smith, J. M. Ball, G. Adamopoulos, D. D. C. Bradley, T. D. Anthopoulos, *Advanced Materials* **2009**, *21*, 2226.

[31] M. J. Lee, S. I. Kim, C. B. Lee, H. X. Yin, S. E. Ahn, B. S. Kang, K. H. Kim, J. C. Park, C. J. Kim, I. Song, S. W. Kim, G. Stefanovich, J. H. Lee, S. J. Chung, Y. H. Kim, Y. Park, *Advanced Functional Materials* **2009**, *19*, 1587.

[32] J. Smith, A. Bashir, G. Adamopoulos, J. E. Anthony, D. D. C. Bradley, R. Hamilton, M. Heeney, I. McCulloch, and T. D. Anthopoulos, *Adv. Mater*. **2010**, *22*, 3598.

[33] P. H. Wobkenber, J. Ball, F. B. Kooistra, J. C. Hummelen, D. M. de Leeuw, D. D. C. Bradley, T. D. Anthopoulos, *Applied Physics Letters* **2008**, *93*.

[34] Y. H. Noh, S. Y. Park, S. M. Seo, H. H. Lee, *Organic Electronics* **2006**, *7*, 271.

[35] J. Veres, S. D. Ogier, S. W. Leeming, D. C. Cupertino, S. M. Khaffaf, *Advanced Functional Materials* **2003**, *13*, 199.

[36] J. Veres, S. Ogier, G. Lloyd, D. de Leeuw, *Chemistry of Materials* **2004**, *16*, 4543.

[37] A. Guite, *Transfer Report*, Imperial College London, **2007**.

[38] S. Y. Park, M. Park, H. H. Lee, *Applied Physics Letters* **2004**, *85*, 2283

[39] D. M. Russell, T. Kugler, C. J. Newsome, S. P. Li, M. Ishida, T. Shimoda, *Synthetic Metals* **2006**, *156*, 769.

[40] M. Berggren, D. Nilsson, N. D. Robinson, *Nature Materials* **2007**, *6*, 3.

[41] M. Tuomikoski, R. Suhonen, M. Valimakia, T. Maaninen, A. Maaninen, M. Sauer, P. Rogin, M. Mennig, S. Heusing, J. Puetz, M. A. Aegerter, *Organic Optoelectronics and Photonics II* **2006**, *6192*, 19204.

[42] H. Yan, Z. H. Chen, Y. Zheng, C. Newman, J. R. Quinn, F. Dotz, M. Kastler, A. Facchetti, *Nature* **2009**, *457*, 679.

[43] M. M. Voigt, A. Guite, D. Y. Chung, R. U. A. Khan, A. J. Campbell, D. D. C. Bradley, F. S. Meng, J. H. G. Steinke, S. Tierney, I. McCulloch, H. Penxten, L. Lutsen, O. Douheret, J. Manca, U. Brokmann, K.

Sonnichsen, D. Hulsenberg, W. Bock, C. Barron, N. Blanckaert, S. Springer, J. Grupp, A. Mosley, *Advanced Functional Materials* **2010**, *20*, 239.

[44] H. Sirringhaus, T. Kawase, R. H. Friend, T. Shimoda, M. Inbasekaran, W. Wu, E. P. Woo, *Science* **2000**, *290*, 2123.

[45] T. Sekitani, Y. Noguchi, U. Zschieschang, H. Klauk, T. Someya, *Proceedings of the National Academy of Sciences of the United States of America* **2008**, *105*, 4976.

[46] J. Z. Wang, Z. H. Zheng, H. W. Li, W. T. S. Huck, H. Sirringhaus, *Nature Materials* **2004**, *3*, 171.

[47] J. Z. Wang, J. Gu, F. Zenhausem, H. Sirringhaus, *Applied Physics Letters* **2006**, *88*.

[48] J. U. Park, M. Hardy, S. J. Kang, K. Barton, K. Adair, D. K. Mukhopadhyay, C. Y. Lee, M. S. Strano, A. G. Alleyne, J. G. Georgiadis, P. M. Ferreira, J. A. Rogers, *Nature Materials* **2007**, *6*, 782.

[49] Y. Y. Noh, N. Zhao, M. Caironi, H. Sirringhaus, *Nature Nanotechnology* **2007**, *2*, 784.

[50] R. J. Kline, M. D. Mcgehee, M. F. Toney, *Nature Materials* **2006**, *5*, 222.

[51] Y. Kim, S. Cook, S. M. Tuladhar, S. A. Choulis, J. Nelson, J. R. Durrant, D. D. C. Bradley, M. Giles, I. Mcculloch, C. S. Ha, M. Ree, *Nature Materials* **2006**, *5*, 197.

[52] L. H. Jimison, M. F. Toney, I. McCulloch, M. Heeney, A. Salleo, *Advanced Materials* **2009**, *21*, 1568.

[53] J. Rivnay, L. H. Jimison, J. E. Northrup, M. F. Toney, R. Noriega, S. F. Lu, T. J. Marks, A. Facchetti, A. Salleo, *Nature Materials* **2009**, *8*, 952.

[54] G. Horowitz, M. E. Hajlaoui, *Synthetic Metals* **2001**, *122*, 185.

[55] H. Sirringhaus, P. J. Brown, R. H. Friend, M. M. Nielsen, K. Bechgaard, B. M. W. Langeveld-Voss, A. J. H. Spiering, R. A. J. Janssen, E. W. Meijer, P. Herwig, D. M. de Leeuw, *Nature* **1999**, *401*, 685.

[56] R. J. Kline, M. D. McGehee, E. N. Kadnikova, J. S. Liu, J. M. J. Frechet, *Advanced Materials* **2003**, *15*, 1519.

[57] H. Ishikawa, X. F. Xu, A. Kobayashi, M. Satoh, M. Suzuki, E. Hasegawa, *Journal of Physics D-Applied Physics* **1992**, *25*, 897.

[58] J. M. Verilhac, R. Pokrop, G. LeBlevennec, I. Kulszewicz-Bajer, K. Buga, M. Zagorska, S. Sadki, A. Pron, *Journal of Physical Chemistry B* **2006**, *110*, 13305.

[59] J. M. Verilhac, G. LeBlevennec, D. Djurado, F. Rieutord, M. Chouiki, J. P. Travers, A. Pron, *Synthetic Metals* **2006**, *156*, 815.

[60] R. J. Kline, M. D. McGehee, E. N. Kadnikova, J. S. Liu, J. M. J. Frechet, M. F. Toney, *Macromolecules* **2005**, *38*, 3312.

[61] H. N. Tsao, D. Cho, J. W. Andreasen, A. Rouhanipour, D. W. Breiby, W. Pisula, K. Mullen, *Advanced Materials* **2009**, *21*, 209.

[62] H. Sirringhaus, N. Tessler, R. H. Friend, *Science* **1998**, *280*, 1741.

[63] A. Salleo, M. L. Chabinyc, M. S. Yang, R. A. Street, *Applied Physics Letters* **2002**, *81*, 4383.

[64] A. Zen, J. Pflaum, S. Hirschmann, W. Zhuang, F. Jaiser, U. Asawapirom, J. P. Rabe, U. Scherf, D. Neher, *Advanced Functional Materials* **2004**, *14*, 757.

[65] R. D. Deegan, O. Bakajin, T. F. Dupont, G. Huber, S. R. Nagel, T. A. Witten, *Nature* **1997**, *389*, 827.

[66] J. A. Lim, W. H. Lee, H. S. Lee, J. H. Lee, Y. D. Park, K. Cho, *Advanced Functional Materials* **2008**, *18*, 229.

[67] S. Hoshino, M. Yoshida, S. Uemura, T. Kodzasa, N. Takada, T. Kamata, K. Yase, *Journal of Applied Physics* **2004**, *95*, 5088.

[68] H. G. O. Sandberg, T. G. Backlund, R. Osterbacka, M. Shkunov, D. Sparrowe, I. McCulloch, H. Stubb, *Organic Electronics* **2005**, *6*, 142.

[69] F. L. Xue, Z. C. Liu, Y. Su, K. Varahramyan, *Microelectronic Engineering* **2006**, *83*, 298.

[70] S. Gamerith, A. Klug, H. Scheiber, U. Scherf, E. Moderegger, E. J. W. List, *Advanced Functional Materials* **2007**, *17*, 3111.

[71] D. Kim, S. Jeong, H. Shin, Y. Xia, J. Moon, *Advanced Materials* **2008**, *20*, 3084.

[72] www.inktec.com

Chapter IX
Conclusion and Future Work

In this Chapter, key results of each experimental chapter are summarized as a conclusion. Also, recommended future works are listed which are based on the experiences from the current research.

Chapter 5: High Performance, Flexible Polymer Light-Emitting Diodes (PLEDs) with Gravure Printed Organic Layers

In Chapter 5, it has been demonstrated that organic layers in an application of PLEDs can be gravure printed and its performance is identical to PLEDs with the organic layers deposited by conventional spin-coating method. PEDOT:PSS as a hole injection layer and LG1300 as a light-emissive layer were gravure printed. It showed that gravure printed PLEDs have a uniform light-emission area, which suggests that surface homogeneity of the printed thin films is very good. Tapping mode AFM measurement indicated that the RMS values of the organic layers achieved ~1.2 nm and ~0.7 nm for PEDOT:PSS and LG1300 layers, respectively. These values are identical to the surface roughness of the spin-coated layers using the same materials. Unlike the gravure printed thin films in Chapter 8, the enhanced performance was not observed as both organic materials are amorphous so that preferred molecular orientation along the printing direction is negligible. PEDOT:PSS is an aqueous solution and its high surface energy larger than surface energy of ITO substrate is problematic, which often produces dewetting. A low boiling point solvent alcohol and a small portion of surfactant were used to improve wetting and disrupting an outward convection flow (coffee stain effect),

respectively. For a case of printing LG1300 dissolved in a non-polar solvent, a mixture of solvent was prepared in order to balance the hydrodynamic movements inside the printed formulations such as an outward convection flow (coffee stain effect) and an inward Marangoni flow. A mixture of a low boiling point and a high boiling point non-polar solvents improved surface uniformity by inducing the Marangoni flow. A maximum luminance of 65,900 cd/m^2 and a maximum efficiency of 8.8 cd/A and 5.4 lm/W were obtained from the gravure printed PLEDs, which are very similar to the performance of spin-coated PLEDs having maximum luminance of 55,700 cd/m^2 and maximum efficiency of 9 cd/A and 5.7 lm/W.

Future Work

To maximize the processing advantages of gravure contact printing for optoelectronic devices, all layers need to be sequentially printed including metallic electrodes. Currently, normal structure PLEDs, where a high workfunction metal is positioned at the bottom and a low workfunction metal is positioned as a top electrode, face a critical problem when printing the top electrode. Low workfunction metals such as Ca or LiF are very sensitive in air ambient and easily oxidized, hence preparation of metallic inks using such materials is not possible. Recently, it has been reported that 'inverted structure' where a high workfunction metal is located as a top electrode is available. A design of inverted structure PLEDs can be the next research subject. Chapter 6 and 7 discuss about inverted PLEDs.

Chapter 6: Flexible Multilayer Hybrid Polymer Light-Emitting Diodes (PLEDs) with a Gravure Printed Cs_2CO_3 Layer

In Chapter 6, it was demonstrated about high efficient F8BT/TFB multilayer inverted PLEDs using a Cs_2CO_3 layer deposited by gravure contact printing type. Currently reported inverted PLEDs have a performance that is inferior to the PLEDs with normal structure attributed to unbalancing of charge carriers (holes and electrons) injection and a recombination zone is formed close to the metal electrodes where the most of excitons and charged carriers are quenched. We introduced a multilayer of F8BT and TFB layer

which has the interface with large energy offsets for both holes and electrons, hence both types of charged carriers can be accumulated at the interface. However, the two polyflourene polymers have similar chemical compositions and can be dissolved in common dispersive organic solvents. We found that F8BT has a lower solubility than TFB polymer and an orthogonal solvent is available, which only dissolves TFB. In addition, an ultra thin layer of Cs_2CO_3 was both spin-coated and gravure printed. To disrupt outward convection flow of Cs_2CO_3 solution (2-ethoxyethanol), a small volume of a surfactant was mixed achieving uniformly printed Cs_2CO_3 layer. Inverted PLEDs with the gravure printed Cs_2CO_3 layer achieved a maximum luminance of 7,200 cd/m^2 and efficiency of 10 cd/A and 3 lm/W which are comparable to the performance of normal structure PLEDs. Inverted PLEDs with the spin-coated Cs_2CO_3 layer using the same materials showed luminance of 10,400 cd/m^2 and efficiency of 3.11 cd/A and 0.94 lm/W. We suggest that enhanced efficiency is attributed to the surface roughness of the Cs_2CO_3 layer formed on either crystal or amorphous ITO. Low heat susceptibility of flexible substrate could only develop amorphous type ITO on the substrate during e-beam sputtering. We found amorphous ITO is in favour to the surface uniformity of Cs_2CO_3 layer which was probed by tapping mode AFM measurement showing the RMS values of 2.68 nm on crystalline ITO and 1.56 nm on amorphous ITO. Furthermore, the uniformity of gravure printed Cs_2CO_3 layer is improved as 1.14 nm RMS. I believe that it is owing to a pressing force between the cylindrical roll and a flexible substrate while inks are transferred. The pressing force reduced voids between Cs_2CO_3 particles and improved an order of the Cs_2CO_3 particles.

Future Work

A next step can be printing of other layers using the same structure PLEDs. For the next step, F8BT and TFB polyflourene polymers can be gravure contact printed. F8BT is a polycrystalline material and it should be intriguing to investigate molecular directionality of printed F8BT and its effect on device performance. Also, a study of solubility parameters such as Hilderbrand and Hansen models for defining solubility of polymers should help with a scientific proof of building a multilayer structure. Solubility of a material is varied by its molecular weight, hence it could tailor its

solubility parameters to appropriate values. Studying of the effect of molecular weight with different lengths of polymer chains and investigation of solubility parameters of other popular polymers could be interesting research topics for realization of fully printed optoelectronic devices.

Chapter 7: Air-Stable, Flexible F8BT/TFB PLEDs having High Efficiency

In Chapter 7, it was demonstrated about high efficient inverted PLEDs with a highly stable top electrode. A high efficiency of 35.86 cd/A and 22.8 lm/W together with a maximum luminance of 51,200 cd/m^2 were obtained at thick layers of both F8BT and TFB. Turn-on voltage was slightly increased to 4.2 V at 100 cd/m^2 owing to the required electric field being higher in thicker layers. To the best of knowledge, the efficiency obtained is the highest efficiency using fluorescent polymeric materials. I suggest that the high efficiency is attributed to the recombination zone positioned at close to the F8BT/TFB interface where exciton and charge carrier transfer are actively occur within its narrow diffusion range (30 nm). The Coulombic force between the accumulated holes and electrons with opposite charge type can be very strong at that region as number of charged carriers at the interface increases. Electroluminance (EL) spectra of device with different thicknesses of F8BT and TFB layers support the argument which shows that EL spectrum of F8BT/TFB bilayer with thicker thickness resembles to the spectrum of F8BT:TFB blend layers, where electron and hole recombination is occurred by barrier free electron-hole capture. In addition, low processing temperature in building the device contributed to demonstration of the device on a flexible PET substrate. High efficient PLEDs with enhanced air-stability on flexible substrates suggest a possibility of printing all layers of the device including metallic electrodes, for example, by a roll-to-roll printing for a fast line production.

<u>Future Work</u>

Gravure printing of all the layers of the same structure with thicker F8BT and TFB layers can be the next step of research. The PEDOT:PSS formulation is already developed previously for spin-coating, which shows a complete wetting onto the TFB

surface. The same formulation can be used for gravure printing. For printing of metallic electrodes, there are several candidate metals can be chosen such as Ag paste inks. In addition, VPP-PEDOT is also a good candidate. To print VPP-PEDOT, firstly, oxidant can be gravure printed prior to vapour phase polymerization process. Also, 1D carbon nanotube or 2D graphene sheet can be used as electrodes. A suggested structure of PLEDs with fully printed layers is a top emission structure with its layers of flexible substrate / Ag / Cs_2CO_3 / F8BT / TFB / PEDOT:PSS / VPP-PEDOT or SW-CNT or Graphene. As I mentioned in Chapter 6, it is surely interesting to investigate any preferred orientation of polycrystalline F8BT polymer layer after gravure printing. With the effect of a fast charge carrier transport in the F8BT layer, it may be possible to reduce a turn-on voltage of the device with thicker layers further.

Chapter 8: Developing Gravure Contact Printed Flexible Polythiophene Thin-Film Transistors (TFTs)

In Chapter 8, fully gravure printed OFETs on the pre-patterned source/drain ITO on PES flexible substrate were successfully demonstrated. A printing speed of 35 m/min was used to print all the layers and we believe that the fast speed can eventually compensate the weakness of organic materials in terms of its material property. P3HT is a polycrystalline p-type semiconductor and 0.1 cm^2/Vs of field-effect mobility has been reported using the material. Polycrystalline materials are intriguing as device performance using this type of materials can be enhanced by modification of processing conditions such as annealing and ambient condition. The high mobility OFETs of 0.03 cm^2/Vs using gravure contact printing technique, which is an order of magnitude higher than the devices with the same structure deposited by spin-coating ($3\text{-}5 \times 10^{-3}$ cm^2/Vs) were obtained. We suggest this performance enhancement is attributed to molecular chain structures after being deposited and there may exist a preferential orientation of P3HT chains along the printing direction. There have been a lot of reports regarding performance enhancement by modifying processing techniques. We used high viscous formulations using high concentration inks and high boiling point solvents. Printing with high viscous inks is similar to printing for graphic arts and it is suitable for high definition patterns but may print with uneven surface roughness. Alternatively,

homogeneity of printed thin films can be significantly improved by using low viscosity inks, which induces sufficient hydrodynamic movements inside the printed formulations while it dries. We discussed this method in Chapter 5 and 6.

Future Work

Investigation of molecular orientation of printed polycrystalline thin films is an interesting experiment to study effects of single-directional driving force on device performance. GIWAXS is such a useful measurement tool to find out any directionalities in organic molecular chains. Currently, a driving voltage of printed OFETs is high around ~10V. To reduce the turn-on voltage, a dielectric material with a high dielectric constant can be implemented. Oxide layers such as ZnO and TiO_2 are popular materials providing both high capacitance and air-stability. Also, printing of SAMs as a gate dielectric layer is another interesting research topic. Development of a cliché with high resolution patterns is vital for printing arrays of transistors, whose width is currently limited to around 100-200 μm.